Filamentarity and inhomogeneities in low dimensional superconductors

Scuola di dottorato Vito Volterra

Dottorato di Ricerca in Fisica – XXXIV Ciclo

Candidate

Giulia Venditti
ID number 1535561

Thesis Advisors

Prof. Sergio Caprara
Prof. Marco Grilli

May 27, 2022

Filamentarity and inhomogeneities in low dimensional superconductors
Ph.D. thesis. Sapienza – University of Rome

This thesis has been typeset by LaTeX and the Sapthesis class.

Version: May 27, 2022

Author's email: g.venditti@uniroma1.it

Do or do not, there is no try.

`Yoda`

Abstract

In this Thesis, I investigate the problem of the interplay between disorder and low dimensionality in superconductors.

From the *microscopic* point of view, I show that the presence of impurities in the superconducting condensate can produce a pairbreaking effect at the Lifshitz transition in multibands superconductors, avoiding or at least circumventing Anderson's Theorem. This is consistent with the observed suppression of the superconducting critical temperature T_c in $SrTiO_3$-based heterostructures as a function of the gate potential V_G. This study allows us to disentangle *microscopic* from *mesoscopic* disorder in $SrTiO_3$-based interfaces: microscopic impurities are in fact necessary to explain the suppression of T_c observed when multiband superconductivity is involved; the global behavior is instead well captured only if the strongly inhomogeneous nature of such compounds is considered.

Indeed, disorder can also appear on a *mesoscopic* length scale. The electronic condensate can in fact segregate into regions large enough to define a local phase but small compared with the sample. The reasons behind this inhomogeneity of the superconducting order parameter can be several, depending on the system in exam: in oxides heterostructures it may be connected to the thermodynamic instability caused by the electrostatic potential confining the electron gas at the interface, in transition metal dichalcogenides the instability may be introduced by the gating ionic liquid, whereas sometimes the phase separation can be caused by the presence of microscopic impurities in addition with the competition of superconductivity with another order parameter, e.g., the charge ordering in the case of cuprates. Such a phase separation may appear as a filamentary structure.

Concerning *mesoscopic* inhomogeneities, I will focus on two different materials.

In $SrTiO_3$-based heterostructures, where filamentary superconductivity is embedded in a metallic matrix, I study the consequences of filamentarity in transport properties, assuming *a priori* a fractal-like organization of the electronic condensate and calculating the complex conductance with a Random Impedance Network model. The geometry of the filamentary structure plays a crucial role, especially in the behavior of the superfluid stiffness as a function of the temperature. Although the motivation of this work is connected to resonant microwave experiments performed on a $LaAlO_3/SrTiO_3$ interface, the results are quite general and can in principle be applied to other materials displaying filamentary superconductivity.

In cuprates, I focus on the phase competition as the most likely reason of filamentarity. The charge ordering-superconducting (CO-SC) competition is studied by means of Monte Carlo simulations within an anisotropic Heisenberg model accounting for the basic physical symmetries involved, the out-of-plane pseudospin component mapping two possible charge density waves (CDW) variants while the in-plane component standing for the SC order parameter. The anisotropy term α is taken as the control parameter, tuning the transition from Berezinskii-Kosterlitz-Thouless (BKT) to the charge ordered state. The phase diagram T_c vs α is studied both in the clean case and in a random field, the presence of *microscopic* impurities being necessary to stabilize the clustering of charge ordered domains and the appearance of filamentary superconductivity.

Ringraziamenti

Questa tesi è il frutto di 3 anni e mezzo di duro lavoro. E dopo 3 anni e mezzo di duro lavoro, sarebbe davvero da ingrati non scrivere i dovuti ringraziamenti.

Devo ringraziare anzitutto il mio gruppo di ricerca, che nonostante il mondo fuori, non mi ha fatto mai sentire il peso del publish or perish *ma continua a perseguire il motto* learn and enjoy.

Un grazie particolare lo devo a Sergio, che ha seguito passo passo la mia crescita professionale dai tempi della Laurea Triennale, in cui ancora non mi era chiaro che avrei intrapreso la faticosa strada della ricerca. Con pazienza e disponibilità ha seguito tutti i miei passi, ha risposto a tutte le mie domande, anche quelle (che reputavo) più banali. È stato forse il capo che tutti vorremmo: mai pressante, ma sempre presente e disponibile. La sua cultura e la sua curiosità intellettuale, che abbraccia non solo la fisica ma, direi, tutto lo scibile umano, sono le qualità che aspiro non solo ad avere, ma a tenermi stretta da qui ai giorni a venire.

Grazie a Marco, che nonostante i suoi mille impegni ha trovato sempre il modo di discutere di fisica con me, che riesce a far ritrovare la motivazione su un progetto anche quando sembra persa.

Grazie a Josè, che è sempre stato disponibile ad aiutarmi e a confrontarsi, che mi ha seguito in modo puntuale nell'ultimo anno e mezzo, restituendomi sempre, oltre alla curiosità scientifica, una gentilezza umana non banale.

Grazie a Maria, per essere un'amica e una collega sensibile e sempre entusiasta.

Grazie a tutti i dottorandi e i postdoc e ad Andrea e Daniele, per le ore del patio, per lo yoga e per aver superato insieme il covid. Senza di loro, questi ultimi due anni di pandemia sarebbero stati davvero insopportabili. Una menzione d'onore va ad Andrea, anche perché ha sempre messo a disposizione la sua casa come fosse un b&b, una palestra, un set fotografico.

Devo ringraziare anche quella massa di nerd sconosciuti che popola i forum di programmazione (StackExchange, StackOverflow, ecc...) senza i quali più della metà di questa tesi non ci sarebbe.

Grazie ai miei genitori, Gabriella e Beppe, che si sorbiscono da 29 anni le mie isterie sul "non ce la farò" e che, anche questa volta, sapevano già prima di me che sarebbe andata bene. Grazie, soprattutto, per avermi cresciuta con la consapevolezza che, tutto sommato, tutto è possibile.

Grazie a mia cugina Valeria, che si sente in colpa perché sa di aver giocato un ruolo nella mia decisione di prendere un Ph.D.

Grazie a tutti gli amici, a quelli di sempre, a quelli nuovi, a quelli con cui non mi sento più.

A Flavio e Cathy, i coinquilini perfetti per vivere in una famiglia in cui non ci sono tutte le complicazioni della famiglia.

A Flavia, Luciano, Andrea, Corinne, Nakia, Riccardo, Monica, Jacopo.

Agli amici scatterati per i due emisferi: Giulia, Filippo, Davide e Angelo, riprova che le distanze fisiche, ormai, non contano più nulla.

Grazie a Cristina e a tutte le coraggiose che si sono imbarcate nei parchi e, nell'ultimo anno, sulla Cassia, pur di continuare a fare danza insieme. Anche alle "meno coraggiose" che purtroppo non hanno potuto.

Grazie alle due amiche con le quali so che posso fare qualsiasi cosa al mondo, se ci loro accanto: Alessia e Ilaria.

Grazie a Simone, per essere meraviglioso.

Sembra brutto metterlo nero su bianco, ma devo ringraziare anche e soprattutto me stessa, per aver tenuto duro, per aver lavorato sodo, per essermi riconosciuta, alla fine, e forse ancora non abbastanza, questi anni di crescita personale e professionale. Poter ringraziare me stessa non è però una conquista che devo a me stessa.

Un doveroso e infinito grazie va quindi a Mariapia, per tutte quelle volte che ha sbattuto il piedino con fare decisamente serio, per le frustrazioni, passate, presenti e future, dirette e indirette. Per i sorrisi, anche se nascosti dalla mascherina. Per avermi regalato la possibilità di riappropriarmi di ciò che è mio. Perché, piano piano, mi sta regalando la possibilità di una nuova, luminosa estate. Grazie al Gruppo.

Infine, grazie a Massimo.

"Forse quello a cui non ci si può opporre
è la realtà della conoscenza; se ci si oppone
alla realtà della ricerca e della conoscenza,
l'individuo muore, perché si lede
la specificità, scusate le parole, della specie
umana che è la ricerca e la conoscenza,
il sapere."

Storia di una ricerca. Lezioni 2002,
Massimo Fagioli

Introduction

More than a century after the discovery of superconductivity in mercury by H. K. Onnes [1], this state of matter still offers many challenges. The systematic study of the phenomenon passed through many phenomenological theories apt to describe the odd observations, concerning in particular the Meissner effect. The London equations and the Ginzburg Landau theories provided fine results, the former having their basis in the Maxwell equations, the latter addressing more generally second order phase transitions. A microscopic theory about the origin of the attractive interaction between electrons will be given only in the early 1950s with the famous Bardeen-Cooper-Schrieffer (BCS) theory [2,3]. However, the discovery of high-temperature superconductivity in cuprates [4] changed the game: until then, the only mechanism hypothesized to justify the effective attraction between electrons (the so-called *glue*) was the electron-phonon coupling, which was however able to predict only superconductors with a low critical temperature T_c. Even today, the origin of superconductivity in cuprates, as in many other materials, is still debated and we still call tautologically "conventional superconductors" the ones well described by the weak electron-phonon coupling of BCS theory, while all the other superconductors are referred to as "unconventional".

On the other hand, the remarkable progress made so far in material science made it possible to engineer really low dimensional systems, such as compounds with truly atomic thickness, paving the way for the observation of new phenomena, among which we find topological phase transitions. One of the most fascinating examples of topological phase transitions remains the one described by the Berezinskii-Kosterlitz-Thouless (BKT) theory [5–7], whose applicability ranges from the quantum metal-insulator transition in one dimension to the Coulomb-gas screening transition in two dimensions, and of course the two-dimensional metal-to-superconductor transition. The power of the BKT transition relies in the fact that it circumvents the Mermin-Wagner theorem [8], which states rigorously that the one- and two-dimensional isotropic Heisenberg models with short range interactions have no long-range order at any finite temperature T. For their work on the transition, Kosterlitz and Thouless have been awarded by the 2016 Nobel Prize in Physics. Nevertheless, the experimental observations in real materials do not often follow literally the BKT predictions. Concerning the superconductive transition, a typical example is the behavior of the superfluid density (or stiffness): according to the BKT theory, the stiffness is expected to exhibit a discontinuous jump to zero as soon as the BKT critical temperature is reached coming from lower T, leading to the sudden vanishing of the superconducting state. In real systems, the presence of disorder at different levels can however smear, broaden and eventually cover the signatures of a BKT

transition.

Nonetheless, the presence of disorder can make things much more complicated yet much more intriguing, sometimes leading to completely new phenomena. This is exactly the case of two-dimensional superconductors, where new and unexpected transport properties arise due to disorder.

For weakly disordered superconductors, Anderson [9] showed that nonmagnetic impurities do not affect significantly the superconducting transition: starting from the BCS theory, the pairing mechanism leading to long-range phase coherence persists and the critical temperature is almost unchanged. Localization effects appear when the disorder is increased toward the strong disorder limit and measurements register a gradual decrease of T_c . However, in such cases, one should expect that superconductivity is drastically suppressed. The answer to this apparent anomaly was given by P. Lee and M. Ma in 1985 [10], following the original idea of Anderson. They proposed that even if single-particle states get localized by disorder, superconductivity can survive if there are enough localized states in a range of energy Δ, i.e., the superconducting gap. However, many mechanisms other than Anderson's localization can intervene, generating spatial inhomogeneities.

In this Thesis, we investigated many ways in which low-dimensionality and disorder interplay, with a particular emphasis on a new paradigm starting to emerge, namely filamentary superconductivity. The very interesting aspect of filamentary superconductivity is the fact that this topic can be addressed in many ways and on many levels of understanding, also because very little is known so far, from the theoretical point of view. In particular, two main materials will be considered as exemplary cases, in which filamentarity can arise from very different causes: $SrTiO_3$-based interfaces and cuprates, both presenting a very rich variety of properties other than superconductivity.

The presence of a highly mobile two-dimensional electron gas (2DEG) was detected at the interface between two insulating perovskite oxides, Strontium Titanate ($SrTiO_3$) and Lanthanum Aluminate ($LaAlO_3$), by Ohtomo and Hwang [11] in 2004. Thereafter, an increasingly intense theoretical and experimental investigation has been devoted to these systems, whose carrier density n can be tuned by means of gate voltage V_G making the 2DEG superconducting, thus opening the way to voltage-driven superconducting devices. Besides, the 2DEG exhibits magnetic properties and a strong and tunable Rashba spin-orbit coupling. Moreover, it is extremely two-dimensional, with a lateral extension of ≈ 5 nm, enhancing the effect of disorder, whose origin can be due to extrinsic and/or intrinsic sources. Similar results hold true also for other heterostructures such as $LaTiO_3/SrTiO_3$, where the role of Lanthanum Aluminate is taken by Lanthanum Titanate $LaTiO_3$. However, the situation about such compounds is still far from being settled, from many points of view. From the microscopic point of view, the very origin of superconductivity is still a matter of intense debate as it is the superconducting dome of their phase diagram T_c vs V_G. As a matter of fact, the suppression of the critical temperature observed at high gate voltages – where multiband superconductivity seems to emerge – is one of the unsolved issues and it will be one of the topics we will address in this Thesis [12, 13].

From a more "macroscopic" point of view, instead, many experimental indica-

tions point towards the strongly inhomogeneous nature of the 2DEG, preventing the observation of a BKT transition: tunneling [14,15], atomic force microscopy [16], and critical current experiments [17] provide clear evidence of an inhomogeneous interface. Transport measurements report further signs of inhomogeneity. Particularly, the large broadening of the resistive transition and the long tails observed at low temperatures cannot be reproduced by reasonable paraconductive effects [18]. Instead, those features can be well described by a percolative scenario within a Random Resistor Network model [19–22]. The tendency to an electronic phase separation [23] has been proposed as the leading mechanism generating a deeply inhomogeneous superconducting state with a rather filamentary character [19]. Recently, new resonant microwave transport measurements on $SrTiO_3$-based interfaces allowed direct access to the superfluid stiffness and the optical conductivity, providing further evidences of filamentary superconductivity [24–27]. In particular, observing the data at different gate voltages two regimes will be identified and they will be referred to as underdoped (UD) and overdoped (OD), depending on whether the carrier density is smaller or larger than the carrier density at which the maximum T_c is observed. The difference between the two regimes will be discussed henceforth in terms of a more or less dense fractal of superconducting filaments in presence of a proximization process on the underlying metal [25–27].

Evidences of filamentary superconductivity have been found also in cuprates. Although the discovery of cuprates dates back to 1986, many issues remain unsolved. Those layered insulating materials display in fact a wide phenomenology once chemically doped. Referring here only to the hole-doped side of their phase diagram, they present an insulating Mott phase at low dopings with long-range antiferromagnetic order; increasing the doping, a superconducting dome is observed above which they undergo a transition to a metallic phase which does not however fit in the standards of a Fermi liquid. Those materials are also good candidates to look for the BKT transition and clear BKT signatures have been recently found in bulk $La_{2-x}Sr_xCuO_4$ [28]. However, the rich phenomenology presented by cuprates is still far from being encompassed into a microscopic and complete theory that can account for all the anomalies observed. What is really intriguing and difficult to model from the theoretical point of view is the presence of many different order parameters, among which we find the charge density and superconducting ones. Recently, evidences of filamentarity have been found in high pulsed magnetic field resistance measurements [29] where filamentary superconductivity has been attributed to the charge ordering-superconducting (CO-SC) competition. As a matter of fact, the CO-SC competition has been studied from the late 1970s [30], i.e., before the discovery of superconductivity in cuprates: both the charge density wave (CDW) and superconductivity are in fact broken symmetry states appearing in solids and requiring an effective attraction between electrons, condensed in real or momentum space. In this competing scenario found in cuprates, filamentary superconductivity appears to be a topologically protected domain boundary between different charge ordered domains, favored by the presence of impurities [31,32].

This Thesis is organized as follows: in Chapter 1 we will review the main aspects of two-dimensional superconductivity. In particular, a quick summary of the Ginzburg-Landau phenomenological theory will be the starting point to introduce

superconductivity in low dimensional systems and the BKT transition will be treated within the ferromagnetic XY model.

In Chapter 2 we will introduce the reader to some experiments performed on low dimensional systems. On the one hand, we will provide some examples of strongly inhomogeneous compounds in which no sign of BKT transition can be tracked despite the low dimensionality. In this context, $SrTiO_3$-based heterostructures will be discussed in detail. Instead, we introduce cuprates as an example of BKT-like physics, presenting the rich phenomenology of their phase diagram and the more recent evidences of a filamentary superconducting state appearing in the underdoped region and tuned by a magnetic field. We will then introduce the model proposed so far to treat the competition between charge order and superconductivity that explained the ground state filamentary superconductivity.

Once the state of the art, both theoretical and experimental, has been described, we will start to investigate some of the many aspects of disorder. In Chapter 3, we will study the role of *microscopic* disorder in the suppression of T_c in multiband systems as a function of the gating potential. Indeed, we will try to unravel and disentangle the role of impurities from the effects of *mesoscopic* inhomogeneities in heavily disordered $SrTiO_3$-based interfaces [12, 13]. The pairbreaking effect observed at the Lifshitz transition in a multiband system has been already attributed to the combined effect of microscopic impurities and an interband repulsive interaction. In our work, we underline the role of strong disorder in circumventing Anderson's Theorem. As a matter of fact, the suppression observed in T_c will be found already when two unpaired bands are considered, the only coupling mechanism being the broadening and mixing of the bands introduced by disorder.

While inhomogeneities at a mesoscopic level affect the T_c curves only by smoothening the minimum at the Lifshitz transition, they are instead of great interest when dealing with transport properties. In Chapter 4 we will present the new evidences of filamentarity in resonant microwave transport experiments on a $LaAlO_3/SrTiO_3$ interface. Those data will be analyzed by means of a Random Impedance Network (RIN) model, being nothing but the extended version at finite frequency of the Random Resistor Network (RRN) [33], already used in the context of percolative metal-to-superconductor transitions. The RRN and its extension to RIN will be explained in detail, in their exact solution and also in their effective medium theory (EMT) approximation. As a matter of fact, a proximization process intervening in strengthening superconductivity will be necessary to capture the phenomenology observed. If, on the one hand, the long tails of the superfluid stiffness can be attributed to the same filaments necessary to percolation, the sudden jump of J_s and the finite value of the optical conductivity at zero temperature will be explained by the thickening of the filaments towards a more two-dimensional structure of the superconducting condensate. The RIN model will be studied before in its EMT solution to capture the main aspects, then in its exact solution where the filamentary geometry will play a crucial role. Here, the filamentary backbone will be given as an external structure, forgetting about its origin.

Chapter 5 is devoted instead to the study of the origin of filamentary superconductivity in cuprates as a result of the CO-SC competition and how this competition is reflected in many physical quantities as functions of temperature. Starting from an Heisenberg model with an effective barrier between CO and SC states, similar

to the one proposed in [31, 32], the SO(3) symmetry of the order parameter is mapped onto a three dimensional pseudospin on a square lattice, where the in-plane component accounts for the BKT superconducting transition while the out-of-plane stands for two different charge ordered states. By means of Monte Carlo simulations, we will try a first attempt to construct a phase diagram, in which the anisotropy term – introduced to tune the transition from BKT to Ising (CO) – will mirror the effects of a magnetic field in a real system. Along with the CO-SC competition, the presence of a random field mimicking impurities will appear to be necessary in order to force the clustering of CO regions and the natural appearance of filamentary superconductivity.

Contents

Chapter 1

Two-dimensional superconductivity: an Overview

"I call our world Flatland, not because we call it so, but to make its nature clearer to you, my happy readers, who are privileged to live in Space."

Flatland: A Romance of Many Dimensions,
Edwin Abbott Abbott

Since the main focus of this work is on two-dimensional materials displaying superconductivity, it is important to talk about the theory of Berezinsky, Kosterlitz and Thouless (BKT). In this Chapter we will therefore present the BKT transition, right after introducing briefly some of the main general aspects of superconductivity in the Ginzburg Landau framework.

1.1 Superconductivity: a glance

Quoting N. Nagaosa [34]: "When we have to explain in a word what superconductivity means, the answer might be that the quantum mechanical phase of the electron system becomes "solid" as if it were a rigid body, and gains rigidity." Indeed, microscopically two key ingredients are involved:

- a weak attractive interaction between electrons, leading to the formation of bounded pairs with opposite spins and momenta, i.e., the Cooper pairs;

- the condensation of Cooper pairs into a *macroscopic* quantum wave function whose global phase becomes rigid.

It is precisely this phase rigidity that gives the two peculiar properties of a super-conductor, i.e., the zero resistance and the perfect diamagnetism. Along with the formation of Cooper pairs and their condensation, two energy scales govern the system: those are, respectively, the energy gap Δ, observable in the quasi particle excitation spectrum, and the superfluid stiffness J_s, i.e., the energy cost required to

twist the phase of the Cooper pair wave function. Typically $\Delta \ll J_s$ and the transition happens in "one-step": this is the case of most conventional superconductors, well described by the Bardeen-Cooper-Schrieffer (BCS) theory [2, 3]. Except for the derivation of the superconducting energy gap in a two band system in Appendix A, we will not explore here other aspects of the BCS theory and we refer the reader to the wide existing literature [35, 36]. Instead, we will quickly describe below the Ginzburg Landau theory for a superconductor that will lead us to the BKT transition. Whenever $J_s \ll \Delta$ a major role is played by phase fluctuations and superconductivity can be destroyed, even if the energy gap remains finite. This is for instance the case of underdoped cuprates (see Section 2.2.1). The role played by phase fluctuations becomes particularly important in two dimensions, where the superconducting transition is led by the vortex-antivortex unbinding of the BKT transition [37].

1.1.1   From Ginzburg-Landau theory to the XY model

The Ginzburg-Landau (GL) theory is a phenomenological theory developed to describe second order phase transitions, such as the ferromagnetic one, and was successively extended to superconductivity [38, 39]. The power of the GL theory relies on the fact that it provides a simple way to describe all the main characteristics of the superconducting transition, i.e, the spontaneous symmetry breaking in relation to the appearance of a global rigid phase and the Meissner effect.

The general form of the GL free energy is

$$F = F_n + \alpha_0(T - T_c)|\psi|^2 + \frac{\beta_0}{2}|\psi|^4 + \frac{1}{2m^*}\left|\left(\frac{\hbar}{i}\nabla - \frac{e^*}{c}\mathbf{A}\right)\psi\right|^2 + \frac{(\nabla \times \mathbf{A})^2}{8\pi} \quad (1.1)$$

where $\psi = |\psi(\mathbf{r})|e^{i\theta(\mathbf{r})}$ is the complex order parameter, F_n is the free energy of the normal state, $\alpha_0, \beta_0 > 0$ are GL parameters to be determined from experiments, $\mathbf{A}$ is the vector potential, m^* is twice the (effective) mass of electrons and $e^* = 2e$ is the charge of the Cooper pair. Note that the amplitude of the order parameter can be identified with the density of Cooper pairs $|\psi|^2 = n_s/2$, where n_s is the density of superconducting electrons per unit volume.

Above the transition, the GL free energy functional is a paraboloid with its minimum in $\psi = 0$. Below the critical temperature T_c and in the absence of magnetic fields and currents, F acquires the typical mexican hat form displayed in Fig. 1.1: the ground state lies on a circle of amplitude $|\psi|$ while the phase has a continuous degeneracy in all range between 0 and 2π. Once the phase of the ground state has been selected, a change in θ is also called a Goldstone mode. Amplitude fluctuations, also called Higgs modes, are then energetically expensive, except at $T \approx T_c$, so we can easily assume $\psi = |\psi|e^{i\theta(\mathbf{r})}$.

When $\mathbf{A} = 0$, the free energy reduces to

$$F = F_n + \alpha_0(T - T_c)|\psi|^2 + \frac{\beta_0}{2}|\psi|^4 + \frac{\hbar^2|\psi|^2}{2m^*}|\nabla\theta(\mathbf{r})|^2 \quad (1.2)$$

The last term can be identified as the kinetic term: its prefactor represents the energy cost to deform the global phase, once suitably converted in an energy scale,
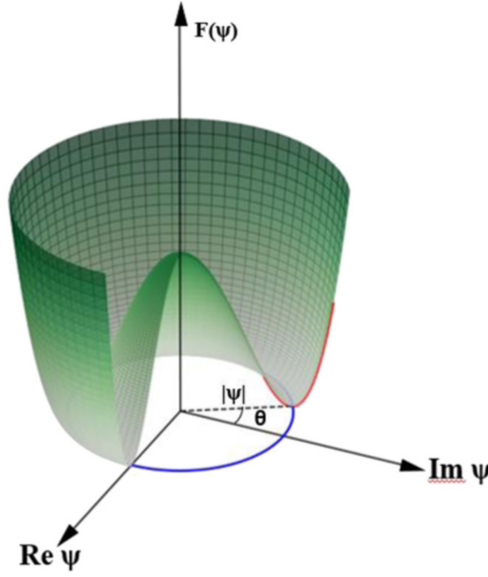
Figure 1.1. Free energy functional of a homogeneous superconductor in the absence of external fields and currents. The free energy minima lie on a circle, whose azimuthal angle is indicated with θ, of radius $|\psi|$, i.e., the amplitude parameter. Fluctuations of the amplitude are indicated in red, while phase fluctuations are in blue (Figure from [37]).

and it will be called superfluid stiffness $J_s \propto \frac{\hbar^2 |\psi|^2}{2m^*}$. We can anticipate and underline the fact that J_s is proportional to the square of the order parameter. In this way, superconductivity can circumvent the Mermin-Wagner theorem. The second order phase transition described by the GL theory is in fact prohibited in dimensions lower than 3 and no long range order is possible in isotropic systems displaying a continuous symmetry, i.e., $\langle \psi \rangle = 0$. This is not surprising, since phase fluctuations are costless.

Note that the energy cost to deform a phase is also intrinsically related to the penetration depth of the system, since the penetration depth is $\lambda_L = \sqrt{mc^2/8|\psi|^2 mc^2}$. Indeed, we can easily obtain the London equation by deriving the free energy functional in Eq. (1.1) with respect to $\mathbf{A}$:

$$\frac{\partial F}{\partial \mathbf{A}} = \frac{\psi_0^2 e^{*2}}{m^* c^2} \mathbf{A} + \frac{\nabla \times (\nabla \times \mathbf{A})}{4\pi} = 0 \qquad (1.3)$$

where the phase fluctuation term has been gauged away with a proper gauge transformation on $\mathbf{A}$. Using the London gauge $\nabla \cdot \mathbf{A} = 0$, the former exactly reduces to the London equation:

$$\nabla^2 \mathbf{A} = \frac{16\pi \psi^2 e^2}{m^* c^2} \mathbf{A} \equiv \frac{1}{\lambda_L^2} \mathbf{A} \qquad (1.4)$$

where $\lambda_L = \sqrt{mc^2/4\pi n_s e^2}$ is the London penetration depth, indicating the thickness in which an external magnetic field can penetrate inside the superconductor. One can then connect the phase rigidity with the Meissner effect by simply noticing that $J_s \propto 1/\lambda_L^2$.

In absence of external fields and currents, one can write the Hamiltonian just as

$$H = \frac{\hbar^2 n_s}{4m^*} \int |\nabla\theta(\mathbf{r})|^2 d\mathbf{r} = J_0 \int |\nabla\theta(\mathbf{r})|^2 d\mathbf{r} \qquad (1.5)$$

This is the kinetic energy term $\frac{1}{2}\frac{n_s}{2}m^* v_s^2$, where $\mathbf{v_s} = \frac{\hbar}{m^*}\nabla\theta(\mathbf{r})$ is the superfluid velocity. Indeed, by definition, the current density in first quantization is $\mathbf{j} = \frac{e^*\hbar}{2m^* i}(\psi^*\nabla\psi - \psi\nabla\psi^*)$ so the supercurrent density is $\mathbf{j_s} = \frac{e^*\hbar}{m^*}|\psi|^2\nabla\theta(\mathbf{r}) = \frac{n_s}{2}e^*\mathbf{v_s}$.

The Hamiltonian in (1.5) can be exactly mapped onto a ferromagnetic XY model [40], which undergoes the BKT transition and it will be discussed in the next Sections. Indeed, coarse graining the system by using as a short distance cutoff the coherence length ξ^1, we can change name to the order parameter from ψ to $\mathbf{s}$, defined on the XY plane and with constant unitary modulus and note that

$$\mathbf{s}_i \cdot \mathbf{s}_j = 1 - \frac{1}{2}(\mathbf{s}_i - \mathbf{s}_j)^2 \qquad (1.6)$$

so the square gradient of the order parameter of Eq (1.5) can be written as spin variables square differences where the integral is replaced by the sum over nearest neighbors, i.e., $|\nabla\theta(\mathbf{r})|^2 \to (1 - \mathbf{s}_i \cdot \mathbf{s}_j)$, thus, neglecting a constant term, we obtain the Hamiltonian for the XY model:

$$H = -J \sum_{<ij>} \mathbf{s}_i \cdot \mathbf{s}_j. \qquad (1.7)$$

where J is now the interaction between neighboring spins.

1.2   The BKT transition

In the early 70's Berezinsky [5] and Kosterlitz and Thouless [6,7] showed that a phase transition occurs in the XY model in two dimensions. In those days, several physicists were investigating the presence, or the absence, of phase transitions in low-dimensional systems (d = 1, 2) with short-range interactions. Mermin and Wagner [8] proved rigorously that the one- and two-dimensional isotropic Heisenberg models, with short range interactions, have no long-range order at any finite temperature. The Beresinskii-Kosterlitz-Thouless (BKT) topological transition circumvents the Mermin-Wagner theorem, considering, as a marker of the ordered phase, the behavior of the correlation function rather than the average value of the single spin. Nonetheless, the theorem is not violated because of the main peculiarity of this phase transition, which is the fact that it occurs without any symmetry breaking. As it will be explained hereafter, topological defects play a central role.

Let us present the BKT transition within the context of its paradigmatic formulation for the classical XY model. The model describes the ferromagnetic interactions between planar spins with unitary modulus $|\mathbf{s}_i|^2 = 1$, placed on a square lattice, whose Hamiltonian reads:

$$H_{XY} = -J \sum_{<i,j>} \mathbf{s}_i \cdot \mathbf{s}_j = -J \sum_{<i,j>} \cos(\theta_i - \theta_j) \qquad (1.8)$$

---

[1]$\xi \sim 4\,\text{Å}$ in type II superconductors so in that case is of the same order of the real lattice spacing of the underlying lattice.

being $\sum_{<i,j>}$ the sum restricted to nearest neighbor spins, J a positive coupling constant and θ_i the angle that the i-th spin forms with a given direction. From (1.8), it is straightforward to recognize that the model admits two different symmetries:

- a continuous global symmetry $U(1)$:

$$\theta_i \to \theta_i + \chi \qquad \forall i; \tag{1.9}$$

- a discrete local symmetry $\mathbb{Z}^m$:

$$\theta_j \to \theta_j + 2\pi m, \qquad m \in \mathbb{Z}. \tag{1.10}$$

As we will see, the latter one is the main responsible for the topological character of this phase transition. Indeed, a *new* spin excitation arises from this symmetry, namely a vortex. We will come back to this point in Section 1.3.

We anticipated that a transition is actually possible if we look at the behavior of the correlation functions, defined as:

$$C_{ij} = \langle \mathbf{s}_i \cdot \mathbf{s}_j \rangle = \left\langle e^{i(\theta_i - \theta_j)} \right\rangle \tag{1.11}$$

where the average $\langle ... \rangle$ is the average over the canonical ensemble of the system:

$$\langle A \rangle = \frac{1}{Z} \int_0^{2\pi} d\theta_1 ... \int_0^{2\pi} d\theta_N A e^{-\beta H_{XY}}, \qquad \beta = \frac{1}{k_B T}. \tag{1.12}$$

In the high-temperature limit, i.e., when $\beta J \ll 1$, one can select the dominant contribution to the above integration and obtain the result [34]

$$C_{ij} = e^{-|\mathbf{r}_i - \mathbf{r}_j|/\xi}, \qquad \xi = \frac{1}{\ln\left(\frac{2T}{J}\right)}. \tag{1.13}$$

Thus, the correlation function decays exponentially with the distance, as in a typical disordered system, with a correlation length that increases as T decreases, without any divergence at finite T.

Let us now consider the low-temperature limit. Assuming that the difference in angle between neighboring spins is slowly varying, we can approximate $\theta_i - \theta_{i+\delta} = a\partial\theta(\mathbf{r})/\partial\hat{\delta}$, where $\theta(\mathbf{r})$ is a smooth function and $\hat{\delta} = \hat{x}, \hat{y}$. The Hamiltonian (1.8) reduces to:

$$H_{XY} \simeq \frac{J}{2} \int d\mathbf{r} |\nabla\theta(\mathbf{r})|^2 = \frac{J}{2} \int \frac{d\mathbf{q}}{(2\pi)^2} \mathbf{q}^2 |\theta_{\mathbf{q}}|^2. \tag{1.14}$$

Note that we mapped the system back to Hamiltonian (1.5).

Referring to the original paper [8] for the complete demonstration, we are going to show now that $\langle \mathbf{s}_i \rangle \to 0$ when $L \to \infty$, so no long-range order is possible at any finite temperature, according to the Mermin-Wagner theorem. The quantity to compute is then

$$\langle \mathbf{s}_i \rangle = \left\langle e^{i\theta_i} \right\rangle = e^{-\langle\theta_i^2\rangle/2} \tag{1.15}$$

where we use a well known property of the average over a Gaussian distribution. Indeed, the preceding calculation is:

$$\left\langle \theta_i^2 \right\rangle = \int \frac{d\mathbf{q}}{(2\pi)^2} \left\langle |\theta_{\mathrm{q}}|^2 \right\rangle = \int_{1/L}^{1/a} \frac{d\mathbf{q}}{(2\pi)^2} \frac{T}{J\mathrm{q}^2} = \frac{T}{2\pi} \ln\frac{L}{a} \tag{1.16}$$

being L the linear size of the system and a the lattice spacing between two neighbors spins; finally

$$\langle \mathbf{s}_i \rangle = e^{-\frac{T}{4\pi J}\ln\left(\frac{L}{a}\right)} = \left(\frac{a}{L}\right)^{\frac{T}{4\pi J}} \xrightarrow[L\to\infty]{} 0. \tag{1.17}$$

Hence, at any nonzero temperature the system has no spontaneous magnetization in the thermodynamic limit.

However, as previously mentioned, observing the behavior of the correlation function at low temperature leads to a very interesting result. Thus, let us calculate

$$C(\mathbf{r}) = \left\langle e^{i(\theta(\mathbf{r})-\theta(0))} \right\rangle = e^{-\frac{1}{2}\left\langle [\theta(\mathbf{r})-\theta(0)]^2 \right\rangle} \tag{1.18}$$

Computing the exponent in Fourier space, we get:

$$
\begin{aligned}
\left\langle [\theta(\mathbf{r}) - \theta(0)]^2 \right\rangle &= \left\langle \int \frac{d\mathbf{q}_1}{2\pi} \theta_{\mathbf{q}_1}(e^{i\mathbf{q}_1\mathbf{r}} - 1) \int \frac{d\mathbf{q}_2}{2\pi} \theta_{\mathbf{q}_2}(e^{i\mathbf{q}_2\mathbf{r}} - 1) \right\rangle \\
&= \int \frac{d\mathbf{q}}{(2\pi)^2}[2 - 2\cos(\mathbf{q}\cdot\mathbf{r})]\left\langle |\theta(\mathbf{q})|^2 \right\rangle \\
&= \frac{T}{\pi J}\int_{1/L}^{1/a} \frac{dq}{q}(1 - \cos(\mathbf{q}\cdot\mathbf{r})) \sim \frac{T}{\pi J}\int_{1/r}^{1/a} \frac{dq}{q} = \frac{T}{\pi J}\ln\left(\frac{r}{a}\right).
\end{aligned}
\tag{1.19}
$$

Substituting in (1.18) we get:

$$C(\mathbf{r}) = e^{-\frac{T}{2\pi J}\ln\left(\frac{r}{a}\right)} = \left(\frac{a}{r}\right)^{\frac{T}{2\pi J}} \tag{1.20}$$

As in the high-temperature regime, the correlation function decays to zero at large distance. However, in this case the decay is much slower with respect to the exponential decay found in the high-temperature case (1.13). In terms of correlation length, the low-temperature power-law decay (1.20) means that $\xi \to \infty$. A drastic change in the correlation functions occurs between the two regimes. Such a change of behavior cannot be "smooth", i.e., a phase transition must occur in between the two regimes. This phase transition must be of a new type, since the standard definition of phase transition in terms of an order parameter (or spontaneous symmetry breaking) is not viable. On the other hand, a finite J in equations 1.13 and 1.14 signals that the system is "rigid" against spin fluctuations, so it is usually called spin stiffness.

1.3 The role of vortices

As previously mentioned, topological excitations, namely vortices, are the best candidates to be responsible for the phase transition we are looking for and they originate from the discrete symmetry (1.10). They are characterized by a winding of the phase of $\pm 2\pi$, going around the center of the vortex:

$$\oint \nabla\theta \cdot d\ell = 2\pi m \tag{1.21}$$

where m represents the vorticity of the vortex itself. It is clear that if a vortex excitation is present in the system one cannot make the assumption of smoothness of

the phase variations in neighboring sites that led us to the approximate form (1.14). The first attempt of Kosterlitz and Thouless [6] was to look at the cost, in terms of free energy, of an isolated free vortex of unitary vorticity. To make this estimate, we would like to rewrite the Hamiltonian (1.8), separating the contribution of vortices from the contribution of spin waves, so we can keep the continuum notation for $\theta(\mathbf{r})$ allowing for configurations that are singular at a position $\mathbf{r}_0$.

The smooth configurations allowed by the Hamiltonian (1.14) are the solutions of the variational equation $\delta H = 0$, i.e.,

$$\nabla^2 \theta(\mathbf{r}) = 0. \tag{1.22}$$

It is then reasonable that vortex-like configurations satisfy the equation:

$$\nabla^2 \overline{\theta}(\mathbf{r}) = 2\pi \delta(\mathbf{r} - \mathbf{r}_0) \tag{1.23}$$

whose solution in $D = 2$ is

$$\overline{\theta} = \arctan \frac{y - y_0}{x - x_0}. \tag{1.24}$$

Since $\nabla\overline{\theta} = (-y/r^2, x/r^2)$, so $\nabla\overline{\theta} \parallel \overrightarrow{d\ell}$, we recover the vortex configuration:

$$\oint \nabla\overline{\theta} \cdot \overrightarrow{d\ell} = \frac{1}{r} \oint d\ell = \frac{1}{r} 2\pi r = 2\pi. \tag{1.25}$$

We can now calculate the energy of the vortex configuration by inserting (1.24) in (1.14), obtaining:

$$E = \frac{J}{2} \int d\mathbf{r} (\nabla\overline{\theta}(\mathbf{r}))^2 = \frac{J}{2} \int_a^L dr 2\pi r \frac{1}{r^2} = \pi J \ln\frac{L}{a}. \tag{1.26}$$

As one can see, the energy of a single vortex configuration shows a logarithmic divergence with the system size L: from this perspective, its generation is unlikely in the thermodynamic limit. Nevertheless, at finite temperature we have also to consider the entropic gain in forming such a vortex configuration. Since the number of independent places where a vortex can be located is $\sim L^2/a^2$ we obtain an entropy:

$$S = \ln\left(\frac{L^2}{a^2}\right) = 2\ln\frac{L}{a}. \tag{1.27}$$

Finally, we can write the free energy of a vortex configuration:

$$F = E - TS = (\pi J - 2T)\ln\frac{L}{a}. \tag{1.28}$$

We can identify a critical temperature T_{BKT} above which the entropic term wins against the energetic one, promoting the proliferation of free vortices in the system:

$$T_{BKT} = \frac{\pi J}{2}. \tag{1.29}$$

The proliferation of such vortices destroys the quasi-long-range order entailed by the power-law decay of the correlation function at low-temperature and it is responsible for the sudden loss of spin stiffness. This rough estimate of the critical

temperature neglects two principal effects: the first one is the vortex-core energy μ_V, the second is the presence of several vortex excitations. The vortex-core energy is the energetic cost to form the vortex at the length-scale of the lattice spacing but it does not grow with the size of the system, hence, neglecting it does not affect the previous calculation. On the other hand, its value controls the thermal activation $e^{\beta\mu_V}$ of vortex-antivortex pairs, that can in principle change the "effective" large-distance coupling J in the previous equation, including the spin stiffness J_s, different from the coupling J of the XY model, even though the two coincide at $T \to 0$.

Nonetheless, the relation between the critical temperature and the (renormalized) stiffness will turn out to be the same as the above (1.29), as we will see in the next Section.

1.4   RG equations

We present here the analytical solution found exploiting the renormalization group (RG) approach.

Let us define the quantities

$$\begin{cases} K = \dfrac{\pi J_s}{T}, \\ g = 2\pi e^{-\beta\mu_V}. \end{cases} \tag{1.30}$$

Addressing the reader to [41] for the complete derivation obtained from the mapping onto the sine-Gordon model, we present the resulting RG equations, with the usual parameterization $\Lambda(\ell) = \Lambda_0 e^{-\ell}$, $\ell = \ln(\frac{L}{a})$

$$\frac{dK}{d\ell} = -K^2 g^2, \tag{1.31a}$$

$$\frac{dg}{d\ell} = (2 - K)g. \tag{1.31b}$$

As already mentioned, the stiffness is identified [42] by the limiting value of K in the thermodynamic limit:

$$J_s \equiv \frac{TK(\ell \to \infty)}{\pi}. \tag{1.32}$$

From the RG differential equations in (1.31), we can immediately recognise two main regimes of the model: $K \gtrsim 2$, region (A) in Fig. 1.2, and $K \lesssim 2$, region (B) in Fig. 1.2. In the first regime, the term on the right side of (1.31b) is negative so g is vanishing while K tends to a finite value ($K \gtrsim 2$, $g \to 0$, $K \to K^*$). According to (1.32), the system shows a finite stiffness while the role of vortices is irrelevant, because of the vanishing of g. On the contrary, the regime $K \lesssim 2$ represents the regime where the vortex fugacity grows leading to the vanishing of K. The initial value of the term containing the vortex core energy μ_V is

$$g_0 = 2\pi e^{-\beta\mu_V} = 2\pi e^{-\beta\overline{\mu_V}J} = 2\pi e^{-\frac{\overline{\mu_V}K(T)}{\pi}} \tag{1.33}$$
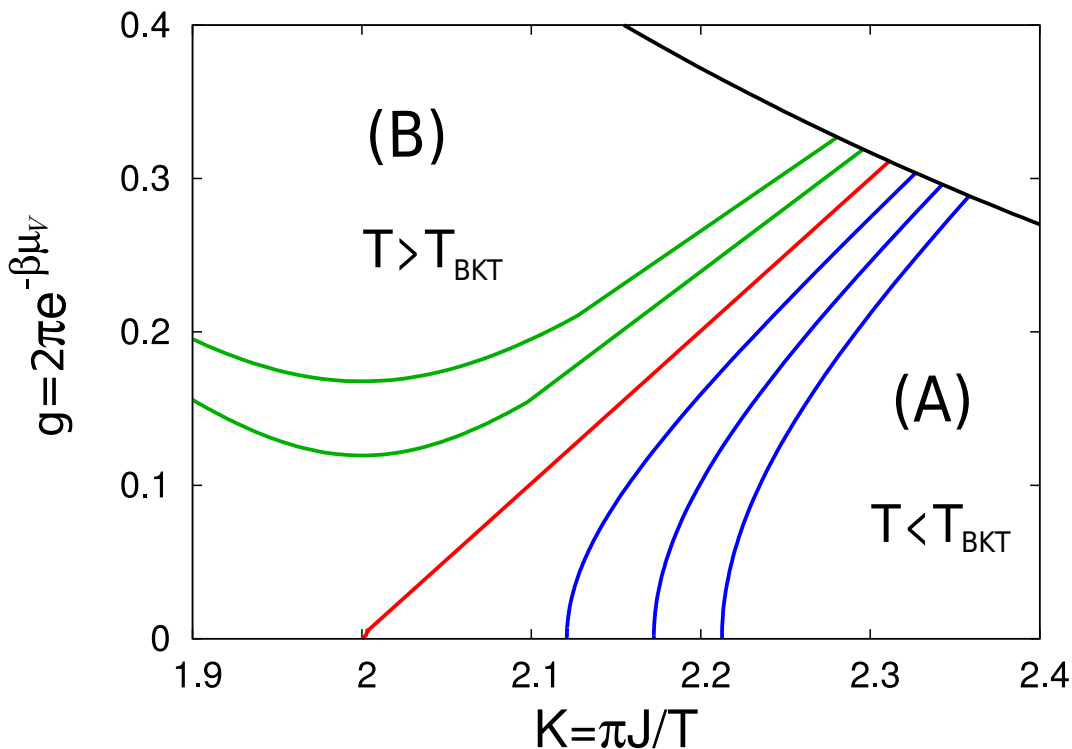
Figure 1.2. RG flow for the BKT problem.

The value of $\overline{\mu_V}$ depends on the model examined: without going into details, this is $\mu_{XY} = \frac{\pi^2}{2}$ in the XY-model and $\mu_{BCS} = \frac{3}{\pi}$ in the BCS-theory [43].

The red line in figure 1.2 corresponds to the critical point $K = 2$, $g = 0$ which defines the universal relation between J_s and T_{BKT}:

$$K(T_{BKT}) = 2 \quad \Rightarrow \quad \frac{\pi J_s(T_{BKT})}{T_{BKT}} = 2. \tag{1.34}$$

As soon as the temperature is increased over T_{BKT} the system loses its rigidity because of free vortices proliferation. The system is now in the (B) region of the phase diagram: as a result one finds

$$K(T_{BKT}^+) = 0 \quad \Rightarrow \quad J_s(T_{BKT}^+) = 0, \tag{1.35}$$

i.e., the superfluid density jumps discontinuously to zero right above the transition. The temperature dependence of $J_s(T)$ is shown in Fig 1.3, where we show in panel a the ideal case, in which the stiffness follows precisely its three-dimensional counterpart up the intersection with the critical line $2T/\pi$ (blue line), while within the RG flow (panel b) $J_s(T)$ starts to be renormalized at lower temperatures. The bare temperature dependence of $J_s(T)$ is assumed to be the one of the BCS model (green line) $J_{BCS}(T) = J_0 \frac{\Delta(T)}{\Delta(0)} \tanh(\Delta(T)/2k_BT)$.

As one can see, approaching the transition from below, the J_s curve in the BKT case is slightly smaller than its bulk counterpart: this is due to the difference between the initial value of K and its limiting value $K^* = K(\ell = \infty)$ under the RG flow. Such a difference is practically zero at $T \ll T_{BKT}$ where the RG flow
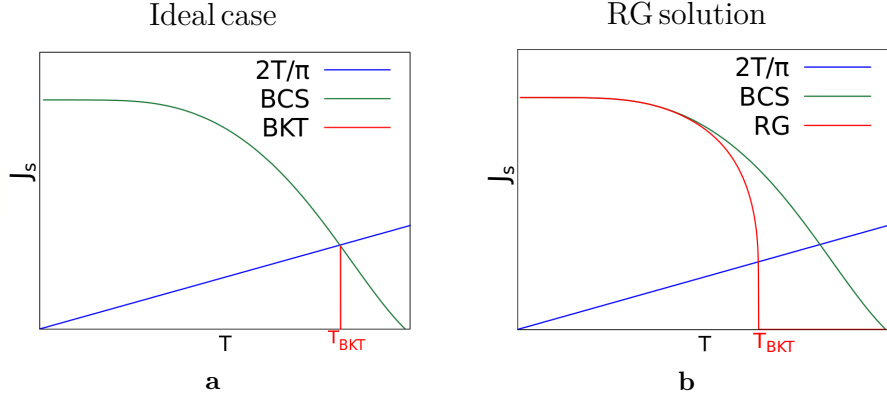
Figure 1.3. Temperature dependence of the superfluid density within the BCS model in the (a) ideal case and (b) within the RG flow solution.

is almost vertical. However as T approaches T_{BKT} vortices renormalize at short distances the superfluid density with respect to its bare value, but still J_s is finite, because at large distances vortices disappear effectively from the system. For this reason one must be very careful in defining what is universal: T_{BKT} is not universal, what is universal is the relation between the renormalized superfluid density and the transition temperature, as encoded in equation (1.32). Indeed, the smaller is the ratio μ_V/J, the larger is the renormalization of J_s due to vortices below T_{BKT}.

We can solve the system step-by-step with a change of variable, to have more control on the size of the system. The final scope is to extrapolate some analytical solution for the stiffness that will be used afterwards.

A convenient change of variables is

$$\begin{cases} x = K - 2 \\ y = 2g \end{cases} \tag{1.36}$$

Now, the RG equations are written as:

$$\frac{dx}{d\ell} = -(x+2)^2 \frac{y^2}{4} \simeq -y^2 \tag{1.37a}$$

$$\frac{dy}{d\ell} = -xy \tag{1.37b}$$

having expanded around the fixed point $x = 0$, $y = 0$. The system is simplified when we note that:

$$x \frac{dx}{d\ell} - y \frac{dy}{d\ell} = 0 \tag{1.38}$$

whence:

$$x^2 - y^2 = A \tag{1.39}$$

where A is a constant of the motion, $A = x_0^2 - y_0^2$, x_0 and y_0 being the initial values for the RG differential equations, calculated once the reference model is defined, e.g. the clean BKT or BCS models.

When $A > 0$ we are in the regime where the superfluid stiffness dominates over the vortex term. Thus, it corresponds to the low-temperature region $T < T_{BKT}$.

Substituting $x = \sqrt{y^2 + A}$ and $-y^2 = A - x^2$ in equation (1.37), one obtains

$$\frac{dx}{d\ell} = A - x^2$$
$$\frac{dy}{d\ell} = -y\sqrt{y^2 + A}$$

(1.40)

whose solutions are:

$$x(\ell) = \frac{\sqrt{A}}{\tanh(\sqrt{A}\ell + \operatorname{arcsinh}(\frac{\sqrt{A}}{y_0}))} \xrightarrow[\ell \to \infty]{} \sqrt{A}$$
$$y(\ell) = \frac{\sqrt{A}}{\sinh(\sqrt{A}\ell + \operatorname{arcsinh}(\frac{\sqrt{A}}{y_0}))} \xrightarrow[\ell \to \infty]{} 0$$

(1.41)

When $A \to 0^+$ we are on the critical line $x_0 = y_0$ of the $x - y$ plane. The RG equations in this regime reduce to

$$\frac{dx}{d\ell} = -x^2$$

(1.42)

whose solution is

$$x = \frac{x_0}{1 + x_0\ell}$$

(1.43)

so that $x \to 0$ logarithmically with the system size.

In the high-temperature regime ($T > T_{BKT}$, $A < 0$), we can introduce another constant C, such that $-A = C > 0$. After having expressed $y^2 = x^2 + C$, the differential equations in (1.37) take the form:

$$\frac{dx}{d\ell} = -(x^2 + C)$$
$$\frac{dy}{d\ell} = -y\sqrt{y^2 - C}$$

(1.44)

with solution:

$$x(\ell) = \sqrt{C} \tan\left(-\sqrt{C}\ell + \arctan(\frac{x_0}{\sqrt{C}})\right)$$

(1.45)

so $x \to 0$ as ℓ increases. Searching for the value ℓ^* at which $x(\ell^*) = 0$ one can find the exponential behavior of the correlation length in the BKT theory:

$$\xi = ae^{b/\sqrt{t}}$$

(1.46)

where $t = \frac{T - T_{BKT}}{T_{BKT}}$ is the reduced temperature and b is a constant that depends on the specific model studied. This last relation will be used to find the BKT fluctuation contribution to conductivity [44]. Obviously the variable of interest in our study is $x(\ell)$. The dependence on the size $\ell = \ln(\frac{L}{a})$ is significant in our disordered scenario.

1.5 $I - V$ characteristics in the BKT theory

The jump of the superfluid density at T_{BKT} produces an anomalous power-law dependence of the $I - V$ characteristics. Let us write the energy of a vortex-antivortex pair at a distance r per unit length in a film of thickness d:

$$\frac{E}{d} = \frac{2\pi J_s}{d}\ln\frac{r}{\xi_0} - \mathbf{f}\cdot\mathbf{r} = \frac{2\pi J_s}{d}\ln\frac{r}{\xi_0} - \frac{I}{Wd}\frac{\Phi_0}{c}r \qquad (1.47)$$

the current density of the film being $j = I/Wd$, where W is the width of the film, Φ_0 is the flux quantum and ξ_0 the correlation length. The force $\mathbf{f}$ is nothing but the Lorentz force produced by the supercurrent that flows in the film. Supposing that the film lies in the $\hat{x}$-$\hat{y}$ plane, the supercurrent flowing in the $\hat{x}$ direction, the Lorentz force moves the vortices perpendicularly with respect to it, with a direction determined by the vorticity $\epsilon_i = \pm 1$, as:

$$\mathbf{f} = \epsilon_i\mathbf{j} \times \hat{z}\frac{\Phi_0}{c}. \qquad (1.48)$$

As one can see from equation (1.47), the supercurrent term tends to unbind the vortices while the log potential tends to confine them. The critical current will be the value of the current above which the vortices separate within the sample. This value occurs when the energy changes sign, i.e., when its derivative vanishes $\partial E(r^*)/\partial r = 0$:

$$r^* = \frac{2\pi J_s cW}{I\Phi_0} \qquad (1.49)$$

corresponding to an energy:

$$E(r^*) = 2\pi J_s \ln\frac{2\pi J_s cW}{\xi_0 I\Phi_0} - 2\pi J_s. \qquad (1.50)$$

When $r^* \leq W$ the current is large enough to separate the vortices. Thus, the minimum current required is

$$I_c = 2\pi J_s\frac{c}{\Phi_0}. \qquad (1.51)$$

If one wants to get an estimate of the critical current near the BKT transition, one has to substitute $2\pi J_s$ with $4T_{BKT}$, according to the universal relation (1.34). Then, since $c/\Phi_0 = 0.5 \cdot 10^{15}$ A/J, one has

$$I_c[A] \simeq 2.76 \times 10^{-8}T_{BKT}[K] \qquad (1.52)$$

Increasing the current over the critical value, one can generate free vortices. If one wants to estimate their density ρ_V one can use a kinetic equation such that

$$\frac{d\rho_V}{dt} = \Gamma(T, I) - \rho_V^2 \qquad (1.53)$$

where Γ is the rate at which vortices are unbound. We can take $\Gamma(T, I) = e^{E(r^*)/T}$. The second term in equation (1.53) accounts for the vortices recombining to form pairs again. In the steady state then one has

$$\rho_V = \Gamma^{1/2} = e^{-E(r^*)/2T}. \qquad (1.54)$$

The electric field generated by the movement of the vortices is proportional to $n_v v_L$, v_L being the drift velocity. Indeed, because of the Lorentz force the vortices can escape the sample flowing in the $\hat{y}$ direction. The phase of the sample slips of 2π each time a vortex drifts across the sample width W; in a time interval Δt a fraction of vortices $\rho_V v_L \Delta t$ escapes, so:

$$\frac{d\Delta\theta}{dt} = 2\pi \rho_V v_L L. \tag{1.55}$$

generating a field in the $\hat{x}$ direction that contrasts the applied current. According to Josephson relation $\Delta V = (\hbar/2e)d\Delta\theta/dt$, the field E_x is equal to

$$E_x = \frac{\Delta V}{L} = \frac{\Phi_0}{c}\rho_V v_L. \tag{1.56}$$

Since the drift velocity is proportional to the applied current, we can conclude that

$$V \sim \rho_V I. \tag{1.57}$$

We can estimate n_v by means of equation (1.54). By using the I_c value (1.51) into equation (1.50) we obtain:

$$\begin{aligned}
E(r^*) &= 2\pi J_s \left(\log \frac{2\pi J_s c W}{\xi_0 \Phi_0 I} - 1 \right) \\
&= 2\pi J_s \left(\log \frac{I_c W}{\xi_0 I} - 1 \right)
\end{aligned} \tag{1.58}$$

where we note that only the first term depends on the applied current. Then the fraction of vortices that contributes to transport can be written as

$$\rho_V \sim e^{-\pi J_s \ln(I_c/I)/T} = \left(\frac{I}{I_c} \right)^{\pi J_s/T} \tag{1.59}$$

This implies that the non-linear behavior of the $I − V$ characteristics is controlled by the exponent

$$V \propto I^{a(T)}, \qquad a(T) = \frac{\pi J_s}{T} + 1. \tag{1.60}$$

According to the BKT critical point at which $J_s(T_{BKT}) = 2T_{BKT}/\pi$, the exponent $a(T)$ will jump from $a(T > T_{BKT}) = 1$ to $a(T_{BKT}) = 3$, as soon as the temperature is lowered down to T_{BKT}, keeping increasing at even lower temperatures.

To summarize, while usually Mermin-Wagner theorem forbids ferromagnetic transitions in low dimensions, the XY model undergoes the BKT topological phase transition, which is led by the proliferation of vortex-antivortex bounded pairs as the temperature increases. Since the GL model for superconductivity can be mapped onto an XY model, a superconducting transition is always possible in two dimensions, where the relevant energy scale becomes the superfluid stiffness J_s, accounting for phase fluctuations (Goldstone mode), rather than the energy gap Δ, connected instead to amplitude fluctuations (Higgs mode) of the Cooper pairs wave function. The universal critical point of the BKT transition is translated in superconducting

systems in the sudden jump to zero of the superfluid stiffness J_s when it crosses the critical line at T_{BKT}, coming from lower temperatures.

In real systems, the detection of a BKT transition is not however straightforward. The presence of disorder can in fact partially or even totally hinder its signatures, such as this jump of J_s or the jump of $a(T)$ in the $I - V$ characteristics, as we will see in the next Chapter.

Chapter 2

Effects of disorder in real systems

"Would you tell me, please, which way I ought to go from here?"
"That depends a good deal on where you want to get to," said the Cat.
"I don't much care where–" said Alice.
"Then it doesn't matter which way you go," said the Cat.
"–so long as I get somewhere," Alice added as an explanation.
"Oh, you're sure to do that," said the Cat, "if you only walk long enough."

Alice's Adventures in Wonderland,
Lewis Carrol

In this Chapter we will summarize some of the main experimental aspects encountered in literature that moved our curiosity, leading the work presented throughout this Thesis. Indeed, in two-dimensional superconductors there is a jungle of intriguing and exotic behaviors, where disorder can appear at different scales and in different ways and the two-dimensional character can play a role itself. In two-dimensional materials superconductivity is in fact expected to belong to the BKT universality class.

Nonetheless, disorder on a mesoscopic scale can prevent the observation of BKT signatures. This topic will be described in Section 2.1 with a particular emphasis on $SrTiO_3$-based heterostructures, for which we will summarize the main aspects of such materials as well as the phenomenology of transport measurements.

On the other side, a BKT like transition is expected in cuprates, whose phase diagram is however so rich that superconductivity can coexist and compete with the charge ordered phase. In this framework, the competing mechanism, along with impurities always present in real systems, is most likely the cause of filamentary superconductivity.

2.1 Hiding BKT under inhomogeneities

As matter of fact, in many materials BKT is not observable despite their two-dimensional character. The signatures indicating the presence of the topological phase transition can be in fact partially or totally masked by the presence of mesoscopic inhomogeneities. The phenomenology of the superconducting transition in many two-dimensional materials points instead towards the direction of a *percolative transition*, that we will briefly present henceforth and will be deeply explored throughout Chapter 4. The presence of a large width of the metal-to-superconductor transition will appear as one of the main smoking guns of mesoscopic inhomogeneities, along with other trends in transport measurements, such as the broadening of tunneling spectra. Moreover, the presence of non-linear $I - V$ characteristics can be attributed to mesoscopic disorder, not to be confused with the $I - V$ non-linearities caused by the proliferation of free vortices of the BKT framework (see Section 1.5) [17]. All those phenomenological features will be presented in the exemplary case of SrTiO$_3$-based interfaces, in which the inhomogeneous nature is particularly evident.

2.1.1 SrTiO$_3$-based interfaces

After the discovery of superconductivity in bulk SrTiO$_3$ about 50 years ago, a two-dimensional electron gas (2DEG) at the interface between two insulating dielectric perovskite oxides has been found, displaying many interesting phases. The carrier density can be tuned by means of a top- or back- gate voltage and the 2DEG can be made superconducting, both in LaAlO$_3$/SrTiO$_3$ and in LaTiO$_3$/SrTiO$_3$ (LTO/STO) interfaces, opening the way to novel electronic phases. The diverse phenomena occurring at oxide interfaces include, among others, exceptional carrier mobilities, magnetism and superconductivity. Our interest will be focused however on the metal-to-superconductor transition.

Indeed, the very origin of the 2DEG at the interface of such compounds is still a debated issue in which disorder is an inextricable ingredient. It it important to point out that the number of carriers in SrTiO$_3$-based interfaces are strictly linked to the growth condition of the sample and the relation between V_G and the chemical potential is not straightforward, as it can be instead in the case of chemical doping. Thus, it is not surprising that it is hard to find in the literature a settled situation concerning, for instance, a complete phase diagram of these compounds. To summarize the knowledge gathered so far, we need to clarify some aspects related to the origin of the 2DEG and its band structure.

Origin of the 2DEG and phase diagram

SrTiO$_3$ has the general Perovskite formula ABO$_3$, where A=Sr and B=Ti and a cubic lattice as in Fig. 2.1b. Along the cubic axis (001) they can be seen as an alternate stack of SrO and TiO$_2$ planes. Different heterostructures are obtained [46], depending of what kind of planes goes to form the interface (SrO- or TiO$_2$-type) between the two constituent compounds, its properties determined also by the direction of the interface with respect to crystal axes, above which is growth a more or less thick layer of LaXO$_3$ (X=Al or Ti). As a matter of fact, the orientation of the interface is crucial from the point of view of the bands involved in the 2DEG.
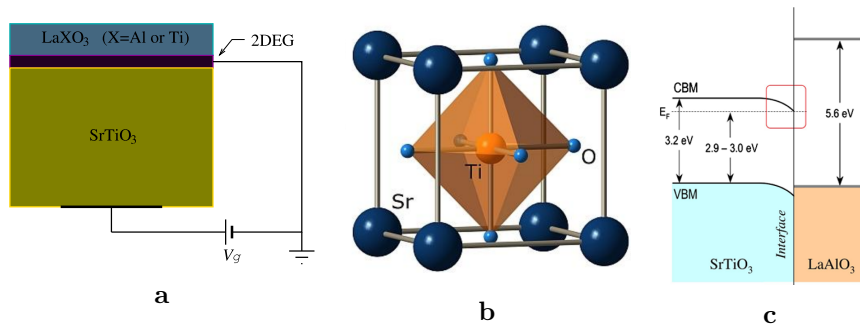
Figure 2.1. (a) Sketch figure of a SrTiO$_3$-based interface, in the back gating configuration. The upmost slab is a LAO (or LTO) cristal with a thickness of a few nanometers; the STO slab below is about 0.5 mm thick. The back gate voltage V_g is used to control the carrier density of the 2DEG (Figure from [22]). (b) Perovskite structure of SrTiO$_3$. (c) Simplified band diagram across LaAlO$_3$/SrTiO$_3$ with band gaps and a qualitative band bending (Figure from [45]).

Here, the valence band comes from the $2p$ orbitals of oxygen while the conduction band comes from the titanium $3d$ orbitals. Because of the crystal field, the valence and the conduction band are split respectively in a high energy doublet e_g and a low energy triplet t_{2g}, the latter corresponding to d_{xy}, d_{xz}, d_{yz} orbitals. When SrTiO$_3$ is used as a substrate in a heterostructure, a quantum well is formed at the interface caused by the bending of the bands, needed to preserve the continuity of the wave function. In Fig. 2.1c on can see the bending of the conduction band and the discontinuity at the interface of the LaAlO$_3$/SrTiO$_3$.

The 2DEG is confined in this quantum potential well, located on the SrTiO$_3$ side of the device. Referring to [47] and [48] for more details, we briefly summarize here the two main mechanisms behind the formation of the 2DEG, namely the presence of oxygen vacancies and the so-called *polar catastrophe*. Both can be present in a given sample, even simultaneously, depending on the growth conditions.

On the one hand, an oxygen vacancy at the interface can act as an impurity donor, the oxygen having valence -2. This is also a common mechanism to dope bulk SrTiO$_3$ and we can refer to it as an *extrinsic mechanism* [49,50,50]. On the contrary, the *polar catastrophe* is an *intrinsic mechanism* caused by the abrupt polar discontinuity between stacked planes of (polar) LaXO$_3$ (X=Al or Ti) and (non-polar) SrTiO$_3$. This generates an oscillating electric field, whose amplitude increases monotonically with the LaXO$_3$ thickness, that can be overcome by electronic reconstruction, transferring extracharge from the LaXO$_2$ side to the interfacial plane of SrTiO$_3$ [51].

Moreover, it has been shown in [23] that the confining electrostatic potential may induce phase separation in the 2DEG, to avoid a thermodynamically unstable state with a negative compressibility. This was proposed as a possible mechanism to explain microscopically the origin of mesoscopic inhomogeneities observed in such materials, about which we will discuss below, at the same time stating the inextricably disordered nature of such compounds.

Some properties will depend on the crystal orientation of the SrTiO$_3$, being the 2DEG confined in that side of the heterostructure. The confinement of carriers near
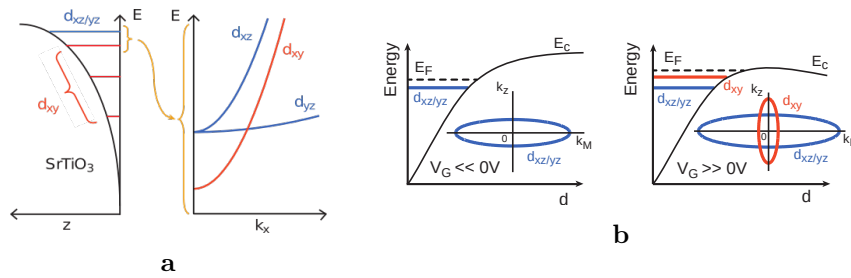
Figure 2.2. (a) Sketch figure of the bands in $LaAlO_3/SrTiO_3$, oriented in the (001)-oriented interface (Figure from [24]). (b) confinement energy E_c in $SrTiO_3$ as a function of the distance to the interface d, the Fermi energy E_F and the position of the different t_{2g} bands at the Γ point in the (110) interface. Insets show the Fermi contours in the k_z ([001]), k_M ([1-10])) plane.

the interface induces the splitting of the spectrum of $d_{xy,xz,yz}$ orbitals into discrete two-dimensional sub-bands. We show in Fig. 2.2 a sketch of the further splitting of the conduction bands in two interfaces of $LaAlO_3/SrTiO_3$, oriented in the (001) (panel a) and the (110) direction (panel b). As one can see, the d_{xy} orbital is lower in energy with respect to the degenerate $d_{xz,yz}$ orbitals in the (001)-interface, while the bands hierarchy is reversed in the (110) case [52].

Depending on the orientation of the interface, different behaviors of T_c as a function of the gate potential are observed. In Fig. 2.3 we presented some examples of $T_c(V_G)$ found in literature for three differently oriented interfaces. (001)-oriented interfaces appear to be non-superconducting at low carrier density, i.e., low V_G, resulting in the non-percolating resistivity. The critical temperature than increases rapidly above some filling threshold, which is likely related to the filling of some sub-band with a high density of states [21,53–55]: in Fig. 2.3a the T_c vs V_G plot is the one calculated in [56]. For (110)- and (111)-oriented interfaces, the situation is quite different, since the system is always superconducting, displaying a finite superconducting critical temperature already at low carrier densities. Many available results show a general trend in which a first slowly increase of T_c is observed upon increasing the carrier density, then T_c decreases more rapidly above an optimal doping value V_G^{opt} (corresponding to the maximum T_c) [57–59]. Note that this is a general trend, although the situation is not completely settled as far as the absolute values of the carrier concentration is concerned. We report here the results for the (110) interface from [58] in Fig. 2.3b and for the (111) interface from [59] in Fig. 2.3c.

Several theoretical concepts have been introduced to describe this non-monotonic behavior. In [59] and [56] the focus was on the electron–electron correlations and spin–orbit interactions, while in [60] the role of the extended s-wave pairing symmetry in the (001)-oriented interfaces was claimed to play a leading role. In any case, there is not necessarily a single explanation for all orientations and it is instead important to distinguish between the (001) and the (110) and (111) interfaces. However, what is really intriguing about the behavior of T_c in the latter two cases is the fact that the decrease of T_c is observed contextually to the involvement of new bands. Many experimental and theoretical predictions point towards the direction of a multiband system at high carrier density above V_G. The decrease of T_c contextually to the
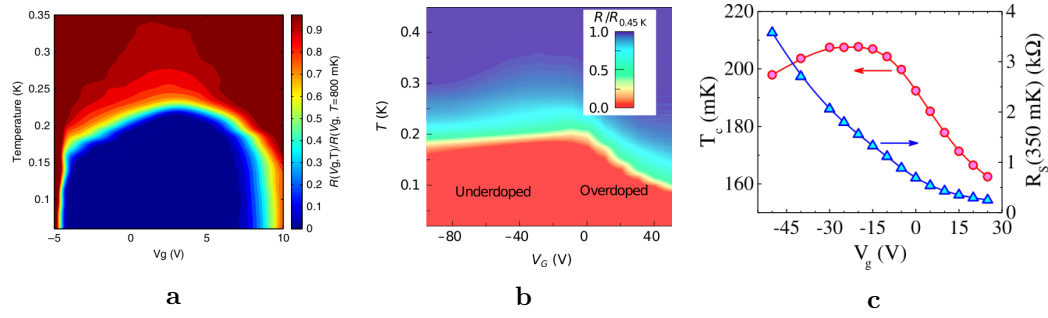
Figure 2.3. The superconducting dome of the critical temperature as a function of gat voltage in the (a) (001)-oriented [56], (b) (110)-oriented [58] and (c) (111)-oriented [59] $LaAlO_3$/$SrTiO_3$ interfaces.
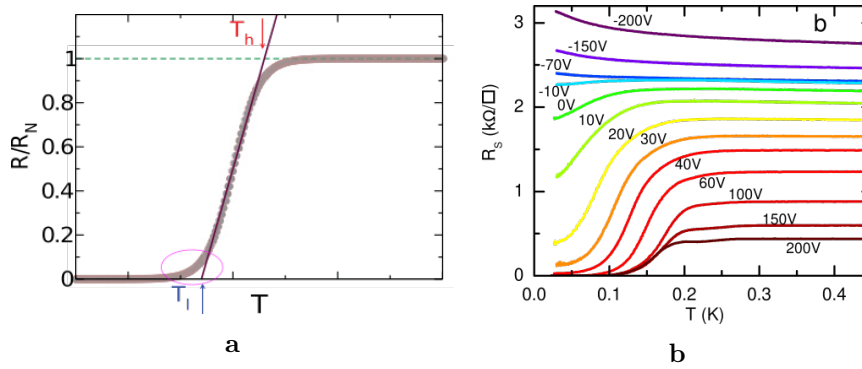

Figure 2.4. Transport measurements in (001)-oriented $LaAlO_3$/$SrTiO_3$ interfaces. (a) Broadening of the resistive transition (Data from [62] and Figure from [18]). (b) Sheet resistivities at various gating potentials [55].

filling of an upper sub-band, i.e., close to the occurrence of a Lifshitz transition, is indeed a counterintuitive mechanism. One possible explanation has been proposed in the Ref. [61], where a two-band system is considered, with an inter-band pairing interaction in the presence of elastic impurity scattering. In particular, for a repulsive inter-band interaction, one finds a strong pair-breaking effect when the chemical potential approaches the bottom of the upper band, i.e., when this second band starts to interact with the first one. This possibility is anyhow interesting since it accounts at the same time for the multiband character of interfaces and the presence of *microscopic* disorder and we will explore it further in Chapter 3

Transport measurements

Among all the odd features in transport measurements displayed by the $SrTiO_3$-based heterostructures, a large broadening of the resistive transition in temperature $R(T)$ along with a tailish behavior in the range of low temperatures is the main hallmark of the presence of mesoscopic inhomogeneities. Calling T_h the temperature of the first downturn of R at high temperature and T_l the one at which the system reaches its superconducting state $R = 0$, as in Fig. 2.4a, the relative width appears to be $(T_h - T_l)/T_l = \Delta T_c/T_l \sim 1$, which is an order of magnitude higher than what
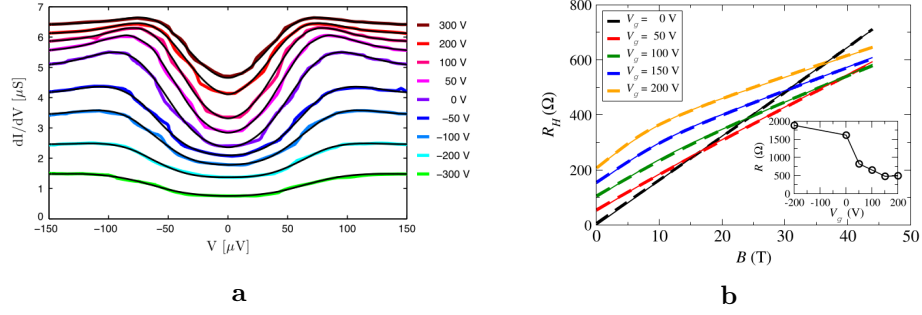
Figure 2.5. (a) Fits (black curves) of the experimental tunneling data of [14] (colored curves) with a Gaussian distribution of $P(T_c)$. The curves at positive (negative) gating have been shifted vertically by $+0.3\,mS$ ($-0.3\,mS$) for a better view. (Figure and caption from [15]. (b) Hall measurements in a $LaTiO_3/SrTiO_3$ at various doping level (Data from [55] and Figure from [22]).

is expected, and a long tail is observed near T_l. For the sake of comparison we recall that in NbN thin films [17,63] the relative width of the transition is $\Delta T_c/T_l \sim 0.3$, the system displaying clear BKT signatures despite the smearing produced by the presence of *microscopic* disorder [64, 65]. Instead, the large broadening of $SrTiO_3$-based heterostructures and other materials cannot be accounted for neither by fluctuating effects of the Cooper pairs *à la* Aslamazov-Larkin [66, 67], nor by BKT fluctuations of the vortex-antivortex core energy *à la* Halperin-Nelson [44], whereas the origin of the tail at low temperatures may seem even more mysterious if inhomogeneities are not considered [18]. Nevertheless, some systems also display a finite residual resistivity at zero temperature in their low doping regime, after a decreasing of the resistivity qualitatively similar to a metal-to-superconductor transition, until an insulating state is reached. This is the case, for instance, of the (001)-$LaAlO_3/SrTiO_3$ heterostructures, shown in Fig. 2.4b. While in the literature this has been sometimes claimed to be a new state of matter and dubbed *quantum metal* [68,69] or *failed superconductor* [70], its source can easily be explained by the intrinsic inhomogeneous nature of the 2DEG [23], as it will be explained in more detail below.

Another strong hint of mesoscopic inhomogeneity is found in the broadening of the coherence peaks in tunneling spectra [14] (see Fig. 2.5a), which is observed at temperatures higher than T_l, i.e., when the system is still metallic and far from its superconducting state, both in $LaAlO_3/SrTiO_3$ [62, 71] and $LaTiO_3/SrTiO_3$ [55, 72] interfaces. Thus, the possibility that the loss of coherence in the differential conductance dI/dV can be due to the presence of a pseudo gap in terms of preformed Cooper pairs is a forced argument [15]. Instead, the suppression of the density of states at the Fermi level caused by an inhomogeneous electron condensate can naturally explain the large coherence peaks at temperatures higher than the critical one.

Besides, measurements of the Hall resistivity in $SrTiO_3$-based interfaces also display a non-trivial feature at large enough doping, i.e., when the density of carriers increases [22, 55]. The anomaly is observed at dopings higher than some optimal value, after which the injection of more electrons does not correspond to a higher
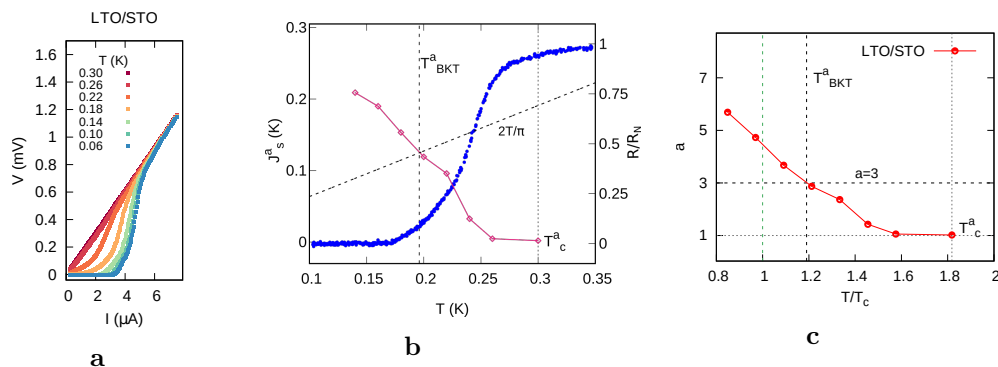
Figure 2.6. Example of the BKT analysis performed on a LaTiO$_3$/SrTiO sample, leading to inconsistent results [17]. (a) Non-linear $I - V$ characteristics at various temperatures. (b) Measured resistivity normalized to its normal state R/R_N (in blue, right axis) superimposed to the superfluid stiffness J_s^a inferred from $a(T)$ (in pink, left axis). (c) Non-linear exponent a extracted from $I - V$ data $V \propto I^a$ as a function of T/T_c, where $T_c = 0.155$ K corresponds to $R = 0$.

conductivity, as it is expected, but to a non-linearity of the transverse resistivity. We present in Fig. 2.5b the anomalous Hall-effect in the LaTiO$_3$/SrTiO$_3$ interface [22,55]. While this scenario is at odds with a simple Drude model, where the resistance only depends smoothly on the carrier density, Biscaras et al. proposed that the non-linearity is associated with the appearance of two types of charge carriers with different mobility, both present in the 2DEG but in different proportions [55]. They refer to these carriers as lower mobility carriers (LMC) and higher mobility carriers (HMC), the former present at all gate voltages, the latter entering at higher V_G and, thus, associated with the filling of an upper band.

Nevertheless, in both LaAlO$_3$/SrTiO and LaTiO$_3$/SrTiO, as in other two-dimensional materials, the presence of non-linearities in the $I - V$ characteristics has been a misleading evidence to claim for BKT physics. In the BKT theory, the non-linearity arises directly from the proliferation of free vortices caused by the application of an external current I that breaks vortex-antivortex pairs, leading to a response in terms of the measured potential V. As it was explained in Section 1.5, this is strictly connected to the jump of the superfluid density J_s, which is one of the peculiar signatures of the BKT transition. The jump of J_s from zero to a finite value (lowering the temperature of the system) happens at the intersection with the critical line $2T/\pi$, i.e., mathematically speaking at the fixed point $J_s(T_{BKT}) = 2T_{BKT}/\pi$. Recalling Eq. (1.60)

$$V \propto I^{a(T)}, \qquad a(T) = \frac{\pi J_s}{T} + 1.$$

it follows that the exponent a is supposed to jump from $a = 1$ – ohmic behavior in the last temperature within the metallic state – to $a(T_{BKT}) = 3$ at the transition. Of course in a purely theoretical framework this jump is supposed to be abrupt while in real systems some smearing is expected. However, in many two-dimensional materials – such as SrTiO$_3$-based interface – the relative width between T_c^a, as we will call the lower temperature at which $a(T_c^a) = 1$, and T_{BKT}^a is far too large $(T_c^a - T_{BKT}^a)/T_{BKT}^a \sim 0.5$ and this analysis of $I - V$ characteristics can lead to
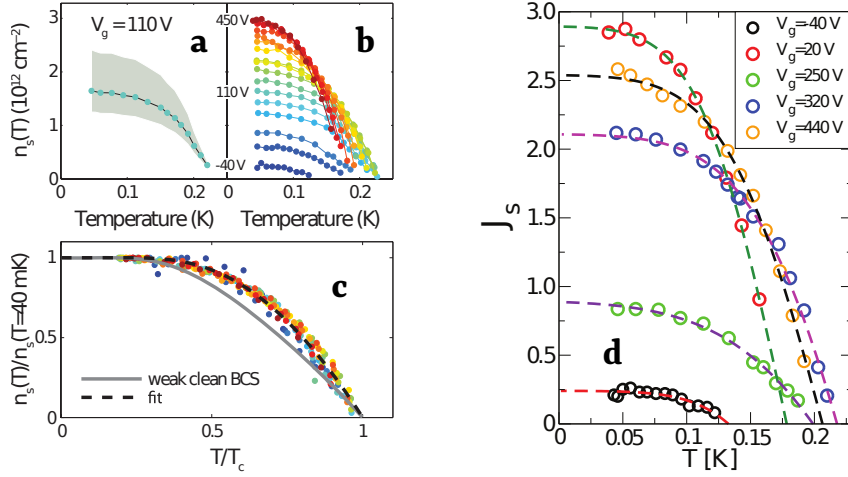
Figure 2.7. (a) Superfluid density in temperature at optimum doping $V_G = 110$ V. The gray area shows a systematic error. (b) Superfluid density in temperature for every gate voltage. (c) Normalized curves from (b). The gray line shows the temperature dependence of a weakly interacting clean BCS s-wave superconductor. The black dashed line is a fit to the data using $n_s \propto 1 - (T/T_c)^{2a}$ ($\Delta = 2.2$ and $a = 1.4$, instead of the BCS values $\Delta=1.13$) (Figures from [73]) (d) Same data (circles) fitted within the inhomogeneous random resistor network model in effective medium theory (Figure from [21]).

inconsistent conclusions, as we show in Fig. 2.6. There, we show the results of the BKT analysis performed on a LaTiO$_3$/SrTiO$_3$ sample whose resistivity is plotted in blue of Fig. 2.6b (right axis) and the superfluid stiffness J_s^a inferred from $a(T)$ is superimposed in pink (left axis), the exponent is presented in Fig. 2.6c as a function of T/T_c, where $T_c = 0.155$ K corresponds to $R = 0$. On the one hand, it is clear that neither $J_s^a(T)$ nor $a(T)$ show any jump, the superfluid stiffness appearing already in the regime of temperatures at which the system is metallic as the extrapolated T_c^a. Note also that T_{BKT}^a is also found above the superconducting state $T_{BKT}^a \approx 1.2 T_c$, thus $(T_c^a - T_{BKT}^a)/T_{BKT}^a < 0$. In other words, assuming *a priori* the presence of BKT physics leads to the conclusion that superconductivity is found when the system is still metallic, as stated from direct measurements of the sheet resistance.

Instead, the superfluid densities in a (001)-LaAlO$_3$/SrTiO$_3$ sample has been measured by means of superconducting quantum interference device (SQUID) in Ref. [73] and we report their data in Fig. 2.7. We limit ourselves to point out here that there is no sign of the peculiar jump of the superfluid density typical of the BKT superconducting transition. The authors also point out that the normalized superconducting densities n_s does not fit in a *homogeneous* BCS scenario (Fig. 2.7c).

Hereafter, we will illustrate how all the previous features, included non-linear $I - V$ characteristics, can be explained in terms of mesoscopic inhomogeneities, within a *percolative transition* scenario.

2.1.2 Percolative transition

All the odd features mentioned above can find a natural interpretation once the presence of disorder on a mesoscopic level is considered. Indeed, considering the
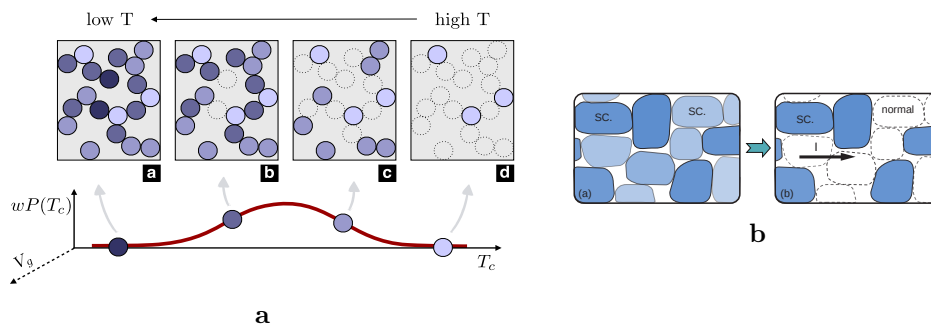
Figure 2.8. (a) Schematic figure of the formation of the inhomogeneous cluster formed by mesoscopic regions of local T_c randomly distributed according to some $P(T_c)$. While lowering the temperature, the puddles are made superconducting and the system can become superconducting ($R = 0$) if the cluster percolates (Figure from [74]). (b) Sketch figure for the appearance of non-linear $I - V$ characteristics arising directly from the inhomogeneities themselves: if an external current is applied to a system made by segregated puddles with local critical currents I_c, the puddles will *break* to their metallic state, thus generating the non-linearities (Figure from [17]).

electronic condensate as segregated into puddles – large enough to define local coherence but small with respect to the sample – the appearance of a global coherent state is related to the possibility for the system to percolate. A *random resistor network* (RRN) model has been successfully applied to explain all the odd transport phenomenology in SrTiO$_3$-based heterostructures, in which the effective resistivity is related to the bond percolation of a two-dimensional sheet of resistors. We limit ourselves here to a generic discussion of the model, which will be described in detail – and expanded – in Chapter 4.

If only a fraction w of the puddles in the 2DEG is allowed to become superconducting, with a local critical temperature T_c randomly distributed according to some $P(T_c)$, the system can transit from the metallic state to the superconducting one smoothly, such that the large broadening of the resistive transition and their tails find a natural explanation. On the other side, a superconducting non-percolating path would display a finite residual resistivity, accounting for the enigmatic *quantum metal* [18, 19]. In Fig. 2.8a the reader can find a schematic representation of the percolating superconducting cluster reached gradually with the lowering of the temperature. Moreover, it has been also shown that the fraction w needed to fit the data increases with doping [21]. In fact, lower fractions of the superconducting condensate are associated to the longer tails observed typically at low dopings and indicating the "difficulty" of the system to form a percolating cluster.

Thus, also the *pseudo gap effects* observed at low dopings in tunneling spectra find their explanation [20, 22].

Note that also Hall effects measurements can be fitted within this framework. Although in fact the non-linear behavior of the Hall resistivity alone is not a clear evidence of inhomogeneities, since in principle LMC and HMC can coexist homogeneously, it is compatible with the existence of mesoscopic disorder [22, 55]. Indeed, in Fig. 2.5b the dashed lines correspond to the theoretical fits of the experimental data (full lines).

Also the non-linearities in the $I - V$ characteristics can be reproduced quite well in a percolative transition scenario. Analogously to what happens to the sheet resistivity when lowering the temperature, the application of an external current I to a superconducting inhomogeneous medium has the effect of locally breaking the coherence in the superconducting puddles, hence generating the non-linearities (Fig. 2.8b).

In the LaALO$_3$/SrTiO$_3$ interfaces the size of a single puddle has been estimated from critical field measurements and finite size scaling [75]. Roughly, the critical field would correspond to the dephasing field B_d inside a single puddle of size L_{pd}, hence from the relation $B_d \sim \phi_0/L_{pd}^2$, ϕ_0 being the quantum flux, one can estimate L_{pd} to be of the order $\sim 100\,\text{nm}$.

The non-BCS behavior of the superconducting densities in Fig. 2.7c [73] then can be explained taking into account the mesoscopic inhomogeneous nature of the 2DEG. In Fig. 2.7d are shown the same experimental data (circles) fitted within the same percolative scenario within an effective medium theory approach. This approximation is consistent with the fact that SQUID probes intrinsically averages over micrometric regions, which are way larger than the estimated size of the puddles.

2.1.3   Transition metal dichalcogenides & other materials

The idea of a percolative transition can be applied also to other two-dimensional materials displaying transport features analogous to the ones already summarized for SrTiO$_3$-based heterostructures.

Indeed, the RRN model was successfully applied to fit the resistivity curves of TiSe$_2$, MoS$_2$ and ZrNCl, the former two belonging to the class of materials of transition metal dichalcogenides (TMDs) while the latter is a transition metal nitride (TMN). Both TMDs and TMNs are layered materials in their bulk structure, where the weak interaction between stacked layers make them belong to the family of Van der Waals materials. In particular, TMDs are characterized by the formula MX$_2$, where M is a transition metal element from group IV (Ti, Zr, Hf), group V (V, Nb or Ta) or group VI (Mo, W), and X is a chalcogen (S, Se or Te), forming layered structures of X-M-X, with the chalcogen atoms in two hexagonal planes separated by a plane of metal atoms [76]. TMN halides' formula is instead MNY where M=Zr or Hf, N is nitrogen and Y = Cl, Br or I. The crystal structure is characterized by double honeycomb metal-nitrogen layers sandwiched by halide layers [77].

In Fig. 2.9 we report the experimental data (full lines) for ZrNCl (a), MoS$_2$ (b) and TiSe$_2$ (c) fitted by means of the RRN model (symbols), borrowed from [74]. This demonstrates the wide applicability of the model, whenever the metal-to-superconductor transition displays the large broadening and tailish behavior of the resistivity that cannot be accounted for by fluctuating effects whatsoever. The authors in [74] also point out that those trends are generally enhanced [77–79] when the doping is not chemical [80]. This can also give some insights about the origin of inhomogeneities being related directly to the doping mechanism. In all three materials the charge carriers were in fact tuned by means of *ionic liquid gating*, which is a technique exploiting electrostatic doping; hence, the authors proposed that the electronic phase separation mechanism leading the inhomogeneities is caused by the interaction of the material with the ionic liquid and the substrate.
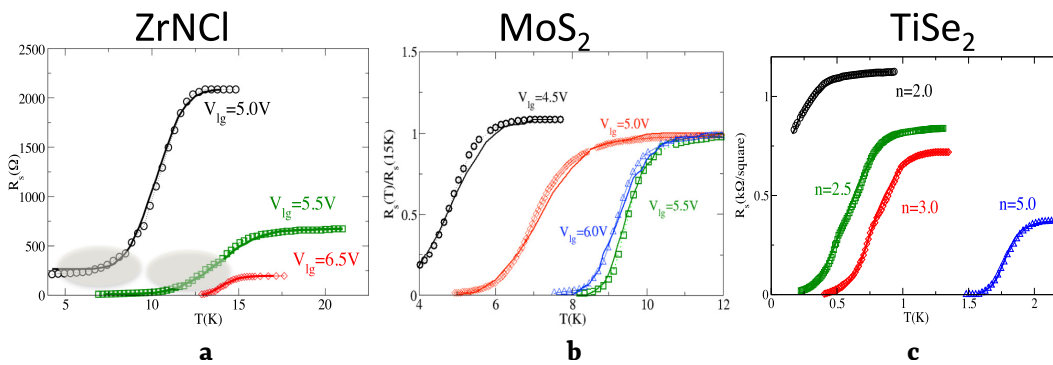
Figure 2.9. Fit (symbols) and experimental resistance (solid curves). (a) ZrNCl (from Ref. [77]) at three different values of the ionic-liquid gating (V_{lg}= 5.0, 5.5, and 6.5 V). (b) MoS$_2$ experiments of Ref. [78] (V_{lg} = 4.5, 5.0, 5.5, and 6.0 V). (c) TiSe$_2$ experiments of Ref. [79] (electron density n= 2.0, 2.5, 3.0, and 5.0×10^{14} cm^{-2}). The tailish character of the resistance curves and the saturating plateau at low electron density and temperature in panel (a) are shaded in gray, marking the regime without a percolating superconducting subset. (Figure and caption from [74])

Two main aspects of the percolating transition were pointed out in [74] about the *geometry* of inhomogeneities. On the one hand, larger *superpuddles* are needed to mimic the rapid downturn of $R(T)$ and its first decrease at high temperatures. Instead, the percolation a low T is related to the long distance connectivity of a filamentary superconducting cluster embedded in the metal: longer tails do not fit in the effective medium scenario, where inhomogeneities are homogeneously distributed, and are in fact associated to a filamentary backbone structure.

2.2 Filamentarity arising from competing orders

The detection of superconductivity in two-dimensional samples in presence of disorder also provides new frameworks, once many competing orders are interacting with superconductivity. In this Section we will summarize some observations made on superconducting cuprates that opened a way towards the study of filamentary superconductivity, here arising from the competition between the tendency of electrons to condensate in momentum space, i.e., superconductivity, and in real space, i.e., the charge density wave (CDW).

2.2.1 Cuprates

Among the variety of (quasi) two-dimensional materials displaying superconductivity, cuprates still offer many challenges. Their crystal structure is made by weakly coupled layers, which will be important from the point of view of BKT physics: in Fig. 2.10 we report the examples of La$_{2-x}$Sr$_x$CuO$_4$, YBa$_2$Cu$_3$O$_{7-x}$ and Bi$_2$Sr$_2$CaCu$_2$O$_{8+x}$ crystal structures. The first cuprate superconductor was found in 1986 in LaBa$_2$Cu$_3$O$_7$ by Bednorz and Müller [4], with a critical temperature of 35 K and after almost 40 years the origin of superconductivity is still debated, as well as the physical mechanism leading the other two mysterious phases, i.e., the *pseudo gap* phase and the strange metal phase.

Cuprates are considered an alternative route for the observation of BKT physics, where superconductivity is expected to be a quasi-two-dimensional phenomenon confined to the CuO_2 layers. The reason to look for BKT physics in such compounds lies in the fact that, in absence of Josephson pairing between planes, the vortex-pair interaction on a single layer is logarithmic at all length scales [81]. However, in the presence of an interlayer Josephson coupling, the logarithmic interaction between vortices holds only up to $\Lambda_J \simeq \xi_0\sqrt{J_\parallel/J_\perp}$, where ξ_0 is the zero-temperature in-plane coherence length, and $J_{\parallel,\perp}$ are respectively the in- and out-of-plane zero-temperature superfluid stiffness so, if the interlayer coupling is weak $J_\perp/J_\parallel \ll 1$ this length scale is large enough to allow for a BKT-like description of the vortex-antivortex interaction, despite the system thickness. This in principle makes such systems the best possible candidates for the detection of the BKT transition. Nevertheless, the situation is still controversial. The first experimental evidence of a BKT transition in cuprates was found in 1999 by Corson et al. [82], who extracted the superfluid stiffness from high-frequency conductivity measurements in $Bi_2Sr_2CaCu2O_{8+x}$. More recently, BKT signatures were found in bulk samples of highly underdoped $La_{2-x}Sr_xCuO_4$ [28], where the paraconductivity effects, determined from magnetoresistance measurements, were compared with the non-linear current-voltage $I - V$ characteristics. On the other side, direct measurements of the inverse penetration depth have shown that in the $YBa_2Cu_3O_{7-x}$ family no BKT jump is observed even in strongly underdoped thick films [83, 84] or crystals [85]. A BKT-like superfluid-density jump is only seen in few-unit-cell thick films of $YBa_2Cu_3O_{7-x}$ [85] or $Bi_2Sr_2CaCu_2O_{8+x}$ [86], but even in this case, as the samples get underdoped, the superfluid density jump gets smeared out. One possible explanation for such a smearing of the BKT signatures can most likely be associated with the presence of competing orders.

Along with superconductivity, cuprates display many other phases, appearing at different chemical dopings. Their phase diagram is presented in Fig. 2.11: at small dopings, the system is an insulating antiferromagnet (AF) up to really high temperatures $\sim 300\,K$ while at higher dopings one finds a superconducting critical line T_c. The superconducting dome extends in a hole doping range between some p_{min} and p_{max} in which, however, other physical mechanisms also intervene.

A charge ordered phase (T_{CDW}) can be observed in the superconducting region of the phase diagram leading to the so-called *stripe* region (dashed in red),the charge order extending above the superconducting critical line, in the pseudogap region (yellow). This name was coined in [87] to address the experimental evidences of gap-like features above the superconducting critical temperature and up to $T^* \gg T_c$ observed in underdoped cuprates [88–90]. Although still largely debated, the origin of the pseudogap has been linked with the appearance of preformed pairs missing of a global phase rigidity [91]. It is worth underlying the importance of charge order (CO) and charge density fluctuations in cuprates. A more accurate definition of CO or charge density wave (CDW) will be given later on, for now let just state that a CDW is a modulation of the electron charge in the lattice, mediated by phonons, leading to the formation of "real space pairs" periodically arranged on the lattice.

Dynamical charge density fluctuations have also been claimed to play a crucial role in restoring the strange metal phase [92].

Leaving aside the strange metal behavior, we will focus on the underdoped region
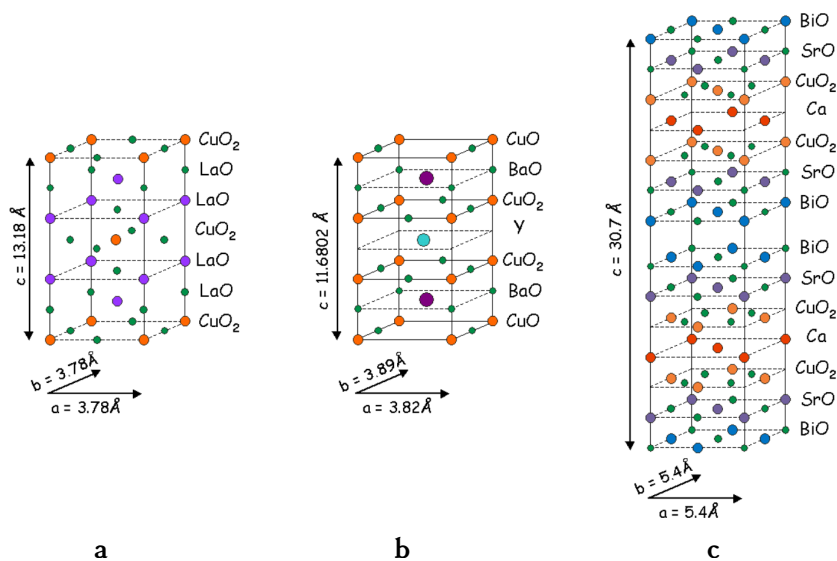
Figure 2.10. Crystal structure of undoped cuprates ($x = 0$): (a) $La_{2-x}Sr_xCuO_4$, (b) $YBa_2Cu_3O_{7-x}$, (c) $Bi_2Sr_2CaCu_2O_{8+x}$. Note that they present, respectively, one, two and three CuO_2 planes. Figures from `http://hoffman.physics.harvard.edu/materials/CuprateIntro.php`

of the superconducting dome where superconductivity and CDW represents two competing orders [92–95].

2.2.2 CDW: a glance

A CDW is produced by an electronic-lattice instability, i.e., mediated by an electron-phonon interaction, leading to a spontaneous periodic modulation of the electron density on the crystal lattice, with a characteristic modulating wave vector .

We limit ourselves to introduce the concept of CDW in the simplest possible two-dimensional example, within the single-band tight-binding model for electrons on a square lattice of lattice constant a. The energy dispersion with respect to the chemical potential μ is given by $\varepsilon_{\mathbf{k}} - \mu = 2t(\cos k_x + \cos k_y)$ where $t > 0$ is the hopping parameter. Being the spin degeneracy equal to 2, the half-filled configuration is obtained with one electron per site ($n = 1$) and the Fermi surface (FS) is a rotated square encased the reduced Brillouin zone (RBZ), as in Fig. 2.12. Note that each point of the FS can be connected to the opposite edge by a vector $\mathbf{Q}$, known as the nesting vector, sketched in red in Fig. 2.12. This perfect nesting condition can be linked to the one-dimensional free electron gas, characterized by the peculiar FS made by two single points at $k = \pm k_F = \pm \pi/a$ where the nesting vector is $Q = 2k_F/a$. Hence, two-dimensional bands look, in general, quasi-one-dimensional along the directions where the nesting occurs and perfectly-1D at half-filling.

By applying an external potential $\phi(\mathbf{r}, t)$ acting on the electron gas, the rearrangement of the charge density $\rho(\mathbf{r}, t)$ can be expressed by means of linear response theory in Fourier space as

$$\rho(\mathbf{q}, \omega) = \chi(\mathbf{q}, \omega)\phi(\mathbf{q}, \omega) \tag{2.1}$$
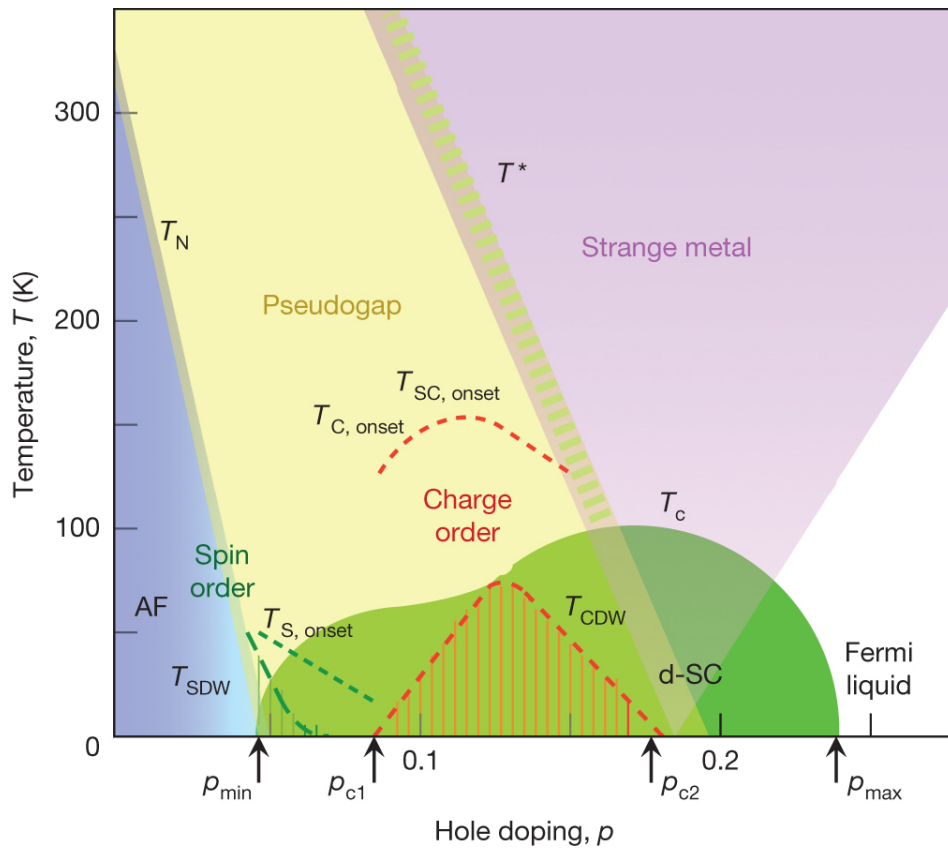
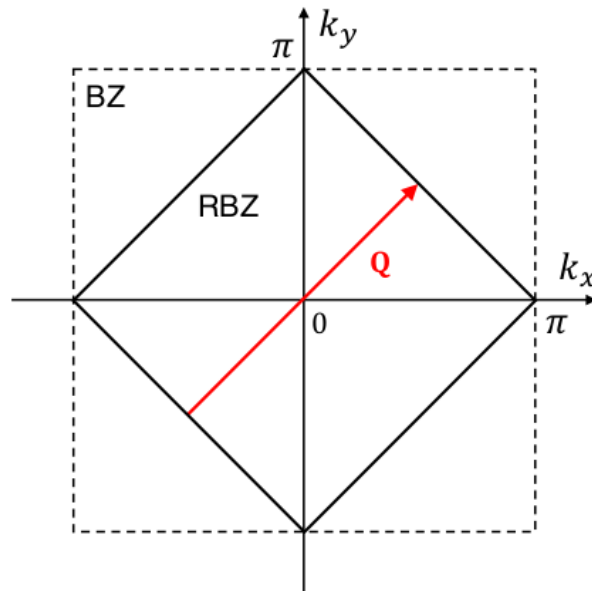**Figure 2.11.** Cuprates' phase diagram (Figure from [96]).

Figure 2.12. Reduced Brillouin Zone (RBZ) for a half filled tight-binding model in 2D at $\mu = 0$. Notice that all the Fermi surface points bordering the RBZ are linked by a single $\mathbf{Q} = (-\pi, \pi)$ vector (red arrow). For simplicity, the lattice constant is set to $a = 1$.
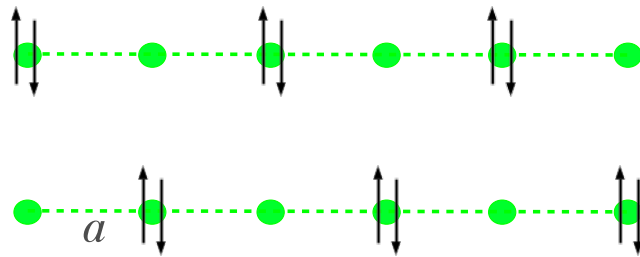
Figure 2.13. Sketch figure of two possible variants of CDW in a one-dimensional chain on ions of lattice spacing a at half filling $n = 1$. The green dots represent the ions while the up/down arrows are the electrons of spin $\pm 1/2$, to fulfill Pauli's exclusion principle, .

where $\chi(\mathbf{q}, \omega)$ is the so-called Lindhard response function:

$$\chi(\mathbf{q}, \omega) = \frac{2}{N} \sum_{\mathbf{k}, i\omega} \frac{f(\varepsilon_{\mathbf{k}}) + f(\varepsilon_{\mathbf{k+Q}})}{\varepsilon_{\mathbf{k}} - \varepsilon_{\mathbf{k+Q}} + i\omega}, \tag{2.2}$$

N being the number of sites in the lattice and $f(\varepsilon_{\mathbf{k}})$ the Fermi function. Since at the nesting vector $\mathbf{Q}$ $\varepsilon_{\mathbf{k+Q}} = \varepsilon_{-\mathbf{k}}$, in the static limit $\omega = 0$ the Lindhard function is

$$\chi(\mathbf{q}, \omega = 0) = \frac{1}{N} \sum_{\mathbf{k}} \frac{1}{\varepsilon_{\mathbf{k}}} \tanh\left(\frac{\varepsilon_{\mathbf{k}}}{k_B T}\right) \sim \frac{N}{2} \ln\left(1.13 \frac{\varepsilon_F}{k_B T}\right) \tag{2.3}$$

showing a logarithmic divergence as a function of T at low temperatures. For different values of the wave vector this divergence will not arise and, therefore, $\chi(\mathbf{q})$ will exhibit a strong peak at $\mathbf{q} = \mathbf{Q}$. The divergent response at $T = 0$ implies that in the presence of any attraction in the particle-hole channel the charge susceptibility will diverge. In other words, at low temperature the electrons will tend to arrange themselves in such a way that there is a net density modulation of period Q: the CDW.

We can picture this charge modulation along one direction naively as a chain of ions of lattice spacing a with the charge distributed with a periodicity $\lambda = 2\pi/Q = 2a/n$. At half filling ($n = 1$) $\lambda = 2a$, and we have two possible variants of the charge modulation on the one-dimensional lattice, as sketched in Fig. 2.13. Note that this situation of strongly correlated electrons can be viewed as preformed "real space Cooper pairs".

Nevertheless, in more realistic systems displaying CDW order – with periodicity longer than $2a$ – the number of variants is usually higher than 2 and the presence of quenched impurities can favor different variants in different regions. The result is a polycrystalline charged ordered state, where many ordered patterns mismatch with one another, preventing the possibility to observe a single ordered state.

We point out that the CDW scenario presented so far is an example of a commensurate CDW, for which both the maximum and minimum charge modulations correspond to lattice sites, so the wavelength of the charge modulation and the underlying lattice spacing a have a common multiple. An incommensurate CDW is instead a modulation of the charge distribution where the ratio between the periodicity of the charge modulation and the lattice site is an irrational number.

2.2.3 Evidences of filamentarity

Having in mind the very basics of CDWs and a global picture of the phenomenology of the cuprates phase diagram, we discuss now some recent experiments strongly suggesting the presence of filamentary superconductivity as a result of the competition between CO and superconductivity, henceforth the CO-SC competition.

Adding the external magnetic field H axis, the phase diagram in Fig. 2.11 should be extruded also in its perpendicular direction. We present here the measurements performed in [29] on a $La_{2-x}Sr_xCuO_4$ sample at various Sr dopings in the underdoped region, i.e., where CO is known to be hidden below the superconducting critical line 2.14. The resistivity curves are measured varying both the amount of Sr in the sample and the external magnetic field H, probing the superconducting-insulating transition: the data in Fig. 2.14a, where different colors refers to different x, identifies the resistivity at $H = 0$ (full lines), H_c (solid lines with dots) and for the maximal field H (dashed lines with crosses). It is crucial to underline the fact that two critical fields are indicated: H_c^* is defined as the field corresponding in a long high temperature plateau of $R(T)$ – in Fig. 2.14b is evidenced the curve corresponding to $x = 0.125$ where the plateau is already present at $H = 0$ – and H_c is the field at which superconductivity is finally suppressed.

Indeed, superconductivity appears to be resilient to the application of a magnetic field, particularly in the vicinity of $x = 0.09$ and $x = 0.19$, while it is suppressed in $x = 0.125$. The resulting phase diagram T_c vs x in Fig. 2.14c shows in fact that well-known superconducting dome at $H = 0$ tends to split into two smaller domes centered around $x = 0.09$ and $x = 0.19$ while increasing H up to $20\,T$. The interesting aspect is that those doping values corresponding to maxima are consistent with the ones at which are expected the QCPs, signaling the presence of the CDW dome (dashed region in Fig. 2.11. In their work [29], Caprara et al. refer to those as "avoided QCPs": in fact, the resistivity of the system at finite H seems to signal the appearance of a superconducting-insulating transition, characterized here by the presence of the plateau, yet the system drops to its superconducting state at finite temperature.

At high magnetic fields, the authors indicates with T_{MIN} the temperature at which, at high fields H, the slope of the resistivity in temperature changes from positive $T > T_{MIN}$ to negative $T < T_{MIN}$ [97], interpreting it as the onset of a polycrystalline CDW. For some doping values, as for instance $x = 0.06$ and $x = 0.08$, another temperature needed to be highlighted, where an inflection point T_{INF} is observed in $R(T)$, signaling the presence of strong Cooper pair fluctuations, eventually driving the system superconducting below some temperature indicated as T_{MAX}. The presence of this inflection point leads again to the direction of a competing CO-SC mechanism, in which superconductivity can only be filamentary. In Fig. 2.15 we report the colorplot of the first (upper panels) and second (lower panels) derivative of $R(T)$ with respect to T as functions of both temperature and magnetic field, for the three exemplary cases of $x = 0.06$, $x = 0.08$ and $x = 0.25$. In the upper panels, the T_{MIN} and T_{MAX} lines marked in purple divide respectively the region with $R'(T) > 0$ (in red) from the ones at $R'(T) < 0$ (in green), thus highlighting the CDW area, while the superconducting state correspond to the white region $(R''(T) < 0)$ in the lower panels. For $x = 0.06$, the line T_{MIN} covers all the

magnetic fields values and is independent from it. Lowering the temperature at low fields $H < 2\,\mathrm{T}$ the system transits to its superconducting state for temperatures lower than T_{MAX}, corresponding to the T_{INF} line, marked in red in the lower panel. The $x = 0.08$ case, where again both CO and superconductivity coexist in a finite range of H, presents the peculiar feature of a marked plateau in $R(T)$ indicated with a yellow spot: in the upper panel, that is the point at which T_{MIN} and T_{MAX} lines converge, while at higher fields a re-entrant superconducting phase still coexist with the CDW one. From the comparison of those two cases, one can conclude that the doping increase has moved the re-entrant superconducting state towards higher fields. Finally, at $x = 0.25$ we enter the high doping region of the superconducting dome where CDWs are suppressed and the superconducting state follows its expected behavior.

The authors propose a schematic phase diagram (Fig. 2.16) that summarizes what was discussed so far. At each doping level, the field H acts as a control parameter, tuning the competition between the superconducting and the charge ordered state. Two QCPs are identified at finite H, indicated respectively with QCP1 and QCP2, and encasing the re-entrant state, in which filamentary superconductivity manifests. The former is what was called "avoided QCP" and corresponds to the field H_c^* at which the bulk SC state is expected to drop yet strong Cooper pairs fluctuations generates the tail entering the CDW side of the phase diagram; the latter (QCP2) corresponds instead to the real critical field H_c that finally suppresses superconductivity.

2.2.4 A model for competition

Following the path of a filamentary superconducting state emerging from the CO-SC mechanism, we present a simple theoretical model that has been proposed in this context. The idea of an interplay between real space ordering, disorder, and momentum space condensation (superfluidity or superconductivity) is not new and has also been invoked in the context of supersolid behavior in ^{4}He [98].

An important theoretical tool to mimic the desired CO-SC competition will be the generalized attractive Hubbard model [31, 32]:

$$H = -t \sum_{<ij>\sigma} c_{i\sigma}^\dagger c_{j\sigma} - U \sum_i n_{i\uparrow} n_{i\downarrow} + V \sum_{<ij>} n_i n_j \qquad (2.4)$$

where t is the hopping amplitude, $c_{i\sigma}^\dagger$ ($c_{i\sigma}$) creates (destroy) a fermion of spin σ at site i, $U > 0$ is the on-site attraction, $n_{i\sigma} = c_{i\sigma}^\dagger c_{i\sigma}$ is the number of fermions, V is the nearest neighbors repulsion and $n_i = n_{i\uparrow} + n_{i\downarrow}$. Referring the reader to [99] for a complete review of the attractive Hubbard model, let us just point out that away from half filling the ground state is purely superconducting, reproducing both the BCS weak coupling limit for $U \ll t$ and the Bose Einstein Condensation (BEC) in the strong coupling limit $U \gg t$. At half filling for $V = 0$ the model has instead a ground state degeneracy between CDW and superconductivity, making it the perfect candidate to study their competition. The repulsive term V is thus needed to break the symmetry, favoring the superconductivity for $V < 0$ or the CDW for $V > 0$. More generically, the Hubbard model has a wide applicability in tuning the competition between different order parameters, not necessarily involving

a

b

c
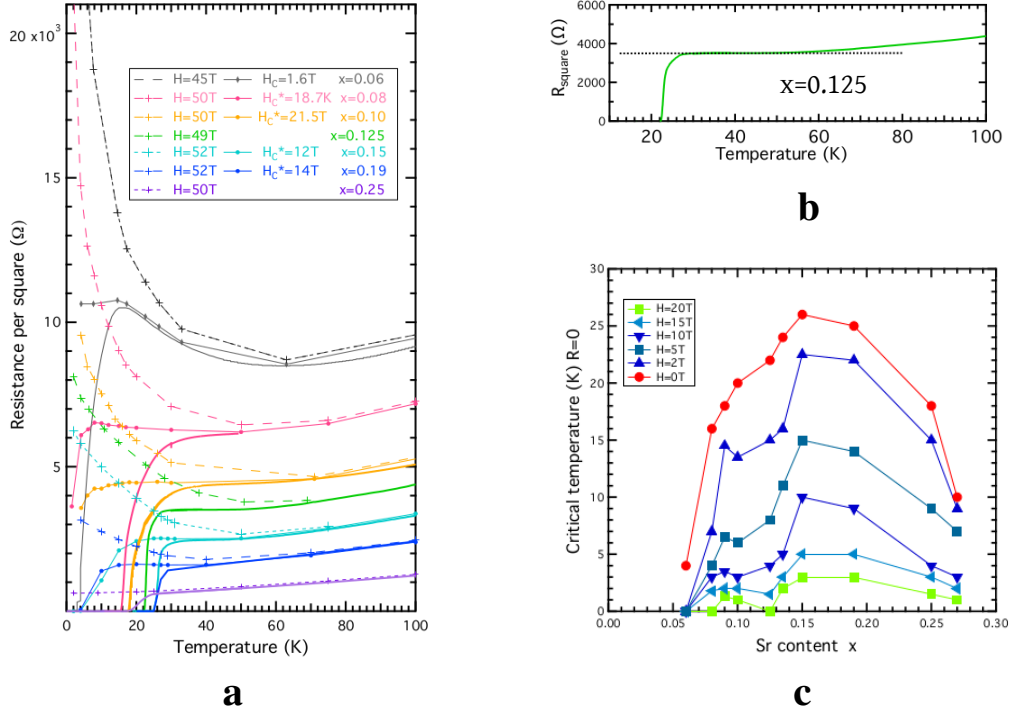
Figure 2.14. (a) Resistivity in temperature at $H = 0$ (full line), $H = H_c^*$ defined as the field at which a long plateau is observed and at some higher field H. (b) Sample at $x = 0.125$ for which the plateau is already present at $H = 0$ in a temperature range around $28\,\mathrm{K}$ and $55\,\mathrm{K}$. (c) Superconducting critical temperature $R = 0$ as a function of Sr doping x at different magnetic fields ranging from 0 to $20\,\mathrm{T}$. (Figures from [29])
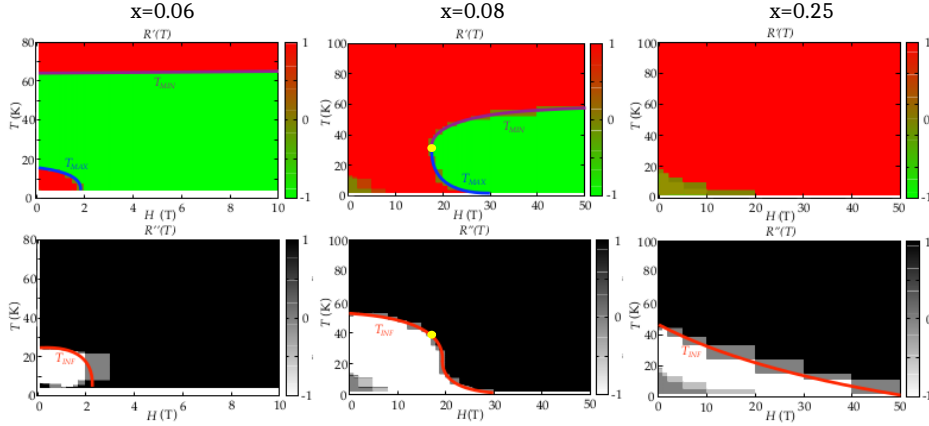
Figure 2.15. Top panels: Color maps of the sign of the sign of $R'(T)$ in the (H, T) plane. As a guide to the eye, the T_{MIN} lines are marked in purple, the T_{MAX} lines are marked in blue and their common point (if any), is marked by a yellow spot signaling the location of the plateau. Bottom panels: Color maps of the sign of $R''(T)$ in the (H, T) plane. The T_{INF} line is marked in red. Left panels: x=0.06; T_{INF} is always much lower than T_{MIN} for this doping. Central panels: $x = 0.08$. Right panels: $x = 0.25$; note that at this doping $R'(T) \geq 0$ is always true (Figure and caption from [29]).

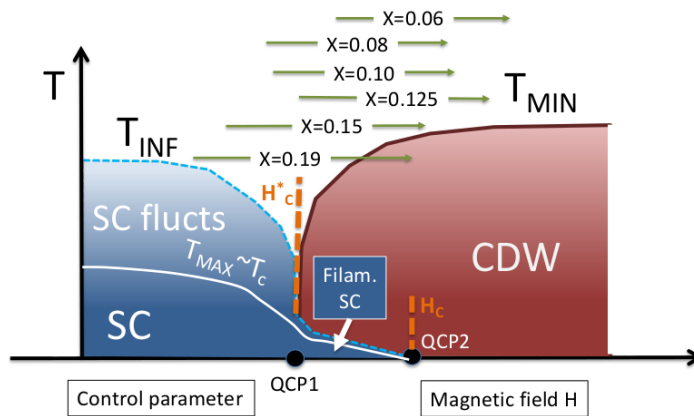**Figure 2.16.** Proposed phase diagram T vs H (Figure from [29]).

superconductivity. For instance, it has been used to tune the competition between ferromagnetism and antiferromagnetism in quasi-one-dimensional $Ce_2O_2FeSe_2$ [100].

For $U \gg t$, the Hubbard model can be exactly mapped onto an antiferromagnetic Heisenberg model (see Fig. 2.17)

$$H = \sum_{<ij>} \left[J_\parallel (s_i^x s_j^x + s_i^y s_j^y) + J_\perp s_i^z s_j^z \right] \tag{2.5}$$

where the pseudospin interactions are $J_\parallel = J = 4t^2/U$ and $J_\perp = J + V$, making more evident the anisotropy introduced by the term V. The mapping between the attractive Hubbard model and antiferromagnet passes through the "attractive-repulsive" transformation [31, 99]. The antiferromagnetic model can be in turn mapped onto a ferromagnetic one by a coarse graining protocol: if a system consist in large patches of ordered regions, the operators s_i^x, s_i^y, s_i^z can be replaced by their expectation values, i.e., the local staggered magnetization, on each of the patches. In other words, the SO(3) symmetry of the Hubbard model can be mapped onto a three dimensional pseudospin, where the up and down directions represent two possible variants of CDW and the in-plane component is the superconducting one. Note that in the generalized Hubbard model, the variants encoded are only 2, but in general there may be more, according to the periodicity of the charge modulation. While strictly speaking the mapping applies to the Hubbard model, one can use the coarse graining argument to apply it to a more general situation in which CDW is in competition with superconductivity. In this framework the implicit assumption is that at least short range order is present, considering regions with linear size greater than the lattice spacing but smaller than the correlation length, over which one can define $\mathbf{s}_i$ with unitary magnitude $|\mathbf{s}_i| = 1$, neglecting fluctuations in the strength of fermion pairing.

In Refs. [31] and [32] the CO-SC competition has been studied at $T = 0$ within this Heisenberg framework, with an effective Hamiltonian defined as

$$H = -J \sum_{<ij>} \mathbf{s}_i \cdot \mathbf{s}_j + G \sum_i (s_i^z)^2 + \frac{w}{2} \sum_i h_i s_i^z \tag{2.6}$$
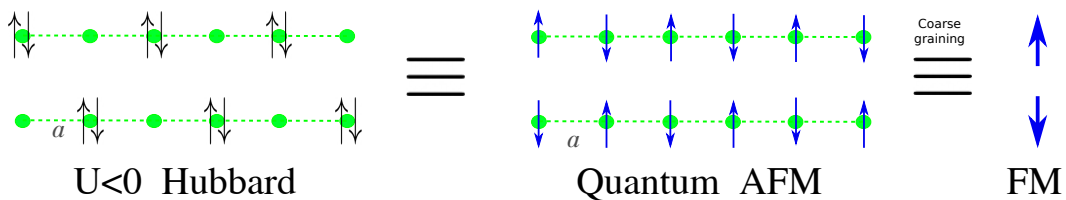
Figure 2.17. Sketch figure of the mapping of a charge density wave from the attractive Hubbard to the quantum antiferromagnet (AFM). Using a coarse graining argument one can locally map the AFM to a classical ferromagnetic system (FM).

where G breaks the symmetry of the spin, favoring the CDW for $G > 0$, and the random field term h_i is a random variable uniformly distributed in $[-1, 1]$ mimicking the impurities, always present in real samples. Varying both G and w, filamentary superconductivity appears as a topologically protected domain wall at the boundaries of two different CDW domain: when the up and down regions are formed, the spins at the interface between the two opposite clusters are forced to smoothly change from an up or down configuration to the opposite, transitioning to an in-plane state, the superconducting (see Fig. 2.18a in which the two possible variants are called A-CDW and B-CDW).

Already at $T = 0$ they managed to model the re-entrant filamentary superconducting state expected by tuning appropriately the anisotropy term G and the impurity strength w. We report the phase diagram presented in [32] in Fig. 2.18b, where the colorplot refers to the value of the superfluid density (called here ρ_s) with respect to the spin interaction J.

The filamentary superconductivity scenario presented so far is still open to many possibilities of understanding. In Chapter 5 we will analyze an Heisenberg model, very similar to the one in Eq. (2.6), trying to move some extra steps towards the comprehension of the phase diagram in Fig. 2.16, addressing the temperature dependence of many physical quantities and the critical temperatures of the phases involved.

2.2.5 Competition in other materials

Hints of filamentary superconductivity have been reported also in iron-based superconductors. A recent review of iron-based materials can be found in Ref. [101]. For our scope, we can just point out that their phase diagram is very similar to the one of cuprates, with an antiferromagnetic phase at low dopings and a superconducting dome at higher hole dopings. A pseudo-gap region is also present. In [102] the presence of filamentary superconductivity has been claimed in $(Ca_{0.73}La_{0.27})FeAs_2$ from transport and magnetotransport measurements at low pressures P=1.6 GPa, becoming bulk at 3.2 GPa. Hints of filamentarity were found instead in antiferromagnetic $CaFe_2As_2$ [103] and, more generally, across the phase diagram of $Ba(Fe,Co)_2As_2$ [104]. In [105] both filamentarity and inhomogeneities are observed to interplay in $Ca_{0.86}Pr_{0.14}Fe_2As_2$ single crystal, the authors pointing out that "filamentary nature is a consequence of nonuniform Pr distribution that develops localized, isolated superconducting regions within the crystals". This last statement in particular seems to be in line with our considerations about the interplay of
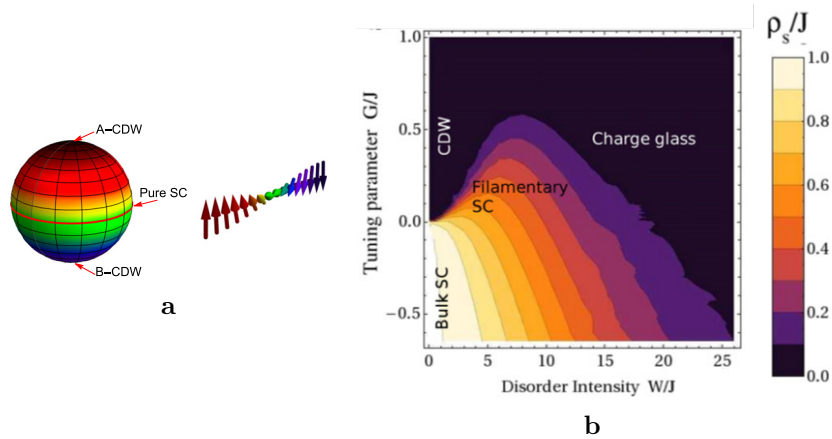
Figure 2.18. (a) The sphere represents the SO(3) symmetry of the pseudo-spin: the in-plane state is the pure superconductor, while up and down states refer to two different CDW variants called A,B-CDW. The flipping of neighbors spins from up to down should necessarily pass from an in-plane state. (b) Zero temperature stiffness ρ_s as a function of both anisotropy parameter G and quenched disorder strength W (Figures from [32]).

competing orders and impurities. Nonetheless, while in cuprates the order parameter involved together with superconductivity is the CDW, no evidence of charge ordering were found so far in iron-based materials, although spin density waves could be a good candidate to consider in order to explore this topic also in iron-based. As a matter of fact, the stripe phase detected in iron-based materials has already been linked to the presence of spin density waves [106, 107].

Chapter 3

Microscopic disorder in a two band superconductor

As it was already stated in the previous Chapter, 15 years after the discovery of superconductivity in $SrTiO_3$-based heterostructures many questions are left open. In particular in Section 2.1.1 we described the problem of the suppression of the critical temperature with the increase of the number of carriers in the system. In this Chapter, we will investigate the possibility that the pairbreaking effect observed can be *simply* caused by the presence of disorder in a multiband system, applying the model proposed by Trevisan et al. in [61] to a specific sample of (110)-oriented interfaces. The work presented in this Chapter was born as an easy task to a theoretician – borrowing a model to fit experimental data – but it turned out to be an interesting and systematic study of the interplay between disorder, multi-band physics, and superconductivity. As a matter of fact, it will offer a way to disentangle the effects of microscopic and mesoscopic disorder.

3.1 Experimental evidences of pair-breaking

Let us present as a starting point the experimental observations on a (110)-oriented $LaAlO_3/SrTiO_3$ sample. It should be pointed out that multi-band superconductivity has been experimentally demonstrated only in the (001) interface, which is the most studied one, while for the (110)-orientation this has been only predicted theoretically. Normal and Hall resistivity measurements follow the trend already presented in Section 2.1 with a suppression of superconductivity in correspondence to an increase of the carrier density. As it was done before [22, 55], Hall resistivities can be fitted with a two carrier model, accounting for two populations of electrons with lower (LM) and higher mobility (HM). The resulting carrier densities n_{Hall}, n_{LM} and n_{HM} and mobilities $\overline{\mu}_{LM}$, $\overline{\mu}_{HM}$ are presented respectively in Fig. 3.1b and 3.1c. Comparing
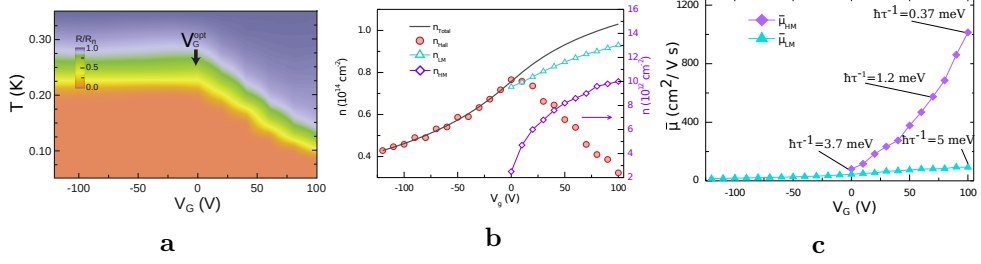
Figure 3.1. (a) Colorplot of the sheet resistance normalized by its value R_n at $T = 0.45\,\mathrm{K}$ as a function of V_G (x axis) and T (left axis). (b) Gate voltage dependence of the carrier density of the low-mobility n_{LM} and high-mobility n_{HM} population of electrons extracted from the two-carrier analysis of the Hall effect. Red circles indicate the Hall carrier density measured in the limit of zero-magnetic field, $n_{Hall}(H \to 0)$ which only gives the correct electron density in the one band regime, i.e., $V_G < 0$. The total carrier density of the 2DEG n_{2D} has been obtained by integration of the gate capacitance and by matching it to n_{Hall} in the one-band regime. (c) Mobility of the less mobile carriers $\overline{\mu}_{LM}$ and the more mobile ones $\overline{\mu}_{HM}$ as a function of the gate voltage.
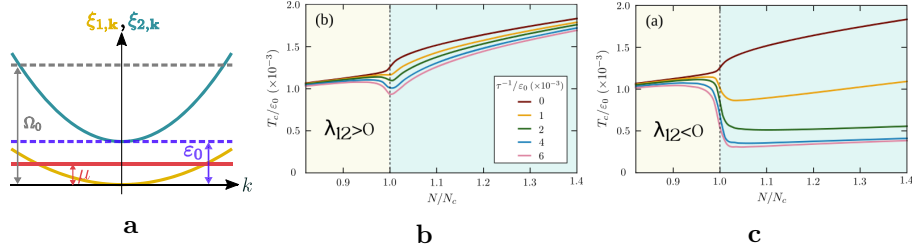
Figure 3.2. Figures from [61]: (a) Scheme of the two band model in which the Debye energy is the greater energy scale at play, hence both bands are always in the BEC limit. Results for the critical temperature as a function of the normalized number of particles N/N_c, N_c being the number of electrons at the Lifshits transition, for a (b) positive $\lambda_{12} > 0$ and (c) negative $\lambda_{12} < 0$ interband coupling constant.

those results and the colorplot of the sheet resistance as a function of the gate potential V_G and the temperature T in Fig. 3.1a one can observe a slight increase of the critical temperature up to an optimal doping $V_G^{opt} = 0$, corresponding to a single band model; then for $V_G \geq V_G^{opt}$ an important suppression of the superconducting state (the orange region) is observed right when the HM carriers enters the system.

We will explore in the next Sections the possibility that this pair-breaking effect at the Lifshitz transition is due to an interband repulsive coupling, as it was suggested in a work by Trevisan et al. [61]. They showed that a two band model with the presence of a weak disorder generates a suppression of the critical temperature as soon as the upper band is involved, whenever the two inter-bands coupling constants are negative $\lambda_{12} = \lambda_{21} < 0$. Note that the greatest scale of energy in their model is the Debye energy, hence both of the bands are always in the Bose-Einstein condensation (BEC) regime.

3.2   Theoretical model

The suppression of the critical temperature observed in $LaAlO_3/SrTiO_3$ interfaces and, more specifically, presented in Fig. 3.1a is at odds with the general idea that an increasing number of carriers involved, especially with a higher mobility, should in principle make available a higher number of Cooper pairs thus strengthening the superconducting state. More precisely, Anderson's theorem [9] states that superconductivity is robust against weak non-magnetic disorder. In his seminal paper, the argument was strictly following from the fact that non-magnetic impurities in s-waves cannot break time-reversal symmetry. It is then more likely that the theorem is circumvented in its assumptions rather than failed.

3.2.1   Parameters

In our attempt to adapt and fit the model proposed in [61] to the data presented, we start by extrapolating what we can from the experiments. Although we are aware that a three-band model would be more appropriate, given the band structure of $SrTiO_3$-based interfaces (see Section 2.1.1), we decided to use a two-band model, where the lower band is an effective single band accounting for the degenerate bands coming from $d_{xz/yz}$ orbitals (see Fig. 2.2b). This will guarantee a more transparent theoretical treatment, without affecting any of the crucial aspects we are interested in. A three-band model would in fact simply require more computational effort and include more free parameters to adjust. From now on, let us simplify the notation, using subscripts 1 and 2 for the lower and upper sub-band instead of LM and HM.

The inverse scattering time τ^{-1} can be extrapolated from the mobility $\mu_i = \frac{e\tau}{m_i}$, where m_i are the effective masses are assumed to be $m_1 = m_{xz/yz} = 2.3m_0$ and $m_2 = m_{xy} = 3.1m_0$, coherently to what is found in literature [108], e and m_0 being respectively the charge and mass of the electron. In Fig. 3.1c we indicated some of the calculated values of the disorder $\hbar\tau^{-1}$, which settles around the value $\hbar\tau^{-1} \sim 5\,\text{meV}$ in the lower band while ranging approximately from $3.7\,\text{meV}$ down to $0.37\,\text{meV}$ in the upper band. As a consequence, we can already state that we are no longer in the limit of weak disorder, as for it was requested by Anderson's Theorem to be valid.

From the measurements of the number of particles in Fig 3.1b one can extrapolate the energy corresponding to the entering of the upper band ε_0 and have already an estimate of the mapping between gate voltage V_G and chemical potential μ. Calculating the density of states (DOS) using the usual formula for non-interacting fermions

$$N_i = 2 \int \frac{d^2k}{(2\pi)^2} \delta\left(\varepsilon - \frac{\hbar^2 k^2}{2m_i}\right) \tag{3.1}$$

we obtain $N_1 = 1.1 \cdot 10^{16}\,\text{m}^{-2}\,\text{meV}^{-1}$, $N_2 = 1.3 \cdot 10^{16}\,\text{m}^{-2}\,\text{meV}^{-1}$. Hence one can calculate $\varepsilon_0 = 90$ meV, corresponding to the value at which $N_1\varepsilon_0 = n_H(V_G^{opt}) \approx 0.8 \cdot 10^{14}$ cm^{-2}. We can then infer the chemical potential variation of the gate potential from V_G^{opt} to $100\,\text{V}$ as $\mu' - \varepsilon_0 \approx 7$ meV. In other words, the gate variation from -100 V to 0 V corresponds to a variation in the chemical potential μ of about $50\,\text{meV}$ while ranging V_g from 0 up to $+100$ V means tuning μ of just 10 meV.

Finally, we will assume a standard BCS coupling mechanism, using as a pairing energy the Debye energy $\Omega = 400 \cdot k_B = 34.5\,\text{meV}$ [56]. It is worth noting that for

bulk SrTiO$_3$ as for SrTiO$_3$-based heterostructures the superconducting mechanism is still a debated issue; however, in [21] it was pointed out that a weak coupling BCS regime can account for the odd behaviors of the superfluid stiffness measured in [73], provided that inhomogeneities are considered. Since the ultraviolet cutoffs are estimated to be $\Lambda_{1,2} > 1\,\text{eV}$ and given that $\mu' - \varepsilon_0 \sim 7\,\text{meV}$ we find that the appropriate model to consider consist in an intermediate regime, sketched in Fig. 3.3: in the lower band the pairing window $\mu \pm \Omega$ is always fully contained within the band as in the standard BCS description, while the upper band stays in BEC regime. When in fact the chemical potential approaches the bottom of the upper band ε_0 an effective coupling between the two bands is already at play, even if the chemical potential is still below the Lifshitz point.
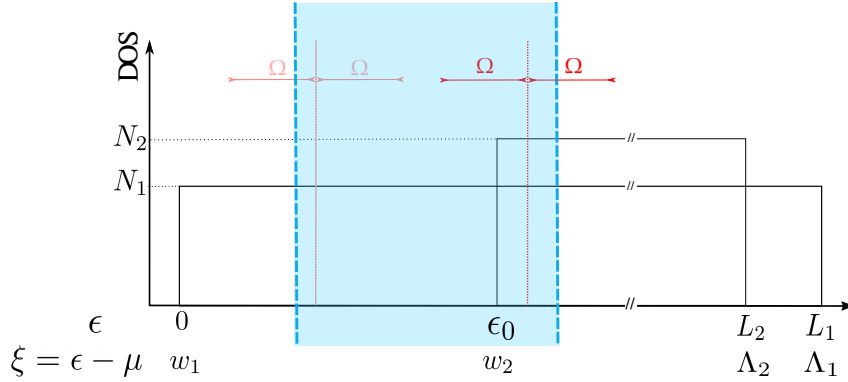
Figure 3.3. Sketch figure of the density of states (DOS) N_1 and N_2 as functions of the energy ε (reduced energy $\xi = \varepsilon - \mu$) of the two-band system. The blue dashed lines highlight the observation window of energy (reduced energy) accessible, so far, through experiments: according to the parameters involved in LAO/STO interfaces, the lower band is well described by the BCS theory, the pairing window $\mu \pm \Omega$ lying entirely in the band, while the upper band stays in the so-called BEC regime.

3.2.2   Two-Band disordered superconductor

Let us present the equations for the two-band disordered model in the mixed BCS-BEC regime of Fig. 3.3. Here, we assumed a constant density of states (DOS) for both bands, N_1 and N_2. We indicate the matrix of the bare coupling constant with

$$\lambda = \begin{pmatrix} \lambda_{11} & \lambda_{12} \\ \lambda_{21} & \lambda_{22} \end{pmatrix},$$

the indices labeling the two bands of the clean system. Note that λ_{ij} is the dimensionless pairing interaction which has to satisfy the relation $g_{12} = \lambda_{12}/N_1 = \lambda_{21}/N_2 = g_{21}$, so $\lambda_{12}, \lambda_{21} > 0$ implies an attractive interaction between the two bands, viceversa $\lambda_{12}, \lambda_{21} < 0$ implies repulsive.

As in Fig. 3.3, we call w_j the lower band edge of the j-band ($j = 1, 2$), and Λ_j the higher band edge; the corresponding reduced energy ξ $w_1 = -\mu$, $w_2 = \varepsilon_0 - \mu$ and $\Lambda_i = L_i - \mu$.

The critical temperature T_c can be calculated from the solution of the linearized

gap equations for the two band model (see Appendix A):

$$\Delta_i = \pi k_B T \sum_{\substack{k,i\omega_n \\ j}} \frac{\widetilde{\lambda}_{ij}}{N_i} \frac{\Delta_j}{(i\widetilde{\omega}_n)^2 + \widetilde{\xi}_{j,k}^2} \tag{3.2}$$

which corresponds to the divergence of the Cooper susceptibility and $\widetilde{\lambda}, \widetilde{\omega}_n$ and $\widetilde{\xi} = \xi + h_n$ are respectively the coupling constant, Matsubara frequency and energy dispersion, corrected by disorder. The effect of disorder will be introduced within the averaged $\hat{T}$-matrix approximation [49,61]. Referring to Appendix B for more details, the self-energy coming from the presence of microscopic impurities homogeneously distributed in the system gives the so-called line corrections to the Matsubara frequencies and the chemical potential.

Thus, the corrected linearized gap equations will be thus be

$$\begin{pmatrix} \Delta_1 \\ \Delta_2 \end{pmatrix} = \begin{pmatrix} \lambda_{11} & \lambda_{12} \\ \lambda_{21} & \lambda_{22} \end{pmatrix} \begin{pmatrix} A_{11} & A_{12} \\ A_{21} & A_{22} \end{pmatrix} \begin{pmatrix} \Delta_1 \\ \Delta_2 \end{pmatrix}, \tag{3.3}$$

where the elements of the matrix A are given by

$$A_{ij} = k_B T \sum_n \frac{M_{ij}}{\det(M)} \int_{\max[-\Omega,w_i]}^{\max[\Omega,w_i]} \frac{d\xi}{\widetilde{\omega}_n^2 + (\xi + h_n)^2}, \tag{3.4}$$

$\widetilde{\omega}_n$ and h_n being, respectively, the Matsubara frequency shifted by disorder effects and the frequency-dependent correction to the chemical potential μ, calculated self-consistently:

$$\begin{cases} \widetilde{\omega}_n = \omega_n + \frac{\Gamma\widetilde{\omega}_n}{2} \sum_{j=1,2} \tilde{f}_{n,j} \\ \\ h_n = -\frac{\Gamma}{2} \sum_{j=1,2} \tilde{g}_{n,j}, \end{cases} \tag{3.5}$$

where $\omega_n = (2n + 1)\pi k_B T$, n ranging over integer numbers, is the Matsubara frequency of the clean system, $\Gamma = \hbar\tau^{-1}/2$ is the disorder-induced broadening and sets the scale for the inverse lifetime of the charge carriers,

$$\tilde{f}_{n,j} = \frac{1}{\pi} \int_{w_j}^{\Lambda_j} \frac{d\xi}{\widetilde{\omega}_n^2 + (\xi + h_n)^2}, \tag{3.6}$$

$$\tilde{g}_{n,j} = \frac{1}{\pi} \int_{w_j}^{\Lambda_j} \frac{(\xi + h_n)d\xi}{\widetilde{\omega}_n^2 + (\xi + h_n)^2}, \tag{3.7}$$

and the matrix

$$M = \begin{pmatrix} 1 - \frac{\Gamma}{2}\tilde{f}_{n,2} & \frac{\Gamma}{2}\tilde{f}_{n,2} \\ \\ \frac{\Gamma}{2}\tilde{f}_{n,1} & 1 - \frac{\Gamma}{2}\tilde{f}_{n,1} \end{pmatrix} \tag{3.8}$$

introduces vertex corrections to the Cooper susceptibility due to disorder [109,110].

We can observe that a huge but necessary simplification we made so far is to consider a constant disorder parameter Γ for both bands and at all chemical potentials. The Hall measurements of the LM and HM carriers in Fig. 3.1c show instead that not only the mobilities are quite different in the two bands, but also that

the scattering rate should strongly depend on doping, especially for what concerns the upper band. Nevertheless, we are focused mainly in the interplay between disorder and multi-band physics: the same way we choose to keep two bands instead of two degenerate bands interacting with a third one, we will keep Γ constant, leaving the system as simple as possible.

3.3   Toy model: single-band system

We first unravel the physics of the single-band system, observing both finite-bandwidth effects and the role of disorder-induced line and vertex corrections. Let us rewrite the linearized gap equation we want to solve as

$$\Delta = \pi k_B T_c \sum_{\omega_n} \Delta \frac{\lambda \varphi_n}{1 - \frac{\Gamma}{2} \varphi_n}, \tag{3.9}$$

where

$$\varphi_n = \frac{1}{\pi} \int_{\min\,(\max\,(-\Omega, w), \Lambda)}^{\max\,(\max\,(\Omega, \Lambda), w)} \frac{d\xi}{\widetilde{\omega}_n^2 + (\xi + h_n)^2},$$

the band ranges from $w = \varepsilon - \mu$ to $\Lambda = L - \mu$, and Ω is the Debye energy. The corrected Matsubara frequency $\widetilde{\omega}_n$ and the correction to the chemical potential h_n, are calculated from the coupled self-consistent equations:

$$\begin{cases} \widetilde{\omega}_n = \omega_n + \frac{\Gamma \widetilde{\omega}_n}{2} \tilde{f}_n \\ h_n = -\frac{\Gamma}{2} \tilde{g}_n \end{cases} \tag{3.10}$$

In Fig. 3.4 the critical temperature T_c is plotted as a function of the chemical potential μ for a finite band ranging between 0 and 500 meV, with a constant DOS. We used here $\Omega = 30$ meV and $\lambda = 0.133$, so $T_c \approx 0.21$ K in the clean case (blue circles in Fig. 3.4). In agreement with Anderson's theorem, a small amount of disorder, $\Gamma = 0.01$ meV, does not change the value of the superconducting critical temperature T_c. On the other hand, when Γ is at least 50 times greater, $\Gamma > 0.5$ meV, a substantial suppression of T_c is found. We would also like to highlight the more pronounced kink in the suppression of superconductivity, observed when both disorder and finite-bandwidth effects are present, at $\mu = w + \Omega$ and $\mu = \Lambda - \Omega$.

Clearly, the only element of pair breaking here is the disorder and finite bandwidth effects are important at the edges of the band in an energy range that is set by the Debye energy Ω. As soon as the chemical potential enters the band and as long as its energy distance from the bottom of the band is smaller than the characteristic Debye energy $\mu < \Omega$, the critical temperature T_c rapidly increases $T_c \sim \sqrt{\mu}$, coherently to previous results [21, 53, 54]. When $\mu \gtrsim \Omega$ enters well inside the band, T_c slowly decreases as a consequence of finite-bandwidth effects. Further increasing μ leads to a nearly constant T_c when μ is around the center of the band, whereas T_c symmetrically increases slowly in the upper half of the band (because of particle-hole symmetry in a single band with constant DOS). These are rather weak effects that might obviously be overcome by other DOS details in real band structures (like, for example, van Hove singularities or Rashba spin-orbit couplings [20, 111, 112]), but they are often overlooked in theoretical analyses and it might be informative
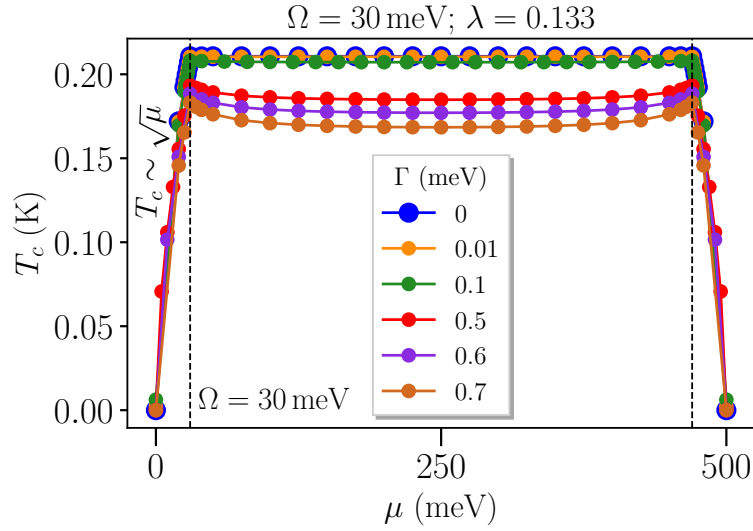
Figure 3.4. Critical temperature T_c as a function of the chemical potential μ for a finite band, extending from $w = 0$ to $\Lambda = 500\,\text{meV}$ for different values of the disorder-induced broadening Γ; the Debye frequency is $\Omega = 30\,\text{meV}$ and the coupling constant is $\lambda = 0.133$.

on some specific features (bandwidth, band edge positions, and so on) of the band structure specifically involved in experiments. When adding the second band, this consideration will be important in order to explain the first slow decrease (or possibly slow increase) in the T_c curve at low doping.
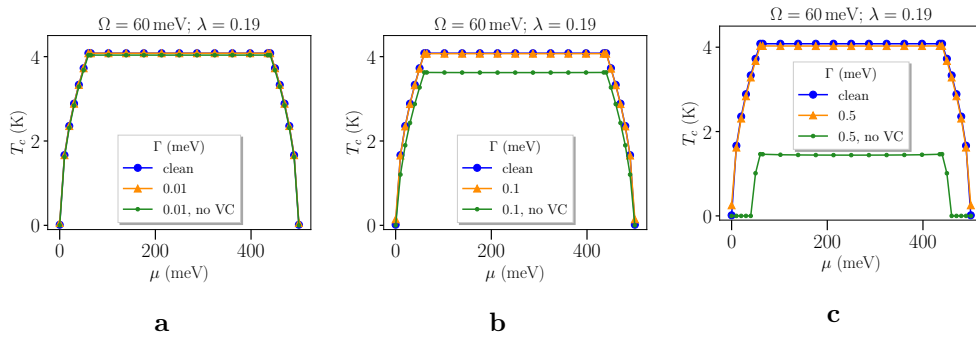
Figure 3.5. Critical temperatures for the single finite band ($w = 0$, $\Lambda = 500\,\text{meV}$, $\Omega = 60\,\text{meV}$, $\lambda = 0.19$) calculated with different disorder-induced broadening (**a**) $\Gamma = 0.01\,\text{meV}$, (**b**) $\Gamma = 0.1\,\text{meV}$ and (**c**) $\Gamma = 0.5\,\text{meV}$. The blue dots correspond to the clean system ($\Gamma = 0$), the dirty cases are plotted in orange while in green one can see the calculation where the vertex correction is suppressed by hand.

We investigated the role of both line and vertex corrections. To emphasize the effects, we considered larger values of the Debye energy Ω and of the coupling constant λ, in particular, taking $\Omega = 60\,\text{meV}$, to enhance finite bandwidth effects at the edges and $\lambda = 0.19$ to increase the bare value of the critical temperature, necessary to appreciate the effects of the corrections. The choice of a higher clean critical temperature is clarified when looking at our results in Fig. 3.5, showing the curves

$T_c(\mu)$ for three growing amounts of disorder $\Gamma = 0.01$, 0.1 0.5, calculated with and without the vertex correction (VC), i.e., the factor $(1 - \Gamma/2\varphi_n)^{-1}$ in Eq. **??**. Looking at Fig. 3.5c, specifically at the green curve corresponding to $\Gamma = 0.5$ meV it is clear that the VC is so important that it can drastically suppress the critical temperature. This is a trend that we observe also in Fig. 3.5b and also slightly in Fig. 3.5a, although the effect here is really small: the line correction, i.e., the correction to the Matsubara frequency in Eq. (3.5), lowers substantially the critical temperature while the vertex correction, i.e., the matrix M in Eq. (3.8), largely compensates the line correction almost completely restoring the *clean* value of the critical temperature $T_c(\Gamma = 0)$. This is a clear manifestation of Anderson's theorem, which, as it is well known, can be rephrased by stating that superconductivity is robust against disorder whenever self-energy (line) corrections coexist and get (largely) canceled by vertex corrections. On the contrary, whenever the wave symmetry or the magnetic character of impurities lead to vanishing or small vertex corrections, the premises for Anderson's theorem to apply no longer hold.

Finally, let us stress once again the importance of the numbers involved. It is in fact of great interest for both theoreticians, whose final goal is to describe real systems, and experimentalists to understand quantitatively how all the parameters and quantities involved interplay and contribute individually to the suppression of T_c. In the case at issue here, we observe that the suppression of the critical temperature due to the presence of disorder is of the same order of magnitude, i.e., few tens of mK, independently of the value of T_c in the clean case. Although this is not surprising, since T_c depends only on the Debye energy Ω and the coupling constant λ, both unrelated to the disorder-induced broadening Γ, the relative suppression on T_c can be significant. Calling $\delta T_c = T_c(\Gamma = 0) - T_c(\Gamma)$ the difference between the critical temperature of the clean system and the one of the disordered system, and comparing our results for $\Gamma = 0.5$ meV in Fig. 3.4 (red dots), where $T_c(\Gamma = 0) = 0.21$ K, and in Fig. 3.5c (orange dots), where $T_c)(\Gamma = 0) = 4.03$ K, we find, respectively, $\delta T_c/T_c(\Gamma = 0) \approx 0.1$ and $\delta T_c/T_c(\Gamma = 0) = 0.01$. This shows that the same disorder becomes relatively more important in systems with lower critical temperature.

3.4 Disordered unpaired bands

Let us introduce here the second band, keeping it unpaired to the other one, i.e., $\lambda_{12} = \lambda_{21} = 0$ so that the system is an intermediate case between the one-band model studied above and the full two-band disordered model. Thus, Eq. 3.3 reduces to

$$\begin{cases} \Delta_1 = \lambda_{11}(A_{11}\Delta_1 + A_{12}\Delta_2) \\ \Delta_2 = \lambda_{22}(A_{21}\Delta_1 + A_{22}\Delta_2) \end{cases} \tag{3.11}$$

Hence, even if formally the inter-band couplings are set to zero, the disorder still couples the two bands because electrons can be scattered from one band to the other. Note that in a heavily disordered system the concept of multiple bands loses its meaning, as disorder mixes the band eigenstates, even though the pairs are still formed within each band separately. The parameters used are $\lambda_{11} = \lambda_{22} = 0.135$ and $\Omega = 34.5$ meV, and the lower edge of the second band is $\varepsilon_0 = 90$ meV. As one can
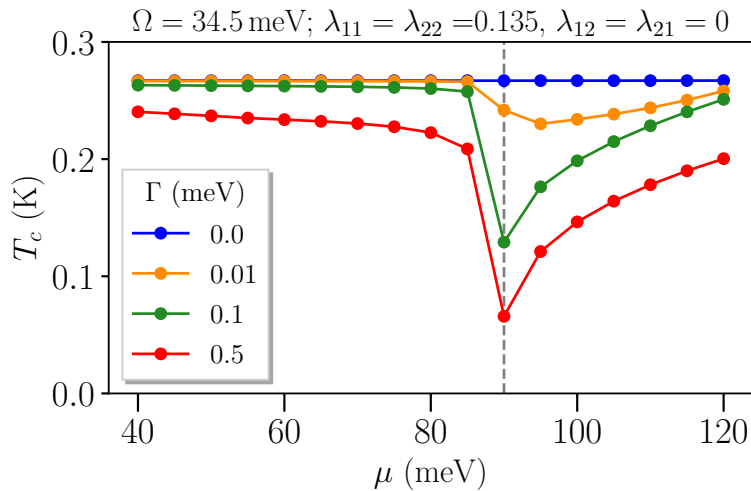
Figure 3.6. Two bands system with no interband coupling $\lambda_{12} = \lambda_{21} = 0$ and different amounts of disorder Γ. Here the parameters used are comparable with the real ones of LAO/STO heterostructures ($\Omega = 34.5\,\text{meV}$ and $\lambda_{11} = \lambda_{22} = 0.135$. As one can see, already $\Gamma = 0.01\,\text{meV}$ is enough to couple the bands and lower the critical temperature. The dashed line indicates the bottom of the upper band $\varepsilon_0 = 90\,\text{meV}$.

see from Fig. 3.6, increasing the chemical potential, a gradual decrease of the critical temperature is observed, coherently with the decrease observed in the toy model of Sec. 3.3, then a substantial suppression of the critical temperature is observed near the Lifshitz transition. Further increasing μ, T_c starts to rise again, while the second band starts to be filled. Eventually, if the chemical potential enters well inside the second band, a situation similar to the one described in Sec. 3.3 should occur, albeit without particle-hole symmetry (for a generic relative position of the two bands), so that the maximum suppression of T_c with respect to the value in the clean two-band system – due to finite-bandwidth effects – is no longer expected to be located when the chemical potential reaches the middle of either bands.

3.5 Two coupled disordered bands

We finally discuss the complete model as presented in Sec. 3.2.2. We choose for the disorder-induced broadening the value $\Gamma = 0.6\,\text{meV}$, corresponding to $\hbar\tau^{-1} = 1.2\,\text{meV}$, and we tune the values of the coupling constants to obtain critical temperatures in the range of the values observed for LAO/STO. For now, we make a further simplification, besides taking Γ as independent of the carrier density, keeping the two DOS equal $N_1 = N_2$; otherwise, one should take the inter-band coupling constants obeying the relation $\lambda_{12} = \lambda_{21} N_2 / N_1$, as we will do in the next Section. Since in the case examined the DOS involved are of the same order (see Section 3.2.1, this simplification is not substantially affecting our results.

Setting $\Omega = 34.5\,\text{meV}$, the initial decrease of the critical temperature is due to finite bandwidth effects, as it was clear from the one band toy model presented in Section 3.3, while λ_{11} tunes the order of magnitude of T_c. The depth and shape of

the well at $\mu \approx \varepsilon_0$ are strongly dependent both on the amount of disorder involved and on the values of the inter- and intraband coupling constants. Similarly to λ_{11}, λ_{22} rules the order of magnitude of T_c when the chemical potential is well inside the upper band ($\mu \gg \varepsilon_0$), so necessarily it will affect both the minimum of the decrease of T_c, at $\mu = \varepsilon_0$, and its rise, for $\mu \gtrsim \varepsilon_0$, as one can see from Fig. 3.7a. A subtler aspect is, however, the role of the inter-band coupling constants. As stated in Ref. [61], sub-leading negative inter-band coupling constants, together with a small disorder, can induce the observed pair-breaking effect, while an attractive inter-band interaction only produce a much smaller suppression of T_c when the chemical potential approaches the edge of the second band.

Nonetheless, in a strongly disordered system this statement is not so clear-cut. In Fig. 3.7b we plot the curves T_c vs μ for different values of the inter-band coupling constant. As one can see, while $\lambda_{12} = \lambda_{21} = -\lambda_{11} \cdot 10^{-1}$ is indeed enough for the critical temperature to be zero in a wide range of values of the chemical potential (90 meV$< \mu <$110 meV, red dots), a sub-leading positive coupling constant $\lambda_{12} = \lambda_{21} = +\lambda_{11} \cdot 10^{-2}$ (orange dots) still generates a suppression of T_c at $\mu = \varepsilon_0$ and the three curves with $-\lambda_{11} \cdot 10^{-2} < \lambda_{12} < +\lambda_{11} \cdot 10^{-2}$ (orange, green and red dots) present almost the same behavior in their increase inside the second band ($\mu > \varepsilon_0$), stating the fact that the main pair-breaking effect at play is the presence of a strong disorder.
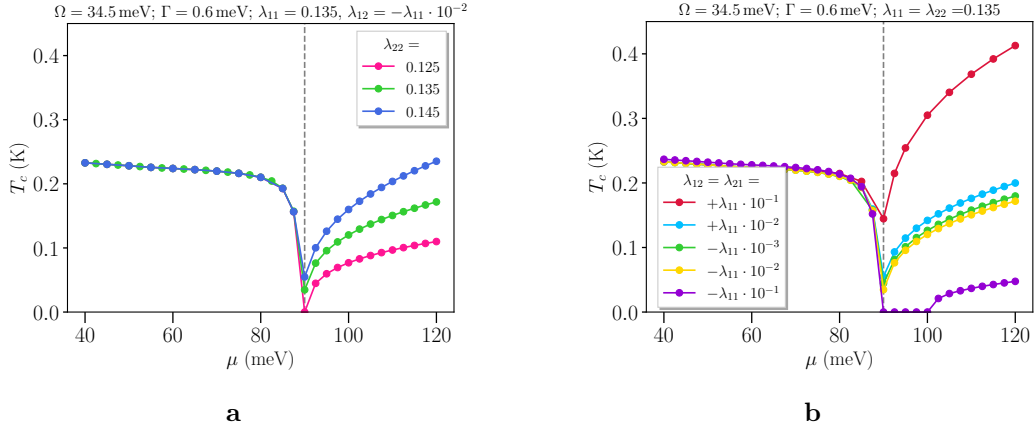
Figure 3.7. Calculations for the complete two-band disordered model presented in Sec.3.2.2. Here, we considered $\Gamma = 0.6$ meV, $\Omega = 34.5$ meV and $\lambda_{11} = 0.135$. The gray dashed line indicates the chemical potential corresponding to the Lifshitz transition, that is, $\varepsilon_0 = 90$ meV. (a) The inter-band coupling constant are fixed as $\lambda_{12} = \lambda_{21} = -\lambda_{11} \cdot 10^{-2}$, while varying λ_{22}. (b) Here, $\lambda_{22} = \lambda_{11}$. while the values of $\lambda_{12} = \lambda_{21}$ are varied.

3.6 T_c suppression in the (110)-LaAlO$_3$/SrTiO$_3$

Let us now finally apply the model to the real sample.
Going back to the experimental measurements, we need to have a clear mapping of the chemical potential μ into the gate voltage V_G. It is worth noting that the doping potential V_G cannot be defined univocally, contrary to chemical doping which is a

Figure 3.8. Corrected DOS at different disorder amounts $\Gamma = 0.1$, 0.6 (green and red) with respect to the clean case $G = 0$. The yellow shaded area corresponds to the experimentally accessed energy range.

far more governable procedure. In Section 3.2.1, we did a first attempt to roughly define the range of chemical doping involved, so as to have realistic numbers of the parameters to work with. To define a more precise m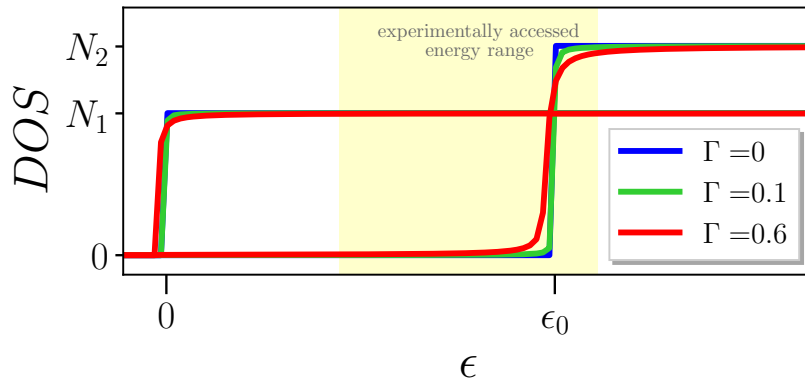apping, on a phenomenological basis, we need first to translate the chemical potential μ in terms of the number of particles $n_{tot}(\mu, T)$ and then infer from their experimental values in Fig. 3.1b the relation $V_G(n_{tot})$. Besides, one needs to know how much the correction due to disorder affects the density of states. Note that this was not necessary before, since the self-energy corrections introduced in the gap equations implicitly correct the bare coupling constants, hence the DOS. We computed the corrected DOS $\widetilde{N_1}$ and $\widetilde{N_2}$ self-consistently according to the following equation:

$$\widetilde{N_i} = \text{Im} \int_{w_i}^{\Lambda_i} \frac{N_i(\xi)}{\epsilon - \xi - \Sigma_i} d\xi = N_i \text{Im}(\Sigma_i) \tag{3.12}$$

where the self-energy relative to the i-th band can be calculated iteratively as

$$\begin{cases} \Sigma_i(\epsilon) = \sum_n \frac{\Gamma}{\pi} \ln \frac{\epsilon - w_i - \Sigma_i}{\epsilon - \Lambda_i - \Sigma_i} \\ \Sigma_i^{n=0} = \frac{i\Gamma}{\pi} \end{cases} . \tag{3.13}$$

In Fig. 3.8 we show $\widetilde{N_1}$, $\widetilde{N_2}$ for two examples of disorder $\Gamma = 0.1$, 0.6 (green and red dots) with respect to the clean case (blue). Since the smearing introduced by the disorder affects almost only the edges of a flat DOS, the lower band appears to be independent from Γ while the upper band gets broadened exactly in the range of energies in which the pairing between the two is relevant. We can stress once again the fact that the very concept of band in a strongly disordered system somehow loses its meaning. The broadening of the upper band is also underlying the fact that we are not dealing with a proper BEC regime: on the one hand, in fact, the BCS lower band is somehow sustaining the formation of Cooper pairs in the upper band and, moreover, the smearing introduced by microscopic disorder drags some electrons of the second band towards states with $\varepsilon < \varepsilon_0$.

Integrating the DOS one obtains the number of particles, then the corresponding gate voltage V_G can be found from the data. The integration should in principle

consider the Fermi statistics $f(\xi) = (1 + e^{\xi/k_B T})^{-1}$, i.e., $n(\mu, T) = \sum_j \int \widetilde{N}_j(\xi) f(\xi) d\xi$ however in the range of temperatures considered here it is not necessary and we can consider the limit of zero temperature. On the other hand, at low values of the disorder Γ, the clean formula for the number of particles can be enough, thus when $\Gamma \lesssim 0.2$ one can use the following expression

$$n(\mu) = k_B T \left[N_1 \ln\left(1 + e^{\mu/k_B T}\right) + N_2 \ln\left(1 + e^{(\mu - \varepsilon_0)/k_B T}\right) \right] \tag{3.14}$$

valid for a clean system and flat DOS.

The data of the superconducting critical temperature can be finally fitted by means of the two disordered bands model described so far. The parameters used to fit the data are $\lambda_{11} = 0.135$, $\lambda_{22} = 0.14$, $\lambda_{12} = -\lambda_{11}/10$, $\lambda_{21} = N_1/N_2 \lambda_{12}$ for the coupling constants and $\Gamma = 0.2$ meV for the disorder, the values of the bare coupling constants being experimentally determined from fits of the critical field measurements of the same sample [13] and are consistent with what was found in literature [53, 61] while the disorder correspond to the lower bound $\hbar \tau^{-1}$ found from mobility measurements (Fig. 3.1c). The V-shape well encountered in all theoretical calculations at the Lifshitz transition may seem a discrepancy with respect to experiments, however one should take into account the presence of mesoscopic inhomogeneity in SrTiO$_3$-based heterostructures. As it was pointed out in Section 2.1.1, the inhomogeneous nature of LaAlO$_3$/SrTiO$_3$ has been largely studied and the typical size of a superconducting puddle in the 2DEG has been estimated to be of the order of ~ 100 nm [75]. Translating the inhomogeneities into fluctuations of chemical potential, we can consider the average value

$$\overline{T}_c(\mu) = \int_{-\infty}^{+\infty} d\mu' T_c(\mu') G\left(\frac{\mu - \mu'}{\sigma}\right) \tag{3.15}$$

where G is a Gaussian distribution of average μ and deviation standard σ. From Fig. 3.9 one can appreciate the agreement between the experimental data (green dots) and the theoretical calculations of T_c averaged with $\sigma = 7$ meV and repulsive couplings (full yellow diamonds), while the non-averaged case $\sigma = 0$ presents the minimum in $\varepsilon_0 = 90$ meV corresponding to approximately $V_G \approx 60$ V (black dashed line). It is worth noting that the very same calculation, with the same parameters and $\sigma = 7$ meV, using an attractive interband pairing $\lambda_{12} > 0$ constant cannot reproduce the suppression of T_c observed in experimental data (black diamonds).

3.7   Concluding remarks

The deep investigation on the two-band disordered model we carried over this Chapter in the unconventional BCS-BEC regime needs perhaps a summary of our main results.

The one-band toy model was a clarifying starting point, since it highlighted the fact that *microscopically* the disorder involved is far from the weak limit. We remark on this aspect to stress the fact that our system relies outside of the premises of Anderson's theorem. On the other side, while finite bandwidth effects were not qualitatively surprising, from the point of view of the shape of the critical temperature as a function of the chemical potential, quantitatively the suppression
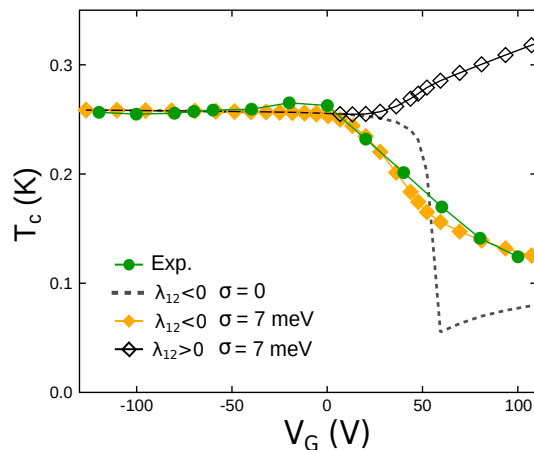
Figure 3.9. Experimental (green circles) and calculated superconducting T_c as a function of the gate voltage V_G both in the case of attractive (black diamonds) and repulsive (orange diamonds) interband coupling, with the variance of the chemical potential disorder $\sigma = 7$ meV and $\Gamma = 0.2$ meV. Dashed line shows the computed curve in absence of meso-scale disorder in the $s_\pm$ scenario.

of T_c at $\Omega < \mu < \Lambda - \Omega$ and the kinky behavior at $\mu = \Omega$, $\Lambda - \Omega$ were much enhanced when a low value of the clean critical temperature were considered. In other words, from the one band model it was already clear that in SrTiO$_3$-based heterostructures, in which the critical temperature is always in the range of hundreds of mK, the effects of impurities at a microscopic level can severely affect the superconductivity.

While adding a second band, the role of intraband and interband coupling constant in tuning T_c is consistent with the expectations. The striking and unexpected result of our study is the pair-breaking effect observed in absence of interband coupling $\lambda_{12} = \lambda_{21} = 0$, hence when the only source of scattering is the presence of impurities.

From the experimental point of view a repulsive coupling between the bands – along with fluctuations of the chemical potential due to *mesoscopic* inhomogeneities – was necessary to reproduce the suppression of T_c at $V > V_G^{opt}$, this was done at constant disorder. Moreover, the chosen value corresponds to the lowest value observed in the upper band. Anyhow, the bare coupling constants were considered constant at all doping, hence one can think that a higher amount of disorder around the Lifshitz transition, which goes towards a more pronounced suppression of T_c, could be balanced by a lowering of the interband couplings. Such a model would however contain too many parameters to be reliable.

What was instead of great theoretical interest and needs for more investigation, is the pairbreaking effect at the Lifshitz transition strictly connected to the presence of *microscopic* disorder. Anderson's theorem can be in fact rephrased in terms of the derivative of T_c with respect to Γ, stating that in an s-wave superconductor in presence of non-magnetic impurities $dT_c/d\Gamma \to 0$ when $\Gamma \to 0$. Instead, we can observe from Fig. 3.10, where we plot $T_c(\Gamma)$ at different chemical potentials, that the theorem, valid when just one band is involved (panel a), does not always hold in the two-band case. In the overdoped regime (panel c) $\mu = 100$ meV, the repulsive interband coupling is necessary to observe a "violation" of the theorem, as it was

$$\lambda_{11} = \lambda_{22} = 0.135; \qquad \lambda_{12} = \lambda_{21} = \pm\lambda_{11}/10$$
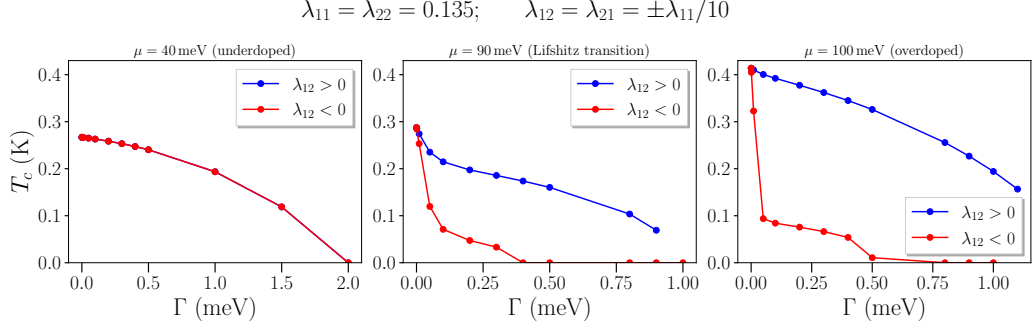
Figure 3.10. Suppression of the critical temperature as a function of the disorder $\Gamma = \hbar\tau^{-1}$
(a) at $\mu = 40\,\mathrm{meV}$, i.e., where the system is underdoped and only one band is involved,
(b) at the Lisfshitz point $\mu = \varepsilon_0 = 90\,\mathrm{meV}$ and (c) at $\mu = 100\,\mathrm{meV}$, where the system is
overdoped but the upper band is still in the BEC limit. The blue curves correspond to
an attractive interband coupling while the red to a repulsive coupling between the two
bands. Here the parameters used are $\lambda_{11} = \lambda_{22} = 0.135$ and $\lambda_{12} = \lambda_{21} = \pm\lambda_{11}/10$.

highlighted in the work of Trevisan et al. [61], while interestingly at the Lifshitz
transition $\mu = 90\,\mathrm{meV}$ both curves for $\lambda_{12} \lessgtr 0$ clearly displays a pairbreaking effect,
enhanced in the repulsive case but present also in the attractive one, demonstrating
that disorder plays a crucial role in the suppression of the critical temperature.

Chapter 4

The Random Impedance Network model

In the previous Chapter the suppression of the critical temperature in a $LaAlO_3/$ $SrTiO_3$ interface was found to be caused mainly by the interplay between the microscopic disorder and the multiband character of the system whereas mesoscopic disorder has the effect of broadening the signature of a Lifshitz transition. As stated in Section 2.1, the observation of a BKT transition in a real two-dimensional superconductor can be prevented by the presence of strong inhomogeneities [17]. One of the main hallmarks of mesoscopic disorder is in fact a large broadening of the transition in the resistivity measurements $R(T)$ which cannot be ascribed to large fluctuations of the superconducting condensate. Instead, in previous works [17–19, 21–23, 74, 113], the physical mechanism leading the transition was proposed to be the one of a *percolative transition* in all those two-dimensional superconductors displaying inhomogeneities on a mesoscopic scale. Within this approach, not only the broadening of $R(T)$ observed in $SrTiO_3$-based interfaces find its interpretation, but also the smearing of the coherence peaks in tunneling spectra, the non-linearity in the $I - V$ characteristics or the residual resistivity at zero temperature of the (001) interface.

In this Chapter, we start observing some new data on a (001)-$LaAlO_3/SrTiO_3$ device where the superfluid stiffness and the optical conductivity are measured by means of resonant microwave transport experiments. In Section 4.1 we start by describing in detail the state of art of the Random Resistor Network (RRN) used to model the percolative transition, explaining both the effective medium theory (EMT) and the exact solution. The new resonant microwave transport data are

then presented in Section 4.2. Finally, Section 4.3 is dedicated to implement the necessary updates needed to globally describe the new experiments, i.e., the Random Resistor Network will consider also finite frequencies becoming a Random Impedance Network (RIN) model. Again, we will discuss both the EMT solution, considering also the possibility of finite frequency dissipative effects, and the exact solution, where the geometry of the superconducting bonds will play a crucial role.

4.1   The RRN Model

Let us first introduce the details of the Random Resistor Network (RRN) model. The simplest RRN model one can imagine is nothing but a 2D square lattice of resistances (see Fig. 4.1a), each one with its own local critical temperature T_c^i, randomly distributed according to a given probability distribution. It is worth noting that each resistor consist in a *puddle* of mesoscopic size, small with respect to the sample size but large enough to have a well defined coherence and a random but well defined local critical temperature. By lowering the external temperature T, the resistors are switched-off to their superconducting state $R^i = 0$ as soon as the condition $T \leq T_c^i$ is verified:

$$R^i = \begin{cases} R_N, & \text{if } T > T_c^i, \\ 0, & \text{if } T \leq T_c^i, \end{cases} \tag{4.1}$$

where R_N is the experimental resistance *per square* of the 2D material in the high-temperature regime. We can consider two class of resistors, i.e., metallic (m) and superconducting (s) resistors: the metallic ones will have a local critical temperature $T_c^i \leq 0$ so that they will maintain their finite resistance $R^i = R_N$ down to $T = 0\,\text{K}$ while the superconducting (s) will have a finite T_c^i, randomly distributed across the sample. It was previously shown that different distributions give rise to qualitatively similar physical properties [19]. For the sake of simplicity, the probability density distributions of the local critical temperatures T_c^i for the superconducting fraction will then be taken as Gaussian:

$$P(T_c^i) = \frac{w_s}{\sqrt{2\pi}\sigma} \exp\left(-\frac{(T_c^i - \mu_{c,s})^2}{2\,\sigma_s^2}\right) \tag{4.2}$$

where $\mu_{c,s}$ and σ_s^2 are respectively the average and the variance. The total weight of the distribution w_s corresponds to the maximum fraction that can become superconducting. A fraction $w_m = 1 - w_s$ of the system will always stay metallic, down to $T = 0\,\text{K}$.

The exact solution of the RRN model for a $L \times L$ square lattice is then the solution of Kirchoff's and Ohm's Law in each bond and node. Calling here R_x^{ij} and R_y^{ij} the resistors at the $(i,j)-$th site, the system of equations reads as:

$$\begin{cases} R_x^{ij} I_x^{ij} = V^{ij} - V^{i,j+1} \\ R_y^{ij} I_y^{ij} = V^{ij} - V^{i+1,j} \\ \sum_{<i,j,\nu>} I_\nu^{ij} = 0 \end{cases} \tag{4.3}$$
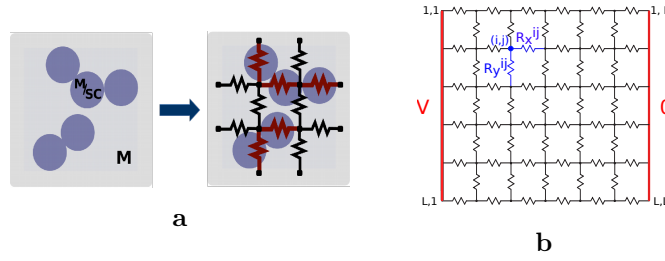
Figure 4.1. Schematic draw of the network of resistors.

where $< i, j, \nu >$ stands for the sum over every bonds connected to site (i, j), in both directions $\nu = x, y$. The total number of equations needed to solve the system is $3L^2 - 2L$, where $2L^2 - 2L$ are the Ohm's law for all the bonds and L^2 are the Kirchoff's equations for all the nodes.

We consider a finite square lattice, with no boundary conditions, and an applied external voltage V, as in Fig. 4.1b. The former equation can be rewritten as a system of linear equations

$$\hat{A} \cdot \vec{x} = \hat{b} \tag{4.4}$$

where $\hat{b}$ contains the known terms, i.e., the external voltage, which can be either V or zero, $\hat{A}$ is a sparse matrix, whose elements of a single row can contain at most three non-zero terms, which can be either ± 1 or R_N; $\vec{x}$ is the vector containing all the unknown currents and potentials. Once the system is solved in $\vec{x}$, the total current flowing from one edge to the other is the sum of the L currents of one column:

$$I = \sum_{i=1}^{L} I_x^{ij} \tag{4.5}$$

Finally, the total resistivity of the lattice is of course the ratio between voltage and current

$$R = V/I. \tag{4.6}$$

4.1.1 Effective medium theory for the RRN model

If the inhomogeneities in the systems are homogeneously distributed and spatial correlations are not so relevant, an effective medium theory (EMT) approach can give us useful insights. The EMT can in fact capture the main features of transport properties, such as the large broadening of the transition and its tailish behavior [18], or even the strong non-linearities observed in $I - V$ characteristics [17]. Instead of solving exactly the system of equations (4.3) presented in the former section, the effective resistance *per square* R_{em} of the 2D system in EMT approximation is given by the solution of the following self consistent equation [33]

$$\sum_{j=m,s} \widetilde{w}_j(T) \frac{R_j - R_{em}}{R_j + R_{em}} = 0 \tag{4.7}$$

where $\widetilde{w}_s(T)$ is the fraction of superconducting bonds at temperature T:

$$\widetilde{w}_s(T) = \int_T^{+\infty} dT_c \, P_s(T_c). \tag{4.8}$$

The corresponding metallic fraction is by definition the sum of the metallic background w_m plus all the superconducting regions with a local critical temperature lower than T, i.e., $w_s - \widetilde{w}_s(T)$:

$$\widetilde{w}_m(T) = w_m + (w_s - \widetilde{w}_s(T)) = 1 - \widetilde{w}_s(T) \tag{4.9}$$

where we have used the condition $\sum_j w_j = 1$ (the sum running on all metallic and superconducting components). We find that the normalization condition consistently holds at all temperatures, so $\sum_j \widetilde{w}_j(T) = 1$.

Having assumed a Gaussian distributions for the corresponding critical temperatures, Eq. (4.8) reads as

$$\widetilde{w}_s(T) = \frac{w_j}{\sqrt{2\pi}\,\sigma_s} \int_T^{+\infty} \mathrm{d}T_c \, \exp\left[-\frac{(T_c - \mu_{c,s})^2}{2\,\sigma_s^2}\right] = \frac{w_s}{2}\left[1 - \mathrm{erf}\left(\frac{T - \mu_{c,s}}{\sqrt{2}\,\sigma_s}\right)\right] \tag{4.10}$$

where $\mathrm{erf}(x) = \frac{2}{\sqrt{\pi}}\int_0^x e^{-z^2}\,dz$ is the error function. It is now evident that $0 \leq \widetilde{w}_j(T) \leq w_j$ and that $\widetilde{w}_s(T) \approx 0$ for $T - \mu_{c,s} \gg \sigma_s$, while $\widetilde{w}_s(T) \approx w_s$ for $\mu_{c,s} - T \gg \sigma_s$.

Since $R_m = R_N$ and $R_s = 0$, the solution of Equation (4.7) can be found analytically [18, 21] and takes the form:

$$\frac{R_{em}(T)}{R_N} = \theta\left[w_s\,\mathrm{erf}\left(\frac{T - \mu_{c,s}}{\sqrt{2}\,\sigma_s}\right) + 1 - w_s\right], \tag{4.11}$$

where $\theta\,(\cdot)$ is the Heaviside step function.

Despite the fact that the EMT neglects all spatial structures, still it can give important insights about the system. The Gaussian distribution in Eq. (4.2) is the key element setting the characteristics of $R(T)$. The broadening of the transition and the downturn of R_{em} are in this way mostly controlled by the average value $\mu_{c,s}$ and variance σ_s, while setting the fraction of superconducting bonds $w_s < 1$ can reproduce the tailish behavior at low temperature. Most importantly, the parameter w_s rules the percolation of the superconducting cluster. Being $w^p \equiv 0.5$ the percolation threshold for a homogeneous distribution of superconducting puddles in a 2D square lattice [33], for each $w_s < w^p$ the effective resistance will saturate to a finite value in the limit $T \to 0\,\mathrm{K}$ (orange curve and yellow shaded area in Fig. 4.2), explaining in this way the so-called "failed superconductor".

4.1.2 Spatially correlated disorder

Each time that spatial correlations cannot be neglected, the percolative nature of the model considered is inextricably related to the geometry of the system. Referring to previous literature [74], let us summarize here some results, explaining at the same time how the filamentarity was implemented in the calculations.

In Refs. [19] and [74], it is shown that the enhanced tailish behavior in the low temperatures of resistivity is most likely due to a filamentary character of the superconducting cluster, whereas the downward curvature at higher temperatures is caused by the presence of larger superconducting clusters with a higher local critical temperature called in [74] *superpuddles*.

In other words, the long distance connectivity is needed for the system to percolate, and in principle it could be a single superconducting filament crossing the
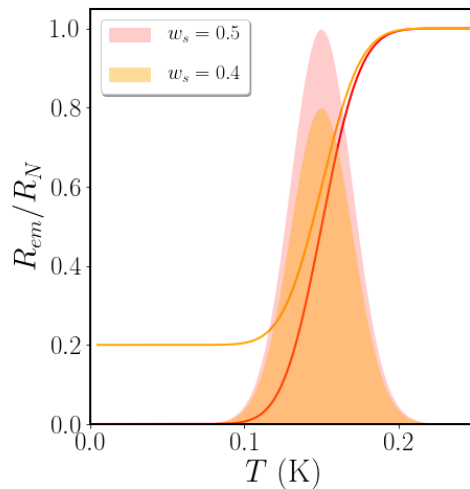
Figure 4.2. Temperature dependence of the effective resistance R_{em} for $\mu_{c,s1} = 0.15\,\mathrm{K}$, $\sigma_s = 0.02\,\mathrm{K}$ and two values of w_s. The red (orange) curve corresponds to the pink (yellow) shaded area. As one can see, as soon as $w_s < 0.5$, the zero-temperature resistance saturates to a finite value. Observe that the area underneath each Gaussian distribution equals the corresponding value of w_s (Figure published in [25]).

network from side to side, causing the long tails observed. Therefore, the skeleton of the superconducting resistors embedded in the metal can be implemented as a fractal like structure. From the operative point of view, the low dimensional cluster is constructed using a *diffusion limited aggregation* (DLA) algorithm. This choice is of course arbitrary and it does not rest on a straight physical reason nor its aim is to demonstrate that the superconducting regions has some defined fractal-like structure. It is simply a technical way to represent strongly inhomogeneous systems with space correlation on large scale.

The fractal is growth by diffusing n_{RW} particles in a square of size $L_\square$ larger than the size of the network ($L_\square > L$). Each particle is a random walker, moving one bond to the right and one bond up or down, with equal probability. This procedure is iterated until the particle stops, as soon as it reaches the top, bottom or right edge, where it sticks, or if it reaches a site already occupied by one of the previously diffused particles: in this case, it takes a step back and it stops. The cluster obtained is defined by all the bonds connecting two stuck particles (Fig. 4.3a). From this super-network, a sub-network of size $L \times L$ is selected and it will be the superconducting backbone of the RRN. Some bulky superpuddles are then superimposed to the DLA fractal generated, as they were needed to capture the depletion of $R(T)$ right at the first downturn of the normal state resistivity. The superpuddles are round clusters of bonds with radius r_{pd}, added randomly to the system until the total fraction of superconducting bonds w_s is reached. Each of the bonds belonging to the DLA fractal and the superpuddles are then assigned to a local critical temperature, according to the distribution in Eq. (4.2). In Fig. 4.3b is shown an example of the final sheet of resistors on which the Kirchoff's and Ohm's laws will be applied: the bonds belonging to the metallic background, highlighted
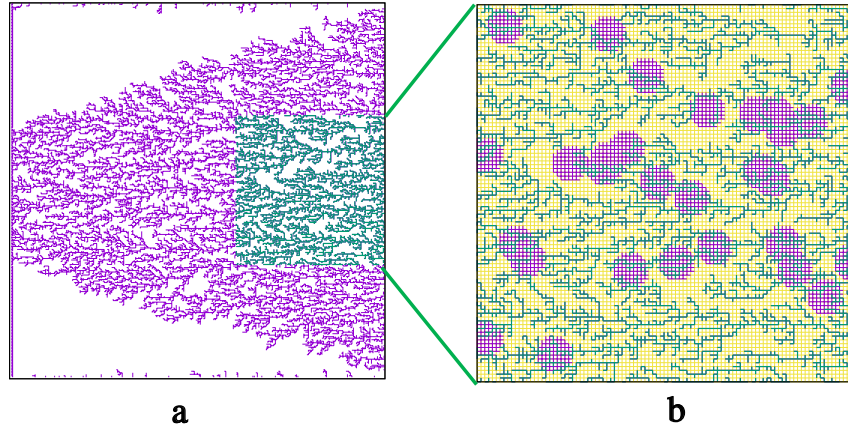
Figure 4.3. (a) Example of a filamentary structure produced by letting 50 000 particles
diffuse across a 250×250 square lattice, according to the DLA prescription. Notice
that the underlying 2D square-lattice grid is not reported for clarity (this is the overall
blank part of the figure) and only its DLA fractal subset is represented. From this
larger fractal, a restricted 100×100 square sublattice is extracted from the original
250×250 to serve as a filamentary skeleton for the superconducting component of our
RRN. (b) Example of a superconducting cluster of our RRN, obtained superimposing
bulkier circular superpuddles (in purple color), of diameter equal to 10 bonds, to the
(green) fractal skeleton generated by means of the DLA prescription. In this panel, the
underlying 2D square-lattice grid is reproduced in light yellow. (Figure and caption
from [74])

in yellow, will have a negative T_c^i, the resistors of the superpuddles will have a T_c^i
distributed according to a Gaussian with average and variance respectively ($\mu_{c,b}$,
σ_b), while the fractal resistors' distribution of critical temperature has ($\mu_{c,f}$, σ_f)
($\mu_{c,f} \leq \mu_{c,b}$).

4.2   New experimental evidences of filamentarity

While the RRN model can explain pretty well the features of the metallic states, it
prevents us to address the superconducting one: once the transition has occurred,
the DC transport measurement cannot highlight the properties of the inhomogeneous
superconducting cluster at lower temperatures.

Fortunately by this time experimentalists have found a way to measure the active
response at finite frequency by means of resonant microwave experiments where the
2DEG behaves like a resonant RLC circuit, giving us direct access to the optical
conductivity g' and the superfluid stiffness J_s [24,27]. To investigate those quantities
the RRN model will be extended to finite frequencies and upgraded to a Random
Impedance Network (RIN) model.

Let us recall that within a homogeneous Drude model the complex AC conduc-
tance g is written

$$g(T,\omega) = \frac{\sigma_0}{1 + \mathrm{i}\omega\tau} \equiv \frac{1}{R + \mathrm{i}\omega L},$$

where $\sigma_0 \equiv ne^2\tau/m$ is the DC conductivity, n is the carrier density, e is the
electron charge, m is the carrier effective mass, and τ the scattering time. Then,
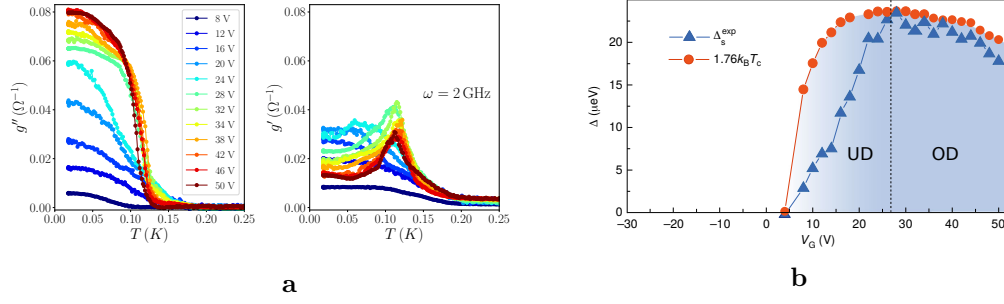
Figure 4.4. (a) Real and imaginary part of the conductivity $g = g' - ig''$ as a function of temperature at different gate voltages. (b) Gap energy $\Delta_s^{exp}(T \simeq 0)$ extracted from superfluid stiffness measurement ($J_s(0) = \frac{\pi\hbar}{4e^2R}\Delta(0)$) as a function of the gate voltage V_G (blue triangles) compared with the expected BCS gap energy $1.76k_BT_c$ (red circles) (Figure from [24]).

the resistance is $R = 1/\sigma_0$ and the inductance is $L \equiv \tau/\sigma_0 = (e^2J_s)^{-1}$, where the superfluid stiffness is $J_s \equiv n/m$. Being the impedance $Z = R + i\omega L$, we define the corresponding conductance $g = Z^{-1} = g' - ig''$. Henceforth, we will refer sometimes to the superfluid stiffness as the imaginary part of the conductivity g'', being the two of them proportional by a constant factor, whose only aim is to convert the unit of measure from an energy to a conductivity and viceversa.

Within resonant microwave transport experiments this reactive response of the system is directly accessible, thus giving us the possibility to study the properties of the superconducting cluster. As a matter of fact, also the superfluid densities n_s measured by means of a SQUID device presented in Section 2.1.1 were accounted by the EMT solution of the RRN [21] extended at small finite frequencies ω. In Fig.4.4a are reported the experimental measurements of the superfluid density and the optical conductivity, carried out on the 2DEG of a (001)-oriented LAO/STO interface for different values of the applied voltage. Experimental data at distinct voltages shows substantially two regimes with different qualitative features, namely overdoped (OD) ($V_g > 26$ V) and underdoped (UD) ($V_g < 26$ V).

This change of regime happening at $V_g = 26$ V was already observed at zero temperature [24], in the superconducting gap Δ at zero temperature as a function of different doping potentials (Fig. 4.4b). In fact, the gap $\Delta(0)$ was indirectly measured from the zero-temperature superfluid stiffness $J_s(0)$, since $J_s(0) = \frac{\pi\hbar}{4e^2R}\Delta(0)$ and it was interpreted as a transition from a Josephson Junction array (JJ-array) to a homogeneous BCS-like case. Today's measurements show that this transition at 26 V remains also at finite T, corresponding to a change in the qualitative behavior of $g'(T)$ and $J_s(T)$, as one can see already from Fig.4.4b. In the following, we will never invoke JJ-array physics, as we think that the intrinsic inhomogeneities are the ones ruling the physics of the system.

In Fig. 4.5 the optical conductivity, superfluid stiffness and DC resistivity are plotted together for different gate voltages, to better capture the features we are interested in. In all the cases, just below the zero-resistance critical temperature T_c, it appears a pronounced tail, characterized by a low value of the superfluid density. Note that T_c is intended to be the percolative temperature at which $R(T) = 0$.
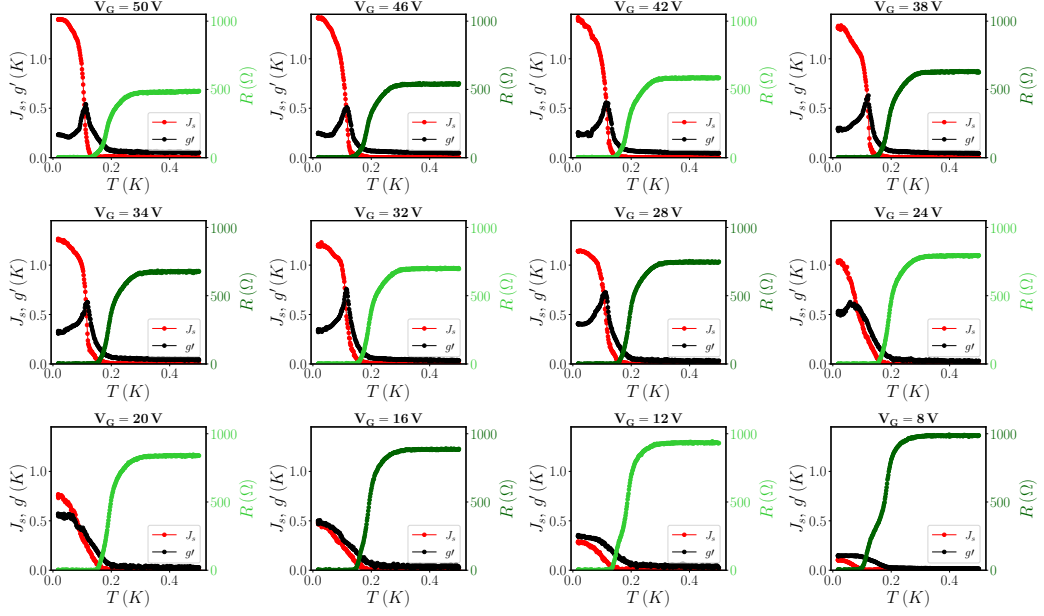
Figure 4.5. DC resistivity (green, right axis) measurements, superfluid stiffness J_s and optical conductivity g' (respectively in black and red on the left axis) measured via resonant microwave transport experiments at frequency $\omega \simeq 2\,\text{GHz}$. The different panels correspond to different gate voltages V_G.

Decreasing further the temperature, at some T_{cross}, the superfluid stiffness raises to a higher value, while the real part of the optical conductivity $g'(\omega)$ reaches its maximum; finally, at very low temperature $T < T_{cross}$, the system recovers what could seem BCS-like trend. These peculiar trends are smeared out by reducing the applied voltage V_G. The jump of the superfluid density tends to be much less pronounced; correspondingly, the peak of $g'(\omega)$ gradually decreases, until it completely disappear for voltage lower than $26V$. Those differences found between the two regimes and the ideal conventional case are summarized in Fig. 4.6. In particular, in the UD regime ($V_g < 26$ V) one can observe that

1 - the resistivity curve $R(T)$ and the superfluid stiffness $J_s(T)$ in temperature are very distant from each other, while normally the two curves overlap;

2 - at $T \lesssim T_c$, J_s starts to increase showing a "bump". At lower T, J_s increases almost linearly;

3 - the conductance g' shows a broaden peak and it saturates at values higher than $g'(T > T_c)$, such that $g'(0) \gtrsim J_s(0)/3$;

while in the OD regime ($V_g > 26$ V):

1 - $R(T)$ and $J_s(T)$ in temperature are far apart, as in the UD regime;

2 - J_s is very small for $T \lesssim T_c$ and, at some lower temperature T_{cross}, it abruptly increases, recovering a BCS-like behavior near $T \simeq 0\,\text{K}$;

3 - g' is very peaked and $g'(0) \ll J_s(0)$

The main possible interpretation followed in this Chapter is the idea of a crossover between a quasi-one-dimensional to a two-dimensional superconducting state that drives the superfluid density jump at $T_{cross} < T_c$. Coherently with the results found in the context of RRN, in which the long tails of $R(T)$ can be understood in terms of a long distance connectivity, we can imagine that the same filamentary superconducting structure is too fragile for the system to have a substantial stiffness. The presence of a superconducting percolating path can guarantee the appearance of a global zero-resistance state, remaining however still very fragile towards an applied current, showing a very low value of the superfluid density. This very thin percolating path formed, in spite of its initial fragility, may become more and more robust as a result of a proximity effect on the metallic substrate, keeping on lowering the temperature. Indeed, by considering the possibility for the metallic substrate to become superconducting via some proximization process, lowering the external temperature, the filamentary backbone will be gradually strengthen by new neighboring superconducting bonds, reaching finally a whole two-dimensional state This avalanche effect will then result in a significant increase of the superfluid stiffness below the critical temperature, at which the first fragile superconducting state forms.

Given the sharpness of the J_s jump, in the high-voltage regime, this process has to be very fast, and very likely due to an avalanche-proximization process occurring just below T_{cross}. Once the whole two-dimensional superconducting state is reached, $J_s(T)$ recovers the standard BCS-like trend, as expected.

The hypothesis of a crossover occurring between a quasi-one-dimensional to a two-dimensional superconducting state can account thus for all the three highlighted features: the presence of a low superfluid-density tail close to T_c, the jump of $J_s(T)$ at T_{cross} and finally the 2D BCS-like behavior at low temperature.

In the following Section we will introduce the extension to finite frequency of the RRN model, more appropriately called Random Impedance Network (RIN) model, explaining step by step how the proximization idea has been numerically implemented, both in the EMT approximation and in the exact solution.

4.3 The RIN Model

Let us present here the extension to finite frequencies of the RRN model presented in Section 4.1. To access the superconducting state, and in particular its optical conductivity and superfluid stiffness, all the resistors R^i will be replaced by complex impedances $Z^i = R^i + i\omega L^i$, hence the change of the name to RIN. Trivially, the condition for the local resistors in Eq. (4.1) translates into

$$Z_i = \begin{cases} R_N + \mathrm{i}\omega L_i, & \text{if } T > T_c^i, \\ \mathrm{i}\omega L_i, & \text{if } T \leq T_c^i, \end{cases} \tag{4.12}$$

where the local inductance L^i can be different depending on the considered component of the system.
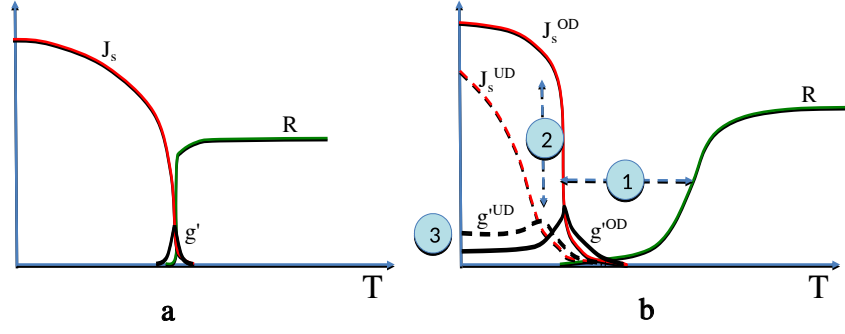
Figure 4.6. Graphical scheme summarizing the observed features (b) with respect to the ideal BCS case (a). The resistive transition (in green) appears broadened and tailish, signature of mesoscopic disorder. (1) A temperature gap between $R(T)$ and $J_s(T)$ (in red) is observed. (2) After presenting a long tail for $T \lesssim T_c$, $J_s(T)$ increases abruptly in the OD regime (full line), recovering the a BCS-like trend, while in the UD case this increase is less steep (dashed line). (3) The optical conductivity g' (in black) displays a peak in correspondence of the increase of J_s, which is more pronounced in the OD regime, saturating to a finite value for $T \to 0$.

In this Section, we will implement in the RIN the idea of proximization anticipated above. In Fig. 4.7, one can find a graphical scheme of the RIN model and the proximization effect, as it will be implemented in this Section.

All the numerical values of the parameters will be taken coherently with the measurements showed in Section 4.2.

4.3.1   Effective medium theory for the RIN model

Let us start solving the EMT for the RIN model, the EMT providing some first insight to start with. Neglecting any spatial structure, we will consider a second superconducting component entering in the system at temperatures lower than the percolating one. We will then have three different components, and three different impedances, distributed across the system according to the corresponding fractions:

- w_{s1}: the superconducting fraction percolating at T_c, with local critical temperatures following a Gaussian distribution with parameters $(\mu_{c,s1}, \sigma_{s1})$;

- w_{s2}: the superconducting fraction arising after proximization, with local critical temperatures also following a Gaussian distribution with parameters $(\mu_{c,s2} \leq \mu_{c,s1}, \sigma_{s2})$;

- $w_m = 1 - w_{s1} - w_{s2}$: the fraction of the residual metallic matrix that will never undergo proximization.

In analogy with the RRN case presented in Section 4.1.1, one can then proceed by solving the EMT equation for the RIN model:

$$\sum_{j=s1,s2,m} \widetilde{w}_j(T) \frac{Z_j - Z_{em}}{Z^j + Z_{em}} = 0 \qquad (4.13)$$
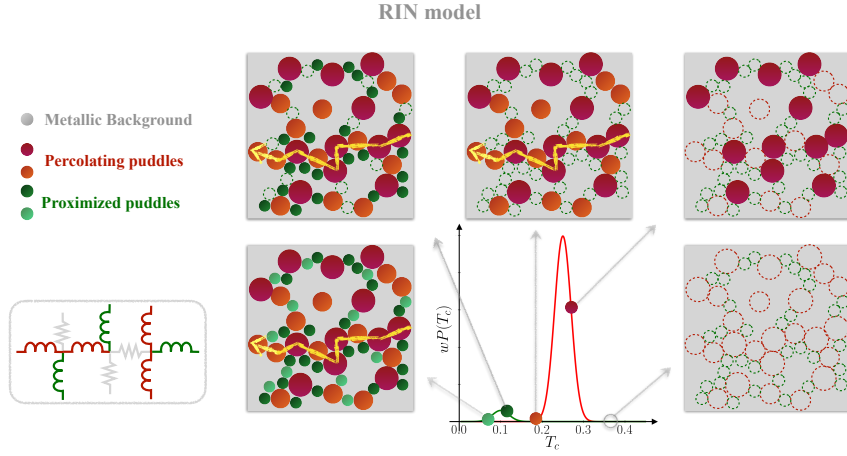
Figure 4.7. Graphical scheme of the Random Impedance Network with proximization, describing the idea of crossover between a one-dimensional to a two-dimensional structure of the superconducting condensate. The red and orange bonds represent the percolative superconducting cluster. As the temperature is lowered, the bonds start to become superconducting. At temperatures lower than the critical temperature of the whole system, a second kind of superconducting resistors gets involved (the green ones), providing a more connected, i.e., two-dimensional structure of the condensate.

where Z_{em} is the effective impedance of the network, the index $j = s1, s2, m$ labels the different components of the inhomogeneous system, and $\widetilde{w}_j(T)$ is the weight of the corresponding component at a temperature T, as defined in Eq. (4.10).

Let us now solve the EMT equation for a generical three-component system at finite frequency. The impedance of the single component is Z_j ($j = 1, 2, 3$), its fraction at temperature T being $\widetilde{w}_j(T) = \widetilde{w}_j$, with the usual constraint $\widetilde{w}_1 + \widetilde{w}_2 + \widetilde{w}_3 = 1$ holding. Once one explicits the sum, Eq. (4.13) takes the form of an algebraic equation of third degree with complex coefficients.

$$Z_{em}^3 + a_1 Z_{em}^2 + a_2 Z_{em} + a_3 = 0, \tag{4.14}$$

where

$$
\begin{aligned}
a_1 &\equiv Z_1 + Z_2 + Z_3 - 2(\widetilde{w}_1 z_1 + \widetilde{w}_2 Z_2 + \widetilde{w}_3 z_3), \\
a_2 &\equiv 2(\widetilde{w}_1 Z_2 Z_3 + \widetilde{w}_2 Z_3 Z_1 + \widetilde{w}_3 Z_1 Z_2) - (Z_1 Z_2 + Z_2 Z_3 + Z_3 Z_1), \\
a_3 &\equiv -Z_1 Z_2 Z_3.
\end{aligned}
$$

One can then define

$$\mathcal{Q} \equiv \frac{3a_2 - a_1^2}{9}, \qquad \mathcal{R} \equiv \frac{9a_1 a_2 - 27a_3 - 2a_1^3}{54}, \tag{4.15}$$

and

$$\mathcal{S} \equiv \sqrt[3]{\mathcal{R} + \sqrt{\mathcal{Q}^3 + \mathcal{R}^2}}, \qquad \mathcal{T} \equiv \sqrt[3]{\mathcal{R} - \sqrt{\mathcal{Q}^3 + \mathcal{R}^2}}, \tag{4.16}$$

where the square and cubic roots in the definition of $\mathcal{S}$ have positive imaginary part.The only physical solution mong the three determinations of the cubic root defining $\mathcal{T}$ is the one that satisfies $\mathcal{T} = -\mathcal{Q}/\mathcal{S}$. The solution of Eq. (4.13) with the appropriate analytic properties (positive imaginary part) is

$$Z_{em} = \mathcal{S} + \mathcal{T} - \frac{1}{3}a_1. \tag{4.17}$$

Going back to the specific case we want to study, the impedances of the three components are then $Z_{\mathrm{m}} = R_0 + \mathrm{i}\omega L_m$, $Z_{\mathrm{s}1} = \mathrm{i}\omega L(T)$, and $Z_{\mathrm{s}2} = \mathrm{i}\omega L_{s2}$. The temperature dependence of the inductance in the percolating cluster accounts for the strengthening induced by the proximization and reads as

$$L(T) = \frac{1}{2}\left[L_{s1}\left(1 + \mathrm{erf}\frac{T - \mu_{c,s1}}{\sqrt{2}\,\sigma_{s1}}\right) + L_{s2}\left(1 - \mathrm{erf}\frac{T - \mu_{c,s2}}{\sqrt{2}\,\sigma_{s2}}\right)\right]. \tag{4.18}$$

It should be noted that this formula is only meant to phenomenologically interpolate between L_{s1}, for $T \gg \mu_{c,s1}$, and L_{s2}, for $T \ll \mu_{c,s2}$.

Let us now compute the EMT solution in Eq. 4.17 in two cases: in a system with constant local inductances and in the case with frequency dependent inductances, accounting for the presence of dissipative vortices. In both cases, we are interested in the effects caused by the introduction of the proximized superconducting component.

EMT Results for constant local inductances

As far as we are interested in understanding the basic features generated by the appearance of a third superconducting component, we need to keep the fraction of the percolating one $w_2 < 1$. Unfortunately, the minimum fraction required for a two-dimensional system in EMT to percolate is $w^p = 0.5$, hence we will need at least $w_{s1} = w^p = 0.5$. Note that if we consider the exact solution of the RIN, instead of the solution of the EMT equation, the minimum fraction to percolate can be in principle a single filament crossing the lattice from side to side. The absolute numbers of fraction chosen here will then not be so much indicative from a point of view of the density of superconducting Cooper pairs in a real system, nevertheless the EMT solution will provide a good toy model to start with. The values of the parameters of the distributions of the critical temperatures, such as the average critical temperatures and the width of the Gaussian are instead chosen according to the measurements presented in Section 4.2. Thus, we choose the angular frequency to be $\omega = 2\,\mathrm{GHz}$, assuming then for the inductances values of the order of the nH, i.e., $L_m \sim 10\,\mathrm{nH}$ for the metallic residue and $L_{s1} \sim L_{s2} \sim 1\,\mathrm{nH}$ for the superconducting components [25].

- $w_{s2} = 0$

The first case to be discussed will be the simplest one, where the system is composed of two kinds of resistors, i.e., the metallic matrix m and the percolating superconducting cluster $s1$. We want to emphasize here that already in an effective medium framework, the basic features mentioned in the introduction of the Chapter are not well captured.

Looking at Fig. 4.8, where the DC resistivity and the real and imaginary conductivity are plotted for different values of w_{s1}, one can convince themselves that

the RIN model for a two component system cannot account for the peculiar features summarized in Fig. 4.6 of Section 4.2. Here the EMT calculations were done using $L_m = 10\,\text{nH}$ and $L_{s1} = 1\,\text{nH}$ and the parameters of the Gaussian distribution of the superconducting component are set to be $\mu_{c,s1} = 0.2\,\text{K}$ and $\sigma_{s1} = 0.02\,\text{K}$. If the system is made by the superconducting component alone, i.e., $w_{s1} = 1$ in Fig. 4.8a, the qualitative scenario observed is quite similar to the conventional one showed in Fig. 4.6a: the stiffness (red dots) rises at percolation, crossing the resistivity (green), and the conductivity (black) is zero except for a peak right at T_c. Moreover, the resistive transition is still too sharp with respect to the experimental data. Instead, at percolating threshold $w_{s1} = 0.5$ in Fig. 4.8c, the resistivity shows a more pronounced tail, coherent with measurements. The real and imaginary response are however superimposed on top of each other, both rising right before T_c, saturating soon to a low value of about $0.02\,\Omega^{-1}$. The intermediate case $w_{s1} = 0.75$ in panel b is just similar to the $w_{s1} = 1$ case, with a slightly more tailish resistivity and a lower saturating value of the imaginary part of the conductance.
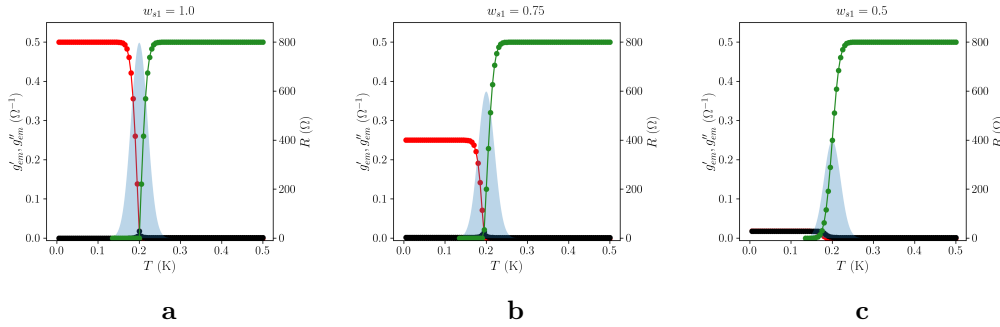

Figure 4.8. EMT calculations of the resistivity (green) and the real (black) and imaginary (red) parts of the conductance without any proximization, for a fraction of superconducting resistors $w_s = 1$ (a), $w_s = 0.75$ (b) and $w_s = 0.5$ (c). The parameters of the Gaussian distribution of the superconducting component are $\mu_{c,s1} = 0.2\,\text{K}$ and $\sigma_{s1} = 0.02\,\text{K}$. $L_m = 10\,\text{nH}$ and $L_{s1} = 1\,\text{nH}$.

- $w_{s2} > 0$

The percolating resistors alone apt to describe very well the properties of the metallic state and the superconducting transition fails at temperatures lower than T_c and cannot reproduce the important increase of the superfluid stiffness observed in real material. We can now introduce a second fraction of superconducting bonds ($w_{s2} > 0$) with a Gaussian distribution centered at a lower temperature ($\mu_{c,s2} < \mu_{c,s1}$) and investigate the impact of this new superconducting fraction on the AC transport properties. In this paragraph, we will keep fixed the fraction of the first (percolating) superconducting bonds to $w_{s1} = 0.5$, as well as the Gaussian distribution of their critical temperatures, with parameters $\mu_{c,s1} = 0.2\,\text{K}$; $\sigma_{s1} = 0.02\,\text{K}$), and we tune individually the parameters relative to the second, proximity-induced, fraction of superconducting bonds. Bare in mind that at percolating threshold, the global resistance of the system will vanish as soon as all the bonds of the superconducting

cluster have switched to their superconducting state (see Fig. 4.2 On the other hand, the finite-frequency response of the system appears already above T_c, at $T \lesssim \mu_{c,1}$: as one can see from the trend of the black curves in Fig. 4.9a, both the superfluid stiffness $J_s \propto -g''_{em}$ (at a fixed low frequency) and the optical conductivity $\sigma = g'_{em}$ start to increase above the percolating temperature, saturating to a constant value around T_c. Let us start by fixing the Gaussian distribution with $\mu_{c,s2} = 0.1\,\mathrm{K}$ and $\sigma_{s2} = 0.02\,\mathrm{K}$, and by tuning the fraction w_2 of proximized bonds. As one can see from Fig. 4.9a, increasing the value of w_2 both g''_m and g'_{em} assume a *two-step* character, which can be smoother or more pronounced depending on the other parameters at play, with opposite trends: while g''_{em} registers a further growth as a consequence of a reduction of the global inductance, the optical conductivity g'_{em} sees a downturn after a sort of plateau, which will become more or less peaked depending on $(\mu_{c,s2}, \sigma_{s2})$ (Fig. 4.9b,c. We also stress that, by increasing w_2, the ratio between the saturation values at $T = 0$ of g''_{em} and g'_{em} strongly increases: a fraction of just $w_2 = 0.07$ proximized bonds make the ratio $g''_{em}(0)/g'_{em}(0)$ 10 times bigger with respect to the case when proximization is not taken into account, and $w_2 = 0$.

We now set the fraction of the proximized bonds to $w_{s2} = 0.03$ and we observe the effects in changing the variance σ_{s2} and the mean value $\mu_{c,s2}$ of the Gaussian distribution of its critical temperatures. A broader probability distribution, i.e., a larger value of σ_{s2}, smoothes out the *two-step* character of both response functions: it broadens the downturn of g'_{em} as well as the increase of g''_{em} (see Fig. 4.9b). On the other hand, the value of $\mu_{c,s2}$ rules the temperature range at which both g'_{em} and g''_{em} start to increase and, quite interestingly, it corresponds to the inflection point of the two curves (see Fig. 4.9c). In general, from Fig. 4.9b,c, one can see that the more the two probability distributions overlap, either because of a larger σ_{s2} or because $\mu_{c,s2}$ is taken closer to $\mu_{c,s1}$, the more the growth of g''_{em} is continuous and the bump of g'_{em} peaks.

So far, we have assumed that both superconducting fractions have the same inductance value $L_{s1} = L_{s2} = 1\,\mathrm{nH}$, while the metallic residue has $L_m = 10\,\mathrm{nH}$. Finally, we look at the effects of changing the relative values of L_{s1} and L_{s2} on the response of the system. Fixing $L_{s1} = 2\,\mathrm{nH}$ we tune the value of L_{s2}. As one can see from Fig.4.9d, the variations of $L_{s1,s2}$ correspond to tuning the magnitude in the zero-temperature limit of g'_{em} and g''_{em}. In particular, an increase (decrease) of L_{s2} with respect to L_{s1} corresponds to a decrease (increase) of the saturation values of both the real and imaginary part of g_{em}. It is worth noting that, while an increase in w_{s2} acts in opposite directions in g'_{em} and g''_{em} (Fig. 4.9a), the decrease of L_{s1} corresponds to an increase of both $g'_{em}(0)$ and $g''_{em}(0)$, albeit with a different magnitude. From $L_{s2} = 2\,L_{s1}$ to $L_{s2} = L_{s1}$, the relative increase of $g''_{em}(0)$ is ≈ 1.3 while for g'_{em} this is ≈ 0.5. Qualitatively, for $L_{s2} \leq L_{s1} = 1\,\mathrm{nH}$ we also observe an increase of g'_{em} in the lower temperature range, while in all other cases we observe a bump and then a decrease, while lowering T.

Finite-Frequency Dissipation

So far, the RIN model proposed considers the inductances L_j ($j = s1, s2$) inside the superconducting clusters as real constants. Nevertheless, one can think of improving the model, using more sophisticated relations for the local inductances, taking for
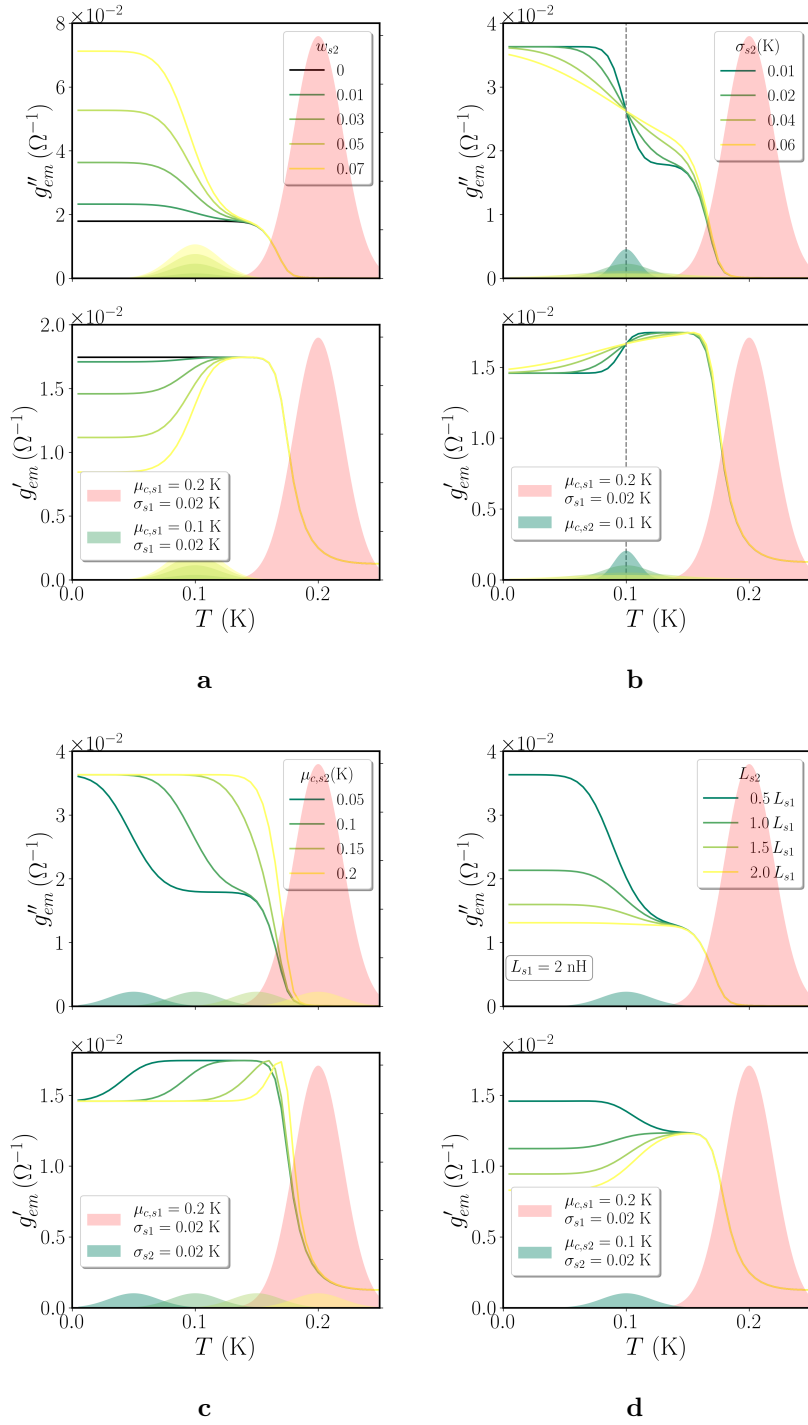
Figure 4.9. EMT calculations of g''_{em} (upper panels) and g'_{em} (lower panels), as a function of the temperature T, for different tuning parameters. The pink filled Gaussian corresponds to the probability distribution of the percolating superconducting component with total fraction $w_{s1} = 0.5$, while the other filled gaussians to the distribution of the proximized bonds. The parameters tuned in each figures are respectively: (**a**) the total fraction w_{s2} of the proximized component; (**b**) its variance σ_{s2}; (**c**) its mean value $\mu_{c,2}$; and (**d**) the value of its inductance L_2 keeping in this case fixed $L_{s1} = 2\,\text{nH}$. Where not specified in the labels, $L_{s1} = L_{s2} = 1\,\text{nH}$, $w_{s2} = 0.03$. In all cases, we kept fixed $R_N = 800\,\Omega$, $L_m = 10\,\text{nH}$ and $\omega = 2\,\text{GHz}$. The areas underneath all Gaussian distributions equal the corresponding fractions w_j.

instance a temperature and/or frequency dependent complex inductance $L_j(T, \omega)$, to account for finite-frequency dissipation processes. In this paragraph, we will explore this possibility.

In Ref. [114], the authors discuss their measurements of impedance in thin films of superconductors at radio frequencies. They propose a dissipation model to fit their data based on "a dynamic pinning in which the dissipation arises from the flux-flow resistance of the moving vortices and the inductance from pinning and acceleration of the back-ground superfluid." We borrow their model, to describe phenomenologically some finite-frequency dissipation effect in our EMT for the RIN. The complex impedance was written as

$$Z = R_0 + Z_\text{v} + \mathrm{i}\omega L_0 \tag{4.19}$$

where

$$Z_\text{v} = A \frac{\mathrm{i}\omega\tau}{1 + \mathrm{i}\omega\tau} \tag{4.20}$$

described the dissipation due to vortices generated by the presence of a magnetic field. In their work, A is proportional to the strength of the magnetic field with the dimensions of a resistance and τ is the relaxation time for vortices. Although in our model, we never introduce an external magnetic field, this relation can be nevertheless used, assuming that the dissipation is due to thermally excited vortices [26]. The expression of the complex impedance can be recast then assuming a frequency dependent complex inductance

$$L(\omega) = L_0 + \frac{A\tau}{1 + \mathrm{i}\omega\tau} \tag{4.21}$$

in Eq. (4.12)

$$Z_i = R_N + \mathrm{i}\omega L(\omega). \tag{4.22}$$

Note that in this paragraph we are considering $L_j = L(\omega)$ the same for all the components in the system.

Recalling that the superfluid stiffness is $J_s \propto g''$, in the superconducting state where $R_0 = 0$ the reactive response of the system is related to the inverse of

$$\mathrm{Im} Z = \mathrm{Re}\, L(\omega) = L_0 + \frac{A\tau}{1 + (\omega\tau)^2} > L_0, \tag{4.23}$$

Hence, the reactive response is strongly reduced for $\omega\tau \gg 1$. Instead, the dissipative response is ruled by the term

$$\mathrm{Re}\, Z_\text{v} = \frac{A(\omega\tau)^2}{1 + (\omega\tau)^2},$$

which is vanishingly small for $\omega\tau \to 0$, and tends from below to the constant value A for $\omega\tau \to \infty$. Thus the parameter A finds its meaning, setting the high-frequency dissipation in the superconducting state.

More generally, within a phenomenological description, the values of the parameters A and τ must be adapted to a specific system. So far, very little is known about thermally generated vortices in two-dimensional superconductors with disorder at

the nanoscale. Hence, we adopted values of the parameters comparable to those used in [114], taking $A = 10^{-3}\,\Omega$ and τ of the order of $1\,\mu$s. To highlight finite-frequency dissipation we take a frequency $\omega = 0.1\,$MHz, so that $\omega\tau \approx 0.1$ is small but not negligible.

In the following, we solve the EMT equation (4.13) for the RIN, assuming that the complex impedance of the superconducting component s is $Z_j = R_0 + Z_v + i\omega L_0$ above the local random critical temperature and $Z_j = Z_v + i\omega L_0$ below it, while the eventual metallic residue has always $Z_j = R_0 + Z_v + i\omega L_0$.

We point out that, despite the apparent resemblance with the physics of the vortex matter [115, 116], all the calculations refer to the case where the magnetic field is absent and the dissipation in the percolative superconducting state is entirely due to thermally excited vortices.

- $w_{s1} = 1$

As before, we will first consider the simplest case of a system where no proximization effects are involved and all the resistors contribute to superconductivity $w_{s1} = 1$. The parameters of the distribution of critical temperatures (Eq. (4.2)) are chosen to be $\mu_{c,s1} = 0.2\,$K, $\sigma_{s1} = 0.05\,$K. The values for resistivity and constant term of the inductance are taken again as typical values of SrTiO$_3$-based oxide interfaces [25]: $R_0 = 600\,\Omega$, $L_0 = 1\,$nH, and $\omega = 0.1\,$MHz, which will allow us to highlight dissipative effects, as already mentioned.

The solution of the EMT equation (4.13), gives a resistance $R = \text{Re}(Z_{\text{em}})$ shown as the blue curve in Fig. 4.10b, whose value coincides with the result obtained for the case $\omega = 0$ (as $\omega L_0 \ll R_0$). The percolative transition occurs at $T = \mu_{c,s1}$, i.e., at percolation threshold, when half of the resistors are switched to their superconducting state as it can be evinced from the distribution of critical temperatures (red shaded area in Fig. 4.10). The width of the percolative transition is ruled by $\sigma_{c,s1}$ and no tail is present.

The imaginary part of the complex conductance g''_{em} becomes relevant below percolation, where the AC response of the RIN is purely reactive, as one can see from Fig. 4.10a). The solution of Eq. (4.13) with no dissipative effects ($A = 0$) is plotted in yellow. As soon as $A > 0$, finite-frequency dissipation suppresses the reactive response of the system below the percolative transition. In the regime $\omega\tau \ll 1$, once we fixed $A = 10^{-3}\,\Omega$, this suppression increases with increasing τ: this is shown in Fig. 4.10a, respectively, for the light blue ($\tau = 0.5\,\mu$s), green ($\tau = 1\,\mu$ s) and red ($\tau = 5\,\mu$s) curves. As we are considering a thermal activation mechanism for dissipation, we can expect that A depends on T. This is shown by the violet curve in Fig. 4.10 labeled with $A(T)$ ($\tau = 5\,\mu$s), where a dependence

$$A(T) = A_0\,e^{-(\mu_{c,s1}-T)/T}, \tag{4.24}$$

is adopted to describe the thermal excitation of vortices, exponentially suppressed at $T = 0\,$K. We take $A_0 = 10^{-3}\,\Omega$ in order to make the comparison with the case of a constant A easier, we assumed that near percolation $A(T) \approx A_0$, so that the curve with variable $A(T)$ collapses onto the curve with $A = A_0$, while smoothly joining the curve with $A = 0$ at low temperature.
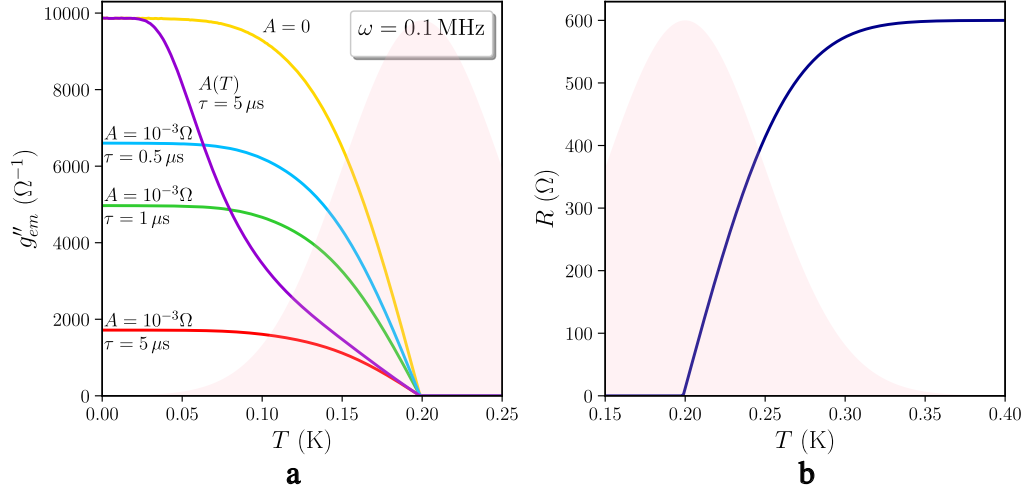
Figure 4.10. (a) Imaginary part of the complex conductance of the RIN within the EMT, g''_{em}, as a function of the temperature T, for $R_0 = 600\,\Omega$, $L_0 = 1\,\text{nH}$, $\omega = 0.1\,\text{MHz}$. The Gaussian distribution of the superconducting critical temperatures is shaded in red; the average value and standard deviation are, respectively, $\mu_{c,s1} = 0.2\,\text{K}$, $\sigma_{c,s1} = 0.05\,\text{K}$; the weight is $w_s = 1$, i.e., all the resistors participate to superconductivity. The values A and τ of the dissipative term $Z_V = A(\text{i}\omega\tau)/(1 + \text{i}\omega\tau)$ are specified for each curve. In particular, for the violet curve labeled by $A(T)$ we took a temperature dependence $A(T) = A_0\,\text{e}^{-(\mu_{c,s1}-T)/T}$, with $A_0 = 10^{-3}\,\Omega$, to describe the thermal excitation of vortices, which is exponentially suppressed at $T = 0\,\text{K}$. (b) The blue curve gives the sheet resistance of the system above percolation, where the effects of Z_V are negligible. All the calculations are carried out assuming zero magnetic field.

• $w_m \neq 0$ $w_{s2} \neq 0$

Let us now consider the more complicated situation where the system also hosts the smaller superconducting cluster *s2* emerging by proximity effect below the percolative transition. As before, the minimum required fraction of superconducting bonds to have a low-temperature global superconducting state is $w_{s1} = \frac{1}{2}$. In this case, the resistive transition is characterized by a very pronounced tail (see the blue curve in Fig. 4.11b). Even after the appearance of a global zero-resistance state, the superconducting cluster is in this case very fragile towards an applied current. The appearance of this second cluster modifies the reactive response of the system in the superconducting phase. The "proximized" superconducting cluster can in fact boost the superfluid stiffness, although it occupies a very small fraction of the system $\overline{w}_{s2} = \frac{7}{100}$.

To describe the enhancement of the stiffness after proximization, we choose $L_{s2} < L_{s1}$ and in particular we take $L_m = L_{s1} = 1\,\text{nH}$ and $L_{s2} = 0.5\,\text{nH}$.

The resulting reactive response without dissipative effects is shown in Fig. 4.11, with the yellow curve labeled by $A = 0$. Below the percolative transition, the reactive response of the superconducting cluster stays very small, until the second superconducting cluster start to nucleate at $T \approx \mu_{c,s2} + \sigma_{s2}$ (the distribution $P_{s2}(T_c)$ is shaded in red), thereby boosting the reactive response of the system. Comparison with Fig. 4.2 shows that now there is a wide temperature gap between the drop of
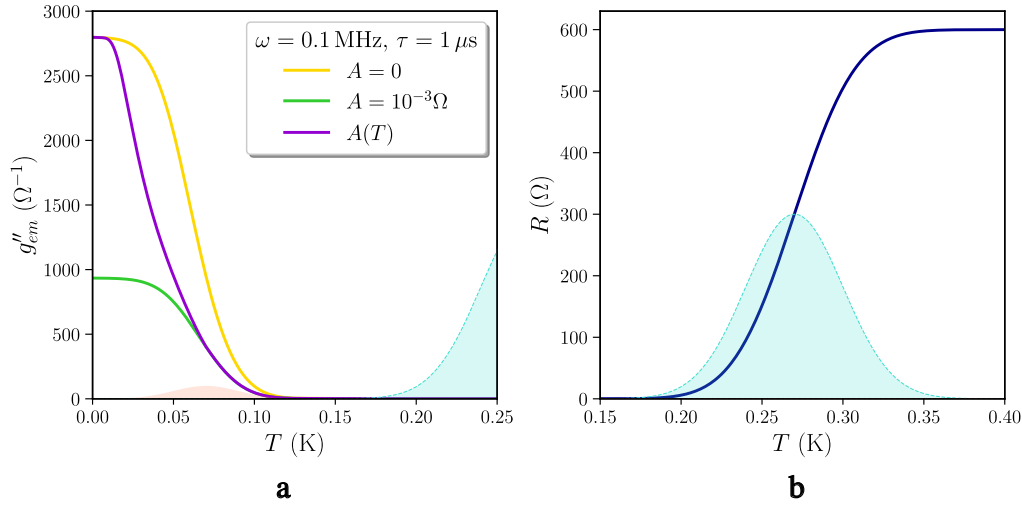
Figure 4.11. (a) Imaginary part of the complex conductance of the three-component RIN within the EMT, g'', as a function of the temperature T, for $R_0 = 600\,\Omega$, $L_{s1} = 1\,\text{nH}$, $L_{s2} = 0.5\,\text{nH}$, $\omega = 0.1\,\text{MHz}$. The Gaussian distribution of the percolating superconducting cluster has mean value $\mu_{c,s1} = 0.27\,\text{K}$, standard deviation $\sigma_{s1}^2 = 0.03\,\text{K}$ and weight $w_{s1} = 0.5$, and it is shaded in light blue; the proximized fraction distribution is shaded in red, its parameters are $\mu_{c,2} = 0.07\,\text{K}$, $\sigma_{s2} = 0.02\,\text{K}$ and $w_{s2} = 0.07$. All the three curves are calculated for $\tau = 1\,\mu\text{s}$ while the values of A are indicated in the legend. For the violet curve we took a temperature dependence $A(T) = A_0 \min[\mathrm{e}^{-(\mu_{c,s2}-T)/T}; 1]$, with $A_0 = 10^{-3}\,\Omega$, to describe the thermal excitation of vortices, which is exponentially suppressed at $T = 0\,\text{K}$. (b) The blue curve gives the sheet resistance of the system above percolation, where the effects of Z_V are negligible.

the resistance in the metallic phase above percolation and the rise of the reactive response below percolation.

As in the previous case, finite-frequency dissipation suppresses the reactive response in the superconducting state, as one can see in Fig. 4.11 comparing the yellow curve where no dissipation is present ($A = 0$) with the green one, where $A = 10^{-3}\,\Omega$ and $\tau = 1\,\mu\text{s}$.

As in the previous case, a thermal generation of the dissipative processes can be taken into account, this time entering in correspondence of the second superconducting fraction, (see the violet curve labeled by $A(T)$ in Fig. 4.11a). Thus we adopted now the expression

$$A(T) = A_0 \min[\mathrm{e}^{-(\mu_{c,s2}-T)/T}; 1], \qquad (4.25)$$

with $A_0 = 10^{-3}\,\Omega$, the reactive response interpolates smoothly between the response with no finite-frequency dissipation, at $T = 0\,\text{K}$, and the response with finite-frequency dissipation, near percolation.

4.3.2   Exact solution of the RIN with proximization

From now on, we will finally focus our attention on the exact solution of the RIN model, i.e., solving the Kirchoff's and Ohm's equations, in a system hosting strong spatial correlations. Baring in mind the discussion of Section 4.2 and the results

obtained from the EMT solution, we keep following the idea of a crossover between a quasi-one-dimensional to a two-dimensional superconducting state driving the superfluid density jump at some $T_{cross} < T_c$. The possibility for the metallic substrate to become superconducting via a proximization process will need however a more "geometrical" way to be applied in the exact solution of the RIN, especially when strongly correlated disorder is taken in analysis as it is the case.

Lowering the external temperature, the filamentary backbone of the system needs to be gradually strengthened by new neighboring superconducting bonds, finally reaching a whole two-dimensional state. While in the UD regime the "bumps" observed may lead us to think of a process happening in two steps, in the OD regime the proximized component of the system suddenly enters, causing an abrupt jump of $J_s(T)$. Numerically, we implemented the proximization in the following way: the i-th metallic bond can be promoted to superconducting if it has at least $n_b^{SC} = 2$ superconducting nearest neighbors and its critical temperature is set to be some fraction of the average critical temperature of superconducting nearest neighbors:

$$T_c^{i,prox} = a_{pr} \frac{1}{N_j} \sum_{j(i)} T_c^j, \tag{4.26}$$

where a_{pr} is a tuning parameter of the proximization process, $\sum_{j(i)}$ staying for the sum over the superconducting nearest neighbor of i and N_j for the number of superconducting neighbors. This proximization process is made n_{update} times, so that we can span the metal background up to the n_{update}-th neighbors of the superconducting filamentary structure.

As a starting point, we show here some results using the DLA algorithm, as it was explained in Section 4.1.2, to build the filamentary superconducting cluster, applying patches of radius $r_{pd} = 5$ until reaching a fraction w superconducting bonds. For the sake of simplicity, we can drop here the subscript s, since we refer to w as the total amount of superconducting resistors, i.e., the percolating fraction, whereas the proximized bonds component strictly depends on the initial cluster and its geometry. As in the RRN in Ref. [74] of Section 4.1.2, we keep two separated gaussians for the critical temperatures of the fractal (with average μ_f and variance σ_f) and the puddles (μ_b, σ_b). For numerical reasons, the assigned impedance to the link is normalized to the experimental value R_N of the normal-state resistivity ($z_i = Z_i/R_N$) and then the total conductance of the network is rescaled to the same value.

In general, the local values of L_i in the single bond can be either L_0, L_f or L_{pr} if the bonds belongs respectively to the metal (or a puddle), the fractal or the proximized bond:

$$L^i = \begin{cases} L_0, & \text{if } i \in m, b, \\ L_f, & \text{if } i \in f, \\ L_{pr} & \text{if } i \in pr \end{cases} \tag{4.27}$$

However, since the model has many parameters, we start by fixing – once and for all – the distributions of the critical temperature of puddles and fractal. The mean value and standard deviations can be chosen according to experimental data and will of course depend on the single configuration of the 2DEG, as one can see from Fig. 4.12a where the resistivity data are shown for all the gate voltages V_G. It is

sufficient to say that $\mu_{c,f}$ and σ_f acts on the percolative temperature and the more or less tailish behavior near T_c, while $\mu_{c,b}$ and σ_b leads the first depletion of $R(T)$ at higher temperatures. One can thus fix the distributions using the mean values and variances as fitting parameters for the resistivity, whereas R_N has to be chosen as the experimental value in the metallic state, i.e., at $T = 0.5\,\mathrm{K}$ in the case considered.

At this stage, we are interested in studying and, possibly, understanding the filamentary nature of the superconducting condensate of the 2DEG, so the fine tuning of all parameters is not our priority. Hence, we decide to set those values to $\mu_{c,f} = 0.19\,\mathrm{K}$, $\mu_{c,b} = 0.24\,\mathrm{K}$ and $\sigma_f = 0.02\,\mathrm{K}$, $\sigma_b = 0.055$. Indeed, the resistivity trends at different gate voltages are qualitatively similar, as one can see from the inset of Fig. 4.12a, where the same data are normalized to their own R_N value. Fig. 4.12b shows the computed $R(T)/R_N$ curves for different values w, using the actual data at $V_G = 28\,\mathrm{V}$ as a benchmark (black line). The distribution of the critical temperatures in the fractal is shaded in blue, while the distribution of local critical temperatures is shaded in purple.For how the network is constructed, a higher w corresponds to more superpuddles and, consequently, to a lowering of the effective resistivity right in the high temperature range of the transition, when the resistors start to be switched to their superconducting state. Note also that all the values of w considered are lower (or equal to) the percolating threshold $w^p = 0.5$, while for the EMT calculation this was the least possible fraction of bonds to have percolation.

Considering now $R_N = 800\,\Omega$ and $w = 0.4$, we look at the finite frequency response of the system. We use $\omega = 2\,\mathrm{GHz}$, as the experimental value, and the values $L_0 = 5\,\mathrm{nH}$, $L_f = 2.5\,\mathrm{nH}$ and $L_{pr} = 0.5\,\mathrm{nH}$, remembering that the value of L_0 does not affect much the global real and imaginary responses, while L_f and L_{pr} can tune the order of magnitude of the saturating values for $T \to 0$. In order to explain the data, the need of a proximization process to be involved is clear looking at Fig. 4.13, where the real g' and imaginary part g'' are shown for different values of a_{pr}, g' plotted in dashed line while g'' in dots. We show the corresponding R in yellow on the right axis as a benchmark. Indeed, looking at the orange curve $a_{pr} = 0$ in Fig. 4.13a, one can see that for one hand g'' crosses the resistivity near T_c while, on the other hand, the saturating value of $g'(0)$ is too low. Nevertheless, L_f and L_{pr} tunes $g''(0)$ without affecting $g'(0)$, whereas the quantities in the superconducting state are not much sensitive to the value L_0. A finite a_{pr} instead, the superfluid stiffness has a second increase, at temperatures lower than T_c if $a_{pr} < 1$ and at $T \sim T_c$ for $a_{pr} = 1$ (in light blue). In particular, one of the peculiar feature observed in the UD regime, i.e., the "bump" observed right below the critical temperature (Fig. 4.5 for $V_G \lesssim 26\,\mathrm{V}$), can be mirrored in the pink curve corresponding to $a_{pr} = 0.5$ where the increase of g'' happens in a two-step way. If not only first nearest neighbors are considered in the proximization process and we span the system more than once ($n_{up} > 1$), a "third" increase of g'' is observed, at even lower temperatures. This is clear from Fig. 4.13, where we tune n_{up}, keeping $a_{pr} = 0.5$.

What it is still missing in this picture is a clear cut between the two regimes. Also, the ratio between the saturating values of the real and imaginary part of the conductivity at $T = 0$, i.e., $g'(0)/g''(0)$, is still too small. Since roughly $g' \propto R/(R^2 + \omega^2 L^2)$, the real part of the conductivity is strictly related to the metallic residue instead of the other parameters involved in the system, such as the magnitude of the inductances $L_{f,pr}$ and the proximization process accounted by a_{pr} and n_{up}.
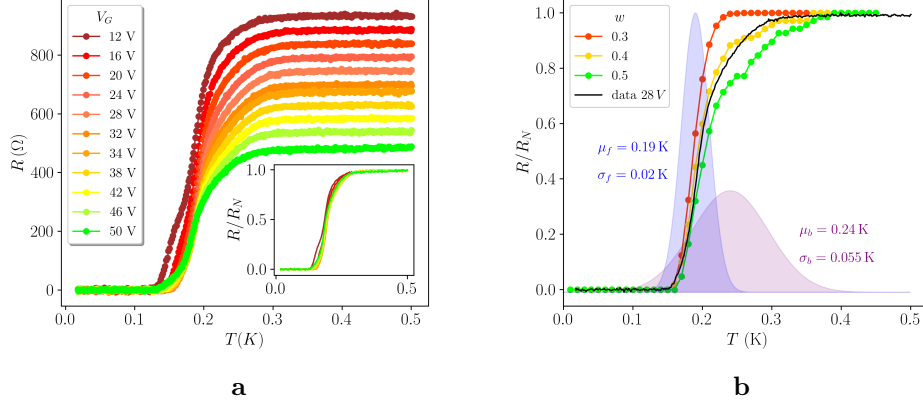
Figure 4.12. (a) DC resistivity transport measurements at various gate voltages. In the inset, the same data are plotted normalized to their normal state value R_N, showing more or less the same features in terms of broadening and tailish behavior near T_c. (b) Exact RIN calculations at zero frequency of the resistivity for a fractal with puddles of radius $r_{pd} = 5$ for different values of the total fraction of superconducting bonds, compared, as a benchmark, with the normalized resistivity of the sample at $V_G = 28\,\mathrm{V}$ (black line). In purple and blue are shaded the Gaussian distributions of puddles and fractal, with average and standard deviation respectively $\mu_b = 0.24\,\mathrm{K}$, $\sigma_b = 0.055\,\mathrm{K}$ and $\mu_f = 0.19\,\mathrm{K}$, $\sigma_f = 0.02\,\mathrm{K}$.

Besides, in the real system the increase of gate voltage corresponds to an increase of the number of carriers in the 2DEG.

In the next Section, we will address the problem of the geometrical structure of the fractal.

4.3.3   The role of geometry

We work here directly on the fractal structure, hoping that it can provide us a deeper understanding of the problem, in particular for what concerns the difference between UD and OD regimes.

Instead of doing one step on the right and one up or down as in the former calculations (see Section 4.1.2), each random walker is now allowed to do r_{DLA} steps to the right and then y_{DLA} steps up or down with a probability $\frac{1}{2}$. As before, a 100×100 network is extrapolated from the super-network constructed with the "improved" DLA algorithm and some patches of radius r_{pd} are then superimposed until a fraction w of superconducting resistors is reached.

In Fig. 4.14, are shown two 250×250 different super-network constructed launching $n_{RW} = 15000$ particles. In panel a, the (orange) superconducting fractal is built from random walkers allowed to do $r_{DLA} = 2$ steps on the right and $y_{DLA} = 2$ steps on the left, while in panel b the constraints were $r_{DLA} = 10$, $y_{DLA} = 7$ in Fig. 4.14b. In both panels, the region colored in blue is the metallic background of the final 100×100 network. In addition to allowing us to study the very role of filamentary in the superconducting state, this procedure enables us to have a higher fraction of the metallic residue without preventing percolation. For the sake of simplicity, we
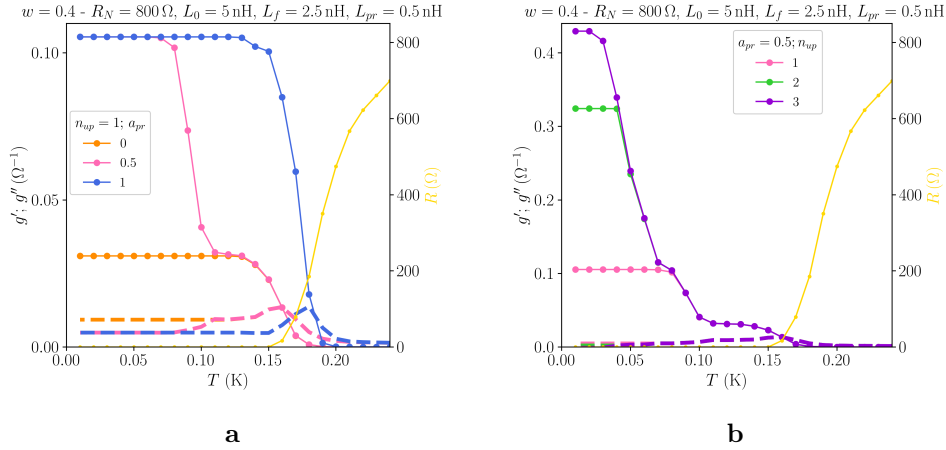
a   **b**

Figure 4.13. RIN calculations at frequency $\omega = 2\,\mathrm{GHz}$ of the real (dashed lines) and imaginary (dotted lines) parts of the conductance $g = g' - ig''$ corresponding to the $w = 0.4$ yellow curve of Fig. 4.12, plotted in both panels on the right axis, as a reminder of the percolating temperature. $g'(T)$ and $g''(T)$ are calculated at different values of a_{pr}, for one update of the bonds $n_{up} = 1$ (a) and at various number of updates n_{up}, keeping $a_{pr} = 0.5$.

will refer to the fractal configurations in Figs. 4.12, 4.14a and 4.14b respectively as the $1 - 1$, $2 - 2$ and $10 - 7$.

From now on, the superconducting structure itself, i.e., r_{DLA}, y_{DLA} and the radius r_{pd}, will be an important fitting parameter. Of course, a systematic and precise analysis would pretend an average on many configurations of the disorder, for the same r_{DLA}, y_{DLA} and r_{pd}, in order to be accurate. Nevertheless, our scope here is to highlight eventual general properties arising from the geometrical filamentary structure of the superconducting condensate, in line with the experimental ones highlighted in Section 4.2. Thus, at this stage, the average over disorder will only complicate the analysis and hinder our way towards understanding. Besides, as the model is so rich, it is easy to get lost in the fine tuning of the parameters. We choose here the fractals extrapolated from the supernetworks in Fig 4.14a and 4.14b, attaching puddles of radius $r = 5$ until reaching $w = 0.3$.

Indeed, since the fractal is less dense, a lower density of superconducting bonds is needed to have percolation with respect to the $1 - 1$ fractal presented in the former section. Tuning then the other parameters, such as a_{pr} and n_{up}, we can investigate how the geometry has affected both the superfluid stiffness and the optical conductivity. Fig. 4.15a and 4.16a show the color maps of the two fractals – respectively the $2 - 2$ and the $10 - 7$ – with a proximization parameter $a_{pr} = 0.4$ for one update of the bonds' lattice ($n_{up} = 1$), the color code indicating the local critical temperature in Kelvin. The real (dotted lines) and imaginary (dashed lines) parts, corresponding to the $2 - 2$ fractal for different values of a_{pr} are plotted in Fig. 4.15b, while Fig. 4.16 shows the same calculations for the $10 - 7$ fractal. Keeping $a_{pr} = 0.4$ fixed, we tune the number of updates of the bonds, showing the calculations in Fig. 4.15d and Fig. 4.16d.
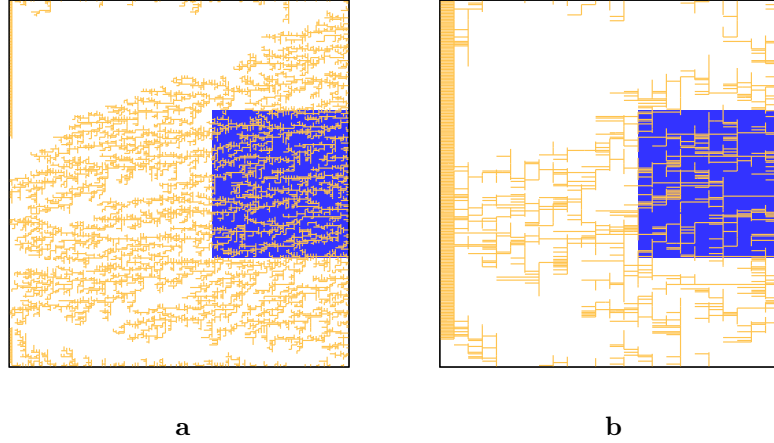
a   b

Figure 4.14. Examples of filamentary structures constructed via the "improved" DLA
algorithm launching n_{rw} =15 000 diffusing particles across a 250×250 square lattice. In
orange are shown the obtained clusters with (a) $r_{DLA} = 2$, $y_{DLA} = 2$ and (b) $r_{DLA} = 10$,
$y_{DLA} = 7$. Highlighted in blue is the metallic region that defines the final 100×100
square lattice.

At a first glance, comparing panels b and d of both Fig. 4.15 and 4.16, we can
already convince ourselves that the geometry is crucial in the proximization, since
it corresponds to a more or less number of resistors involved in the process. In
fact, the orange curve corresponding in both panels b to $a_{pr} = 0$ does not present
significant differences: $g''(T)$ starts to increase around $T = 0.17\,\mathrm{K}$, reaching quite
soon the saturating value $g''(0) \sim 0.02$. In other words, if no proximization process
is considered the finite frequency response of the system is independent from the
geometry of the superconducting condensate. Although, it can be argued that a
more tailish behavior is observed in the $10-7$ curve, stating again the need of a
more filamentary structure to account for the data, particularly in the UD regime.
If a proximization process is involved, the difference between the two configurations
is more definite: a finite a_{pr} boosts $g''(T)$ up to $0.07\,\Omega^{-1}$ in the $2-2$ case while
for the $10-7$ fractal $g''(T)$ reaches the value $0.03\,\Omega^{-1}$. The a_{pr} value sets the
temperature at which this increase of $g''(T)$ is observed, while correspondingly $g'(T)$
slightly decreases. The other significant difference between the two configurations
is then the ratio of the saturating values of the real and imaginary part which is
$g'(0)/g''(0) \sim 0.05$ for the $2-2$ and $g'(0)/g''(0) \sim 0.14$ for the $10-7$ fractal.

Once a_{pr} is fixed, we can see the effect of increasing the number of updates. As
one can guess, this provides an additional increase of the superfluid stiffness, at
the expense of the optical conductance. This happens at even lower temperatures.
In fact, at each update the metallic bonds surrounding the superconducting ones
gain a local critical temperature which is gradually smaller by a factor $a_{pr} < 1$
with respect to the average critical temperature of their neighbors. Thus, from
panels d of Figs.4.15 and 4.16 we observe an important growth of $g''(T)$, happening
around $T \sim 0.05$. Besides, spanning the network more than 4 times appears to be
worthless: the stiffness has already increased its value sixfold, and the next bonds
to be proximized will have a negligible critical temperature. It should be noted
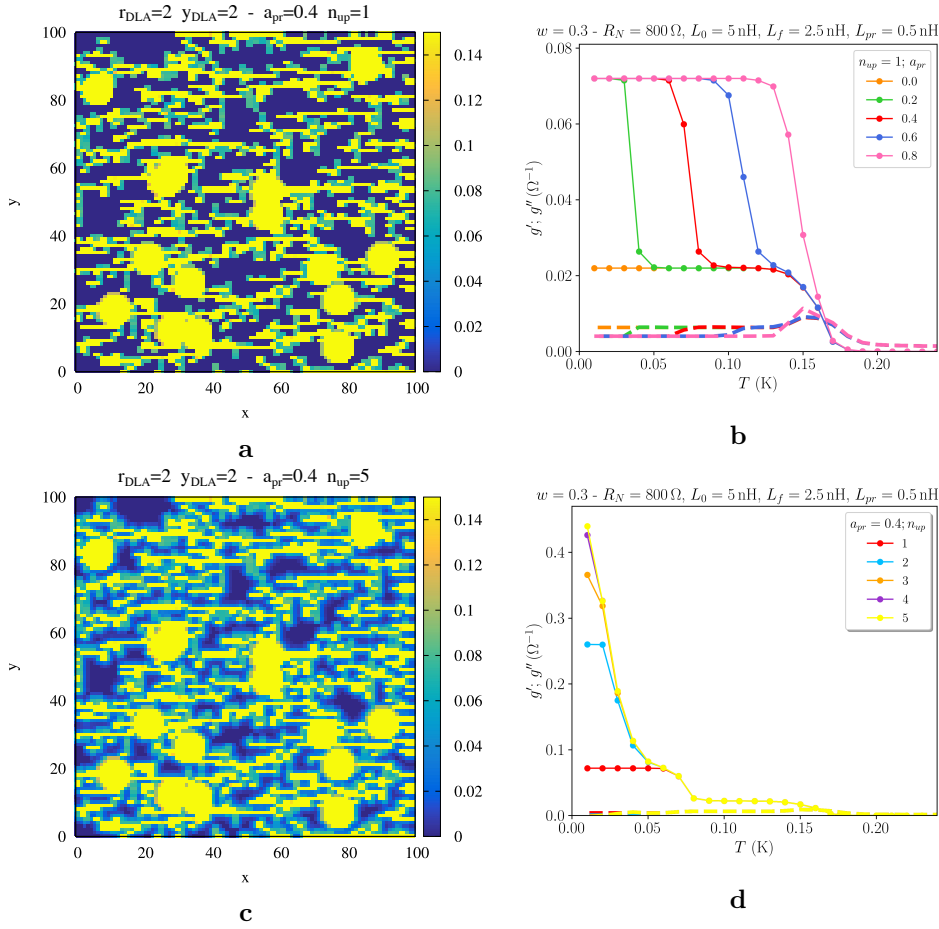
Figure 4.15. (a) Color map of the local critical temperatures in a 100×100 $2 - 2$ fractal with $r_{pd} = 5$ and proximization parameters $a_{pr} = 0.4$ and $n_{up} = 1$. (b) Corresponding RIN calculations of $g'(T)$ (dashed lines) and $g''(T)$ (dotted lines) for $n_{up} = 1$ and different values of a_{pr}. (c) Colormap of the same fractal in (a), updated $n_{up} = 5$ times. (d) RIN calculations of $g'(T)$ (dashed lines) and $g''(T)$ (dotted lines) for $a_{pr} = 0.4$ and different values of n_{up}. All the calculated quantities are made at frequency $\omega = 2\,\mathrm{GHz}$.

that in the $2 - 2$ case the saturating value $g''(0)$ increases more gradually with n_{up} with respect to the $10 - 7$ case. The boost given to $g''(T)$ from the new proximized bond is relatively greater at $n_{up} = 2$ in the latter: looking at the light blue curves with respect to the red ones for $T \to 0$, $g''_{n_{up}=2}/g''_{n_{up}=1} \lesssim 5$ in the $10 - 7$ while $g''_{n_{up}=2}/g''_{n_{up}=1} \sim 3.5$ in the $2 - 2$. Concerning instead the absolute values of $g''(0)$, they are higher in the former case, where the enlarging of the fractal covers almost all the sheet, as it is clear observing the printed configurations for $n_{up} = 5$, $a_{pr} = 0.4$ in panels c of both figures.

Before drawing any conclusion, let us state that so far all the calculations within the exact solution of the RIN model were calculated with tunable but yet constant local inductances, so the conductivity is a simple result of the percolation of the network, as it was the resistivity in the RRN. In principle, however, one can expect that at a microscopic scale the inductance of each bond has its own local
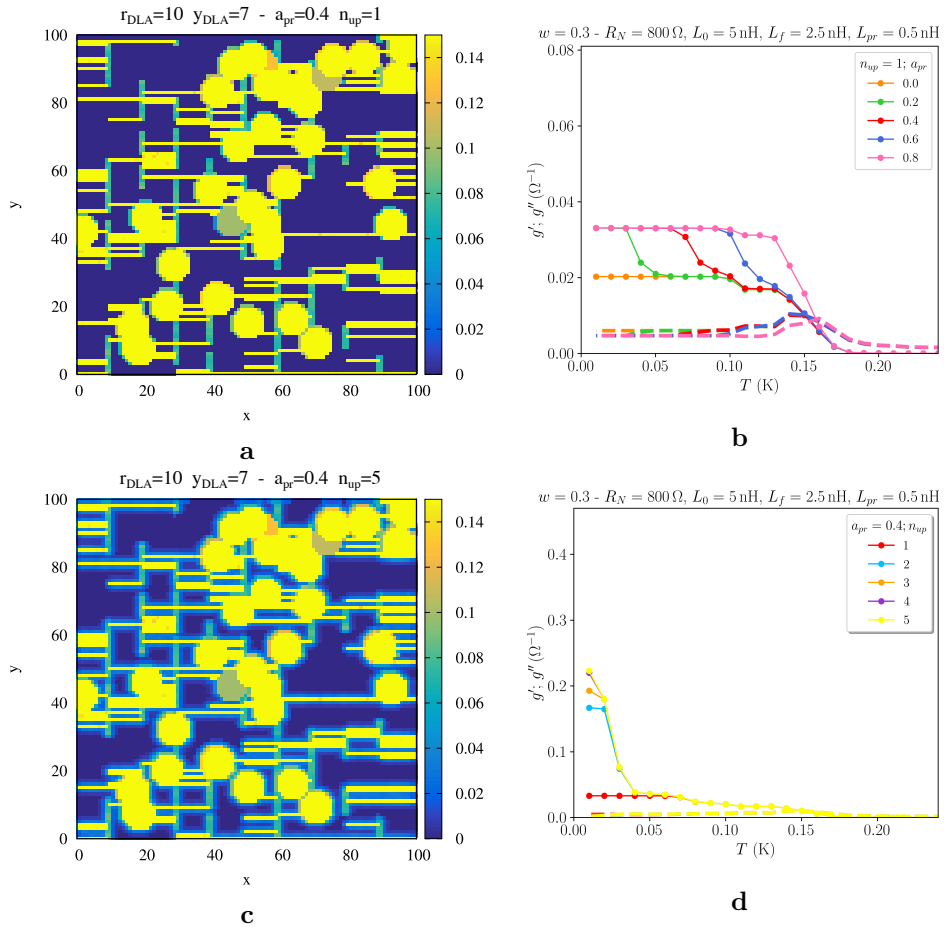
Figure 4.16. (a) Color map of the local critical temperatures in a 100×100 $10 - 7$ fractal with $r_{pd} = 5$ and proximization parameters $a_{pr} = 0.4$ and $n_{up} = 1$. (b) Corresponding RIN calculations of $g'(T)$ (dashed lines) and $g''(T)$ (dotted lines) for $n_{up} = 1$ and different values of a_{pr}. (c) Colormap of the same fractal in (a), updated $n_{up} = 5$ times. (d) RIN calculations of $g'(T)$ (dashed lines) and $g''(T)$ (dotted lines) for $a_{pr} = 0.4$ and different values of n_{up}. All the calculated quantities are made at frequency $\omega = 2\,\mathrm{GHz}$.

temperature dependence.One can thus exploit some physical relation, obtaining smoother curves with respect to those found with constant L_i. Referring to previous works where Josephson junction physics was considered, as in Refs. [17, 24], we can thus use the Ambegaokar-Baratoff formula, developed for Josephson junctions with a constriction [35]. Using the approximate formula for the temperature dependence of the gap

$$G(\tau) = \left(1 - \frac{\tau^4}{3}\right)\sqrt{1 - \tau^4}, \qquad \frac{\Delta(0)}{k_B T_c} \simeq 1.76 \tag{4.28}$$

and the fact that $J_s \propto L$, the temperature dependence of the local inductance can be written as

$$L_i(T) = L_i G(\tau) \tanh\left(\frac{1.76\, G(\tau)}{2\,\tau}\right). \tag{4.29}$$

4.3.4 Concluding remarks

In summary, we showed in this Chapter how new unexpected transport features can arise from filamentary superconductivity. In spite of the phenomenological approach to this topic, we can successfully interpret the very peculiar trends observed in LAO/STO. In particular, the starting idea was the one of a proximization process occurring at temperatures lower than the critical one. In the context of EMT this idea was implemented in terms of a second superconducting fraction, tunable by means of its distribution of local critical temperatures, giving us some major insights about the problem. While addressing the exact solution, geometry really plays a crucial role, the proximization process being modeled as an enlargement of the superconducting backbone. Indeed, a more sparse fractal produces longer tails in the superfluid stiffness and the sudden rise due to proximization is more pronounced in denser structures. Furthermore, a less compact cluster allows us to consider networks with a higher fraction of metallic residue, needed in order to explain the saturation values of the optical conductances at various voltages.

In Fig. 4.17 we show the calculations of resistivity (green), superfluid stiffness (red) and optical conductivity (black) for the two considered fractals, where all the other parameters are kept to be the same, the proximization constants being set to $n_{up} = 1$ and $a_{pr} = 0.6$ and temperature dependent local inductances following Eq. (4.29). The tailish behavior of $g''(T)$, smoothened even further by the temperature dependence, can be observed in both cases whereas at lower temperatures the difference between the two namely cases is really appreciable.

The residual conductivity is a little bit higher in panel b, albeit one can argue that its absolute value is still too low. One possibility to increase it might be to account for finite frequency dissipative effects also in the exact solution of the RIN model, that were instead considered and studied here only in the EMT approximation and only in the imaginary part of the conductivity. As we pointed out, those effects needed that $\omega\tau$ is low but not negligible in order to have noticeable effects. However, once filamentary superconductivity is observed, the presence of dissipative vortices in the lattice remains an open issue to be addressed, both theoretically and experimentally.
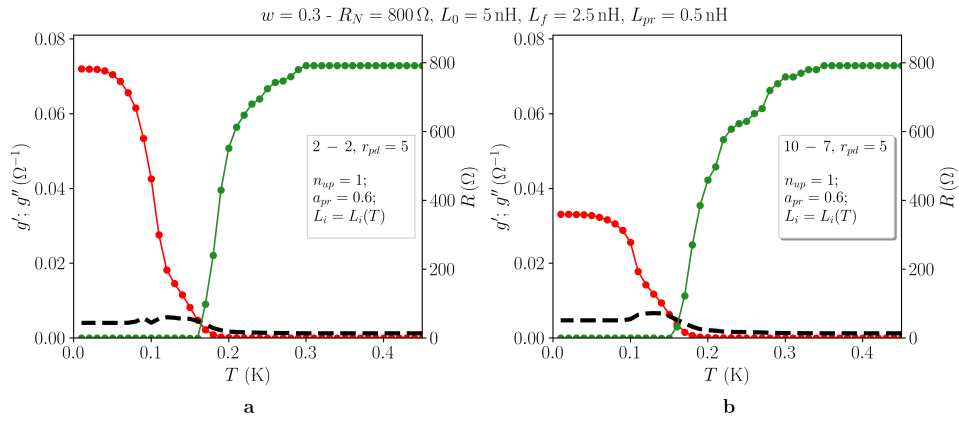
Figure 4.17. Comparison between the resistivity (green), real (black) and imaginary (red) parts of the conductivity calculated with the RIN model for the $2-2$ fractal (a) and the $10-7$ fractal (b) configurations in Fig. 4.14, with superpuddles of radius $r_{pd} = 5$ superimposed until the fraction $w = 0.3$ of superconducting bonds is reached. The local inductances follow the relation in Eq. (4.29), the bare values being $L_0 = 5\,\text{nH}$, $L_f = 2.5\,\text{nH}$ and $L_{pr} = 0.5\,\text{nH}$ and the proximization parameters are $a_{pr} = 0.6$ for $n_{up} = 1$ update of the network.

Chapter 5

Filamentarity arising from CO-SC competition

"Your ancestors called it magic, but you call it science. I come from a land where they are one and the same."

Thor Odinson, Thor, film 2011

In the former Chapter the presence of filamentary superconductivity was assumed from the observation of transport measurements in $LaAlO_3/SrTiO_3$ interfaces and "imposed" as an initial condition in the RIN model. We treat in this Chapter instead the problem of its origin in the context of cuprates.

As it was stated in Section 2.2, filamentary superconductivity can appear sometimes as a result of competing orders. In cuprates, as in the case of many iron-based superconductors, hints of filamentary superconductivity can be observed in some regions of the phase diagram. In the case of cuprates, where the presence of CO and charge density fluctuations pervades a good part of the diagram, the tendency of electrons to condensate in real space or in momentum space can explain the so-called *stripe* region, characterized by the presence of a *pseudo-gap* [29, 31, 32].

In this Chapter we will study this competition by means of the anisotropic Heisenberg model in random field, similar to the model explained in Section 2.2.4. The final goal is to study the behavior in temperature of transport measurements, such as the superfluid stiffness J_s and the fraction of CO given by the magnetization m_z. At a coarse grained level, the CDW and superconducting order parameters will be encoded in the SO(3) symmetry of the pseudospins $\mathbf{s}_i$, where the up and down states represent two different CDW variants and the in-plane state is instead the superconducting state. The complete Hamiltonian we will study will be the following:

$$H = \underbrace{-J \sum_{<i,j>} s_i^{xy} \cdot s_j^{xy}}_{H_{XY}} \underbrace{-\alpha J \sum_{<i,j>} s_i^z s_j^z}_{\alpha H_z} + \underbrace{+b \sum_i 8(s_i^z)^2 \left(1 - (s_i^z)^2\right)}_{b\,H_b:\text{ effective CO-SC barrier}} + \underbrace{\frac{w}{2} \sum_i h_i s_i^z}_{\text{random field}} \quad (5.1)$$

where the indices i and j runs over the two-dimensional square lattice of linear size L

and lattice spacing set to 1 and $< i, j >$ indicates nearest neighbors sites. Here s_i^{xy} is the projection of $\mathbf{s}_i$ on the xy-plane and H_{XY} formally coincides with the XY model Hamiltonian described in Chapter 1, with the important difference that out-of-plane fluctuations are here allowed; H_Z is instead the Ising-like component tuned by the parameter α. The in-plane s_i^{xy} component of the pseudospin represents then the superconducting state, while the out-of-plane encodes for two CDW variants. The parameter α will play a similar role as the single ion anisotropy used in Refs. [31, 32]. The out-of-plane random field term will mimic the impurities in a real system, h_i being statistical independent quenched random variables with a flat probability distribution between -1 and $+1$. The effective CO-SC barrier term H_b is necessary in order to break the pathological supersymmetry of the negative-U Hubbard model, in which CDW and SC are degenerate also to an infinite number of intermediate "supersolid" phases, represented by all other pseudospin directions. In general there is no general symmetry of nature that enforces that degeneracy therefore one would expect that in a generic model supersolid phases have a different energy. The effective barrier potential H_b, whose amplitude is tuned by the parameter b, will be necessary to break the degeneracy.

The parameter α will be the main control parameter tuning the two main phases, represented in experiments by the magnetic field H (see Fig. 2.16 Section 2.2.3). Indeed, the bare anisotropic Heisenberg model displays a superconducting BKT transition for $\alpha < 1$ while the Ising transition encoding the CDW phase is found when $\alpha > 1$.

We will build up the model one step at a time, studying the behavior of the system in temperature via Monte Carlo simulations.

In Section 5.1 we will introduce the reader to Monte Carlo simulations and describe how we implemented our code. In Section 5.2 we will define and summarize the main thermodynamic quantities we will be referring to during the Chapter. Thus, we can start to build our model. The bare anisotropic Heisenberg model $H = H_{XY} + \alpha H_Z$ will be our benchmark: in Section 5.3 we will describe its main features and its phase diagram, relying on previous results found in literature as a reference [117–119]. We will refer sometimes to the anisotropic Heisenberg model as a XXZ model, as it is often used in literature.

Once the benchmark will be set, we will start to trigger the ground state of our model, studying in Section 5.4 the clean XXZ model with the barrier term potential: $H = H_{XY} + \alpha H_Z + bH_b$.

Finally, we will address in Section 5.5 the complete model for the CO-SC competition.

5.1 Monte Carlo simulations

In order to study the physical quantities related to the effective Hamiltonian in Eq. (5.1) as functions of the temperature, we will perform Monte Carlo (MC) simulations on a two-dimensional square lattice of linear size L with periodic boundary conditions. MC simulations are indeed a powerful and very versatile tool, largely used in statistical mechanics, to achieve thermodynamic equilibrium without the need of sampling all the phase space, when an analytical solution of the problem is not

possible.

The basic principles on which it is based are the ergodicity and detailed balance, used in order to construct a Markov chain whose purpose is to achieve thermalisation in the smallest possible number of iterations. On the one hand, ergodicity requires the accessibility of any configuration with non-zero Boltzmann weight to any configuration with non-zero Boltzmann weight. This assures that the system can reach its ground state independently of the initial conditions. On the other hand, the detailed balance principle, stating the equivalence between each elementary process and its reverse, prevents the simulation from being trapped in a limit cycle.

Metropolis algorithm

There are many ways to implement MC simulations and the particular choice of the algorithm depends on the system under consideration, to ensure the fastest thermalization possible. In order to sample the correct canonical distribution, in our simulations we used a Metropolis algorithm. To be pedantic, we will call the two zenital and azimuthal angles of the i-th pseudo-spin respectively

$$\theta \in [0, 2\pi), \qquad \varphi \in [-\pi, +\pi]$$

such as the coordinates are then

$$\begin{cases} s_i^x = \cos\theta_i \sin\varphi_i \\ s_i^y = \sin\theta_i \sin\varphi_i \\ s_i^z = \cos\varphi_i. \end{cases} \tag{5.2}$$

Each Metropolis step consist in the update of all $L^2 = N$ pseudospins of the lattice. The new pseudospin s_i' is updated in the following way

$$\begin{cases} \theta_i' = \theta_i + \delta\theta, \qquad \delta\theta \in [-\frac{\pi}{4}, +\frac{\pi}{4}] \\ \cos(\varphi_i') \in [-1, 1] \end{cases}$$

and the new configuration is unconditionally accepted if it lowers the energy of the system $\Delta E_i = E^{new} - E^{old} < 0$, otherwise it is accepted with the canonical probability $e^{-\beta \Delta E_i}$, where $\beta = 1/(k_B T)$ is the usual inverse temperature. In the following, we will work in units of measure such that $k_B = 1$, as it is customary in such studies.

The lattice can be updated spanning all the pseudospins sequentially or randomly. This choice is in general almost irrelevant in terms of computational times. One of the few exceptions in which a small bias can be introduced by spanning the lattice sequentially is when the spatial correlation functions are under exam. We performed the simulations updating the system in order until we encountered the spin-spin correlation function $C^{zz}(r) \sim < s_i^z s_{i+r}^z >$ in Section 5.5. In that case, we had to change the protocol in the Metropolis iteration. Instead of updating each and every pseudospin sequentially, we extract randomly and update N pseudospins at each Metropolis step.

Furthermore, we have used the Simulated Annealing algorithm to favor the thermalisation of the system during its temperature evolution. Indeed, lowering

the temperature, the free energy landscape (especially in the presence of disorder) can develop several local minima corresponding to different metastable states. The Simulated Annealing procedure is one of the most used algorithms to prevent the system to be trapped in a local metastable minimum. This process consist in giving as initial state to a lower temperature the final state of the higher one: in the highest temperature considered the system is let evolve from an initial configuration of random spins, until it reaches its equilibrium state, then the temperature is slightly decreased and a new thermalization starts from the final configuration of the previous one. This process is iterated until the lowest temperature of interest is achieved.

Overrelaxation

In Section 5.3, in order to speed up the thermalization time, the Metropolis algorithm will be accompanied by the Overrelaxation method, which consists in microcanonical steps, needed to better explore the phase space of configurations without changing the energy of the system. In other words, if the Hamiltonian can be written as

$$H = \sum_i \mathbf{s}_i \cdot \mathcal{H}_i \qquad (5.3)$$

where $\mathcal{H}_i$ is the local field acting on $\mathbf{s}_i$ produced by all the other pseudospins, the new pseudospin is calculated such that $\mathbf{s}_i{}' \cdot \mathcal{H}_i = \mathbf{s}_i \cdot \mathcal{H}_i$. Hence:

$$\mathbf{s}_i{}' = -\mathbf{s}_i + 2\frac{\mathbf{s}_i \cdot \mathcal{H}_i}{|\mathcal{H}_i|^2}\mathcal{H}_i. \qquad (5.4)$$

In a two-dimensional pseudospin symmetry, i.e., the XY model, $\mathbf{s}_i{}'$ is univocally defined as the mirrored vector in the XY plane of $\mathbf{s}_i$ with respect to $\mathcal{H}_i$. Instead, in the case where the pseudospin has three dimensions, there is a whole cone around $\mathcal{H}_i$ that assures a constant scalar product. We will thus consider as symmetry plane the one orthogonal to the plane containing $\mathcal{H}_i$ and $\mathbf{s}_i$.

In the bare XXZ model both Metropolis and Overrelaxation procedures will be used. Once the barrier term H_b in Eq. (5.1) will be introduced, the Hamiltonian will be no longer of the form in Eq. (5.3), thus only Metropolis iterations will be used in the MC simulations.

5.2 Thermodynamic observables

In the following Sections, where we will study the anisotropic Heisenberg model, adding then the barrier term and a random field, we will address two main phase transitions, namely the BKT topological phase transition and the ferromagnetic second order transition. For the sake of definiteness, we point out here that the ferromagnetic transition we refer to is analogous to the transition of the two-dimensional Ising model, with the sudden emergence of a magnetization in the out-of-plane direction, since no ferromagnetic transition can occur in-plane. Let us summarize here all the thermodynamic quantities we will focus on hereafter, that will be necessary in our study.

Starting with the more trivial ones, having called $N = L^2$ the total number of sites, the average density of energy is simply

$$\langle e \rangle = \frac{\langle E \rangle}{N} \tag{5.5}$$

where E is the energy calculated on the single pseudospin configuration and $\langle \bullet \rangle$ refers to the thermal average, i.e., the average over different configurations sampled within the MC simulations. The specific heat is therefore

$$C_V = \frac{N}{T^2}(\langle e^2 \rangle - \langle e \rangle^2). \tag{5.6}$$

We will refer to the magnetization along the ν axes ($\nu = x, y, z$) as

$$m_\nu = \frac{1}{N}\sum_i s_i^\nu \tag{5.7}$$

whereas the susceptibility will always be defined as

$$\chi^{\nu\nu} = N \langle m_\nu^2 \rangle. \tag{5.8}$$

and we will refer to the in-plane susceptibility as $(\chi^{xx} + \chi^{yy})/2$.

We point out for sake of definiteness that in the ferromagnetic transition the ground state is doubly degenerate, meaning that the free energy has two equivalent minima centered in the two configurations corresponding to all pseudospins up ($s_z^i = 1$, $\varphi_i = 0$) and all pseudospins down ($s_z^i = -1$, $\varphi_i = \pi$). Numerically, this can lead to the so-called spin flips, particularly in small systems. As a matter of fact, a finite size system, whose pseudospins are aligned in one of the two directions, has a finite probability to flip to the opposite state due to thermal fluctuations. This means that the global magnetization of the system can change sign during a simulation run, maintaining coherent its modulus. For this reason, it will be more convenient in Ising-like models, as it is often, to observe the absolute value of the out-of-plane magnetization $|\langle m_z \rangle|$, instead of $\langle m_z \rangle$.

Moreover, the out-of-plane magnetization defines only theoretically T_c^{CO} as the temperature at which $\langle m_z \rangle$ becomes finite. In numerical simulations, in fact, magnetization, as many other quantities, is sensitive to finite size effects. Thus, another important physical quantity in Heisenberg models is the fourth moment of the pseudospin distribution function. In particular, the Binder cumulant defined as

$$U_L = 1 - \frac{\langle m_z^4 \rangle}{3\langle m_z^2 \rangle^2} \tag{5.9}$$

is a very useful parameter to detect the critical temperature of a transition, in particular for Ising-like models [120–122]. In the thermodynamic limit $L \to \infty$, its value is supposed to go to zero $U_L \to 0$ at high temperatures $T \to \infty$, while $U_L \to 2/3$ in the ordered phase $T \to 0$. The critical temperature T_c^{CO} can be identified as the crossing point temperature where different curves $U_L(T)$ at different sizes L meet. The advantage of this procedure is to be detached from any bias that can be introduced by fitting functions or by *a priori* scaling hypothesis and, at

the same time, U_L depends only on quantities that are directly measurable in the numerical simulation. Henceforth, the Binder cumulant will be used to define the Ising critical temperature T_c^{CO} corresponding to the charge ordered phase.

Concerning instead the BKT superconducting transition, one of the key thermodynamic quantities in this context is the superfluid stiffness J_s, which is by definition the variation of free energy with respect to a phase twist (of the in-plane phase θ):

$$J_s = -\frac{1}{\beta} \frac{\partial^2 \ln Z(\delta\theta)}{\partial \delta\theta^2}\Big|_{\delta\theta=0} \tag{5.10}$$

where $Z = \int \prod d\theta_i d\varphi_i \exp(-\beta H(\delta\theta, \varphi))$ is the canonical partition function of the superconducting system and $\delta\theta$ is the stretching of the relative phase $(\theta_i - \theta_j)$ in the direction x of the torsion and β is the inverse temperature. Neglecting the terms independent on the in-plane phase θ, the XY term of the total Hamiltonian presented in Eq. (5.1)

$$H(\delta\theta) = H_{XY}(\delta\theta) = -J \sum_{<i,j>} (s_i^x s_j^x + s_i^y s_j^y) =$$

$$= -J \sum_{<i,j>} (\sin\varphi_i \sin\varphi_j \cos(\theta_i - \theta_j + \delta\theta) + \sin\varphi_i \sin\varphi_j \cos(\theta_i - \theta_j)). \tag{5.11}$$

The second derivative of (5.10) gives a diamagnetic and a paramagnetic term:

$$J_s = J_d - J_p \tag{5.12}$$

$$J_d = \frac{J}{L^2} \langle \sum_i \sin\varphi_i \sin\varphi_{i+x} \cos(\theta_i - \theta_{i+x}) \rangle \tag{5.13}$$

$$J_p = \frac{\beta J}{L^2} \langle \left(\sum_i \sin\varphi_i \sin\varphi_{i+x} \sin(\theta_i - \theta_{i+x}) \right)^2 \rangle \tag{5.14}$$

As already stated in Section 1.2, the main signature of a BKT transition occurring is the jump of the superfluid stiffness. In Section 1.4, we stated that the universal BKT jump happens at the intersection with the critical line:

$$J_s(T_{BKT}) = \frac{2T_{BKT}}{\pi}.$$

It is worth noting that in literature, the superfluid stiffness is also referred to the Helicity modulus Υ and it is sometimes calculated from a real twist of the phase, obtained performing the simulations both with periodic and antiperiodic boundary conditions: for instance, in Refs [119, 123] the helicity modulus in calculated by integrating

$$\frac{1}{2} \frac{d(\beta\Upsilon)}{d\beta} = \frac{U_a - U_p}{\pi^2} = \frac{dU}{\pi^2}, \tag{5.15}$$

where $U_{a,p}$ are the internal energies of the system with anti-periodic and periodic boundary conditions. The minimum of $d\Upsilon/dT$ is supposed to be consistent, in the limit of large size, with the intersection and crossing point of $\Upsilon(L,T)$ with the critical line $2T/\pi$, defining the BKT transition.

However, along our study we will follow another method to determine the BKT critical temperature T_{BKT}, exploiting the definition of the superfluid stiffness given in Eq. (5.14), which is independent of the use of boundary conditions. Since in the context of simulations it is clearly impossible to reach the thermodynamic limit and the system remains finite, let us here derive the scaling relation we will use to address and define the BKT superconducting state, referring the reader to Refs. [124] for more details.

Starting from the solution of the RG equations discussed in Section 1.4, we can rewrite Eq. (1.43) as

$$x = \frac{1}{\ell + c} \tag{5.16}$$

where we recall that $x = \pi J_s/T - 2$ and $c = x_0^{-1}$ is a constant determined from the initial conditions of the RG flow $x(\ell_0)$ and $\ell = \ln(L/a)$, a being the lattice spacing. At the critical point $x = x(L, T = T_{BKT})$ and we can substitute the definition of x in the former, obtaining:

$$J_s(L, T_{BKT})\frac{\pi}{2T_{BKT}} = 1 + \frac{1}{2\ln(L) + c} = 1 + \frac{1}{2\ln(L/L_0)} \tag{5.17}$$

Finally, recalling the universal relation $J_s(\infty, T_{BKT}) = 2T_{BKT}/\pi$ we obtain:

$$J_s(\infty, T) = \frac{J_s(L, T)}{(1 + (2\ln(L/L_0))^{-1})} \tag{5.18}$$

Once the curves of superfluid stiffness for finite systems and different linear sizes L are rescaled with the former, they will all assume the same value at criticality. Henceforth, the crossing point of all the superfluid stiffness curves can be used to determine the critical temperature of the transition in the limit of infinite size. With this purpose, from the superfluid stiffness numerical data, we search for the value of the parameter L_0 giving the best crossing point at finite temperature, obtaining a quite accurate estimate for T_{BKT}.

Obviously, there are still other ways to extrapolate the critical temperature from a BKT system, starting for instance from the critical exponents. We mention the most relevant ones here, for the sake of completeness.

Approaching the transition from above, i.e., $T \to T_{BKT}^+$, the in-plane susceptibility χ and the correlation length ξ both diverge exponentially as:

$$\chi \sim e^{1/\sqrt{b_\chi(T - T_{BKT})}} \tag{5.19}$$

$$\xi \sim e^{1/\sqrt{b_\xi(T - T_{BKT})}} \tag{5.20}$$

and remain infinite at $T < T_{BKT}$.

On the other hand, we already mentioned in Section 1.2 that one of the peculiarities of the BKT transition relies in the spatial correlation between the in-plane pseudospin components, which is exponentially suppressed above the transition but power law diverging below:

$$< s_i^x s_{i+r}^x + s_i^y s_{i+r}^y > \sim e^{-r/\xi} \qquad T > T_{BKT} \tag{5.21}$$

$$< s_i^x s_{i+r}^x + s_i^y s_{i+r}^y > \sim \frac{1}{r^\eta} \qquad T \leq T_{BKT} \tag{5.22}$$

While in fact in usual Heisenberg systems the phase transition is explicitly announced by the appearing of a finite order parameter, i.e., the magnetization, defining the presence of a long range order, in two dimensions the in-plane magnetization is always zero and transition is led by the proliferation of free vortices, that can be tracked from the change of behavior of the spin-spin correlation function. The critical exponent η, which assumes the value $\eta = 1/4$ at criticality $T = T_{BKT}$, can be connected with the correlation length and the in-plane susceptibility and the correlation length:

$$2 - \eta(T_{BKT}) = \frac{b_\chi}{b_\xi}. \tag{5.23}$$

5.3   The anisotropic Heisenberg model

Let us build our model for competition presented in Eq. (5.1) one step at a time, starting from the anisotropic Heisenberg model. We consider a two-dimensional square lattice with periodic boundary conditions of three-dimensional spins, parametrized as in Eq. (5.2). The Hamiltonian is

$$H = H_{XY} + \alpha H_z = -J \sum_{<i,j>} (s_i^x s_j^x + s_i^y s_j^y) - \alpha J \sum_{<i,j>} s_i^z s_j^z \tag{5.24}$$

where $\sum_{<i,j>}$ indicates the sum over neighboring site indices i and j. Let us also set from now on the ferromagnetic interactions to be $J = 1$. The key parameter here is α. Indeed, for $\alpha < 1$ the ground state of the system will be represented by a configuration in which all the pseudospins are in plane ($\varphi_i = 0$), belonging to the BKT universality class, with the continuous global symmetry U(1). In this case, however, the reader will note that the limit case $\alpha = 0$, often referred to as the XX0 model, is not equivalent to an XY model: while in fact the Hamiltonian is formally the same, in the former the pseudospins are free to rotate in all the three dimensions increasing the entropic term of the free energy with a consequent suppression of the critical temperature.

When instead $\alpha > 1$ the ground state will be the one with all the pseudospins parallel in the out-of-plane direction, with the double degeneracy up or down.

Finally, we recall that the limit case $\alpha = 1$ exactly corresponds to the isotropic Heisenberg model, in which no long-range order is possible, according to the Mermin-Wagner theorem [8], and no topological phase transition is present.

Approaching the isotropic limit from below, a useful formula for $T_{BKT}(\alpha)$ was calculated by Menezes et al. in [125] in the mean field approximation:

$$T_{BKT}(\alpha) = \frac{2J}{e + I(\alpha)}. \tag{5.25}$$

Here $I(\alpha)$ is an integral defined as

$$I(\alpha) = \frac{1}{(2\pi)^2} \int_{-\pi}^{\pi} d^2\mathbf{k} \frac{1}{1 - \alpha\gamma_k} \tag{5.26}$$

$$\gamma_q = \frac{1}{2}(\cos(q_x) + \cos(q_y)) \tag{5.27}$$

and the spin stiffness J_s was computed as the solution of the following self-consistent equation:

$$J_s = \left[1 - \frac{T}{2J}I(\alpha)\right]\exp\left(-\frac{T}{2JJ_s}\right). \tag{5.28}$$

Eq. (5.25) reduces to

$$T_{BKT}(\alpha) \to \frac{2\pi J}{A + \ln(1-\alpha)^{-1}}. \tag{5.29}$$

in the isotropic limit $\alpha \to 1$, stating that T_{BKT} vanishes logarithmically in the isotropic limit. The logarithmic behavior is however difficult to reproduce with numerical analysis without a significant computational effort, which was beyond the scope of this work. Nevertheless, the result by Menezes et al. in Eq. 5.25 was found in the mean field approximation thus its comparison with numerical simulations can only be generic and concern the orders of magnitude involved.

Instead, we compared our results of the XXZ model for $\alpha < 1$ with the results of Refs. [117–119].

In particular, we can affirm that the in-plane and out-of-plane susceptibilities and the specific heat are in perfect agreement with the simulations performed in [117, 118]. We considered thermal averages over 10^5 MC configurations, after discarding a transient of 10^4 MC steps, where each MC step is a combination of $t_M = 2$ Metropolis iterations and $t_{OR} = 4$ Overrelaxation steps. Fig. 5.1 shows the in-plane susceptibility $(\chi^{xx} + \chi^{yy})/2$ of the $\alpha = 0$, 0.5 cases, where our calculations and the ones by Cuccoli et al. [118] are superimposed.
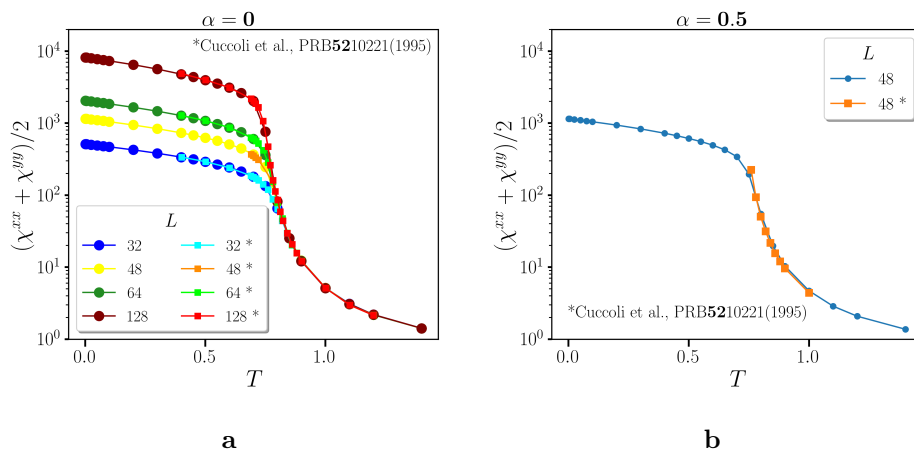

Figure 5.1. Comparison of the in-plane susceptibility $(\chi^{xx} + \chi^{yy})/2 = (N\langle m_x^2\rangle + N\langle m_y^2\rangle)/2$ (dots) with the calculations of Cuccoli et al. in Ref. [118] (squares). (a) Results of the XX0 model ($\alpha = 0$) for different linear size ($L = 32, 48, 64, 128$) (b) Results for the XXZ model with anisotropy parameter $\alpha = 0.5$ in a $L = 48$ size lattice. The thermal averages are made over 10^5 MC configurations, after discarding a transient of 10^4 MC steps, where each MC step is a combination of $t_M = 2$ Metropolis iterations and $t_{OR} = 4$ Overrelaxation steps.

The out-of-plane susceptibility is instead shown in Fig. 5.2 for values of the anisotropy parameter $\alpha = 0$, 0.5, 0.95, 0.99. As one can see, the calculations for $\alpha = 0$ and $\alpha = 0.5$ show a very low response in the $z-$direction, monotonically decreasing

and apparently independent of the size L of the system. Instead, approaching the isotropic limit $\alpha = 0.95$, 0.99 a peak appears in correspondence to the critical temperature of the system.
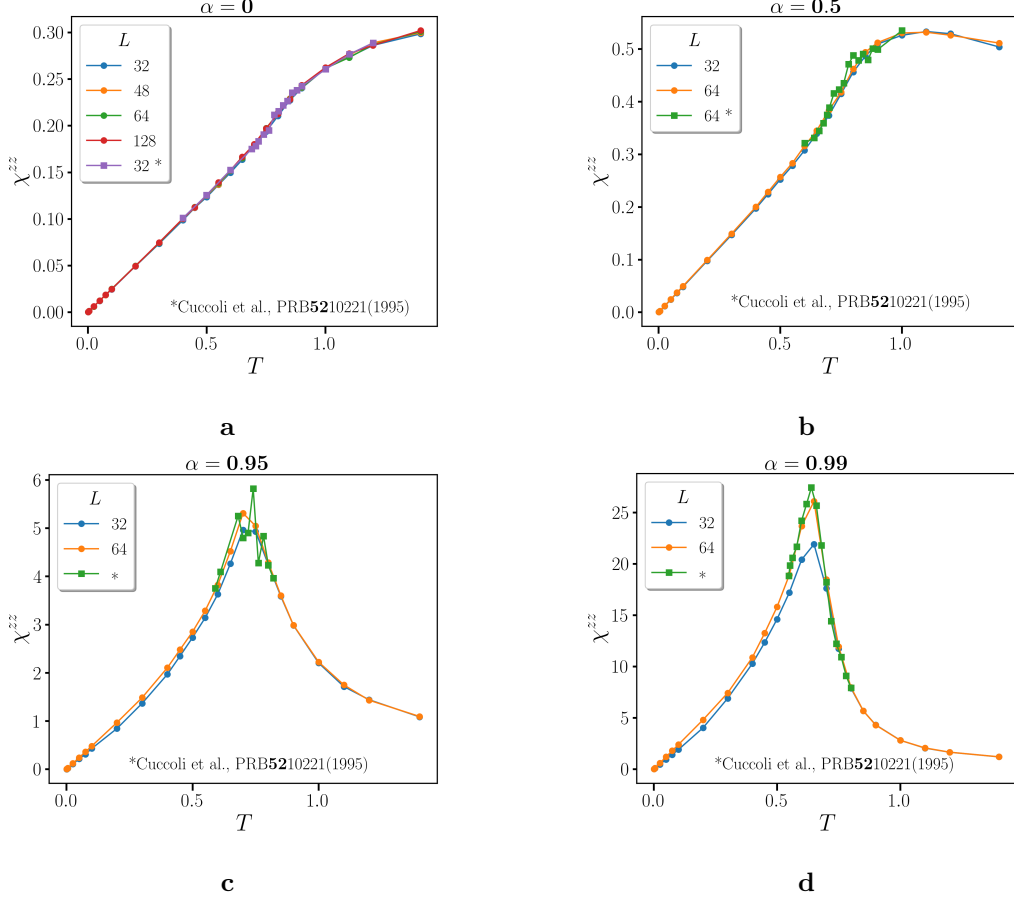

a   **b**

c   **d**

Figure 5.2. Comparison of the out-of-plane susceptibility $\chi^{zz} = N\langle m_z^2\rangle$ (dots) with the calculations of Cuccoli et al. in Ref. [117] (squares) for the XXZ model at various anisotropies values. (a) Results for $\alpha = 0$ ($L = 32, 48, 64, 128$) (b) $\alpha = 0.5$ ($L = 32, 64$) (c) $\alpha = 0.95$ ($L = 32, 64$) and (d) $\alpha = 0.99$ ($L = 32, 64$) . As before, the thermal averages are made over 10^5 MC configurations, after discarding a transient of 10^4 MC steps, where each MC step is a combination of $t_M = 2$ Metropolis iterations and $t_{OR} = 4$ Overrelaxation steps.

The specific heat C_V presented in Fig. 5.3 presents a peak for all values of α considered, right above the critical temperature. In Refs. [117] and [118], the authors highlight that $C_V(T)$ displays a maximum at a temperature about 10% higher than the T_{BKT} they calculate. Note that the values of T_{BKT} we calculated are consistent with theirs, at least in a confidence range of order 1% to 5% (see below in Fig. 5.4a).

Finally, we show the phase diagram in Fig. 5.4, where in panel a we specifically compare the BKT critical temperatures we deduced with the values found in literature. Although the comparison shows a general consistency of the data computed, this consistency may seem a little stretched, particularly if we compare our results (green dots) with the ones from Lee et al. [119] (orange squares). It is worth noting,
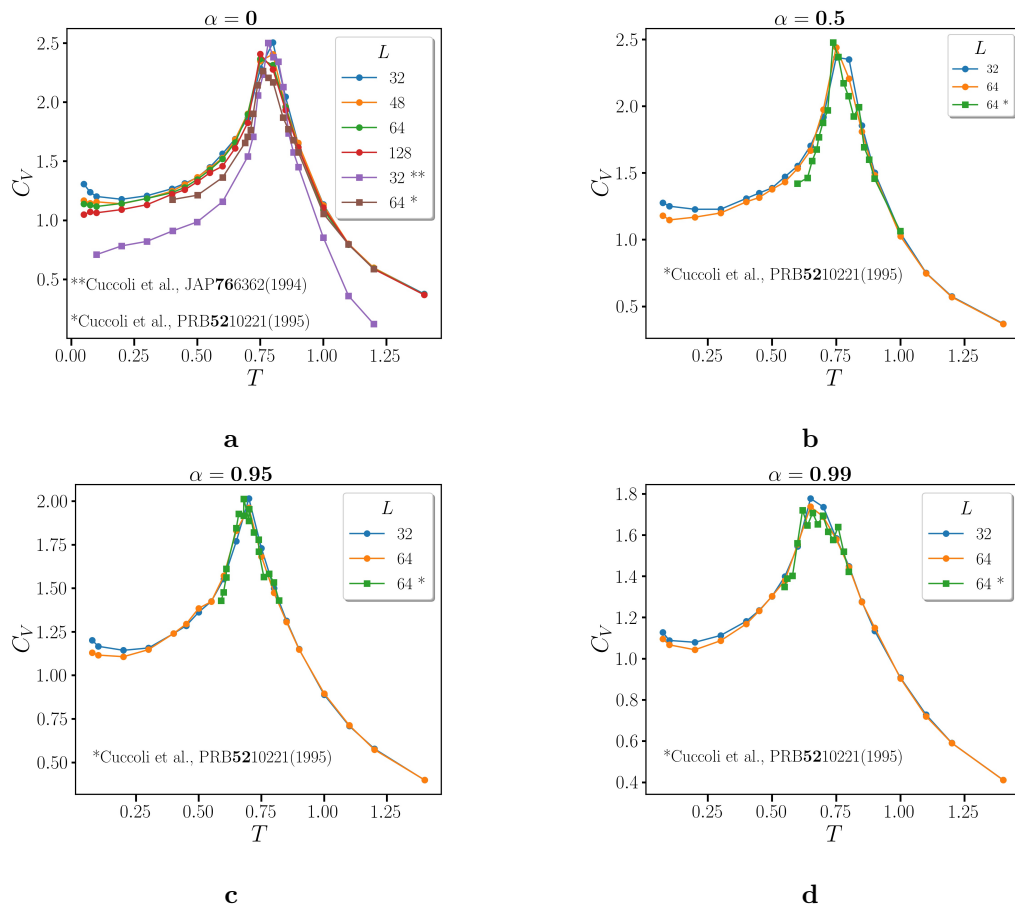
Figure 5.3. Specific heat $C_V = N(\langle e^2 \rangle - \langle e \rangle^2)/T^2$ at different values of the anisotropy and for different values of the linear size L as indicated in legends. Results for (a) $\alpha = 0$, (b) $\alpha = 0.5$, (c) $\alpha = 0.95$, (d) $\alpha = 0.99$ Our simulations are compared with the ones from [117] and [118]. Thermal averages made over 10^5 MC configurations, after discarding a transient of 10^4 MC steps, where each MC step is a combination of $t_M = 2$ Metropolis iterations and $t_{OR} = 4$ Overrelaxation steps.

however, that the main bias introduced is the protocol adopted to define the critical temperature. As a matter of fact, all the computations of in-plane and out-of-plane susceptibilities and specific heat were perfectly in agreement.In their papers, Cuccoli et al. [117, 118] deduce the critical temperatures from the fits of simulation data using Eq. (5.19) and Eq. (5.20), which are both exponentially divergent quantities in the thermodynamic limit and hence more sensitive to finite size effects. Instead, the advantage of the scaling relation for J_s used here to compute T_{BKT} for $\alpha < 1$ works well already at small sizes, as it happens with the Binder cumulant U_L, adopted to address the ferromagnetic transition observed for $\alpha > 1$.

Finally, let us present the results of our computations from which we extrapolated the complete phase diagram presented in Fig. 5.4b. Here the red dots represents the BKT critical temperatures T_{BKT} obtained via the scaling relation in Eq. (5.18), while the green triangles indicates the ferromagnetic transition in the out-of-plane directions, calculated with the crossing point of the Binder cumulant U_L, defined
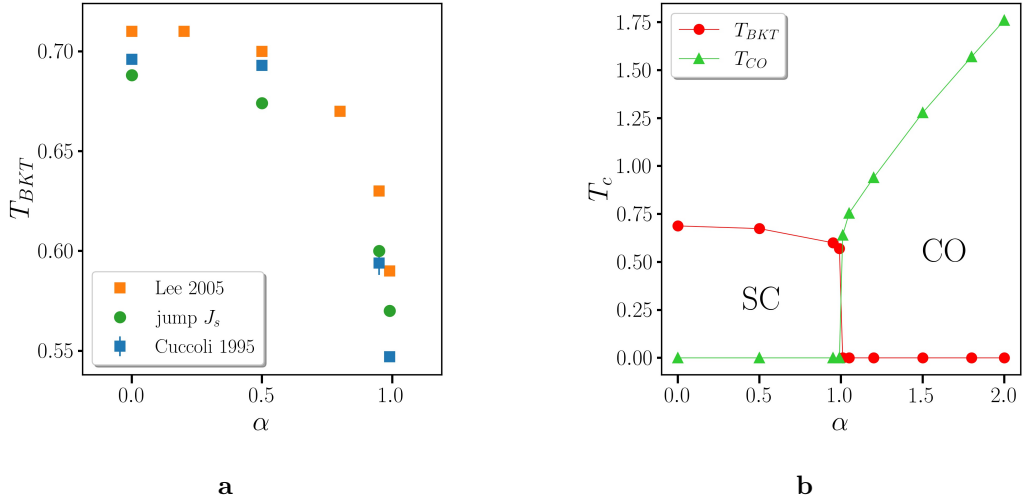
a

b

Figure 5.4. Phase diagram T_c vs α. (a) The critical temperatures T_{BKT} calculated from the jump of the superfluid stiffness J_s (green dots) are compared with some results found in literature, in particular from Ref. [119] (Lee 2005, orange squares) and from Ref. [117] (Cuccoli 1995, blue squares). (b) Full phase diagram. The red points indicates the superconducting BKT transition calculated from the BKT scaling relation in Eq. (5.18) while the green triangles represents the ferromagnetic transition extrapolated by means of the Binder cumulant in Eq. (5.9).

in Eq. (5.9), at different sizes. Note that we checked that for $\alpha \geq 1$ the superfluid stiffness was zero at all temperatures, without even displaying any size effect, whence the red points along $T_{BKT} = 0$ for $\alpha \geq 1.01$. Likewise, any out-of-plane magnetization was observed in all simulations with $\alpha \geq 0.99$. This is consistent with the fact that no phase transition is expected for $\alpha = 1$, neither BKT nor ferromagnetic.

In Fig. 5.5 the results of superfluid stiffness are shown, with and without the scaling factor $1/(1 + (2\ln(L/L_0))^{-1})$ in the two limit cases considered here, namely $\alpha = 0$ and $\alpha = 0.99$.

From Fig. 5.5a one can observe that already at small sizes of the lattice, the scaling relation is a powerful tool to extrapolate a quite accurate estimate of the BKT critical temperature, thus reducing the computational time needed. In both panels and insets the BKT critical temperature is indicated with a dashed vertical line and it is deduced as the temperature at which we found the best crossing point of the rescaled J_s and the critical line $2T/\pi$ (full black line). The BKT points are then $T_{BKT} = 0.69$ and $T_{BKT} = 0.57$ respectively for $\alpha = 0$ and $\alpha = 0.99$, with fitting parameters $L_0 = 1.4$ and $L_0 = 0.5$, as indicated in the figures. We point out that the superfluid stiffness in $\alpha = 0.99$ (Fig. 5.5b) is much more affected by finite size effects with respect to all other cases with smaller values of anisotropy. This is related to the fact that we are approaching the isotropic limit, where the critical temperature T_{BKT} is expected to go to zero logarithmically as $\alpha \to 1$, the relation presented in Eq. (5.29).

As previously stated, we did not perform simulations in the range $0.99 < \alpha < 1.01$, since it would have required more computational effort, irrelevant to the aim of our
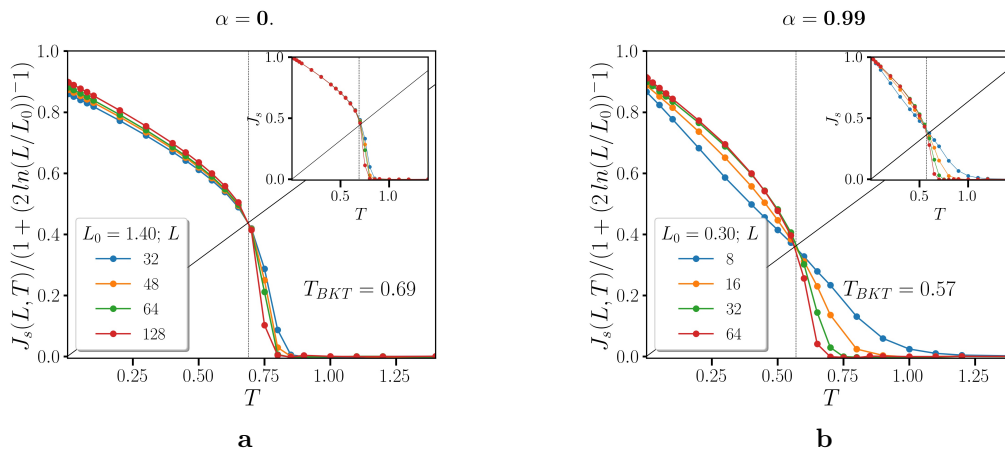
work.

Figure 5.5. Extrapolations of T_{BKT} through the crossing point of $J_s/(1 + (2\ln(L/L_0))^{-1})$ with the critical line $2T/\pi$ (full black line), using the BKT scaling relation defined in Eq. (5.18), in the two opposite cases $\alpha = 0$ (a) and $\alpha = 0.99$ (b). In the inset are shown the corresponding unscaled superfluid stiffness J_s. The BKT critical temperatures are marked with vertical dashed lines and the fitting parameters L_0 are indicated in legends. Here, each MC step is made by 2 Metropolis and 4 Overrelaxation iterations, discarding the first 10^4 steps and calculating the averages on 10^5 measurements.

Concerning the $\alpha > 1$ side of the phase diagram in Fig. 5.4b, we present in Fig. 5.6 the result of two representative cases, namely $\alpha = 1.01$ and $\alpha = 2$. The ferromagnetic transition is clearly visible from the insets of both Figs. 5.6a and 5.6b, where the absolute value of the out-of-plane magnetization is shown. As it is customary in numerical simulations of Ising models, we plot the absolute value $\langle |m_z| \rangle$ instead of $\langle m_z \rangle$ to avoid the noise that could be introduced by spin flips. The critical temperature T_c^{CO} is indicated as a vertical dashed line, deduced here from the crossing point of the Binder cumulant U_L and reported also in the inset. In particular, we found in those cases that the ferromagnetic critical temperature is $T_c^{CO} = 0.65$ for $\alpha = 1.01$, i.e., in the vicinity of the isotropic limit, and it monotonically increases up to $T_c^{CO} = 1.76$ at $\alpha = 2$.

In this Section, we studied the bar anisotropic Heisenberg model, where no extra term of the Hamiltonian was added. This was useful in order to have a first clear benchmark of the simplest case possible, to be comparable with the forthcoming results.

5.4   CO-SC barrier potential

From now on, we can start to explore less known scenarios, extending the anisotropic Heisenberg model. We add the effective barrier term in the Hamiltonian, which now reads as:

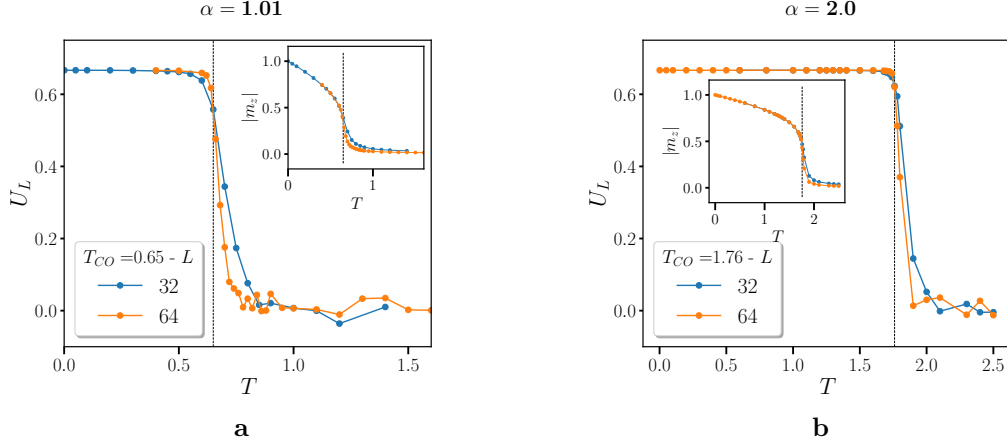$$H = H_{XY} + \alpha H_z + b H_b \tag{5.30}$$

Figure 5.6. Extrapolations of ferromagnetic critical points using the Binder cumulant $U_L = 1 - \langle m_z^4 \rangle / 3 \langle m_z^2 \rangle^2$, for $\alpha = 1.01$ (a) and for $\alpha = 2$ (b). In the inset are shown the corresponding out-of-plane magnetizations $\langle |m_z| \rangle$. The vertical dashed lines mark the critical temperature T_c^{CO} and its value is indicated in the legends. Here, each MC step is made by 2 Metropolis and 4 Overrelaxations steps iterated 5 times, discarding the first $4 \cdot 10^4$ steps and calculating the averages on $2 \cdot 10^4$ measurements.

where the barrier term H_b, already presented at the beginning of the Chapter in Eq. (5.1), is

$$H_b = \sum_i 8(s_i^z)^2 \left(1 - (s_i^z)^2\right) = \sum_i \left(1 - \cos(4\varphi_i)\right). \tag{5.31}$$

The use of powers of s_i^z instead of the $\cos(4\varphi_i)$ is just a numerical trick to accelerate the computational time, since trigonometric functions are slower in the C language in which the code is written. As already pointed out, from now on the overrelaxation procedure has no meaning since the barrier term H_b cannot be written in terms of $\sum_i \mathbf{s}_i \cdot \mathcal{H}_i$ with $\mathcal{H}_i$ independent of $\mathbf{s}_i$.

Since our aim is to trigger the CO-SC competition, we will consider the case where the tuning parameter of the barrier potential is positive $b > 0$, such that the three relevant values of the order parameter $s_i^z = 0, \pm 1$, corresponding to the in-plane and out-of-plane directions, corresponds to minima of the effective potential.

In the bare anisotropic Heisenberg model, the phase diagram presented in Fig. 5.4b can be described as composed simply by two lines, one of them indicating the ferromagnetic transition and the other one the BKT transition, both dropping to zero logarithmically approaching the isotropic limit. The former one has its non-zero values of T_c^{CO} on the right side of $\alpha = 1$, where the order parameter is the out-of-plane magnetization $\langle m_z \rangle = \frac{1}{N} \langle \sum_i s_z^i \rangle$, which can assume in its ground state the values ± 1. The region of the phase diagram $\alpha < 1$ is on the other hand a topological phase transition, lead by the proliferation of free vortices, phenomenon that can be tracked by the change of behavior of the spatial correlation function, circumventing in this way the Mermin-Wagner theorem. The free energy minimum in this case does not provide any indication about the appearance of a phase transition. Its ground state is represented by all parallel in-plane spins, hence $s_z^i = 0 \, \forall i$, with continuous global degeneracy of symmetry $U(1)$. Its free energy is always as a convex function

of m_z^i with one minimum in $m_z^i = 0$ at all temperatures. Although this picture is not accurate, it can be useful to imagine the phase diagram as splitted into two regions, one in which the free energy is minimum in $m_z = 0$ (the superconducting phase) for $\alpha < 1$ and one with two equivalent minima in $m_z = \pm 1$ (the charge ordered phase).

When an effective barrier potential as H_b is considered, the topology of the free energy will change across the phase diagram and a region in which the free energy will present simultaneously three minima will appear in the vicinity of $\alpha = 1$. The entropic term, together with the amount of anisotropy α, will tune the absolute values of those minima leading to metastable states and spinodal points appearing in the phase diagram. The barrier b will stabilize the BKT transition also for values of the anisotropy $\alpha > 1$: the higher is the barrier, the higher will be the value of α needed to suppress the superconducting response.

Thus, in order to study such intricate phase diagram we will deal with three issues separately: first, we will address only the BKT and the ferromagnetic transitions, forgetting for a moment about metastability and first order transitions, using a barrier $b = 1$, which will enhance the region $\alpha > 1$ in which superconductivity is still stable. Then we will try to construct a more complete phase diagram, including metastability and studying analytically the spinodal points at $T = 0$. However, to address the issue of first order transition and metastability numerically, we will need to lower the barrier down to $b = 0.1$.

5.4.1 Phase diagram for $b = 1$

Let us consider for now a barrier parameter $b = 1$. We point out that the barrier potential bH_b is in this way so high that thermodynamic equilibrium is really difficult to achieve with simulations since the system cannot explore all the phase space, unless it runs for a very huge number of MC steps. Nevertheless, some interesting results can still be found. We will however present our simulations for systems cooled down using the Simulated Annealing algorithm with a maximum cooling rate of $\delta T = 0.05$, averaging the thermal observables on 10^4 MC configurations every $t_M = 40$ Metropolis iterations, discarding away the first $2 \cdot 10^4$ MC configurations. The phase diagram constructed and presented in Fig. 5.7 clearly shows that the BKT line survives for values $\alpha \gg 1$, up to $\alpha = 1.325$. All the points were extracted as in Section 5.3: the circular dots represents the T_{BKT} temperature computed with the scaling relation of the superfluid stiffness and the triangles are used to indicate the Ising transition temperature T_c.

The physical quantity that can give a quick insight about the nature of the transition involved as the anisotropy value α varies is the susceptibility. Merely comparing the in-plane $(\chi^{xx} + \chi^{yy})/2$ and out-of-plane χ^{zz} responses, defined as in Eq. (5.8) one can discriminate between the two. While in fact a superfluid density J_s is associated with an in-plane susceptibility that diverges exponentially approaching the transition from above $T \to T_{BKT}^+$ (see Eq. (5.19)) and a finite out-of-plane susceptibility, as discussed for the XXZ model in Section 5.3, the situation will be generally reversed in the ferromagnetic transition.

As a matter of fact, this can be observed in Fig. 5.8 where the in-plane and out-of-plane susceptibilities at various level of anisotropy in the range $0.95 < \alpha < 1.5$ are plotted, where we tuned the barrier to $b = 1$. The data computed are referred to
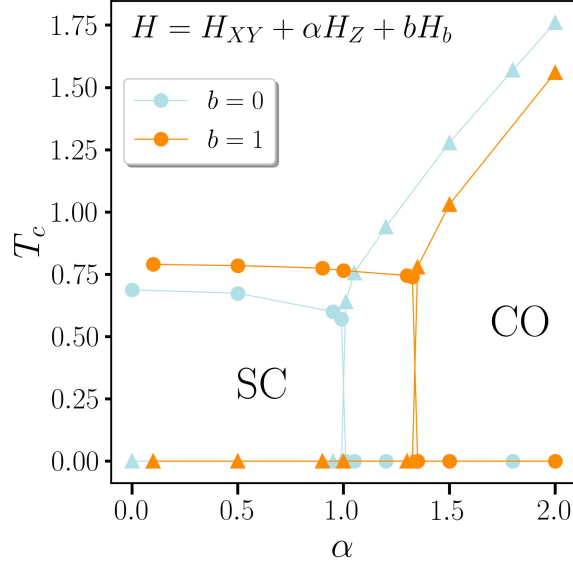
Figure 5.7. Phase diagram T_c vs α for the anisotropic Heisenberg model with the presence of a barrier $b = 1$ (orange), compared with the results found in the bare XXZ model ($b = 0$ in light blue). As before, the circle dots indicating the BKT transition are calculated using the BKT scaling law for the superfluid stiffness in Eq. (5.18) and the triangles are calculated from the crossing point of the Binder cumulant in Eq. (5.9) at different linear sizes L of the lattice. While for the bare XXZ model $\alpha = 1$ represents the critical value discriminating between a BKT and a ferromagnetic transition, the presence of a barrier stabilize superconductivity up to $\alpha = 1.325$.

a size $L = 64$ and the thermal averages are taken over 10^4 MC configurations every $t_M = 40$ Metropolis steps, discarding the first $2 \cdot 10^4$ MC configurations. As one can see, the in-plane response of the system is relevant for values of anisotropy as large as $\alpha = 1.325$, way greater than the isotropic Heisenberg limit, while the corresponding out-of-plane susceptibilities decrease down to values of order 10^{-4}. Let us notice that a peak in χ^{zz} is observed in the data corresponding to $\alpha = 1.3$, 1.325 (green and light blue curves) right above their BKT temperature, while all the χ^{zz} plots for $\alpha \leq 1$ seem to collapse on the same monotonic curve. This is coherent with the results found in the pure anisotropic Heisenberg model, as the out-of-plane response of the BKT situation gets more peaked when approaching the Ising transition.

The situation gets reversed as soon as $\alpha \geq 1.35$, where the response of the system is in the out-of-plane direction. The $\alpha = 1.35$ curve (in dark violet) in particular seems to be a critical value of anisotropy, for the in-plane susceptibility appears to be about to diverge while lowering the temperature down to $T = 0.8$, where it assumes the value $\simeq 228$, dropping at $T = 0.75$ to $\simeq 0.5$; correspondingly, χ^{zz} jumps from the value $\simeq 3.4$ to $\simeq 273$.

We can also observe that this trend is also present in the specific heat. From Fig. 5.9 we see the presence of a peak in correspondence of the critical temperature. In particular, the maximum specific heat is found slightly above T_{BKT} for all those curves displaying a BKT transition ($\alpha < 1.35$) – the region between $0.74 < T < 0.79$
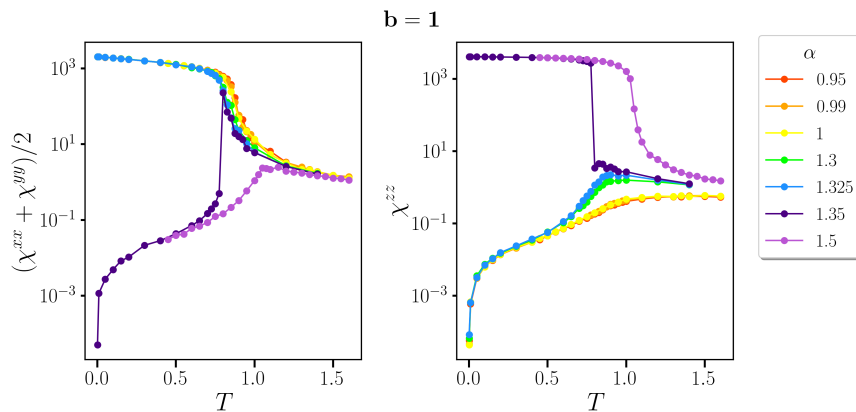
Figure 5.8. In-plane $(\chi^{xx} + \chi^{yy})/2$ and out-of-plane χ^{zz} susceptibilities for $b = 1$ for different values of anisotropy α for a barrier parameter $b = 1$ and size $L = 64$. The thermal averages are made on 10^4 MC configurations every $t_M = 40$ Metropolis iterations, discarding away the first $2 \cdot 10^4$ MC configurations.

in which all the T_{BKT} values collapses is highlighted in yellow – while for the ferromagnetic transition $\alpha \geq 1.35$ the peak is right were the critical temperature T_c is found, as indicated by a dashed line of the same color of the C_V curve.

Finally, let us introduce operatively the definition for the total density of vortices. A vortex (anti-vortex) is calculated in the lattice whenever a variation of 2π (-2π) of the in-plane angle $\theta_{i,j}$ is found in a closed path of a single plaquette. Let us slightly change the notation, defining the in-plane phase difference at site $\mathbf{r}_k$ in the $\hat{\nu}$-direction $(\hat{\nu} = \hat{x}, \hat{y})$ as

$$\phi_{\hat{\nu}}(\vec{r}_k) = [\theta(\mathbf{r}_k) - \theta(\mathbf{r}_k + \hat{\nu})]_{-\pi}^{+\pi} \tag{5.32}$$

the notation $[\cdot]_{-\pi}^{+\pi}$ meaning that we take the value modulus 2π so the angle lies in the interval $(-\pi, \pi]$, we can define the circulation of the in-plane phase around a plaquette sited in $\vec{r}_k$ as:

$$\phi_{\hat{x}}(\mathbf{r}_k) + \phi_{\hat{y}}(\mathbf{r}_k + \hat{x}) - \phi_{\hat{x}}(\mathbf{r}_k + \hat{y}) - \phi_{\hat{y}}(\mathbf{r}_k) = 2\pi m_k \tag{5.33}$$

where m_k is the integer vorticity in the phase angle $\theta(\mathbf{r}_k)$ going around the plaquette [126]. Summing over all positive (negative) vorticity for unit length we obtain the density of vortices $\rho_V > 0$ $(\rho_{AV} < 0)$, defining the total as $\rho_{V,tot} = \rho_V - \rho_{AV}$.

In Fig. 5.10 we observe the evolution in temperature of the total density of vortices ρ_V, meaning the sum over vortices and anti-vortices, comparing the last value of the anisotropy in which we find a BKT transition, i.e., $\alpha = 1.325$, and the first one in which the ferromagnetic transition appears, i.e., $\alpha = 1.35$. As one can observe, the density of vortices follows the typical exponential BKT behavior in the $\alpha = 1.325$ case (Fig. 5.10a). Instead, for the $\alpha = 1.35$ curve, $\rho_{V,tot}$ start to be exponentially suppressed lowering the temperature down to its critical value, marked in Fig. 5.10b with a vertical dashed line, then a sudden proliferation of free vortices is observed, indicating a re-entrant state that starts in a BKT-like framework at high temperature below which the system drops into a ferromagnetic state, in perfect
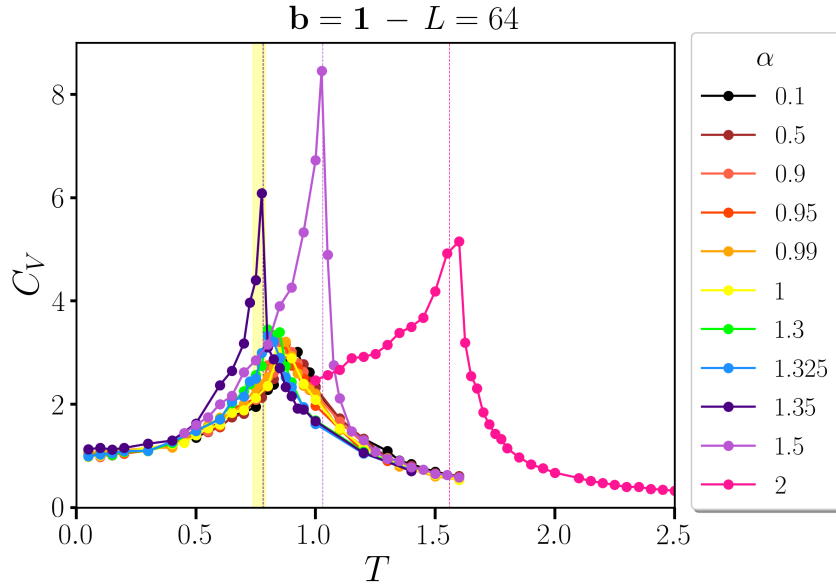
Figure 5.9. Specific heat C_V for the $b = 1$ case at various anisotropy values α at size $L = 64$. The T_{BKT} temperatures are all in the yellow highlighted temperature range, while the ferromagnetic critical temperatures T_c are indicated with a dashed line of the same color of the corresponding α. The thermal averages are made on 10^4 MC configurations every $t_M = 40$ Metropolis iterations, discarding away the first $2 \cdot 10^4$ MC configurations.

agreement with the trend found in the in-plane and out-of-plane magnetizations. Note that such re-entrant phase is also detected by finite size effects in the superfluid stiffness plotted in the inset of Fig. 5.10b. At high temperature, the paramagnetic phase seems to undergo a BKT transition, as it is visible from the tails of J_s, while instead at $T \simeq 0.76$ (vertical dashed line) the system develops a finite out-of-plane magnetization and J_s drops to zero right.

5.4.2   Spinodal points at $T = 0$

As it was stated at the beginning of this Section, the phase diagram T_c vs α of Hamiltonian (5.30) is a little more intricate than the bare anisotropic Heisenberg model presented in Section 5.3 and it will present a re-entrance of the superconducting state, caused by the presence of the barrier, while two first order lines terminating at $T = 0$ are expected.

The study of metastable states is particularly challenging, either in real experiments and using numerical methods.

What one can do however is to search for the critical values $\alpha^*(b)$ for which a local minimum of the free energy disappears along the $T = 0$ line of the T_c vs α phase diagram. Indeed, increasing α at zero temperature – where all pseudospins are supposed to be parallel $\varphi_i = \varphi \, \forall i$ – the free energy will have a single global minimum in $\varphi = 0$ up to some $\alpha = \alpha_{CO}^*(b)$, after which two new *local* minima in $\varphi = 0, \pi$ will appear. Crossing the isotropic point $\alpha^* = 1$ the situation gets reversed:
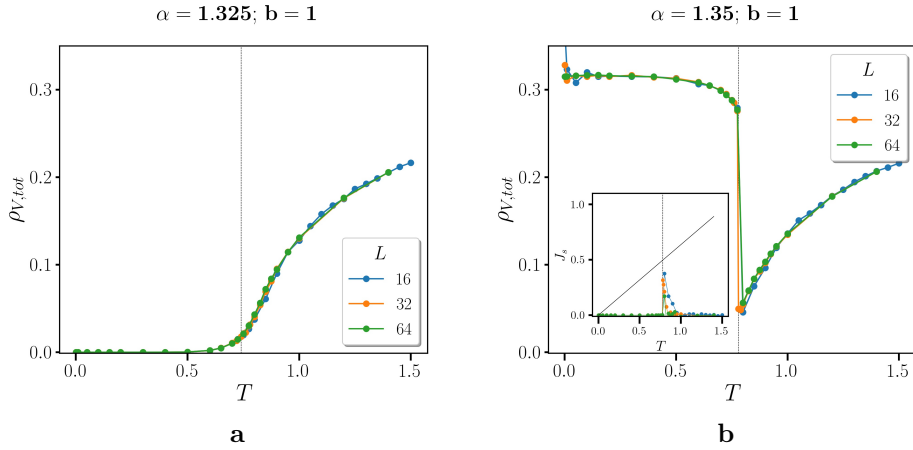
Figure 5.10. Total density of vortices and antivortices $\rho_{V,tot}$ as a function of temperature. (a) For $\alpha = 1.325$ the decay of $\rho_{V,tot}$ is exponential when lowering the temperature, confirming the BKT nature of the transition. (b) $\alpha = 1.35$ shows a re-entrant phase as $\rho_{V,tot}$ seems to decay exponentially lowering T down to a temperature T_c where vortices suddenly proliferate. T_c, marked with the vertical dashed line, which was deduced from U_L. In the inset, the same trend is also confirmed by the finite size effects of J_s.

the new global minima will be $\varphi = 0, \pi$ and the $\varphi = 0$ configuration will become a local minimum, disappearing at some $\alpha_{SC}^*(b)$. In other words, moving along the $T = 0$ line of the phase diagram, we are looking for

- $\alpha \le \alpha_{SC}^*(b)$ such that $\frac{\partial^2 H}{\partial \varphi^2}|_{\varphi=\pi/2} > 0$

- $\alpha \ge \alpha_{CO}^*(b)$ such that $\frac{\partial^2 H}{\partial \varphi^2}|_{\varphi=0,2\pi} > 0$

Writing the Hamiltonian as

$$H = - \sum_{<ij>} \cos(\theta_i - \theta_j) \sin(\varphi_i) \sin(\varphi_j) - \alpha \sum_{<ij>} \cos(\varphi_i) \cos(\varphi_j) - b \sum_i (1 - \cos(4\varphi_i))$$

we look for the solutions α_{CO}^* and α_{SC}^* for $T = 0$. The out-of-plane component can either be $\varphi = 0, \pi/2, \pi$, corresponding respectively to $s^z = +1, 0, -1$, thus we can take $\cos(\theta_i - \theta_j) = 0$ and $\varphi_i = \varphi$. Neglecting all constants and considering first neighbors interactions, we can simplify the former Hamiltonian to

$$\frac{1}{N} H(\varphi) = 2(1 - \alpha) \cos^2(\varphi) - b \cos(4\varphi) \tag{5.34}$$

whose first derivative with respect to is

$$\frac{1}{N} \frac{\partial H}{\partial \varphi} = -2 \sin(2\varphi)(1 - \alpha) + 4b \sin(4\varphi) =$$
$$= -2 \sin(2\varphi)(1 - \alpha) - 8b \sin(2\varphi) \cos(2\varphi) =$$
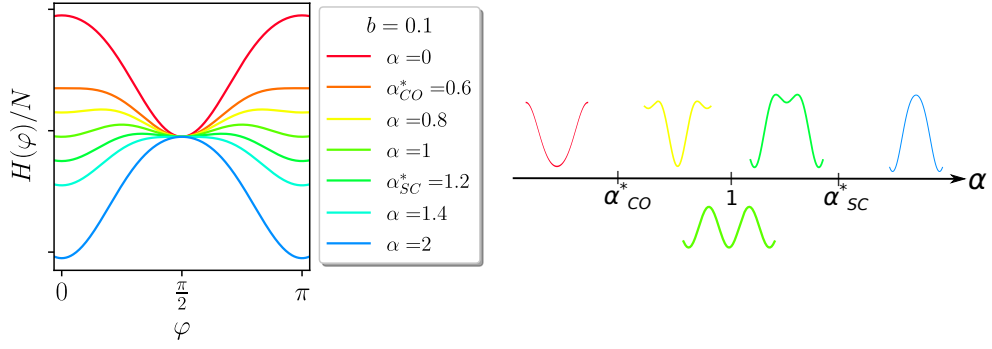$$= -2 \sin(2\varphi)((1 - \alpha) + 4b \cos(2\varphi)) \tag{5.35}$$

Figure 5.11. (a) Hamiltonian $H(\varphi)$ in Eq. (5.34) for a barrier parameter $b = 0.1$ at various tuning parameter α, ranging from 0 to 2. (b) Sketch figure of the $T = 0$ line of the phase diagram as a function of the tuning parameter α. The shape of $H(\varphi)$ displays a single minimum in $\varphi = \pi/2$ (SC) for values $0 < \alpha < \alpha^*_{CO}$; at $\alpha = \alpha^*_{CO}$ two other local minima appears in $\varphi = 0, \pi$ (CO); for $\alpha = 1$ we find three equivalent minima; in the range $1 < \alpha < \alpha^*_{SC}$ the CO states are global minima while SC survives as a local minimum; for $\alpha > \alpha^*_{SC}$ only the two equivalent CO minima survives.

Taking one more derivative, we obtain

$$\frac{1}{N}\frac{\partial^2 H}{\partial \varphi^2} = 4\cos(2\varphi)(\alpha - 1) + 16b\cos(4\varphi) =$$

$$= 4\cos(2\varphi)(\alpha - 1) + 16b(2\cos^2(2\varphi) - 1) \quad (5.36)$$

Then substituting $\varphi = \pi/2$ and $\varphi = 0, \pi$ we obtain

$$\alpha^*_{SC}(b) = 1 + 4b \quad (5.37)$$

and

$$\alpha^*_{CO}(b) = 1 - 4b \quad (5.38)$$

Note that we could have guessed those values already from the non-trivial solutions of $\partial H/\partial \varphi = 0$ from the occurrence of the two maxima in $\cos(2\varphi) = \frac{(1-\alpha)}{4b}$, whose reality condition is precisely $\alpha^*_{CO}(b) < \alpha < \alpha^*_{SC}(b)$ thus signaling the presence of three local minima.

In Fig. 5.11 we report Hamiltonian for $T = 0$ in Eq. (5.34) at various tuning parameter $\alpha > 0$, calculated for a barrier parameter $b = 0.1$: the system displays a single global minimum at $\varphi = \pi/2$, corresponding to the superconducting state for values ranging from 0 to $\alpha^*_{CO} = 0.6$, after which the system develops two other local minima in $\varphi = 0, \pi$, signaling the appearance of metastable CO states; at $\alpha = 1$ a first order phase transition switches the global SC minimum into a local one while the CO states becomes global minima; the superconducting state finally disappears for $\alpha > \alpha^*_{SC} = 1.4$.

The situation has been settled concerning the $T = 0$ state and it is now time to look for the complete phase diagram including finite temperatures.

5.4.3 Phase diagram for $b = 0.1$

We select now the barrier parameter $b = 0.1$ in order to construct a phase diagram in which we can also numerically study the equilibrium transition temperatures.

As it is known, the experimental and computational study of the correct equilibrium state, to extract the first order transition critical temperature and to determine spinodal points, is not a trivial problem that will be treated here in a very simple way.

Within MC simulations we decide to use small sizes, mostly $L = 4$, taking histograms from which we calculate an effective probability that allows us to construct a free energy. The need for a small size is a consequence of the fact that the free energy barrier between the minima grows exponentially with the number of sites of the system considered.

Although we are aware that this is not the most accurate method, it can however give quick and approximate yet insightful results.

An effective free energy is constructed starting from the histograms of m_z. Note that we naively consider $m_z = 0$ as the superconducting state although this is not completely exact, since the system may not have a macroscopic stiffness. We evolve a small system, typically $L = 4$, for a time much greater than the time strictly needed to perform a realistic thermal average over the configurations.

The system evolves for $5 \cdot 10^5$ MC steps after discarding the first $5 \cdot 10^5$, each MC step being $t_M = 50$ Metropolis steps. We construct an effective discrete probability density function $P_{eff}(m_z)$ from the histograms of $m_z = \frac{1}{N} \sum_i s_i^z$, calculated at each MC step. The effective free energy of the $k-$th bin is then constructed as $F_k = -T \ln(P_k / \sum P_k) \equiv F(m_z)$. This procedure is performed both cooling down the system from a random initial condition and by heating up the system, prepared the metastable state, i.e., all pseudospins up if $\alpha < 1.05$ and all in-plane parallel pseudospins if $\alpha > 1.05$, in order to check that the chosen protocol does not affect the result. Once we have all the effective free energies $F(m_z)$ at each temperature for both protocols, we can infer the first order critical temperature $T_{1^{st}OT}$ and the spinodal temperature T_{sp}.

The first order transition temperature will correspond to the one at which the minimum of free energy changes from $m_z = \pm 1$ to $m_z = 0$ increasing the temperature. Hence, we consider the minima of the effective $F(m_z)$ constructed from the histograms at each T so to have the minimum free energy $F_{min}(T)$ for both the phases we are interested in: in particular, we look for the minimum value in $m_z = 0$, for the superconducting state, and the minimum near $m_z = \pm 1$, for the CO state. As an example, we report the resulting $F_{min}(T)$ in Fig. 5.12a for the $\alpha = 1.04$ case, were the superconducting state is shown in red and the CO in green. The crossing point between the two curves is the first order critical temperature. One can of course check from the histograms that this temperature really corresponds to the coexistence of all three states. For this reason, we report some histograms corresponding to the $\alpha = 1.04$ case in panels b, c, d and e of Fig. 5.12, where the distribution of m_z is in light blue (left axis) and the corresponding $F(m_z)$ is in purple (right axis). One can easily see how at $T = 0.25$ (panel b) $F(m_z)$ displays three minima, the global ones being in $m_z = \pm$ (CO); then, increasing the temperature to $T = 0.30$ the three minima are equivalent while at $T \geq 0.35$ the global minimum lies in $m_z = 0$.

The spinodal points are trickier to address. We fitted the data $F(m_z)$ in the region around $m = 0.5$ to look for the temperature at which the curvature changes from downward to upward. The difference is here more subtle but it can be seen
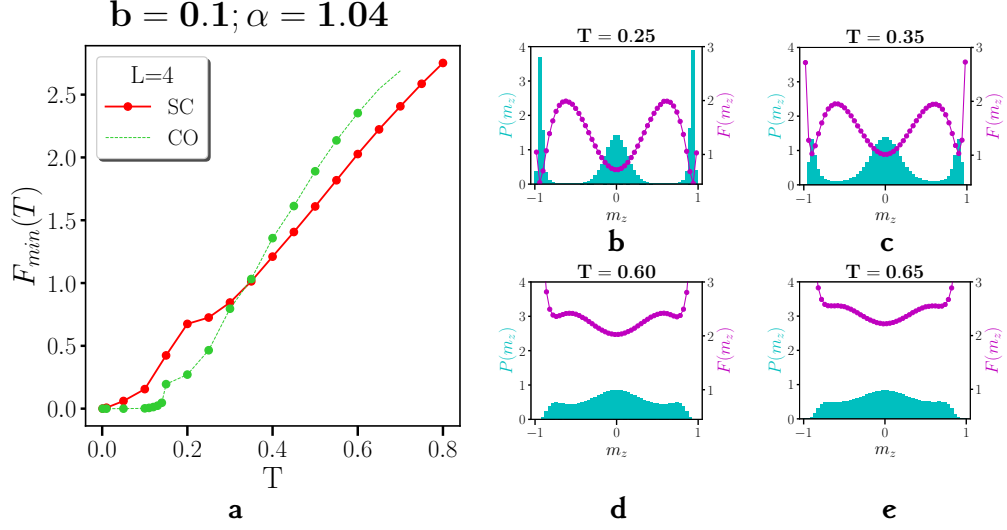
Figure 5.12. Effective free energies and probability distributions of m_z for a system of linear size $L = 4$ with $\alpha = 1.04$, $b = 0.1$. (a) Local minimum of the free energy as a function of temperature $F_{\min}(T)$. The red curve corresponds to the minimum of $F(m_z \approx 0)$ while the colored dots $F(m_z \approx 1)$ of panel (a). The crossing temperature between the two indicates the first order transition $T_{1^{st}OT}$. (b) Effective probability density function $P(m_z)$ and free energy $F(m_z)$ for $T = 0.25$, (c) for $T = T_{1^{st}OT} = 0.35$. (d) $T = 0.60$ and (e) $T = T_{sp} = 0.65$. The free energies $F(m_z)$ at each temperature were constructed from the distribution of m_z within $5 \cdot 10^5$ MC steps, after discarding away the first $5 \cdot 10^5$, each MC step made by $t_M = 50$ Metropolis iterations

from panels d and e of Fig. 5.12, in panel e the curvature near $m_z = \pm 1$ being finally flat.

This procedure was repeated for many values of α in order to construct a reliable phase diagram for a barrier parameter $b = 0.1$. The resulting phase diagram is shown in Fig. 5.13. The orange circles indicate the BKT transition temperature T_{BKT} extrapolated by means of the scaling relation in Eq. (5.18), the superconducting transition surviving up to $\alpha = 1.04$, while for $\alpha \geq 1.05$ the Ising (CO) transition temperature $T_{CO}(\alpha)$ is indicated with orange triangles and deduced by means of the Binder cumulant U_L. The points in brown along the line $T = 0$ are theoretical points: the two stars in $\alpha^*_{CO} = 0.6$ and $\alpha^*_{SC} = 1.4$ are the spinodal points at $T = 0$, calculated as described in Section 5.4.2, and the brown square at $\alpha^* = 1$ is where the free energy has three equivalent minima in $m_z = 0, \pm 1$. The red stars correspond to the spinodal points and the yellow squares are the first order critical temperatures, inferred from the histograms of m_z, the behavior of effective free energy $F(m_z)$ and $F_{min}(T)$.

The resulting phase diagram is very interesting. We report a cartoon figure of it in Fig. 5.14a. As already discussed, metastability regions appear, bounded by two spinodal lines. As the temperature increases, the region of metastability shrinks to a single point, which seems to coincide with the triple point where charge ordered, superconducting and disordered phases meet. The first order line separating the CO
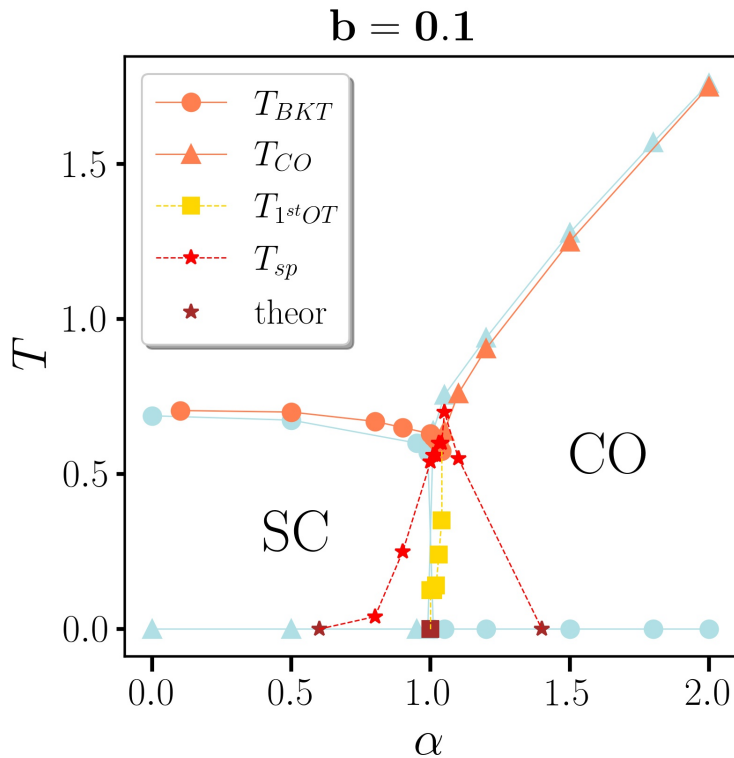
Figure 5.13. Phase diagram T_c vs α for the XXZ model with a barrier $b = 0.1$. The light blue shaded lines refer to the bare XXZ model. The orange dots are the T_{BKT} points calculated with the BKT scaling law while the orange triangles refers to the ferromagnetic transition for which T_c is found by use of the Binder cumulant U_L, the squares refers to the first order transition while the stars indicates the spinodal points. The brown points in $T = 0$ are calculated analytically, while yellow squares and red stars are computed from the effective free energies $F(m_z)$ and $F_{min}(T)$.

phase and the superconductor is almost vertical, indicating that the two phases have similar entropy, as one can check using the Clausius-Clapeyron relation. We can thus make a first comparison with the case of ^{4}He, whose phase diagram is shown in Fig. 5.14b.. Here, it was the almost vertical line separating the solid and superfluid phases that led to the hypothesis that superfluidity was a low entropy phase, as a crystal, fueling explanations based on condensation in momentum space instead of real space. Concerning again the CO-SC competition, one can then observe that the same first order line is not exactly vertical and a re-entrance appears, thus finding that near $\alpha \gtrsim 1$ one can make a transition from the CO state to the superconductor by increasing the temperature. This clearly means that the superconducting phase has actually slightly higher entropy than the CO phase. A posteriori, this result is reasonable as the CDW has two gapped transverse modes while superconductivity has only one gapped mode plus a Goldstone mode. Thus, just considering low laying excitations near $T = 0$, it is reasonable that the superconductor can have larger thermal fluctuations and entropy. Interestingly, the re-entrant behavior of the
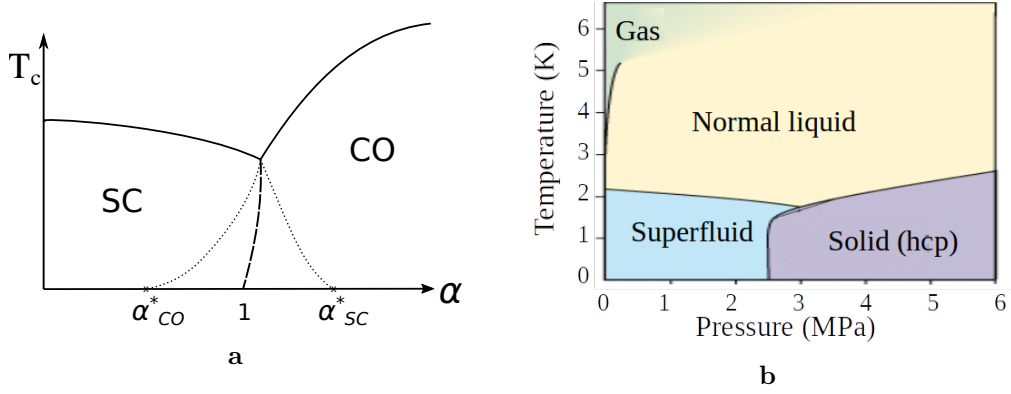
Figure 5.14. (a) Cartoon sketch of the phase diagram of the XXZ model with the CO-SC effective barrier potential $H = H_{XY} + \alpha H_Z + b H_b$. Solid lines stand for the second order phase transition, the thick dashed line indicates the first order phase transition between the SC and CO states and the thin dotted lines are spinodal lines. (b) Clausius-Clapeyron phase diagram of the ^{4}He (Figure adapted from wikimedia commons).

superconducting phase is also reminiscent to the phase diagram of ^{4}He, in which we find a range of pressures in which the solid ^{4}He, if heated, transit to its superfluid state before becoming a simple liquid. In ^{4}He, however, this happens in the high temperature part of the phase diagram, while here we observe it at low temperatures. In fact, in the low temperature region, the sloop of our phase diagram and the one of ^{4}He have opposite sign. We speculate that this qualitative difference is due to the fact that in our case the CO has no Goldstone mode while in the case of ^{4}He the crystal has sound (Goldstone) modes.

It is worth noting that the model for describing the CO-SC competition in a dirty system discussed in Section 2.2.4 had many similarities with the supersolid-superfluid competition in ^{4}He. It is then very interesting, yet not so surprising, that the analogy is maintained already in the clean system.

5.5 CO-SC competition: XXZ model, barrier potential and a random field

We finally address the complete Hamiltonian, adding the external random field term along the easy-axis. Once both the barrier term b and the amount of disorder w along the out-of-plane axis are considered, a very rich 4-dimensional phase diagram of T_c will be associated to the complete Hamiltonian

$$H = - \sum_{<i,j>} s_i^{xy} \cdot s_j^{xy} - \alpha \sum_{<i,j>} s_i^z s_j^z + 8b \sum_i (s_i^z)^2 \left(1 - (s_i^z)^2\right) + \frac{w}{2} \sum_i h_i s_i^z \quad (5.39)$$

where h_i is a random variable uniformly distributed in $[-1, 1]$.

It is worth noting that in previous works [31, 32] the problem of filamentary superconductivity was already studied introducing a very similar model, although at $T = 0$ (see Section 2.2.4). In that case, a single-ion anisotropy was the key term to trigger the competition in the isotropic Heisenberg model in random field.

Introducing a random field, the ground state in the CDW state changes. The system breaks apart into a polycrystalline CDW: at the interface of two different domains, both ordered phases are frustrated and superconductivity wins. Once a reasonable amount of impurities is added to the system, clusters of up and down regions are created near those impurities, separated from a one dimensional superconducting interface where filamentary superconductivity appears as a domain wall between domains with opposite local magnetization and superconductivity is hence topologically protected.

In our context, the situation gets more intricate, yet interesting. On the one hand, because we addressed the problem of the anisotropic Heisenberg model, of its evolution in temperature and, in particular, of its phase diagram T_c vs α. On the other hand, we showed already in the last Section how the barrier term we considered accounts for the competition between the CDW and the superconductor, generating metastable states. Nevertheless, adding a random field, it is natural to expect to recover similar signatures of filamentary superconductivity. We will keep working on the construction of the phase diagram T_c vs α with $b = 0.1$, fixing w such that the amount of disorder is suitable to observe filamentary superconductivity. In Fig. 5.15 we report some snapshots of the final configuration scenario of pseudospins at temperature $T = 0.001$ for a size $L = 64$ lattice with anisotropy $\alpha = 1.05$ for different realizations of disorder, with $w = 0, 2, 5, 10$. The colormaps show the s_i^z component of the pseudospin in the two-dimensional lattice, the color code being displayed on the right hand side, ranging from 1, in green, to 0, in red, to -1, in blue. Those ground states are consistent with the results found in [31, 32]: in absence of disorder, the system goes through a CO transition represented by a state with all pseudospins pointing up, corresponding to the two CDW variants; increasing the disorder w, the system gets fragmented into up and down regions, divided by filamentary superfluid clusters represented by in-plane pseudospins. This is particularly evident in the $w = 5$ panel, in which we can distinguish filamentary clusters surrounding the out-of-plane regions. Therefore, we will keep the amount of disorder fixed to $w = 5$ in the forthcoming discussion.

Once the amount of disorder is set, we can start to study the behavior in temperature of those main physical quantities carrying information about the transition. Henceforth, every curve will have to be averaged not only on MC configurations, but also on different disorder realizations. It is worth noting that, especially for $L \geq 64$, 10 disorder realizations are enough to have reasonable errors. For the sake of definiteness, the errorbars relative to disorder will be simply:

$$\sqrt{\sigma_{\mathcal{O}}^2} = \sqrt{\overline{\mathcal{O}^2} - \overline{\mathcal{O}}^2} \tag{5.40}$$

where the overline $\overline{\mathcal{O}}$ indicates the average over different disorder realizations of some physical quantity $\mathcal{O}$.

In the next Sections we will describe our main results: going across the phase diagram, the usual BKT region in $\alpha < 1$ will not be very much affected by strong disorder, whereas for $\alpha \gtrsim 1$ we will find filamentary superconductivity. Moreover, for $\alpha \gg 1$ the ground state will be fragmented into up and down regions, hence ferromagnetism will survive only locally so we will be forced to define somehow a new criterion for the transition.
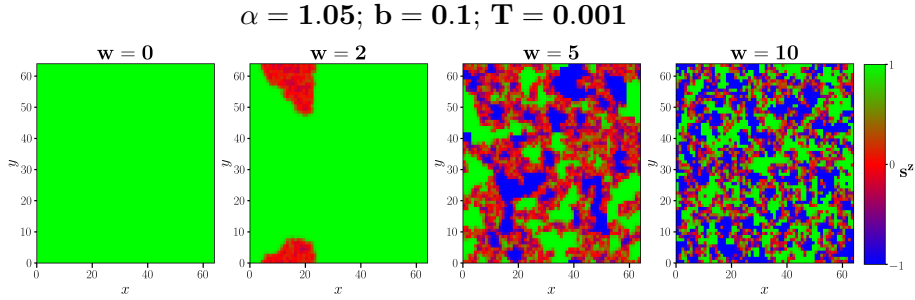
$$\alpha = 1.05; \ b = 0.1; \ T = 0.001$$

Figure 5.15. Snapshots of the pseudospin configurations at $T = 0.001$ for a $L = 64$ lattice with anisotropy $\alpha = 1.05$ and barrier parameter $b = 0.1$ for different realization of disorder, with $w = 0, 2, 5, 10$. The color code legend on the right hand side indicates the s^z component of the spin, ranging from green $s^z = 1$ to red $s^z = 0$ to blue $s^z = -1$. All the pseudospin configurations shown are the final scenario: for the clean case ($w = 0$) this corresponds to the $6 \cdot 10^4$−th step, while for the disordered configurations ($w = 2, 5, 10$) the system evolved for 10^5 MC steps, each MC step made by $t_M = 50$ Metropolis iterations.

5.5.1 $\ \alpha \gg 1$: polycrystalline CDW

Let us focus before on the $\alpha \gg 1$ side of the phase diagram. The presence of a random field along the z-axis forces the system to fragment into up and down clusters, whereas in-plane pseudospin configurations (SC) are of course energetically disadvantaged the more the system is far from the degeneracy point $\alpha = 1$. The usual order parameter $\langle m_z \rangle$ and its Binder cumulant U_L, used to address the Ising (CO) transition , do not provide in this case a reliable criterion to determine the critical temperature and a different approach is needed. To convince the reader about this last statement, we show in Fig. 5.16 some examples of *different definitions of magnetization*. We used a lattice of linear size $L = 128$ and anisotropy $\alpha = 1.5, 1.7, 2$ (respectively in panels a, b and c),averaging all the curves over 10 different realization of disorder with strength $w = 5$. Remembering that $\langle \bullet \rangle$ stays for the thermal average over MC configurations, the orange curve in all panels is the usual magnetization averaged over disorder:

$$\overline{\langle m_z \rangle} = \overline{\langle | \frac{1}{N} \sum_i s_i^z | \rangle}$$

Trivially, since the ground state is now divided into up and down regions this physical quantity loses its meaning, as it was predictable. Moreover, the errorbars are of the same order of the average value, thus resulting in an overall error interval twice as large as the mean value. One can on the other hand think to define some quantities involving the out-of-plane component of the spin.

For instance, one can be inspired by the definition of staggered magnetization used in the context of antiferromagnetic transitions. In that case the lattice is divided into two sub-lattices, with positive and negative magnetizations in the ground state, whose subtraction gives the total staggered magnetization with unitary value $m_{AF} = 1$ at $T = 0$. In our model, however, it is impossible to define two, or even three, sub-lattices in a proper way, for the up, down and in-plane components

of the spin. Hence, we defined some sort of staggered magnetization as follows

$$\overline{\langle m_z^{AF} \rangle} = \overline{\langle \frac{1}{N} \sum_i |s_i^z| \rangle},$$
(5.41)

which is plotted in purple in Fig. 5.16. Likewise, one can define the out-of-plane fluctuations of the spin

$$\overline{\langle m_z^{2,AF} \rangle} = \overline{\langle \frac{1}{N} \sum_i (s_i^z)^2 \rangle},$$
(5.42)

shown in green. While those quantities seems to be better defined in our model with respect to the usual magnetization, they do not provide a good order parameter to describe the system: if on the one hand both carry the information about the total fraction of the out-of-plane component in the lattice and their errorbars are rather small, they do not present any indication about some transition happening.
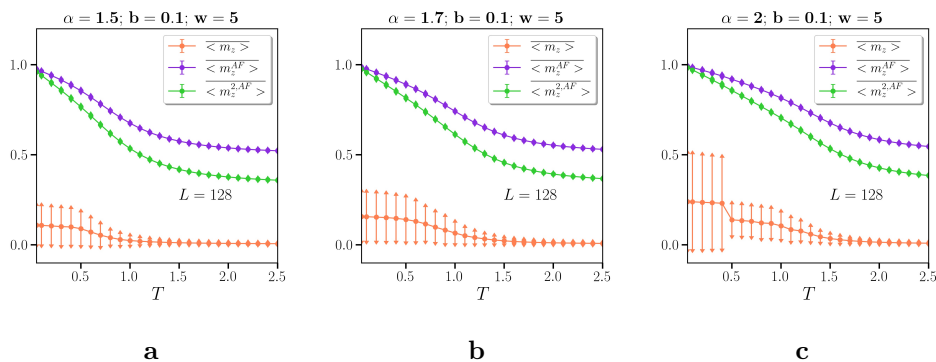

Figure 5.16. While trying to define the ground state for $\alpha \gg 1$ we observed different possible observables involving the out-of-plane pseudospin component: the usual magnetization $\overline{\langle m_z \rangle}$ (orange), $\overline{\langle m_z^{AF} \rangle}$ (purple) and $\overline{\langle m_z^{2,AF} \rangle}$ (green) defined in Eqs. (5.41) and (5.42). We report here the results for (a) $\alpha = 1.5$, (b) $\alpha = 1.7$ and (c) $\alpha = 2$. All curves refer to size $L = 128$ and are averaged over 10 different realizations of disorder with $w = 5$.

In the following, we will study the spatial correlation function that will provide us more information.

5.5.2 Correlation length of the out-of-plane component

Let us show some snapshots at different temperatures of the $\alpha = 2$ anisotropic case for a single realization of disorder. In Fig. 5.17a are reported the colorplots of the out-of-plane pseudospin component s^z for the final pseudospin scenario generated at temperatures $T = 2.5, 1.5, 1.0, 0.001$, displayed respectively from left to right. All the final scenarios plotted correspond to the 10^5-th MC step, each one made by $t_M = 50$ Metropolis iterations, the annealing algorithm playing an important part in speeding up the thermalization process especially in the random field framework. Lowering the temperature from $T = 2.5$, where the system is clearly in its paramagnetic phase, the up and down clusters that will represent the ground state at $T = 0.001$ start to aggregate already at $T = 1.5$ and are clearly visible at $T = 1.0$, although still with a certain degree of disorder. However, some reliable
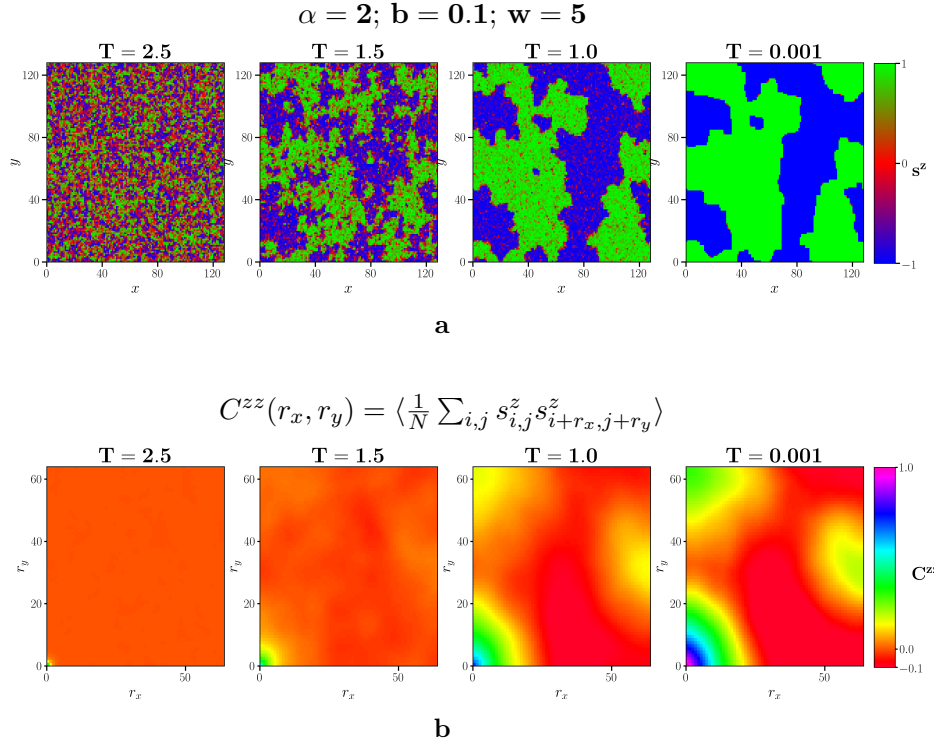
Figure 5.17. (a) Snapshots of the pseudospin configurations for a $L = 128$ lattice with anisotropy $\alpha = 2$ and barrier parameter $b = 0.1$ for the same realization of disorder, with $w = 5$. The temperature is lowered from left to right, in particular $T = 2.5$, 1.5, 1.0, 0.001. The color code legend on the right hand side indicates the s^z component of the spin, ranging from green $s^z = 1$ to red $s^z = 0$ to blue $s^z = -1$. The pseudospin scenarios shown are the final ones, after the system evolved for 10^5 MC steps, each MC step made by $t_M = 50$ Metropolis iterations. (b) Out-of-plane spin-spin correlation function $C^{zz}(r_x, r_y)$, i.e., density-density response, at the same temperature, for the same realization of disorder of the snapshots. The thermal average is done over 100 different pseudospin configurations.
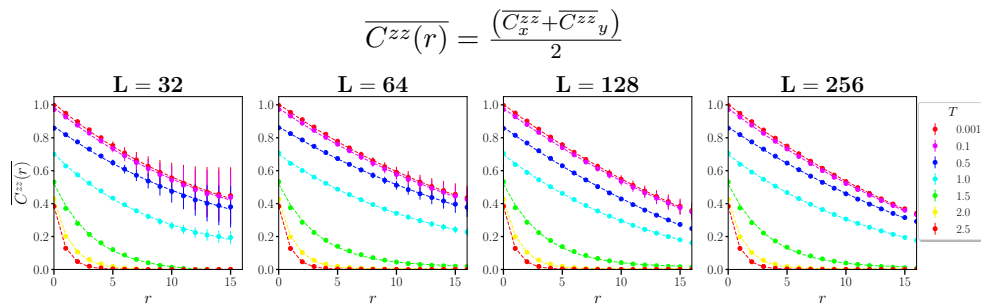
$$\overline{C^{zz}(r)} = \frac{\left(\overline{C^{zz}_x} + \overline{C^{zz}_y}\right)}{2}$$

Figure 5.18. $C^{zz}(r_x, r_y)$ averaged over 10 different realization of disorder and symmetrized with respect to the r_x and r_y directions, plotted at for $L = 32, 64, 128, 256$ at various temperatures. The errorbars refers to the average over disorder and the dashed lines are the exponential fits.

criterion to determine the transition between the paramagnetic to the "clustered" phase should be defined.

Therefore, the spatial correlation function $C^{zz}(\mathbf{r})$ of the out-of-plane component of the pseudospin can be a well defined quantity to address such a state. The out-of-plane spin-spin correlation function in our model corresponds to the density-density response and it reads as:

$$\overline{C^{zz}(r_x, r_y)} = \overline{\langle \frac{1}{N} \sum_{i,j} s^z_{i,j} s^z_{i+r_x, j+r_y} \rangle} \tag{5.43}$$

where we averaged over all the pseudospins $\sum_{i,j}$, the MC configurations, i.e., the thermal average $\langle \bullet \rangle$, and the different disorder realizations. Note that since we used periodic boundary conditions, the distance between two different pseudospin runs in the range $0 < r_x, r_y < L/2$.

In Fig. 5.17b we show the out-of-plane spatial correlation function for the same realization of disorder of the displayed snapshots. The thermal average for $C^{zz}(\searrow)$ is made here over 100 pseudospin configurations, saved after a transient of $2 \cdot 10^3$ MC steps, each one made by $t_M = 100$ Metropolis iterations and a transient of $2 \cdot 10^3$. We point out that the Metropolis steps are now made randomly. This choice was made to reduce the bias that is introduced in $C^{zz}(r_x, r_y)$ when the lattice is spanned in an ordered way, from which thermodynamic quantities were immune. Here we double the autocorrelation time ($t_M = 100$) and the computational time is reduced.

The strong spatial anisotropy of the s^z_i component, evidently visible in the snapshots for $T \leq 1.0$, are transposed in the $C^{zz}(r_x, r_y)$ of the same configuration. Since large clusters of up and down regions appear lowering the temperature, it is not so surprising that we find negative spin-spin correlations. To restore almost completely the spatial isotropy, one needs to average over many disorder realizations, bearing in mind that we are ultimately interested to have some information about the average size of up and down clusters. In other words, in order to extrapolate the correlation length ξ^z in the most accurate way possible we need that the correlation function is almost the same in all directions, at least in the limit $\mathbf{r} \to 0$.

Once $C^{zz}(\mathbf{r})$ is averaged over many disorder realizations, spatial isotropy is restored, as we checked that $\overline{C^{zz}(r_x, r_y)}$ was the same in the directions $(r_x, 0)$, $(0, r_y)$
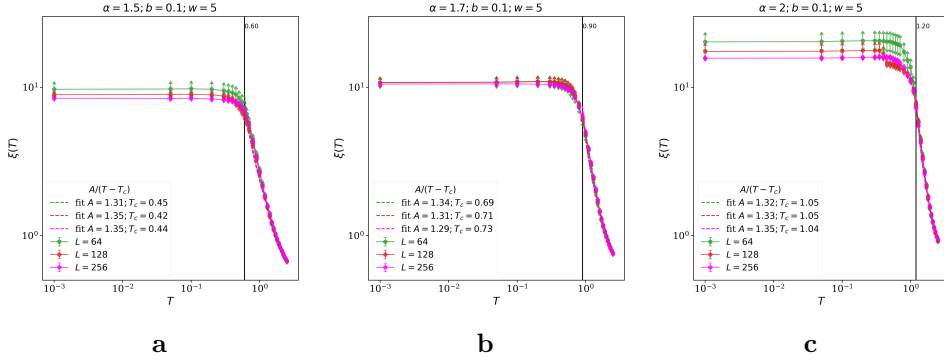
Figure 5.19. Correlation length $\xi^z(T)$ in logarithmic scale for sizes $L = 64, 128, 256$ for (a) $\alpha = 1.5$, (b) $\alpha = 1.7$, (c) $\alpha = 2$. The numerical data fitted with the function $\xi^z = A/(T - T_c)$ are those in the right region of the vertical line, assuming that the system at high T still belongs to the random field Ising model universality class, hence its critical exponent is $\nu = 1$.

and on the diagonal $r_x = r_y$. We study the spatial correlation functions $\overline{C^{zz}(\mathbf{r})}$ in the proximity of $|\mathbf{r}| \to 0$, hence we take the range $[0, 16) \times [0, 16)$. Moreover, we symmetrised $C^{zz}(\mathbf{r})$ with respect to the $(r_x, 0)$ and $(0, r_y)$ directions before fitting the data. Simplifying here the notation, we refer to the correlation function along the r_x and r_y axes respectively as C_x^{zz}, C_y^{zz}, thus

$$\overline{C^{zz}(r)} = \frac{\left(\overline{C_x^{zz}} + \overline{C^{zz}}_y\right)}{2} \propto \exp\left(-\frac{r}{\xi^z}\right). \tag{5.44}$$

One interesting feature of such clustered state we are examining consist in the fact that the decay of the correlation function does not seem to follow some size dependence for $|\mathbf{r}| \to 0$, as it can be seen from Fig. 5.18, where $\overline{C^{zz}(\mathbf{r})}$ is plotted in the same range $[0, 15]$ for different sizes of the system, doubling it from 32 to 256, for the case $\alpha = 2$ for various temperatures. The computed $\overline{C^{zz}(\mathbf{r})}$ are indicated with dots and errorbars refers to different disorder realizations, whereas dashed lines are the exponential fit of the data, from which we extrapolate ξ^z. Obviously, the independence from the size of the system will be preserved also in the behavior of the correlation length.

The correlation lengths ξ^z extrapolated are plotted as function of the temperature T for sizes $L = 64, 128, 256$ for the three values of $\alpha \gg 1$ that we examined, in particular, the $\alpha = 1.5$ case is shown in Fig. 5.19a, $\alpha = 1.7$ in Fig. 5.19b and $\alpha = 2$ case is shown in Fig. 5.19c. It is not surprising that we do not observe a clear dependence on the size L. Although, what is quite interesting is the fact that the saturation value for $T \to 0^+$ not only does not display an increasing monotonic behavior with L, but even seems to be slightly decreasing with the size. The emblematic case happens for $\alpha = 1.7$, where all the curves collapse on the same saturating value $\xi(T \to 0) \sim 10$. A possible interpretation of the phenomenon, yet not definite and still open, is the possibility that the system at high temperature still belongs to the random field Ising model universality class. Indeed, at high temperature the presence of the barrier potential in the Hamiltonian is masked by

the presence of strong thermal fluctuations. Hence, to define a critical temperature, we imagined this was an applicable scenario and we fitted the data with this ansatz. The $\xi(T)$ curves were fitted assuming *a priori* a random field Ising model critical exponent $\nu = 1$ to extract T_c:

$$\xi(T) = \frac{A}{T - T_c} \tag{5.45}$$

The results of the fitting parameter are displayed in Figs. 5.19a, 5.19b and 5.19c, obtaining $T_c = 0.42 \pm 0.05$ for $\alpha = 1.5$, $T_c = 0.90 \pm 0.02$ for $\alpha = 1.7$ and $T_c = 1.20 \pm 0.01$ for $\alpha = 2$.

5.5.3 $\alpha \gtrsim 1$: filamentary superconductivity

Finally, let us spend a few words about the BKT transition, trying a first attempt towards the description of filamentary superconductivity.

In Section 5.4, where we introduced the effective barrier H_b to introduce the CO-SC competition in the clean system, we already observed how the presence of the barrier alone strengthens the superconducting state even for values $\alpha \gtrsim 1$ of the phase diagram, whereas in the anisotropic Heisenberg model the BKT transition temperature is supposed to go to zero logarithmically as the isotropic limit is approached from below, i.e., $T_{BKT}(\alpha) \to 2\pi J/(A + \ln(1-\alpha)^{-1})$ for $\alpha \to 1^-$ (Eq. (5.29)).

Once disorder is set in the system, this framework might change. We already know that uncorrelated disorder should not affect substantially the BKT phase transition, at least in the $\alpha < 1$ region of the phase diagram [64] whereas correlated disorder, on the other side, can mask the presence of a BKT transition by smearing its very signatures, such as the jump of the superfluid density, providing a natural interpretation of the tails observed experimentally [65]. Besides, in the context of XY models it has been shown that disorder can also support and strengthen the superconducting state once a transverse magnetic field is applied: instead of fragmenting the global phase coherence, the presence of disorder can in fact work against thermal phase fluctuations [127].

Considering all of the above, it is not surprising that superconductivity is robust against the disorder introduced with the random field. Leaving aside for a moment the case $\alpha = 1.1$, which will deserve some more attentions, the superfluid stiffness for $\alpha < 1.1$ maintains almost intact all of its signatures, except for its saturating value $J_s(T \to 0)$, which is suppressed by the presence of an important fraction of pseudospins in the out-of-plane direction, forced by the quenched disorder.

The scaling relation in Eq. (5.18), used towards all the Chapter to extrapolate the superconducting critical temperature, works fine. The crossing point is still clearly visible also for anisotropy values slightly above the isotropic limit, although it is not so precise as in the clean case. We present in Fig. 5.20 the crossing point of the superfluid stiffness – rescaled with Eq. (5.18) – for the values $\alpha = 1$ and $\alpha = 1.05$ and sizes $L = 16, 32, 64, 128, 256$. The extrapolated $T_{BKT} \pm \delta T_{BKT}$ is indicated with a vertical dotted line and a gray shaded area, shown also in the insets, where the corresponding J_s is presented as it is, i.e., without being rescaled. Note that the errorbars on J_s refers to the uncertainty caused by different realizations of

disorder and they naturally reduce with the size, despite the fact that small sizes were averaged over more runs. In particular, we averaged over 20 runs for $L = 16, 32$, 15 for the size $L = 64$, 10 for $L = 128$ and 7 for $L = 256$. As usual, the tail observed in J_s becomes less and less evident as L increases, and all curves collapse on the same average value for $T < T_{BKT}$. The saturating value $J_s(T \to 0)$ in both cases is suppressed by about 50% with respect to its expected value in absence of disorder, where $J_s(0) = 1$.
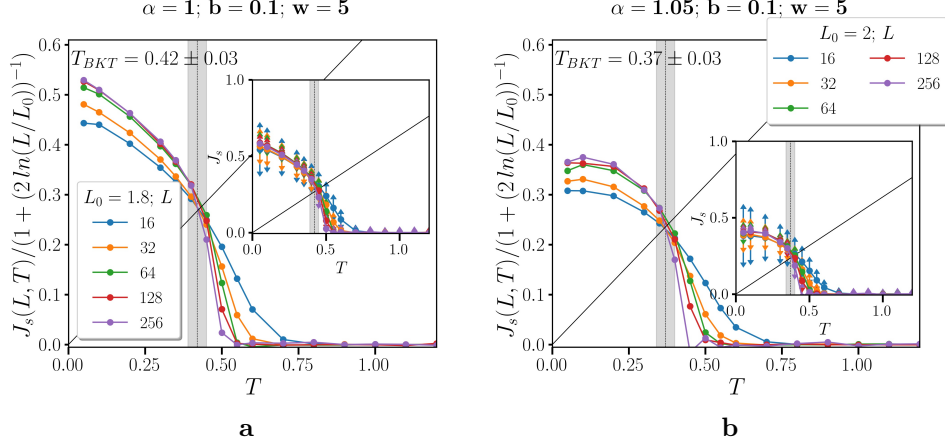

Figure 5.20. Crossing point of the rescaled superfluid stiffness $J_s(L,T)/(1+(2\ln(L/L_0))^{-1})$ with the BKT critical line $2T/\pi$ (full black line) at various size for (a) $\alpha = 1$ and (b) $\alpha = 1.05$. The vertical dashed line indicates the extrapolated T_BKT. In insets are represented the corresponding unscaled J_s with errorbars.

Last but not least, let us consider the case $\alpha = 1.1$, where we find a finite superfluid stiffness J_s and yet the usual BKT scaling relation does not work properly, as one can see observing Fig. 5.21a. Rescaling the curves at different L with the customary logarithmic factor does not lead to a clear and definite crossing point of all $J_s(L,T)$ with the critical line $2T/\pi$. Moreover, comparing the behavior of the rescaled functions with their corresponding J_s shown in the inset, one can observe that not much has changed. One can also point out that the stiffness displays a downward curvature in the low temperature limit, arguing that the finite superconducting response we observe is nothing but a finite size effect. On the one hand, however, a 256×256 lattice with periodic boundary conditions should provide already a reasonable size to observe reliable thermodynamic quantities; in addition, 9 configurations of disorder were considered for this size. On the other hand, the superfluid density at low temperature does not seem to be size dependent at $T \to 0$. Therefore, we proceeded to fit the data at our disposal anyway, trying to be as reasonable as possible in the choice of L_0, which however is not so decisive. The extrapolated $T_{BKT} = 0.31 \pm 0.08$ was also compared with the minimum value of the derivative of the superfluid stiffness $\partial J_s/\partial T$, along the line of Refs. [119, 123]: in these works, the crossing point of the superfluid stiffness of the bare anisotropic Heisenberg model was calculated by integrating Eq. (5.15) and the crossing point was consistent with the minimum of $\partial J_s/\partial T$ in the limit of large size, already at $L = 64$. As the BKT critical temperature is not clearly defined, neither with the scaling
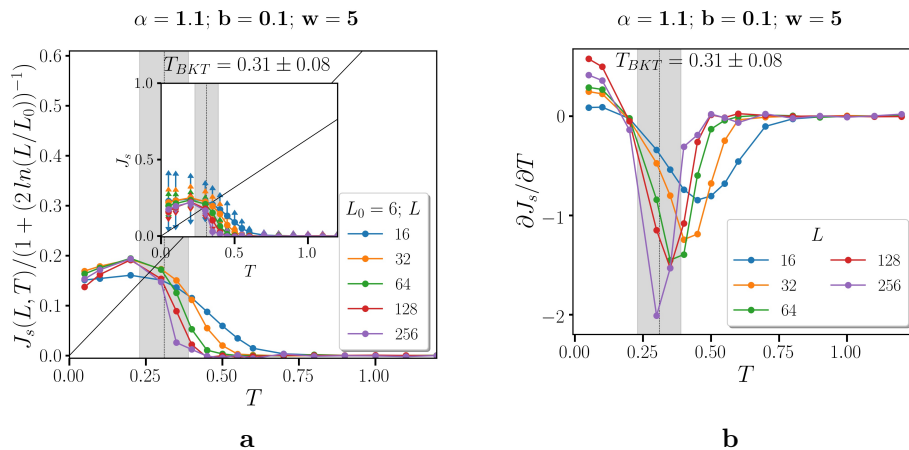
Figure 5.21. (a) Crossing point of the rescaled superfluid stiffness $J_s(L,T)/(1 + (2\ln(L/L_0))^{-1})$ with the BKT critical line $2T/\pi$ (full black line) at various size for $\alpha = 1.1$, in insets are represented the corresponding unscaled J_s with errorbars. (b) Corresponding temperature derivative of the superfluid stiffness $\partial J_s/\partial T$. In both panels, the vertical dashed line and the gray shaded area indicatea the extrapolated T_{BKT} and its errorbar $T_{BKT} = 0.31 \pm 0.08$.

relation nor the derivative of J_s, we considered a large uncertainty, highlighted in gray in both panels a and b of Fig. 5.21. It is worth noting that some crossing point between almost all curves $J_s(L)$ (with the exception of $L = 64$) is visible in Fig. 5.21a, but it does not however intersect the critical line $2T/\pi$. This fact can be linked to the emergence in the system of some new scales presumably related to the geometrical structure of the system, along with the typical sizes of vortex-antivortex pairs in BKT theory.

Indeed, the fact that the BKT transition and its signatures are pretty confused can be taken as a sign of a very interesting open problem that needs to be explored further. In Fig. 5.22 we show the snapshots of the final pseudospin scenario in a single disorder configuration for a size $L = 128$ system. The system is cooled down from a temperature $T = 2.5$ and at $T = 1.2$ we still observe a disordered phase. Lowering the temperature, superconducting filaments (in red) start to emerge at temperatures around $T = 0.6$. A filamentary structure is rather definite at $T = 0.3$, i.e, inside the BKT critical temperature interval we extrapolated with the scaling relation. Lowering again T, the spatial structure stays rather fixed down to $T = 0.001$, and the up and down areas are more definite as the red filaments also appear.

5.5.4 Phase diagram for $b = 0.1$ and $w = 5$

We can conclude this Section by summarizing the results obtained so far, finally sketching a first attempt of a phase diagram T_c vs α of the complete Hamiltonian presented in Eq. (5.39) for the barrier tuning parameter $b = 0.1$ and quenched disorder $w = 5$. This is shown in Fig. 5.23a, where it is superimposed to the standard anisotropic Heisenberg model phase diagram we illustrated in Section 5.3, plotted here in light blue just as a visual benchmark.

The BKT physics, expected in $\alpha < 1$ and stabilized here up to $\alpha = 1.05$, does not
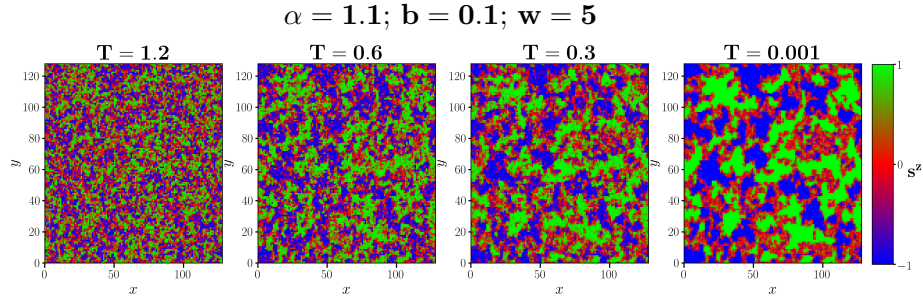
$\alpha = \mathbf{1.1}; \; \mathbf{b} = \mathbf{0.1}; \; \mathbf{w} = \mathbf{5}$

Figure 5.22. Snapshots of the pseudospin configurations for the $L = 128$ lattice with anisotropy $\alpha = 2$ and barrier parameter $b = 0.1$ for the same realization of disorder ($w = 5$). The temperature is lowered from left to right, in particular $T = 1.2, 0.6, 0.3, 0.001$. The color code legend on the right hand side indicates the s^z component of the spin, ranging from green $s^z = 1$ to red $s^z = 0$ to blue $s^z = -1$.

a

b
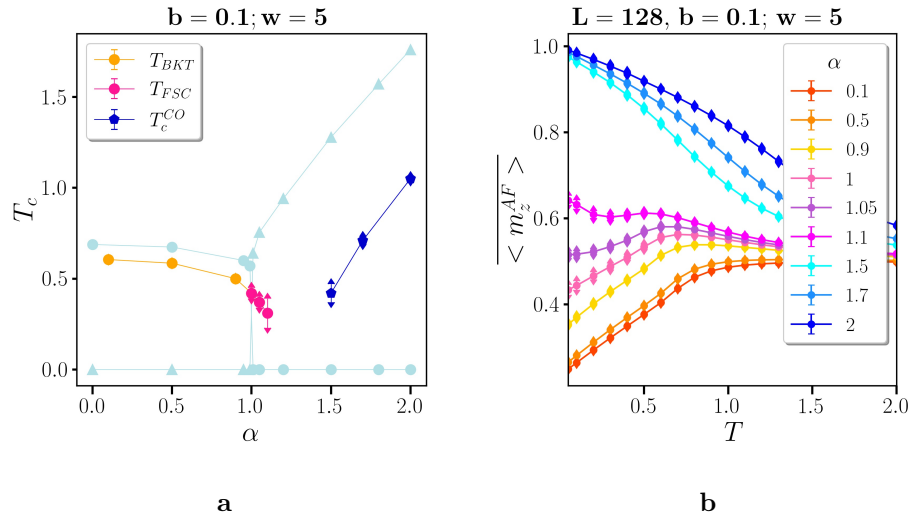
Figure 5.23. Phase diagram T_c vs α for the complete Hamiltonian presented in Eq. (5.39) with $b = 0.1$ and $w = 5$. The light blue phase diagram is the one for the bare XXZ model, calculated in Section 5.3. The blue pentagons indicates the charge ordered state (see Section 5.5.2) and T_c^{CO} was deduced from $\xi^z(T)$. The dots refers to the BKT critical temperature calculated by means of the scaling relation in Eq. 5.18. We distinguish here the values of $\alpha < 1$ (in orange), where the BKT transition is almost unaffected by disorder, and the $\alpha \gtrsim 1$ (in magenta), where the we start to observe filamentary superconductivity.

present surprising features. The orange dots correspond here to the standard BKT transition $\alpha < 1$. For those values of anisotropy, the usual BKT scaling relation holds and the crossing point between different $J_s(L)$ gives clean and quick results in terms of the BKT critical temperature. The T_{BKT} points are lower than those found in the absence of both barrier and quenched disorder, meaning that superconductivity is partially suppressed, as one can see comparing orange dots with the light blue ones of the bare anisotropic Heisenberg model. While the lowering of the critical temperature T_{BKT} with respect to the clean system at $b = 0$ was predictable, the random field is able to suppress also the saturating value of the superfluid stiffness at $T \rightarrow 0$, i.e., $J_s(T = 0) < 1$, yet the system stays in the BKT universality class.

Going towards $\alpha \geq 1$, we enter the region in which filamentary superconductivity (T_{FSC}) is expected. From Fig. 5.24, where we summarize the snapshots at $T = 0.001$ for various α, one can see that up to $\alpha \leq 0.9$ the ground state is represented by almost all pseudospins in-plane (in red). Slightly increasing the anisotropy $\alpha = 1$, 1.05, 1.1 one can observe the emergence of up (green) and down (blue) clusters appearing in the lattice, surrounded by a filamentary structure of superconducting spins. Alongside, the BKT superconducting response at low temperature is halved with respect to the clean case. However, for $\alpha = 1$, 1.05 the usual BKT scaling relation was applicable almost effortless whereas the case $\alpha = 1.1$ was more delicate, hence the large errorbar in the phase diagram. We used the BKT scaling relation to indicate its T_{FSC} temperature, aware of the fact that more analysis is needed.

Far away from the isotropic limit for $\alpha \gg 1$, the presence of the barrier together with quenched disorder has the effect of drastically changing the ground state and the system tends to a state composed by large disordered clusters of up and down local magnetizations. Hence, we cannot state that this regime belongs anymore to the Ising universality class, as it was for $\alpha > 1$ in the clean anisotropic Heisenberg model with $b = 0$ (light blue triangles) and $b \neq 0$. The need to find some reliable criterion to address this phase transition led us to consider the spin-spin spatial correlation function of the out-of-plane component. Thus, we fitted the correlation lengths found at different temperature: after realizing that the saturating value in the low temperature regime $\xi^z(T \rightarrow 0)$ was not monotonically increasing with L, we assumed *a priori* the critical exponent of the random field Ising model, in order to deduce the critical temperature, indicated in Fig. 5.23a as T_c^{CO}. This *ansatz* is based on the assumption that the system at high temperature is still in the random field universality class, due to large thermal fluctuations overcoming the barrier potential. Lowering the temperature, the large value of the anisotropy together with the barrier and the strong disorder act in the direction of creating such up and down structures, as it is shown in Fig. 5.24.

Finally, we can use the definition of magnetization presented in Eq. (5.41) to quantify the out-of-plane pseudospin component. What we called $\overline{< m_z^{AF} >}$, although it does not provide a clear cut in any definition of a phase transition, it defines the fraction of pseudospins pointing in the out-of-plane direction and it can give some insights about the ground state when looking at many α values, ranging in all the phase diagram proposed, as it was done in Fig. (5.23b).

The clear cut between the curves $a \geq 1.5$ and the ones at $\alpha \leq 1.1$ is the saturating value, which is $\overline{< m_z^{AF} >} = 1$ in the former case and $\overline{< m_z^{AF} >} < 1$ in the latter.

Moreover, those values of anisotropy that we identified as BKT-like scenarios
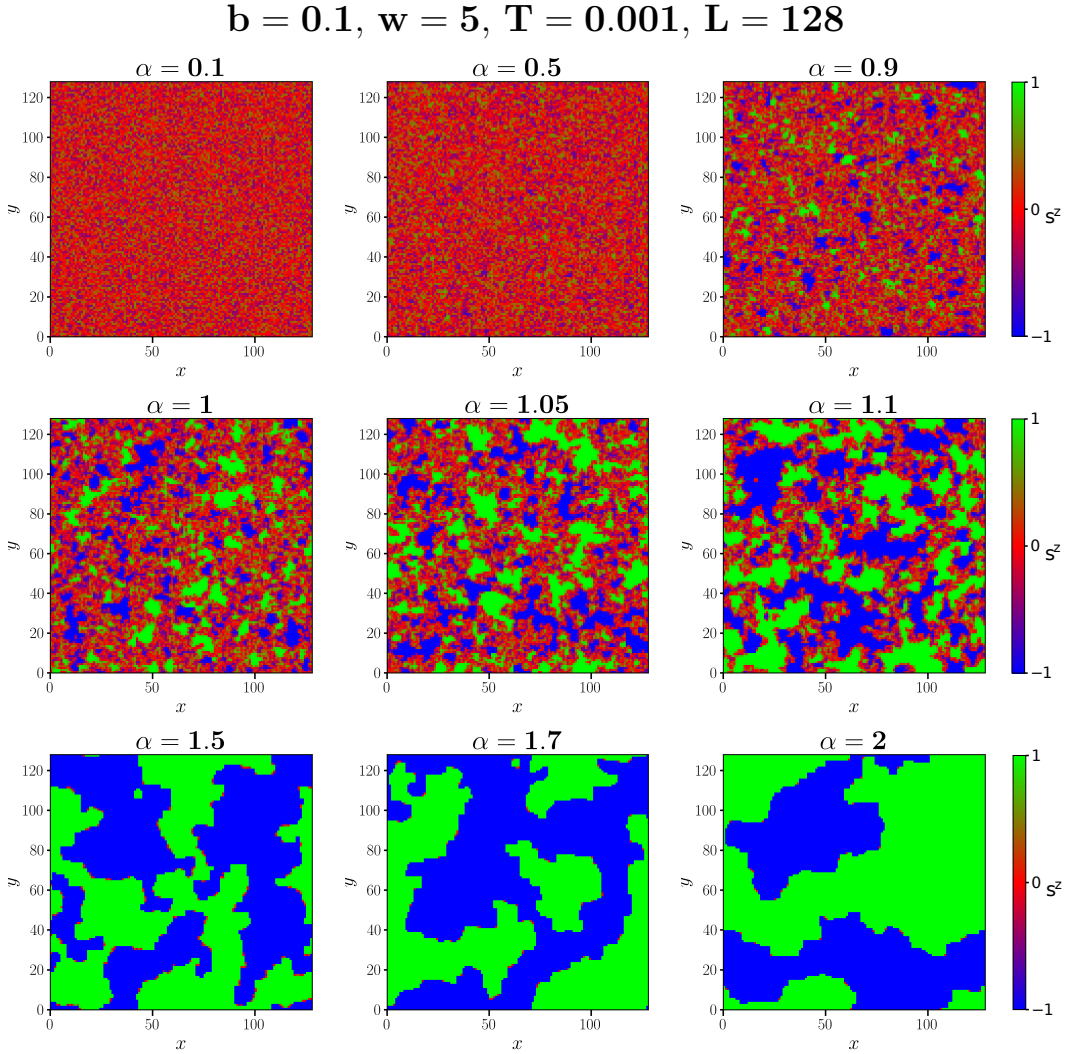
Figure 5.24. Ground state ($T = 0.001$) final configuration of pseudospins for a lattice of linear size $L = 128$ of the complete Hamiltonian in Eq. (5.39) with $b = 0.1$ and $w = 5$ at various anisotropies α.

$\alpha \leq 1$ present a decreasing behavior for temperatures lower than their critical one $T < T_{BKT}$.

For $\alpha = 1.05$ and especially $\alpha = 1.1$ one can note some sort of crossover between the two regimes: lowering the temperature, the fraction of out-of-plane pseudospins seems to increase, down to a temperature where a kink in $\overline{< m_z^{AF} >}$ is observed. Lowering the temperatures towards zero, the $\alpha = 1.05$ curve (in violet) does not decrease monotonically, saturating to a value approximately ~ 0.5. The $\alpha = 1.1$ case (in magenta) increases again, consistently with what we found in the corresponding superfluid stiffness.

Although it may seem evident, it must be pointed out that the work presented so far, although satisfactory in many aspects, is still in a preliminary stage. For instance, many more points of the phase diagram presented in Fig. 5.23a needs to be studied, in order to fill the gap in the range $1.1 < \alpha < 1.5$. On the other hand, a systematic

analysis of the in-plane correlation function $C^{xy}(r_x, r_y)$ would be necessary to study the superconducting correlation length. On the other hand, while the out-of-plane correlation function $C^{zz}(r_x, r_y)$ carried no information for values $\alpha \leq 1.1$, one may find that in a narrow region both charge-charge and superconducting responses are needed, as it was for the $\alpha = 1.35$ value of the clean system, discussed in Section 5.4.1, where both susceptibilities were indicating the re-entrant state. More importantly, we observed that the usual BKT relation was already starting to fail in addressing the superconducting transition for $\alpha = 1.1$, despite the finite superfluid stiffness. One can argue that the phase rigidity is only connected to a size effect, although we did not see an important suppression of J_s doubling the size of the system from $L = 16$ to $L = 256$.

Finally, it could be interesting to introduce the filamentary superconducting patterns arising from CO-SC competition into the RIN model, to study also transport measurement.

Conclusions and outlooks

> *"Tell me one last thing," said Harry. "Is this real? Or has this been happening inside my head?"*
> *"Of course it is happening inside your head, Harry, but why on earth should that mean that it is not real?"*

<div style="text-align: right">

Harry Potter and the Deathly Hallows,
Joanne Kathelin Rowling

</div>

In this Thesis, we investigated the problem of the interplay between disorder and low dimensionality in superconductors, where disorder can affect the system in many ways.

From the microscopic point of view, we addressed the issue of the suppression of the superconducting critical temperature in $SrTiO_3$-based heterostructures as a function of the gate potential V_G. The peculiarity of this pairbreaking effect observed is that it seems to coincide with the presence of multiband superconductivity, thus avoiding, or at least circumventing, Anderson's Theorem. Using an effective two-band model for a disordered superconductor, the maximum effect of pairbreaking was already found to be precisely at the Lifshitz transition [61], although the pairbreaking was claimed to be caused mainly by the repulsive coupling between the two bands.

In Chapter 3, we applied the same model using more reliable parameters, extrapolated from critical fields and Hall measurements on a (110)-$LaAlO_3/SrTiO_3$ interface: indeed, multiband superconductivity was found to be in an intermediate BCS-BEC regime, where the pairing window $\mu \pm \Omega$ is always fully contained within the lower band as in the standard BCS description, while the upper band stays in the BEC regime.

Although the model may be further improved – for instance considering a doping dependent tensor $\Gamma_{ij}^{-1}(\mu)$ instead of a global constant disorder Γ – two main aspects are already standing out.

First, from a purely theoretical point of view, we observed that a strong pairbreaking effect is intrinsically connected with the presence of microscopic disorder at the Lifshitz transition, and this is independent from the attraction or repulsion between the two bands involved, as it is indeed observed in unpaired bands. This is a striking result and more can be done in this direction, to better understand what symmetry breaking is involved at the Lifshitz point in presence of non-magnetic disorder.

Second, this study allowed us to disentangle microscopic from mesoscopic disor-

der in SrTiO$_3$-based interfaces: the dirty limit is in fact necessary to explain the suppression of T_c observed when multiband superconductivity is involved, where a role is most likely played also by the effective repulsion between the two bands; the global behavior is instead well captured only if the strongly inhomogeneous nature of such compounds is considered.

As a matter of fact, the presence of submicrometric inhomogeneities has been widely discussed in literature – not only in the context of SrTiO$_3$-based interfaces – the main consequence being the inability to observe BKT signatures. This was confirmed also by some recent transport experiments on a LaAlO$_3$/SrTiO$_3$ sample, where the superfluid stiffness and the optical conductivity were measured via a resonant RLC microwave circuit, the stiffness showing no signatures of the peculiar BKT jump. In Chapter 4, we analyzed those measurements in terms of a percolative transition scenario.

To this aim the RRN model, already used to account for the large broadening of the resistive transition, was extended to finite frequency, the resistors being substituted by complex impedances so the resulting model was called more appropriately RIN. Here, the main features were explained in terms of a filamentary superconducting structure embedded in a metallic background and enlarged by some proximization effect apt to strengthen superconductivity.

Filamentarity was already invoked in such systems to account for the long tails of the resistive transition, this scenario being consistent with the long tails of J_s observed right below the percolative temperature ($R = 0$); besides, the rather high value of the optical conductivity at low temperatures provides another indication that the system still presents an important metallic residue.

This quasi-one-dimensional picture of the electronic condensate however is not sufficient to describe the sudden jump of J_s, which tends to be more pronounced with the increase of voltage doping. Hence, some proximization process must intervene on the underlying metal.

After a preliminary study within the EMT approximate solution of the RIN model, we solved the RIN exact solution, where geometry plays a crucial role. In particular, the two regimes of doping identified – UD and OD – can be explained in terms of a more or less dense fractal of superconducting filaments. The increase of J_s at temperatures lower than the critical one finds its meaning in the resulting proximized background, whose superconducting condensate appears as a quasi-two-dimensional system in the OD case, justifying the abrupt jump of J_s, while, on the other side, a more sparse fractal produces the longer tails and the more smooth behavior of J_s in the UD regime.

While we can state the emergence of an interesting phenomenology connected with filamentary superconductivity, at least two more paths can be followed towards a wider comprehension of it. On the one hand, more can be done including dissipative effects, addressed quickly in this Thesis only in the EMT approximation and only concerning the superfluid response, to recover the higher values found in the residual conductivity. For instance, one can consider the possibility that Abrikosov-like vortices can be generated in the system, i.e., in any closed loop of superconducting current, contributing to dissipation. Although it is insightful, the phenomenological approach of the RIN neglects the very cause of why such filamentary structure can

arise. While it has been suggested in fact that in SrTiO$_3$-based heterostructures and TMDs, the inhomogeneities are due to phase separation of the electronic condensate caused by electron instability [23], this does not answer the question: why phase separation sometimes collapses into this fractal-like structure? And, moreover, what is the physical origin of the proximization of the filamentary structure?

Another aspect of filamentary superconductivity was treated in Chapter 5, concerning this time its origin in cuprates superconductors. Along the lines of the model proposed in [31, 32], superconducting filaments are expected to appear as the topologically protected boundaries between two different CDW wave variants, hence directly resulting from the competition between the tendency of electrons to condensate in real or in momentum space. A similar idea of competing orders was also applied to solid ^{4}He, in which superfluid characteristics can be caused to the frustration of the solid phase at grain boundaries [98]. We studied the CO-SC competition by means of Monte Carlo simulations within an anisotropic Heisenberg model accounting for the basic physical symmetries involved, where the out-of-plane pseudospin component maps two possible CDW variants while the in-plane component stands for the superconducting order parameter. In particular, the anisotropy term α tuning the out-of-plane component of the Hamiltonian was taken as the control parameter, playing the same role as the external magnetic field H in real systems [29]. The bare anisotropic Heisenberg model, used as an initial benchmark, identifies two kinds of transition: the BKT superconducting one for $\alpha < 1$ and the Ising one (CO) for $\alpha > 1$, while in the isotropic point $\alpha = 1$ no transition is possible according to Mermin-Wagner theorem [8]. A tunable effective potential barrier H_b was introduced to trigger the CO-SC competition, breaking the SO(3) symmetry also in $\alpha = 1$. The phase diagram T_c vs α was then studied in the clean case and with a random field, apt to mime impurities.

Concerning the clean case, we found the emergence of metastability and a first order transition between CO and superconductivity; the phase diagram was studied both analytically for $T = 0$ and numerically at finite temperature for a barrier potential parameter $b = 0.1$. A triple point was found at $\alpha \gtrsim 1$, were the second order line of the Ising transition met with the BKT line and the first order line, this last one terminating in $\alpha = 1$; from this triple point also two spinodal lines come out, terminating at $T = 0$ in $\alpha^*_{SC,CO} = 1 \pm 4b$. A re-entrant superconducting state is found for $\alpha \gtrsim 1$, underlying the analogy between supersolid-superfluid competition in ^{4}He and the CO-SC competition in cuprates.

Introducing a random field, the CO state breaks into a polycrystalline CDW, where filamentary superconductivity can arise from the frustration of two different CDW domains. We tuned opportunely the amount of disorder to observe such one-dimensional-like superconducting clusters in the $T \simeq 0$ pseudospins configuration. Concerning the states at $\alpha \gg 1$, where superconductivity is fully suppressed, the polycrystalline state has been studied by means of the spatial correlation function of the out-of-plane direction, since the magnetization was no more a reliable criterion to address the state. On the other hand, superconductivity was found to be resilient up to values $\alpha \gtrsim 1$, consistently with experiments [29]. Specifically, both the critical temperature T_{BKT} and the saturating value of $J_s(T \to 0)$ were slightly suppressed for $\alpha < 1$, although clear BKT signatures were still observables. This was not

the case for $\alpha \gtrsim 1$, where a finite superfluid stiffness was found, indicating the presence of a phase rigidity of the system, but the BKT scaling relation was not so straightforward to apply and the BKT jump of J_s was difficult to address. This was particularly true for $\alpha = 1.1$, while for $\alpha = 1$ and $\alpha = 1.05$ the situation was more settled.

So far, we only scratched the surface in the study of the main properties of filamentary superconductivity in cuprates. While on the one hand we confirmed that filamentary superconductivity appears as a topologically protected boundary between different CDW variants, many issues are left to be solved, concerning, for instance, the universality class of the superfluid response at $\alpha \geq 1.1$. Among the many possible paths, the next one to follow would be the study of the in-plane spatial correlation function and the corresponding correlation length, apt to analyze the vortex dissipation in $\alpha = 1.1$ as in all the range between $1.1 < \alpha < 1.5$, where we expect BKT signatures to be definitely suppressed but were we still expect some superfluid response of the system.

Finally, the Heisenberg model, where the filamentarity arises naturally as a consequence of the CO-SC competition, and the RIN model, where instead the filamentarity is imposed by hand, can be connected to one another in order to study both the presence of vortices and the percolative nature of the transition.

Appendix A

Two band superconductivity

In this Section, we will derive the general BCS formula for the gap equation in a multi-band system. Calling $g_{\alpha\beta}$ the dimensional couplings in the bands indices α and β, the BCS Hamiltonian reads as

$$H = \sum_{\substack{k,\sigma \\ \alpha}} \xi_{\alpha,k} c^\dagger_{\alpha,k\sigma} c_{\alpha,k\sigma} - \sum_{\substack{k,k' \\ \alpha,\beta}} g_{\alpha\beta} c^\dagger_{\alpha,k\uparrow} c^\dagger_{\alpha,-k\downarrow} c_{\beta,-k'\downarrow} c_{\beta,k\uparrow} \tag{A.1}$$

where k and k' are the moment indices, σ indicates the fermionic spin and c and $c^\dagger$ are respectively the annihilation and creation operators. Renaming $A^\dagger_\alpha = <c^\dagger_{\alpha,k\uparrow} c^\dagger_{\alpha,-k\downarrow}>$ and $A_\beta = <c_{\beta,-k'\downarrow} c_{\beta,k\uparrow}>$, the mean field approximation lead us to write

$$\begin{aligned}
c^\dagger_{\alpha,k\uparrow} c^\dagger_{\alpha,-k\downarrow} c_{\beta,-k'\downarrow} c_{\beta,k\uparrow} &= <c^\dagger_{\alpha,k\uparrow} c^\dagger_{\alpha,-k\downarrow}> c_{\beta,-k'\downarrow} c_{\beta,k\uparrow} + \\
&\quad + c^\dagger_{\alpha,k\uparrow} c^\dagger_{\alpha,-k\downarrow} <c_{\beta,-k'\downarrow} c_{\beta,k\uparrow}> + \\
&\quad - <c^\dagger_{\alpha,k\uparrow} c^\dagger_{\alpha,-k\downarrow}><c_{\beta,-k'\downarrow} c_{\beta,k\uparrow}> \\
&= A^\dagger_\alpha c_{\beta,-k'\downarrow} c_{\beta,k\uparrow} + c^\dagger_{\alpha,k\uparrow} c^\dagger_{\alpha,-k\downarrow} A_\beta - A^\dagger_\alpha A_\beta.
\end{aligned} \tag{A.2}$$

Using the anti-commutation relations, the kinetik term in Eq. (A.1) takes the form:

$$c^\dagger_{\alpha,k\uparrow} c_{\alpha,k\uparrow} - c^\dagger_{\alpha,-k\downarrow} c_{\alpha,-k\downarrow} + 1.$$

Finally, with the help of the Nambu notation:

$$\psi^\dagger_{\alpha,k} = \begin{pmatrix} c^\dagger_{\alpha,k\uparrow} \\ c_{\alpha,-k\downarrow} \end{pmatrix}, \qquad \psi_{\alpha,k} = (c_{\alpha,k\uparrow}, c^\dagger_{\alpha,-k\downarrow}) \tag{A.3}$$

one can write the effective mean field Hamiltonian as

$$H_{MF} = \sum_{k,\alpha} \psi^\dagger_{\alpha,k} \hat{\mathcal{H}}_{\alpha,k} \psi_{\alpha,k} + \sum_{k,\alpha} \xi_{\alpha,k} + \sum_{\substack{k \\ \alpha,\beta}} g_{\alpha\beta} A^\dagger_\alpha A_\beta \tag{A.4}$$

with

$$\hat{\mathcal{H}} = \begin{pmatrix} \xi_{1,k} & \Delta_1 & 0 & 0 \\ \Delta_1^* & -\xi_{1,k} & 0 & 0 \\ 0 & 0 & \xi_{2,k} & \Delta_2 \\ 0 & 0 & \Delta_2^* & -\xi_{2,k} \end{pmatrix} \tag{A.5}$$

The associated Green's function is defined as $G^{-1} = i\omega_n - \hat{\mathcal{H}}$, so the free energy potential assumes the form

$$F = -T \ln \mathcal{Z} = -T \sum_{k,i\omega_n} \text{Tr}(\ln G) - \sum_{k,\alpha} \xi_{\alpha,k} + \sum_{\substack{k \\ \alpha,\beta}} g_{\alpha\beta} A_\alpha^\dagger A_\beta. \qquad (A.6)$$

The self-consistent gap equations for the two bands system can be found from $\frac{\partial F}{\partial \Delta_\alpha} = 0$ and can be written as

$$\Delta_\alpha = k_B T \sum_{\substack{k,i\omega_n \\ \beta}} \frac{g_{\alpha\beta}\Delta_\beta}{\omega_n^2 + \xi_{\beta,k}^2 + \Delta_\beta^2} \qquad (A.7)$$

where k_B is the Boltzmann constant.

Note that $g_{\alpha\beta}$ refers to the dimensional couplings and they should respect the relation $g_{12} = g_{21}$ in order for the Hamiltonian to be hermitian. Henceforth we will define the matrix of dimensionless couplings $\hat{\lambda}$ such that $\lambda_{\alpha\beta} = g_{\alpha\beta}N_\alpha$, N_α being the density of state of band α. Summing over Matsubara frequencies one can use the relation $k_B T \sum_{i\omega_n} \frac{1}{i\omega_n - a} \frac{1}{i\omega_n - b} = \frac{f(a) - f(b)}{a - b}$ where $f(x) = (1 + \exp(x/k_B T))^{-1}$ is the Fermi distribution, we can rewrite the term

$$k_B T \sum_{i\omega_n,k} \frac{1}{(i\omega_n)^2 + \xi_{\alpha,k}^2 + \Delta_{\alpha,k}^2} = \sum_{|k|<\Omega} \frac{1}{2(\xi_{\alpha,k}^2 + \Delta_{\alpha,k}^2)} \tanh\left(\frac{\xi_{\alpha,k}^2 + \Delta_{\alpha,k}^2}{2k_B T}\right) \quad (A.8)$$

valid for a clean system in the BCS limit, with a Debye energy Ω. Finally, linearizing the gap equation at the critical point the former becomes $N_\alpha \ln(1.13\Omega/k_B T_c)$ and we obtain

$$\Delta_\alpha = \sum_\beta \lambda_{\alpha\beta} \Delta_\beta \ln\left(\frac{1.13\Omega}{k_B T_c}\right) \qquad (A.9)$$

Appendix B

Self energy corrections: the averaged $T-$matrix

We derive here the self-energy corrections caused by the presence of non-magnetic impurities in a two band superconducting system [61, 128].

Let us define the scattering potential matrix $\hat{U}$ with respect to the band index, which accounts for intra- and inter-band scattering, as

$$\hat{U} = \begin{pmatrix} v\tau_3 & u\tau_3 \\ u\tau_3 & v\tau_3 \end{pmatrix} \tag{B.1}$$

where v and u defines respectively the intra- and inter-band scattering rates, τ_i being the set of Pauli Matrices

$$\tau_0 = \begin{pmatrix} 1 & 0 \\ 0 & 1 \end{pmatrix}; \quad \tau_1 = \begin{pmatrix} 0 & 1 \\ 1 & 0 \end{pmatrix}; \quad \tau_3 = \begin{pmatrix} 0 & -i \\ i & 0 \end{pmatrix}; \quad \tau_3 = \begin{pmatrix} 1 & 0 \\ 0 & -1 \end{pmatrix} \tag{B.2}$$

The Green's functions of the two-band system can also be written in terms of the band index as

$$\hat{G} = \begin{pmatrix} \mathcal{G}_{\mathbf{k},i} & 0 \\ 0 & \mathcal{G}_{\mathbf{k},i} \end{pmatrix} \tag{B.3}$$

where $\mathcal{G}_{\mathbf{k},i}$ is the Green's function of the i-th band:

$$\mathcal{G}_{\mathbf{k},i} = \frac{1}{(i\omega_n)^2 + \Delta_{\mathbf{k},i}^2 + \xi_{\mathbf{k},i}^2} \begin{pmatrix} i\omega_n + \xi_{\mathbf{k},i} & \Delta_{\mathbf{k},i} \\ \Delta_{\mathbf{k},i}^* & i\omega_n - \xi_{\mathbf{k},i} \end{pmatrix}, \tag{B.4}$$

ω stands for the Matsubara real frequencies, $\xi = \varepsilon - \mu$ is the reduced energy and Δ is the superconducting gap.

The corrected scattering matrix $\hat{T}$ for a single impurity in a singlet superconductor (*s*-wave symmetry) can be found by means of the Dyson equation, written in its compact form as

$$\hat{T} = \hat{U} + \hat{T}\hat{G}\hat{U} \tag{B.5}$$

which exactly accounts for and sums over the processes of multiple scattering off that impurity. Being the scattering matrix $\hat{U}$ only dependent on the band index, so

it will be the $\hat{T}$-matrix:

$$\hat{T}_{ij} = \hat{U}_{ij} + \sum \hat{U}_{il} \left[\sum_{\mathbf{k}'} \mathcal{G}_{\mathbf{k},l} \right] \hat{T}_{lj}. \tag{B.6}$$

Solving it, we have

$$\hat{T} = (\hat{U}^{-1} - \hat{G})^{-1}$$

At this point, calculating explicitly all the terms $\hat{T}_{ij}$ one finds that the off-diagonal terms (in the band index) are all linear combinations of odd powers of u and v. Then, assuming an homogeneous distribution of impurities and averaging over u and v the off-diagonal terms disappears and the $\hat{T}$ matrix becomes diagonal in the band index, restoring the translational invariance [128]. Note that, although we kept separated the band indices and the intra- and inter-band scattering rates, both the diagonal terms $\hat{T}_{11}$ and $\hat{T}_{22}$ contains u and v, meaning that the impurities have in fact coupled the two bands, still respecting the momentum conservation.

The self-energy in the i-th band $i = 1, 2$ can be thus taken as $\Sigma_i = n_{imp}T_{ii}$, n_{imp} being the number of impurities considered in the system. We also assumed that $u = v$ and, moreover, we can use the Born approximation result for which $\hbar\tau^{-1} = n_{imp}|u|^2$ [129], where τ is the mean free time between collisions. We can then correct the Green's function in the i-th band with the self-energy

$$G_i = \frac{1}{i\omega_n\tau_0 + \xi_{\mathbf{k},i}\tau_3 - \Delta_i\tau_1 - \Sigma_i} \tag{B.7}$$

where Σ takes the general form

$$\Sigma_i = \Sigma_\omega\tau_0 + \Sigma_\mu\tau_3 + \Sigma_{\Delta_i}\tau_1. \tag{B.8}$$

However, from the averaging over the impurities the correction to the gap is found to be zero $\Sigma_{\Delta_i} = 0$. The diagonal terms of the self-energy are instead:

$$\begin{cases} \Sigma_\omega = \frac{\Gamma\widetilde{\omega}_n}{2} \sum_{j=1,2,\mathbf{k}} \frac{1}{N_j} \frac{1}{\widetilde{\omega}_n^2 + (\xi_{\mathbf{k}}+h_n)^2} \\ \\ \Sigma_\mu = -\frac{\Gamma}{2} \sum_{j=1,2,\mathbf{k}} \frac{1}{N_j} \frac{(\xi_{\mathbf{k}}+h_n)}{\widetilde{\omega}_n^2 + (\xi_{\mathbf{k}}+h_n)^2} \end{cases} \tag{B.9}$$

where we have substituted the Born result as $\Gamma = \hbar\tau^{-1}/2$, $\omega_n = (2n+1)\pi k_B T$, n ranging over integer numbers, is the Matsubara frequency of the clean system and N_j is the DOS of the j-th band.

By transforming the sum over $\mathbf{k}$ in the integral over ξ, ranging in the finite band having edges w_j and Λ_j , we can define the functions

$$\tilde{f}_{n,j} = \frac{1}{\pi} \int_{w_j}^{\Lambda_j} \frac{d\xi}{\widetilde{\omega}_n^2 + (\xi + h_n)^2},$$

$$\tilde{g}_{n,j} = \frac{1}{\pi} \int_{w_j}^{\Lambda_j} \frac{(\xi + h_n)d\xi}{\widetilde{\omega}_n^2 + (\xi + h_n)^2},$$

finally writing the self-consistent form given in Eq. (3.5)

$$\begin{cases} \widetilde{\omega}_n = \omega_n + \frac{\Gamma\widetilde{\omega}_n}{2} \sum_{j=1,2} \tilde{f}_{n,j} \\ \\ h_n = -\frac{\Gamma}{2} \sum_{j=1,2} \tilde{g}_{n,j}. \end{cases}$$

Appendix C

Vertex corrections

We can derive the vertex correction to the gap equation in (A.7) within the more compact notation of Feynman diagrams:

The dotted line is the impurity scattering correction, i.e., the inverse scattering time $\hbar\tau^{-1}/2$. Note that we consider $\tau_{\alpha\beta}^{-1} = \tau^{-1}$ as a constant along all Chapter 3. The corrected vertex (double line) is then:

$$L_{\alpha\beta} = \frac{\hbar\tau_{\alpha\beta}^{-1}}{2} + \frac{\hbar\tau_{\alpha\beta}^{-1}}{2} \left(\int G(\xi)_\gamma d\xi \right) L_{\gamma\beta} \tag{C.1}$$

We can re-arrange the terms as

$$\left[L_{\alpha\gamma}\delta_{\gamma\beta} + \frac{\hbar\tau_{\alpha\beta}^{-1}}{2} \left(\int G(\xi)_\gamma d\xi \right) L_{\gamma\beta} \right] = \frac{\hbar\tau_{\alpha\beta}^{-1}}{2} \tag{C.2}$$

so that

$$M_{\alpha\gamma}^{-1} \hat{L}_{\gamma\beta} = \frac{\hbar\tau_{\alpha\beta}^{-1}}{2} \tag{C.3}$$

having defined $M_{\alpha\gamma}^{-1} = \delta_{\alpha\gamma} - \frac{\hbar\tau_{\alpha\beta}^{-1}}{2} \int G(\xi)_\gamma d\xi$.

Finally we obtain

$$L_{\gamma\beta} = M_{\gamma\alpha} \frac{\hbar\tau_{\alpha\beta}^{-1}}{2} \tag{C.4}$$

and the bare coupling constants λ are

$$\lambda_{\alpha\beta} \to \lambda_{\alpha\beta} \frac{M_{\alpha\beta}}{\det(M)}. \tag{C.5}$$

Remembering that we defined a constant disorder $\Gamma = \hbar\tau^{-1}/2$ and

$$\tilde{f}_{n,\alpha} = \frac{1}{\pi} \int_{w_\alpha}^{\Lambda_j} \frac{d\xi}{\tilde{\omega}_n^2 + (\xi + h_n)^2}, \tag{C.6}$$

the matrix M takes its final form of Eq. (3.8)

$$M = \begin{pmatrix} 1 - \frac{\Gamma}{2}\tilde{f}_{n,2} & \frac{\Gamma}{2}\tilde{f}_{n,2} \\[2mm] \frac{\Gamma}{2}\tilde{f}_{n,1} & 1 - \frac{\Gamma}{2}\tilde{f}_{n,1} \end{pmatrix} \tag{C.7}$$

Bibliography

[1] H. K. Onnes, "The discovery of superconductivity," *Commun. Phys. Lab*, vol. 12, p. 120, 1911.

[2] J. Bardeen, L. N. Cooper, and J. R. Schrieffer, "Microscopic theory of super-conductivity," *Physical Review*, vol. 106, no. 1, p. 162, 1957.

[3] J. Bardeen, L. N. Cooper, and J. R. Schrieffer, "Theory of superconductivity," *Physical review*, vol. 108, no. 5, p. 1175, 1957.

[4] J. G. Bednorz and K. A. Müller, "Possible high T_c superconductivity in the $Ba - La - Cu - O$ system," *Zeitschrift für Physik B Condensed Matter*, vol. 64, no. 2, pp. 189–193, 1986.

[5] V. L. Berezinsky, "Destruction of long-range order in one-dimensional and two-dimensional systems having a continuous symmetry group I. Classical systems," *Soviet Physics JETP*, vol. 32, no. 3, pp. 907–920, 1972.

[6] J. M. Kosterlitz and D. J. Thouless, "Ordering, metastability and phase transitions in two-dimensional systems," *Journal of Physics C: Solid State Physics*, vol. 6, no. 7, p. 1181, 1973.

[7] J. Kosterlitz, "The critical properties of the two-dimensional XY model," *Journal of Physics C: Solid State Physics*, vol. 7, no. 6, p. 1046, 1974.

[8] N. D. Mermin and H. Wagner, "Absence of ferromagnetism or antiferro-magnetism in one-or two-dimensional isotropic Heisenberg models," *Physical Review Letters*, vol. 17, no. 22, p. 1133, 1966.

[9] P. W. Anderson, "Theory of dirty superconductors," *Journal of Physics and Chemistry of Solids*, vol. 11, no. 1-2, pp. 26–30, 1959.

[10] M. Ma and P. A. Lee, "Localized superconductors," *Physical Review B*, vol. 32, no. 9, p. 5658, 1985.

[11] A. Ohtomo and H. Hwang, "A high-mobility electron gas at the $LaAlO_3/SrTiO_3$ heterointerface," *Nature*, vol. 427, no. 6973, pp. 423–426, 2004.

[12] G. Venditti, M. Grilli, and S. Caprara, "On the superconducting critical temperature of heavily disordered interfaces hosting multi-gap superconductivity," *Coatings*, vol. 12, no. 1, p. 30, 2022.

[13] G. Singh, G. Venditti, G. Saiz, G. Herranz, F. Sánchez, A. Jouan, A. Feuillet-Palma, J. Lesueur, M. Grilli, S. Caprara, and N. Bergeal, "Two-gap s±-wave superconductivity in an oxide interface,"

[14] C. Richter, H. Boschker, W. Dietsche, E. Fillis-Tsirakis, R. Jany, F. Loder, L. F. Kourkoutis, D. A. Muller, J. R. Kirtley, C. W. Schneider, *et al.*, "Interface superconductor with gap behaviour like a high-temperature superconductor," *Nature*, vol. 502, no. 7472, pp. 528–531, 2013.

[15] D. Bucheli, S. Caprara, and M. Grilli, "Pseudo-gap as a signature of inhomogeneous superconductivity in oxide interfaces," *Superconductor Science and Technology*, vol. 28, no. 4, p. 045004, 2015.

[16] F. Bi, M. Huang, C. W. Bark, S. Ryu, S. Lee, C.-B. Eom, P. Irvin, and J. Levy, "Electro-mechanical response of top-gated $LaAlO_3$/$SrTiO_3$ heterostructures," *arXiv preprint arXiv:1302.0204*, 2013.

[17] G. Venditti, J. Biscaras, S. Hurand, N. Bergeal, J. Lesueur, A. Dogra, R. C. Budhani, M. Mondal, J. Jesudasan, P. Raychaudhuri, S. Caprara, and L. Benfatto, "Nonlinear $I - V$ characteristics of two-dimensional superconductors: $Berezinskii - Kosterlitz - Thouless$ physics versus inhomogeneity," *Phys. Rev. B*, vol. 100, p. 064506, Aug 2019.

[18] S. Caprara, M. Grilli, L. Benfatto, and C. Castellani, "Effective medium theory for superconducting layers: A systematic analysis including space correlation effects," *Physical Review B*, vol. 84, no. 1, p. 014514, 2011.

[19] D. Bucheli, S. Caprara, C. Castellani, and M. Grilli, "Metal–superconductor transition in low-dimensional superconducting clusters embedded in two-dimensional electron systems," *New Journal of Physics*, vol. 15, no. 2, p. 023014, 2013.

[20] D. Bucheli, M. Grilli, F. Peronaci, G. Seibold, and S. Caprara, "Phase diagrams of voltage-gated oxide interfaces with strong Rashba coupling," *Physical Review B*, vol. 89, no. 19, p. 195448, 2014.

[21] S. Caprara, J. Biscaras, N. Bergeal, D. Bucheli, S. Hurand, C. Feuillet-Palma, A. Rastogi, R. Budhani, J. Lesueur, and M. Grilli, "Multiband superconductivity and nanoscale inhomogeneity at oxide interfaces," *Physical Review B*, vol. 88, no. 2, p. 020504, 2013.

[22] S. Caprara, D. Bucheli, N. Scopigno, N. Bergeal, J. Biscaras, S. Hurand, J. Lesueur, and M. Grilli, "Inhomogeneous multi carrier superconductivity at $LaXO_3$/$SrTiO_3$ (X = Al or Ti) oxide interfaces," *Superconductor Science and Technology*, vol. 28, no. 1, p. 014002, 2014.

[23] N. Scopigno, D. Bucheli, S. Caprara, J. Biscaras, N. Bergeal, J. Lesueur, and M. Grilli, "Phase separation from electron confinement at oxide interfaces," *Physical review letters*, vol. 116, no. 2, p. 026804, 2016.

[24] G. Singh, A. Jouan, L. Benfatto, F. Couëdo, P. Kumar, A. Dogra, R. Budhani, S. Caprara, M. Grilli, E. Lesne, *et al.*, "Competition between electron pairing and phase coherence in superconducting interfaces," *Nature communications*, vol. 9, no. 1, pp. 1–8, 2018.

[25] G. Venditti, I. Maccari, M. Grilli, and S. Caprara, "Superfluid properties of superconductors with disorder at the nanoscale: A Random Impedance Model," *Condensed Matter*, vol. 5, no. 2, p. 36, 2020.

[26] G. Venditti, I. Maccari, M. Grilli, and S. Caprara, "Finite-frequency dissipation in two-dimensional superconductors with disorder at the nanoscale," *Nanomaterials*, vol. 11, no. 8, p. 1888, 2021.

[27] G. Singh, A. Jouan, G. Venditti, I. Maccari, J. Lesueur, M. Grilli, S. Caprara, and N. Bergeal, "Superfluid density and intrinsic proximity effect in filamentary superconductors,"

[28] P. Baity, X. Shi, Z. Shi, L. Benfatto, and D. Popović, "Effective two-dimensional thickness for the Berezinskii − Kosterlitz − Thouless−like transition in a highly underdoped $La_{2-x}Sr_xCuO_4$," *Physical Review B*, vol. 93, no. 2, p. 024519, 2016.

[29] S. Caprara, M. Grilli, J. Lorenzana, and B. Leridon, "Doping-dependent competition between superconductivity and polycrystalline charge density waves," *SciPost Physics*, vol. 8, no. 1, p. 003, 2020.

[30] C. Balseiro and L. Falicov, "Superconductivity and charge-density waves," *Physical Review B*, vol. 20, no. 11, p. 4457, 1979.

[31] A. Attanasi, "Competition between superconductivity and charge density waves: the role of disorder," *arXiv preprint arXiv:0906.1159*, 2009.

[32] B. Leridon, S. Caprara, J. Vanacken, V. Moshchalkov, B. Vignolle, R. Porwal, R. Budhani, A. Attanasi, M. Grilli, and J. Lorenzana, "Protected superconductivity at the boundaries of charge-density-wave domains," *New Journal of Physics*, vol. 22, no. 7, p. 073025, 2020.

[33] S. Kirkpatrick, "Percolation and conduction," *Reviews of modern physics*, vol. 45, no. 4, p. 574, 1973.

[34] N. Nagaosa, *Quantum field theory in condensed matter physics.* Springer Science & Business Media, 1999.

[35] M. Tinkham, *Introduction to superconductivity.* Courier Corporation, 2004.

[36] P.-G. De Gennes and P. A. Pincus, *Superconductivity of metals and alloys.* CRC Press, 2018.

[37] P. Raychaudhuri and S. Dutta, "Phase fluctuations in conventional superconductors," *Journal of Physics: Condensed Matter*, vol. 34, no. 8, p. 083001, 2021.

[38] L. D. Landau and V. L. Ginzburg, "On the theory of superconductivity," *Zh. Eksp. Teor. Fiz.*, vol. 20, p. 1064, 1950.

[39] V. L. Ginzburg and L. D. Landau, "On the theory of superconductivity," in *On Superconductivity and Superfluidity*, pp. 113–137, Springer, 2009.

[40] P. M. Chaikin, T. C. Lubensky, and T. A. Witten, *Principles of condensed matter physics*, vol. 10. Cambridge university press Cambridge, 1995.

[41] T. Giamarchi, "Oxford university press. quantum physics in one dimension," *International Series of Monogr (Clarendon Press, 2004)*, 2004.

[42] D. R. Nelson and J. Kosterlitz, "Universal jump in the superfluid density of two-dimensional superfluids," *Physical Review Letters*, vol. 39, no. 19, p. 1201, 1977.

[43] L. Benfatto, C. Castellani, and T. Giamarchi, "Broadening of the Berezinskii − Kosterlitz − Thouless superconducting transition by inhomogeneity and finite-size effects," *Physical Review B*, vol. 80, no. 21, p. 214506, 2009.

[44] B. Halperin and D. R. Nelson, "Resistive transition in superconducting films," *Journal of low temperature physics*, vol. 36, no. 5, pp. 599–616, 1979.

[45] K. Yoshimatsu, R. Yasuhara, H. Kumigashira, and M. Oshima, "Origin of metallic states at the heterointerface between the band insulators $LaAlO_3$ and $SrTiO_3$," *Physical review letters*, vol. 101, no. 2, p. 026802, 2008.

[46] R. Pentcheva and W. E. Pickett, "Electronic phenomena at complex oxide interfaces: insights from first principles," *Journal of Physics: Condensed Matter*, vol. 22, no. 4, p. 043001, 2010.

[47] Y.-Y. Pai, A. Tylan-Tyler, P. Irvin, and J. Levy, "Physics of $SrTiO_3$-based heterostructures and nanostructures: a review," *Reports on Progress in Physics*, vol. 81, no. 3, p. 036503, 2018.

[48] L. Yu and A. Zunger, "A polarity-induced defect mechanism for conductivity and magnetism at polar–nonpolar oxide interfaces," *Nature communications*, vol. 5, no. 1, pp. 1–9, 2014.

[49] Y. Chen, N. Pryds, J. E. Kleibeuker, G. Koster, J. Sun, E. Stamate, B. Shen, G. Rijnders, and S. Linderoth, "Metallic and insulating interfaces of amorphous $SrTiO_3$-based oxide heterostructures," *Nano letters*, vol. 11, no. 9, pp. 3774–3778, 2011.

[50] G. De Luca, A. Rubano, E. d. Gennaro, A. Khare, F. M. Granozio, U. S. di Uccio, L. Marrucci, and D. Paparo, "Potential-well depth at amorphous-$LaAlO_3$/crystalline-$SrTiO_3$ interfaces measured by optical second harmonic generation," *Applied Physics Letters*, vol. 104, no. 26, p. 261603, 2014.

[51] N. Nakagawa, H. Y. Hwang, and D. A. Muller, "Why some interfaces cannot be sharp," *Nature materials*, vol. 5, no. 3, pp. 204–209, 2006.

[52] G. Herranz, G. Singh, N. Bergeal, A. Jouan, J. Lesueur, J. Gázquez, M. Varela, M. Scigaj, N. Dix, F. Sánchez, *et al.*, "Engineering two-dimensional superconductivity and Rashba spin–orbit coupling in $LaAlO_3$/$SrTiO_3$ quantum wells by selective orbital occupancy," *Nature communications*, vol. 6, no. 1, pp. 1–8, 2015.

[53] R. Fernandes, J. Haraldsen, P. Wölfle, and A. V. Balatsky, "Two-band superconductivity in doped $SrTiO_3$ films and interfaces," *Physical Review B*, vol. 87, no. 1, p. 014510, 2013.

[54] D. Valentinis, D. Van Der Marel, and C. Berthod, "BCS superconductivity near the band edge: Exact results for one and several bands," *Physical Review B*, vol. 94, no. 2, p. 024511, 2016.

[55] J. Biscaras, N. Bergeal, S. Hurand, C. Grossetête, A. Rastogi, R. Budhani, D. LeBoeuf, C. Proust, and J. Lesueur, "Two-dimensional superconducting phase in $LaAlO_3$/$SrTiO_3$ heterostructures induced by high-mobility carrier doping," *Physical review letters*, vol. 108, no. 24, p. 247004, 2012.

[56] E. Maniv, M. B. Shalom, A. Ron, M. Mograbi, A. Palevski, M. Goldstein, and Y. Dagan, "Strong correlations elucidate the electronic structure and phase diagram of $LaAlO_3$/$SrTiO_3$ interface," *Nature communications*, vol. 6, no. 1, pp. 1–7, 2015.

[57] S. Shen, B. Chen, H. Xue, G. Cao, C. Li, X. Wang, Y. Hong, G. Guo, R. Dou, C. Xiong, *et al.*, "Gate dependence of upper critical field in superconducting (110) $LaAlO_3$/$SrTiO_3$ interface," *Scientific reports*, vol. 6, no. 1, pp. 1–6, 2016.

[58] G. Singh, A. Jouan, G. Herranz, M. Scigaj, F. Sánchez, L. Benfatto, S. Caprara, M. Grilli, G. Saiz, F. Couëdo, *et al.*, "Gap suppression at a Lifshitz transition in a multi-condensate superconductor," *Nature materials*, vol. 18, no. 9, pp. 948–954, 2019.

[59] P. Rout, E. Maniv, and Y. Dagan, "Link between the superconducting dome and spin-orbit interaction in the (111) $LaAlO_3$/$SrTiO_3$ interface," *Physical review letters*, vol. 119, no. 23, p. 237002, 2017.

[60] M. Zegrodnik and P. Wójcik, "Superconducting dome in $LaAlO_3$/$SrTiO_3$ interfaces as a direct consequence of the extended s-wave symmetry of the gap," *Physical Review B*, vol. 102, no. 8, p. 085420, 2020.

[61] T. V. Trevisan, M. Schütt, and R. M. Fernandes, "Unconventional multiband superconductivity in bulk $SrTiO_3$ and $LaAlO_3$/$SrTiO_3$ interfaces," *Physical review letters*, vol. 121, no. 12, p. 127002, 2018.

[62] A. Caviglia, S. Gariglio, N. Reyren, D. Jaccard, T. Schneider, M. Gabay, S. Thiel, G. Hammerl, J. Mannhart, and J.-M. Triscone, "Electric field control of the $LaAlO_3$/$SrTiO_3$ interface ground state," *Nature*, vol. 456, no. 7222, pp. 624–627, 2008.

[63] M. Mondal, S. Kumar, M. Chand, A. Kamlapure, G. Saraswat, G. Seibold, L. Benfatto, and P. Raychaudhuri, "Role of the vortex-core energy on the Berezinskii − Kosterlitz − Thouless transition in thin films of nbn," *Physical review letters*, vol. 107, no. 21, p. 217003, 2011.

[64] I. Maccari, L. Benfatto, and C. Castellani, "The BKT universality class in the presence of correlated disorder," *Condensed Matter*, vol. 3, no. 1, p. 8, 2018.

[65] I. Maccari, L. Benfatto, and C. Castellani, "Disordered XY model: Effective medium theory and beyond," *Physical Review B*, vol. 99, no. 10, p. 104509, 2019.

[66] L. Aslamasov and A. Larkin, "The influence of fluctuation pairing of electrons on the conductivity of normal metal," *Physics Letters A*, vol. 26, no. 6, pp. 238–239, 1968.

[67] A. Larkin and A. Varlamov, *Theory of fluctuations in superconductors*, vol. 127. OUP Oxford, 2005.

[68] L. Li, C. Chen, K. Watanabe, T. Taniguchi, Y. Zheng, Z. Xu, V. M. Pereira, K. P. Loh, and A. H. Castro Neto, "Anomalous quantum metal in a 2D crystalline superconductor with electronic phase nonuniformity," *Nano letters*, vol. 19, no. 6, pp. 4126–4133, 2019.

[69] A. Tsen, B. Hunt, Y. Kim, Z. Yuan, S. Jia, R. Cava, J. Hone, P. Kim, C. Dean, and A. Pasupathy, "Nature of the quantum metal in a two-dimensional crystalline superconductor," *Nature Physics*, vol. 12, no. 3, pp. 208–212, 2016.

[70] A. Kapitulnik, S. A. Kivelson, and B. Spivak, "Colloquium: anomalous metals: failed superconductors," *Reviews of Modern Physics*, vol. 91, no. 1, p. 011002, 2019.

[71] N. Reyren, S. Thiel, A. Caviglia, L. F. Kourkoutis, G. Hammerl, C. Richter, C. W. Schneider, T. Kopp, A.-S. Rüetschi, D. Jaccard, *et al.*, "Superconducting interfaces between insulating oxides," *Science*, vol. 317, no. 5842, pp. 1196–1199, 2007.

[72] J. Biscaras, N. Bergeal, A. Kushwaha, T. Wolf, A. Rastogi, R. C. Budhani, and J. Lesueur, "Two-dimensional superconductivity at a Mott insulator/band insulator interface $LaAlO_3/SrTiO_3$," *Nature communications*, vol. 1, no. 1, pp. 1–5, 2010.

[73] J. A. Bert, K. C. Nowack, B. Kalisky, H. Noad, J. R. Kirtley, C. Bell, H. K. Sato, M. Hosoda, Y. Hikita, H. Y. Hwang, *et al.*, "Gate-tuned superfluid density at the superconducting $LaAlO_3/SrTiO_3$ interface," *Physical Review B*, vol. 86, no. 6, p. 060503, 2012.

[74] G. Dezi, N. Scopigno, S. Caprara, and M. Grilli, "Negative electronic compressibility and nanoscale inhomogeneity in ionic-liquid gated two-dimensional superconductors," *Physical Review B*, vol. 98, no. 21, p. 214507, 2018.

[75] J. Biscaras, N. Bergeal, S. Hurand, C. Feuillet-Palma, A. Rastogi, R. Budhani, M. Grilli, S. Caprara, and J. Lesueur, "Multiple quantum criticality in a two-dimensional superconductor," *Nature materials*, vol. 12, no. 6, pp. 542–548, 2013.

[76] Q. H. Wang, K. Kalantar-Zadeh, A. Kis, J. N. Coleman, and M. S. Strano, "Electronics and optoelectronics of two-dimensional transition metal dichalcogenides," *Nature nanotechnology*, vol. 7, no. 11, pp. 699–712, 2012.

[77] Y. Saito, Y. Kasahara, J. Ye, Y. Iwasa, and T. Nojima, "Metallic ground state in an ion-gated two-dimensional superconductor," *Science*, vol. 350, no. 6259, pp. 409–413, 2015.

[78] J. Ye, Y. J. Zhang, R. Akashi, M. S. Bahramy, R. Arita, and Y. Iwasa, "Superconducting dome in a gate-tuned band insulator," *Science*, vol. 338, no. 6111, pp. 1193–1196, 2012.

[79] L. Li, E. O'Farrell, K. Loh, G. Eda, B. Özyilmaz, and A. C. Neto, "Controlling many-body states by the electric-field effect in a two-dimensional material," *Nature*, vol. 529, no. 7585, pp. 185–189, 2016.

[80] D. Bhoi, S. Khim, W. Nam, B. Lee, C. Kim, B.-G. Jeon, B. Min, S. Park, and K. H. Kim, "Interplay of charge density wave and multiband superconductivity in $2H - Pd_xTaSe_2$," *Scientific reports*, vol. 6, no. 1, pp. 1–10, 2016.

[81] G. Blatter, M. V. Feigel'man, V. B. Geshkenbein, A. I. Larkin, and V. M. Vinokur, "Vortices in high-temperature superconductors," *Reviews of modern physics*, vol. 66, no. 4, p. 1125, 1994.

[82] J. Corson, R. Mallozzi, J. Orenstein, J. Eckstein, and I. Bozovic, "Vanishing of phase coherence in underdoped $Bi_2Sr_2CaCu_2O_{8+\delta}$," *Nature*, vol. 398, no. 6724, pp. 221–223, 1999.

[83] D. Broun, W. Huttema, P. Turner, S. Özcan, B. Morgan, R. Liang, W. Hardy, and D. Bonn, "Superfluid density in a highly underdoped $YBa_2Cu_3O_{6+y}$ superconductor," *Physical review letters*, vol. 99, no. 23, p. 237003, 2007.

[84] Y. Zuev, M. S. Kim, and T. R. Lemberger, "Correlation between superfluid density and T_c of underdoped $YBa_2Cu_3O_{6+x}$ near the superconductor-insulator transition," *Physical review letters*, vol. 95, no. 13, p. 137002, 2005.

[85] I. Hetel, T. R. Lemberger, and M. Randeria, "Quantum critical behaviour in the superfluid density of strongly underdoped ultrathin copper oxide films," *Nature Physics*, vol. 3, no. 10, pp. 700–702, 2007.

[86] J. Yong, M. Hinton, A. McCray, M. Randeria, M. Naamneh, A. Kanigel, and T. Lemberger, "Evidence of two-dimensional quantum critical behavior in the superfluid density of extremely underdoped $Bi_2Sr_2CaCu_2O_{8+x}$," *Physical Review B*, vol. 85, no. 18, p. 180507, 2012.

[87] T. Timusk and B. Statt, "The pseudogap in high-temperature superconductors: an experimental survey," *Reports on Progress in Physics*, vol. 62, no. 1, p. 61, 1999.

[88] C. Renner, B. Revaz, J.-Y. Genoud, K. Kadowaki, and O. Fischer, "Pseudogap precursor of the superconducting gap in under-and overdoped $Bi_2Sr_2CaCu_2O_{8+\delta}$," *Physical Review Letters*, vol. 80, no. 1, p. 149, 1998.

[89] A. Loeser, Z.-X. Shen, D. Dessau, D. Marshall, C. Park, P. Fournier, and A. Kapitulnik, "Excitation gap in the normal state of underdoped $Bi_2Sr_2CaCu_2O_{8+\delta}$," *Science*, vol. 273, no. 5273, pp. 325–329, 1996.

[90] H. Ding, T. Yokoya, J. C. Campuzano, T. Takahashi, M. Randeria, M. Norman, T. Mochiku, K. Kadowaki, and J. Giapintzakis, "Spectroscopic evidence for a pseudogap in the normal state of underdoped high-T_c superconductors," *Nature*, vol. 382, no. 6586, pp. 51–54, 1996.

[91] V. M. Loktev, R. M. Quick, and S. G. Sharapov, "Phase fluctuations and pseudogap phenomena," *Physics Reports*, vol. 349, no. 1, pp. 1–123, 2001.

[92] R. Arpaia, S. Caprara, R. Fumagalli, G. De Vecchi, Y. Peng, E. Andersson, D. Betto, G. De Luca, N. Brookes, F. Lombardi, *et al.*, "Dynamical charge density fluctuations pervading the phase diagram of a Cu-based high-T_c superconductor," *Science*, vol. 365, no. 6456, pp. 906–910, 2019.

[93] J. Chang, E. Blackburn, A. Holmes, N. B. Christensen, J. Larsen, J. Mesot, R. Liang, D. Bonn, W. Hardy, A. Watenphul, *et al.*, "Direct observation of competition between superconductivity and charge density wave order in $YBa_2Cu_3O_{6.67}$," *Nature Physics*, vol. 8, no. 12, pp. 871–876, 2012.

[94] D. LeBoeuf, S. Krämer, W. Hardy, R. Liang, D. Bonn, and C. Proust, "Thermodynamic phase diagram of static charge order in underdoped $YBa_2Cu_3O_y$," *Nature Physics*, vol. 9, no. 2, pp. 79–83, 2013.

[95] J.-J. Wen, H. Huang, S.-J. Lee, H. Jang, J. Knight, Y. Lee, M. Fujita, K. Suzuki, S. Asano, S. Kivelson, *et al.*, "Observation of two types of charge-density-wave orders in superconducting $La_{2-x}Sr_xCuO_4$," *Nature communications*, vol. 10, no. 1, pp. 1–6, 2019.

[96] B. Keimer, S. A. Kivelson, M. R. Norman, S. Uchida, and J. Zaanen, "From quantum matter to high-temperature superconductivity in copper oxides," *Nature*, vol. 518, no. 7538, pp. 179–186, 2015.

[97] G. Boebinger, Y. Ando, A. Passner, T. Kimura, M. Okuya, J. Shimoyama, K. Kishio, K. Tamasaku, N. Ichikawa, and S. Uchida, "Insulator-to-metal crossover in the normal state of $La_{2-x}Sr_xCuO_4$ near optimum doping," *Physical Review Letters*, vol. 77, no. 27, p. 5417, 1996.

[98] S. Balibar and F. Caupin, "Supersolidity and disorder," *Journal of Physics: Condensed Matter*, vol. 20, no. 17, p. 173201, 2008.

[99] R. Micnas, J. Ranninger, and S. Robaszkiewicz, "Superconductivity in narrow-band systems with local nonretarded attractive interactions," *Reviews of Modern Physics*, vol. 62, no. 1, p. 113, 1990.

[100] L.-F. Lin, Y. Zhang, G. Alvarez, A. Moreo, and E. Dagotto, "Origin of insulating ferromagnetism in iron oxychalcogenide $Ce_2O_2FeSe_2$," *arXiv preprint arXiv:2105.09239*, 2021.

[101] G. Biswal and K. Mohanta, "A recent review on iron-based superconductor," *Materials Today: Proceedings*, vol. 35, pp. 207–215, 2021.

[102] M. Li, J. Huang, W. Guo, R. Yang, T. Hu, A. Yu, Y. Huang, M. Zhang, W. Zhang, J.-M. Zhang, *et al.*, "Pressure tuning of the iron-based superconductor $(Ca_0.73La_0.27)FeAs_2$," *Physical Review B*, vol. 103, no. 2, p. 024502, 2021.

[103] H. Xiao, T. Hu, A. Dioguardi, A. Shockley, J. Crocker, D. Nisson, Z. Viskadourakis, X. Tee, I. Radulov, C. Almasan, *et al.*, "Evidence for filamentary superconductivity nucleated at antiphase domain walls in antiferromagnetic $CaFe_2As_2$," *Physical Review B*, vol. 85, no. 2, p. 024530, 2012.

[104] H. Xiao, T. Hu, S. He, B. Shen, W. Zhang, B. Xu, K. He, J. Han, Y. Singh, H. Wen, *et al.*, "Filamentary superconductivity across the phase diagram of $Ba(Fe, Co)_2As_2$," *Physical Review B*, vol. 86, no. 6, p. 064521, 2012.

[105] K. Gofryk, M. Pan, C. Cantoni, B. Saparov, J. E. Mitchell, and A. S. Sefat, "Local inhomogeneity and filamentary superconductivity in Pr-doped $CaFe_2As_2$," *Physical review letters*, vol. 112, no. 4, p. 047005, 2014.

[106] E. W. Carlson, D. X. Yao, and D. K. Campbell, "Spin waves in striped phases," *Phys. Rev. B*, vol. 70, p. 064505, Aug 2004.

[107] J. Zhao, D.-X. Yao, S. Li, T. Hong, Y. Chen, S. Chang, W. Ratcliff, J. W. Lynn, H. A. Mook, G. F. Chen, J. L. Luo, N. L. Wang, E. W. Carlson, J. Hu, and P. Dai, "Low energy spin waves and magnetic interactions in $SrFe_2As_2$," *Phys. Rev. Lett.*, vol. 101, p. 167203, Oct 2008.

[108] Z. Wang, Z. Zhong, X. Hao, S. Gerhold, B. Stöger, M. Schmid, J. Sánchez-Barriga, A. Varykhalov, C. Franchini, K. Held, *et al.*, "Anisotropic two-dimensional electron gas at $SrTiO_3$ (110)," *Proceedings of the National Academy of Sciences*, vol. 111, no. 11, pp. 3933–3937, 2014.

[109] D. Markowitz and L. P. Kadanoff, "Effect of impurities upon critical temperature of anisotropic superconductors," *Physical Review*, vol. 131, no. 2, p. 563, 1963.

[110] S. Caprara, S. De Palo, C. Castellani, C. Di Castro, and M. Grilli, "Disorder effects in the t-J model," *Physical Review B*, vol. 131, p. 11996, 1995.

[111] E. Cappelluti, C. Grimaldi, and F. Marsiglio, "Topological change of the Fermi surface in low-density Rashba gases: application to superconductivity," *Physical review letters*, vol. 98, no. 16, p. 167002, 2007.

[112] S. Caprara, F. Peronaci, and M. Grilli, "Intrinsic instability of electronic interfaces with strong Rashba coupling," *Physical review letters*, vol. 109, no. 19, p. 196401, 2012.

[113] S. Caprara, G. Dezi, N. Scopigno, and M. Grilli, "Intrinsic inhomogeneity of 2d crystalline superconductors," *SUPERSTRIPES*, p. 163, 2017.

[114] A. Fiory and A. Hebard, "Radio-frequency complex-impedance measurements on thin film two-dimensional superconductors," in *AIP Conference Proceedings*, vol. 58, pp. 293–298, American Institute of Physics, 1980.

[115] J. Rodriguez, "Degradation of phase coherence by defects in a two-dimensional vortex lattice," *Physical review letters*, vol. 87, no. 20, p. 207001, 2001.

[116] J. Rodriguez, "Macroscopic phase coherence of defective vortex lattices in two dimensions," *Physical Review B*, vol. 72, no. 21, p. 214503, 2005.

[117] A. Cuccoli, V. Tognetti, P. Verrucchi, and R. Vaia, "Critical behavior of the two-dimensional easy-plane ferromagnet," *Journal of Applied Physics*, vol. 76, no. 10, pp. 6362–6364, 1994.

[118] A. Cuccoli, V. Tognetti, and R. Vaia, "Two-dimensional XXZ model on a square lattice: A Monte Carlo simulation," *Physical Review B*, vol. 52, no. 14, p. 10221, 1995.

[119] K. W. Lee, C. E. Lee, and I.-m. Kim, "Helicity modulus and vortex density in the two-dimensional easy-plane heisenberg model on a square lattice," *Solid state communications*, vol. 135, no. 1-2, pp. 95–98, 2005.

[120] K. Binder, "Finite size scaling analysis of Ising model block distribution functions," *Zeitschrift für Physik B Condensed Matter*, vol. 43, no. 2, pp. 119–140, 1981.

[121] D. Landau, "Non-universal critical behavior in the planar XY-model with fourth order anisotropy," *Journal of Magnetism and Magnetic Materials*, vol. 31, pp. 1115–1116, 1983.

[122] M. Hasenbusch, "The binder cumulant at the Kosterlitz − −Thouless transition," *Journal of Statistical Mechanics: Theory and Experiment*, vol. 2008, no. 08, p. P08003, 2008.

[123] K. W. Lee and C. E. Lee, "Monte carlo study of the Kosterlitz − Thouless transition in the heisenberg model with antisymmetric exchange interactions," *Physical Review B*, vol. 72, no. 5, p. 054439, 2005.

[124] H. Weber and P. Minnhagen, "Monte carlo determination of the critical temperature for the two-dimensional XY model," *Physical Review B*, vol. 37, no. 10, p. 5986, 1988.

[125] S. Menezes, M. Gouvêa, and A. Pires, "Calculation of the spin stiffness for 2D easy-plane magnets," *Physics Letters A*, vol. 166, no. 5-6, pp. 330–334, 1992.

[126] S. Teitel, "The two-dimensional fully frustrated XY model," in *40 Years of Berezinskii–Kosterlitz–Thouless Theory*, pp. 201–235, World Scientific, 2013.

[127] I. Maccari, L. Benfatto, and C. Castellani, "Uniformly frustrated XY model: strengthening of the vortex lattice by intrinsic disorder," *Condensed Matter*, vol. 6, no. 4, p. 42, 2021.

[128] X. Chen, V. Mishra, S. Maiti, and P. Hirschfeld, "Effect of nonmagnetic impurities on s±superconductivity in the presence of incipient bands," *Physical Review B*, vol. 94, no. 5, p. 054524, 2016.

[129] A. A. Abrikosov, L. P. Gorkov, and I. E. Dzyaloshinski, *Methods of quantum field theory in statistical physics.* Courier Corporation, 2012.